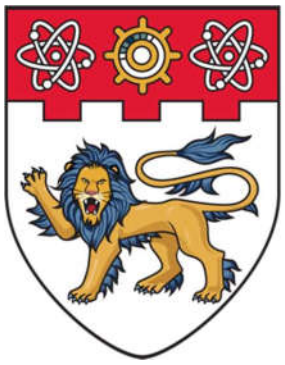

NANYANG TECHNOLOGICAL UNIVERSITY
SINGAPORE

LIGHT-TUNABLE TWO-DIMENSIONAL ELECTRONIC DEVICES

ZHU CHAO

SCHOOL OF MATERIALS SCIENCE AND ENGINEERING

2019

LIGHT-TUNABLE TWO-DIMENSIONAL ELECTRONIC DEVICES

ZHU CHAO

SCHOOL OF MATERIALS SCIENCE AND ENGINEERING

A thesis submitted to the Nanyang Technological University
in partial fulfilment of the requirement for the degree of
Doctor of Philosophy

2019

Statement of Originality

I hereby certify that the work embodied in this thesis is the result of original research and has not been submitted for a higher degree to any other University or Institution.

Dec 19, 2019
Date

Zhu Chao
ZHU CHAO

Supervisor Declaration Statement

I have reviewed the content and presentation style of this thesis and declare it is free of plagiarism and of sufficient grammatical clarity to be examined. To the best of my knowledge, the research and writing are those of the candidate except as acknowledged in the Author Attribution Statement. I confirm that the investigations were conducted in accord with the ethics policies and integrity standards of Nanyang Technological University and that the research data are presented honestly and without prejudice.

21 Dec 2019
.....
Date


.....
LIU ZHENG

Authorship Attribution Statement

This thesis contains material from 2 papers published in the following peer-reviewed journals in which I am listed as an author.

Chapter 4 is published as **C. Zhu**, Y. Chen, F. Liu, S. Zheng, X. Li, A. Chaturvedi, J. Zhou, Q. Fu, Y. He, Q. Zeng, H. J. Fan, H. Zhang, W. J. Liu, T. Yu, and Z. Liu. Light-tunable 1T-TaS_2 charge-density-wave oscillators. *ACS Nano* **12**, 11203-11210 (2018). DOI: 10.1021/acsnano.8b05756.

The contributions of the co-authors are as follows:

- I, Dr. Fucai Liu and A/Prof Zheng Liu co-designed the research.
- I fabricated devices, performed all electrical measurements and Joule-heating simulation.
- Dr. Yu Chen performed the Raman characterization, who was under the supervision of Prof. Ting Yu.
- I performed the temperature-dependent I-V measurement with the help from Dr. Shoujun Zheng, who was under the supervision of Prof. Hong Jin Fan.
- Dr. Xiaobao Li performed the oscillation frequency calculation for curve fitting.
- Dr. Apoorva Chaturvedi provided single crystals, with the supervision from Prof. Hua Zhang.
- Dr. Jiadong Zhou, Dr. Qundong Fu, Dr. Yongmin He, Dr. Qingsheng Zeng, and Dr. Wen-Jun Liu helped on sample preparations and contributed in data analysis.
- I, Dr. Fucai Liu, and A/Prof Zheng Liu prepared the figures and co-wrote the manuscript with the comments from all the coauthors.

Chapter 6 is published as F. Liu, **C. Zhu**, L. You, S. J. Liang, S. Zheng, J. Zhou, Q. Fu, Y. He, Q. Zeng, H. J. Fan, L. K. Ang, J. Wang, and Z. Liu. 2D black phosphorus/$SrTiO_3$-based programmable photoconductive switch. *Advanced Materials* **28**, 7768-7773 (2016). DOI: 10.1002/adma.201602280.

The contributions of the co-authors are as follows:

- Dr. Fucai Liu and A/Prof Zheng Liu co-designed the experiment.
- I and Dr. Fucai Liu fabricated the devices and performed all the optoelectronic measurements.
- Dr. Shijun Liang did the simulation under the supervision of Prof. Lay Kee Ang.
- Dr. Shoujun Zheng, Dr. Jiadong Zhou, and Dr. Qundong Fu helped on the characterization of BP and $SrTiO_3$.
- Dr. You Lu, Dr. Yongmin He and Dr. Qingsheng Zeng helped on sample preparations and device fabrications.
- Prof. Chuanhong Jin performed the TEM characterization.
- Prof. Hong Jin Fan, Prof. Junling Wang, and Prof. Zheng Liu analyzed the data.
- Dr. Fucai Liu wrote the manuscript with input from all the authors.

Dec 19, 2019 . . . . . Date

Zhu Chao . . . . . ZHU CHAO

Abstract

Two-dimensional materials have drawn great attentions due to their atomic thin nature and enriched excellent physical and chemical properties. With their high mobility, suppressed short channel effect, enhanced gate control, additional valley degree of freedom and the ability to form various van der Waals heterostructures, 2D materials are believed to be promising candidates for the next generation electronics and optoelectronics. A great variety of 2D material based electronic and optoelectronic devices have been fabricated, including the field effect transistors, photo detectors, solar cells, sensors, nonvolatile memories, and other novel functional devices.

By now, a lot of efforts have been put on the control of electronic properties of 2D materials and 2D electronic devices. However, most studies have focused on the electric field control by the gate. Other control methods are insufficiently studied. Achieving various control of 2D electronics and optoelectronics is important, especially for cases where a gate control is inaccessible. Light as a powerful tool of localized excitation and heating, can achieve the tailoring and modifications of 2D materials with arbitrary patterns. On the other hand, due to the increasing demand of huge computation, the optical computing and optical-electronic hybrid computing become potential alternatives to the miniaturization of electronic transistors. Therefore, studying the light control of 2D electronic devices is fundamentally important and necessary for the wide applications of 2D materials in the future electronics, optoelectronics, and novel functional devices.

To achieve the light control of electronic properties of 2D materials and 2D electronic devices, the thesis demonstrates the wide availability of light control on 2D materials and 2D electronics, where three systems are considered, including the metallic 1T-TaS_2, the semiconducting 2H-WSe_2, and the semiconductor/insulator heterostructure of narrow-gap BP and wide-gap $SrTiO_3$. Specifically, the light tunability is demonstrated by: the light-tunable CDW phase transition in 1T-TaS_2 and CDW oscillators, the light-ablation-induced controlled hole doping in 2H-WSe_2 and the direct-light-patterned WSe_2 logic circuits, and

the wavelength-dependent persistent conductivity switching in BP/$SrTiO_3$ heterostructure and the light-tunable multistage nonvolatile memory.

Firstly, the light control of bias-induced CDW phase transition in 1T-TaS_2 is demonstrated. The direct evidence from in-situ characterization of the bias-induced NCCDW-ICCDW phase transition was provided by the in-situ Raman measurement. The role of Joule heating in the bias-induced CDW transition was evaluated. Inspired by the Joule heating effect, the light heating was used to tune the bias-induced CDW phase transition. And based on this light-tunable phase transition, a CDW oscillator was demonstrated, where the oscillation frequency could be continuously tuned by the light intensity.

Secondly, the laser-induced controlled hole doping in 2H-WSe_2 is presented. Controllable light-ablation-induced hole doping of 2H-WSe_2 was achieved. Various types of characterization were performed to understand the underlying mechanism. A further photocurrent mapping was performed on the laser patterned WSe_2 P-N junction, indicating a complex junction profile could be achieved. A direct-light-patterned NOR gate circuit was demonstrated, showing comparable performances with other logic circuit fabrication methods.

Thirdly, the light-induced wavelength-dependent persistent switching of conductivity in the BP/$SrTiO_3$ heterostructure is demonstrated. Inspired by previous work of photodoping, BP devices on $SrTiO_3$ were studied, showing an enhanced photoresponsivity as well as a persistent switching on the conductivity. Specifically, a visible light illumination could turn on the BP channel while a UV light illumination could turn off the BP channel. Wavelength-dependent photo switching behavior was studied under different temperatures to understand its mechanism. The light-tunable multistage nonvolatile memory was demonstrated in the BP/$SrTiO_3$ device, which showed a very long retention time at low temperature.

Lay Summary

Two-dimensional materials are very thin materials with the thickness in the nanometer scale, formed by atoms stacked layer by layer. One layer of atoms usually has a thickness (the size in the z direction) smaller than 1 nm. In electronic devices, the current is carried by electrons. For electrons in 2D materials, their motions in the z direction are significantly constrained, leading to unique properties different from the traditional bulk materials. In the semiconductor industry, making small-size devices is essential to perform faster computation, which however encounters fundamental problems as the device size becomes smaller and smaller. 2D materials can overcome these problems in principle and that is why 2D materials have drawn great attentions. The properties of devices based on 2D materials can be controlled by external stimuli, such as electrical, mechanical, chemical and optical methods. Among them, the electrical control method is the most extensively studied while other methods are insufficiently studied. However, there are cases where the electrical control is inaccessible or not preferred. Thus, studying of other control methods is necessary. On the other hand, due to the increased demand of huge computation, the optical computer and optical-electronic hybrid computer are believed to be promising alternatives to the traditional electronic computer. Therefore, studying the optical control of 2D material devices using the light becomes important for their future applications in such fields.

The purpose of this thesis project is to demonstrate the wide availability of the light control of the electronic properties of 2D material devices. In the thesis of the light control of 2D materials, three different systems were investigated, which were the metal (TaS_2), the semiconductor (WSe_2) and the semiconductor/insulator hybrid structure ($BP/SrTiO_3$). The light tunability of the electronic properties of these systems were achieved, based on which, different types of electronic devices were demonstrated. The presented results have shown that the light can be used widely to control the electronic properties of various kinds of 2D materials and structures, which provides more opportunities for the wide range of applications of 2D materials. The outcomes are summarized as the following.

Firstly, in the metallic TaS_2, there are different states with distinct conductivity. With a voltage applied across the TaS_2, by changing the amplitude of the voltage, TaS_2 can be changed between two different states. In this project, the light control of this state change was achieved. Based on this light control, a light-tunable oscillator was demonstrated. For the oscillator, a fixed DC input voltage was applied into the circuit, and an output voltage with oscillating amplitude could be obtained. By adjusting the light intensity, the oscillation frequency could be tuned continuously.

Secondly, there are two kinds of current carriers, where are the negatively charged electrons and positively charged holes. In a semiconductor, only one kind of the carrier dominates the current flow. If electrons are dominant, then the semiconductor is n-type. Otherwise it is p-type. In this project, the laser-induced change of WSe_2 from the n-type to the p-type was achieved. And based on this, a logic circuit was demonstrated, which could perform logic computations.

Thirdly, memory is the device used to store data. If the stored data are preserved even when the electric power is off, then it is called nonvolatile memory. In this project, by shining light with different wavelength onto the semiconducting/insulating hybrid structure of $BP/SrTiO_3$, conductivity with huge difference (up to 10^6 ratio) could achieved. This change in conductivity could persist even when the light illumination was removed. Based on this, a light-tunable nonvolatile memory was demonstrated.

Acknowledgements

I would like to thank my supervisor Assoc. Prof. Liu Zheng for his professional instructions, insightful advices, patient guidance and strong supports on my PhD project. I deeply appreciate his guidance on the experiment plan, data analysis and interpretation, manuscript writing, and scientific figure plot. His enthusiasm on the research has influenced me a lot.

I would like to thank Dr. Liu Fucai for his kindness helps and guidance on the research. I have learnt much from him. I would like to thank Dr. Fu Qundong for his great helps on my research work and PhD life. I would like to thank Dr. Zhou Jiadong, Dr. Zeng Qingsheng, Dr. Wang Xiaowei, Dr. He Yongmin, Dr. Yu Peng, Dr. Deng Ya, Dr. Zhu Chao, Dr. Wang Hong, Dr. Wang Xingli and all other group members for their help on my research and life.

I would like to thank Dr. Zhao Xiaoxu and Prof. Stephen J. Pennycook from NUS for their help on the STEM characterization. I would like to thank Dr. Chen Yu and Prof. Yu Ting from SPMS for their help on Raman characterization. I would like to thank Dr. Zheng Shoujun from SPMS for his help on device fabrications. I would like to thank Mr. Cao Xun and Prof. Huang Yizhong for their help on the FIB. I would like to thank Dr. Apoorva Chaturvedi and Prof. Zhang Hua for their help on single crystal samples.

I would like to thank the technical staff of MSE and FACTS, especially for their helps on AFM, SEM, and XPS. I would like to thank the administrative staff of MSE for their help on my PhD study. I would like to thank technical staff of CA2DM, NUS for their help in the equipment training and operation.

I am grateful to my parents for their supports and encouragement.

Table of Contents

Abstract i

Lay Summary iii

Acknowledgements v

Table of Contents vii

Table Captions xiii

Figure Captions xv

Abbreviations xxix

Chapter 1 Introduction **1**

1.1 Hypothesis/Problem Statement 2

1.2 Objectives and Scope 3

1.3 Dissertation Overview 4

1.4 Findings and Outcomes/Originality 6

References 6

Chapter 2 Literature Review **11**

2.1 Control of Electronic Properties of 2D Materials 12

2.1.1 Electric Field Control 13

2.1.2 Strain Control 19

2.1.3 Chemical Doping 23

2.1.4 Light Control....26
2.2 2D Electronic Devices....29
2.2.1 2D Electronics in High Frequency Applications....30
2.2.2 Logic Circuits Based on 2D Materials....33
2.2.3 Nonvolatile Memory Devices Based on 2D Materials....37
2.3 Research Gaps....41
2.4 Scope of PhD Thesis....42
References....43

Chapter 3 Experimental Methodology....55
3.1 Rationale for Selection of Materials....56
3.2 Device Fabrication....56
3.2.1 Mechanical Exfoliation....56
3.2.2 Sample Transfer....57
3.2.3 Vacuum Annealing....59
3.2.4 Electron Beam Lithography....60
3.2.5 Maskless Photolithography....61
3.3 Characterization....62
3.3.1 Atomic Force Microscopy....62
3.3.2 Raman Spectroscopy....65
3.3.3 Ultraviolet-Visible Spectroscopy....66
3.3.4 Scanning Electron Microscopy....67
3.3.5 Transmission Electron Microscopy....70
3.3.6 Electron Energy Loss Spectroscopy....71
3.3.7 X-Ray Photoelectron Spectroscopy....72

3.3.8 Electronic Device Characterization 72
3.4 Simulation and Calculation 75
3.4.1 Simulation of Temperature Change by Joule Heating 75
3.4.2 Calculation of Oscillation Frequency of a TaS_2 Oscillator 76
3.4.3 Calculation of Mobility, Threshold Voltage and Carrier Density 77
3.4.4 Calculation of Schottky Barrier Height 78
3.4.5 Calculation of Inverter Gain 79
3.4.6 Calculation of Photoresponsivity and Time Constant 79
3.5 Overview of Methodologies 80
References 80

Chapter 4 Light-Tunable Oscillators Based on Metallic 1T-TaS_2 83
4.1 Introduction 84
4.2 Experimental Methods 85
4.2.1 Crystal Synthesis and Device Fabrication 85
4.2.2 Raman Spectra Test 85
4.2.3 Temperature-Dependent *I-V* Characterization 86
4.2.4 Joule Heating Simulation 86
4.2.5 Light-Tuned TaS_2 Oscillator Measurement 86
4.3 Principle Outcomes 87
4.3.1 Structure and Characterization of 1T-TaS_2 87
4.3.2 In-Situ Raman Test for Bias-Induced CDW Transition in 1T-TaS_2 88
4.3.2.1 Temperature-Dependent Raman Measurement 88
4.3.2.2 In-Situ Raman Measurement 89
4.3.3 Joule Heating Effect in the Bias-Induced CDW Phase Transition 91

4.3.3.1 Temperature-Dependent CDW Phase Transition 91
4.3.3.2 Evaluation of Joule Heating Effect 91
4.3.4 Light-Tunable CDW Oscillators 95
4.3.4.1 Light-Tuned CDW Phase Transition 95
4.3.4.2 CDW Oscillator Based on 1T-TaS_2 97
4.3.4.3 Light-Tuned CDW Oscillators 99
4.4 Conclusions 100
References 101

Chapter 5 Light-Patterned Logic Circuits Based on Semiconducting WSe_2 105
5.1 Introduction 106
5.2 Experimental Methods 107
5.2.1 Device Fabrication 107
5.2.2 Hole Doping by Laser Ablation 107
5.2.3 Raman and Photocurrent Mapping 107
5.2.4 SKPM Measurement 108
5.2.5 SEM Imaging 108
5.2.6 STEM and EELS Measurement 108
5.2.7 FET and Logic Circuit Measurement 109
5.3 Principle Outcomes 109
5.3.1 Characterization and Laser Ablation of 2H-WSe_2 109
5.3.1.1 Structure and Characterization 109
5.3.1.2 Laser Ablation 110
5.3.2 Laser-Induced Controlled Hole Doping in 2H-WSe_2 112
5.3.2.1 FET Performances 112

5.3.2.2 Schottky Barrier Height Measurement....115
5.3.2.3 SKPM Characterization....117
5.3.3 Mechanism of Laser-Induced Hole Doping....118
5.3.3.1 Raman Signals....118
5.3.3.2 XPS Results....119
5.3.3.3 STEM and EELS Results....120
5.3.4 Photocurrent Mapping Test of Laser-Written P-N Junctions....122
5.3.4.1 Photocurrent Mapping Results....122
5.3.4.2 SKPM Results and Discussion....124
5.3.5 Direct Logic Circuit Writing....125
5.3.5.1 Direct Patterning of a NOR Gate Circuit....125
5.3.5.2 NOR Gate Circuit Performances....126
5.4 Conclusions....127
References....128

Chapter 6 Light-Programmable Nonvolatile Memory in the BP/$SrTiO_3$ Semiconductor/Insulator Heterostructure....133
6.1 Introduction....134
6.2 Experimental Methods....135
6.2.1 Device Fabrication....135
6.2.2 TEM Characterization....136
6.2.3 Raman Characterization....136
6.2.4 Transmission Spectrum Characterization....136
6.2.5 Optoelectronic Measurement....136
6.3 Principle Outcomes....137

6.3.1 Basic Characterization of BP and $SrTiO_3$ 137
6.3.1.1 Basic Characterization of BP 137
6.3.1.2 Transmission Spectrum of $SrTiO_3$....138
6.3.2 Optoelectronic Measurement of BP on Silicon Substrate....139
6.3.3 Light-Tuned BP/$SrTiO_3$ Nonvolatile Memory....140
6.3.3.1 Light-Tuned Persistent Switching of BP/$SrTiO_3$....140
6.3.3.2 Wavelength-Dependent Photo Response....141
6.3.3.3 Temperature-Dependent Time Constant....143
6.3.3.4 Light-Tunable Multistage Nonvolatile Memory 144
6.4 Conclusions 145
References....146

Chapter 7 Discussion and Future Work....149
7.1 General Discussion....150
7.2 Reconnaissance Work Not Included in Main Chapters....152
7.3 Outstanding Questions 154
7.4 Outlook and Perspectives 156
7.5 Outcomes Reflected in the Original Hypothesis 157
References....158
Publications 161

Table Captions

Table 4.1 Parameters for the simulation of the temperature change induced by Joule heating. Thermal conductivity values are referred to Refs [32,34-39].

Table 5.1 Parameters for the XPS peak fitting of the heavily ablated sample (100 × lens, NA = 0.8, 1.16 MW/cm^2, 0.6 s per μm scan).

Figure Captions

Figure 2.1 Crystal structures of typical 2D materials. (a) Graphene. (b) Black phosphorus. (c) Boron nitride. Grey: Boron. Blue: Nitrogen. (d) Group-III chalcogenides. Purple: Group-III element (Ga or In). Yellow: Chalcogen. Transition metal dichalcogenides in 2H (e) and 1T (f) phase. Green: Transition metal element. Yellow: Chalcogen. (g) MXenes.

Figure 2.2 Diagram of band alignment of selected materials. From left to right: 2D metals, 2D semimetals, hBN, black phosphorus, TMDs, Group-III chalcogenides, traditional inorganic 3D semiconductors, organic semiconductors, semiconducting SWCNT, PbS quantum dots and metals used for contact electrodes. For metals and semimetals, the work function is shown. For hBN and semiconductors, the location of bandgap is shown. D/I indicates a direct or indirect bandgap. p/n indicates a hole or electron dominant transport behavior.

Figure 2.3 Ionic liquid gate induced superconductivity in 2H-MoS_2. (a) Schematic diagram of a 2H-MoS_2 transistor with an ionic liquid gate and an oxide back gate. (b) Transfer characteristics of the transistor under different ionic liquid gate (V_{LG}) or back gate voltage (V_{BG}). (c) Temperature-dependent sheet resistance of MoS_2 under different V_{LG}, where an insulator-metal-superconductor phase transition exists. (d) Temperature-dependent sheet resistance of MoS_2 under different V_{BG}, where an insulator-metal phase transition exists. (e) Sheet resistance under different temperatures and carrier concentration. (f) Temperature-dependent normalized sheet resistance under different V_{LG} and V_{BG}.

Figure 2.4 Gate-induced superconductivity in magic-angle twisted bilayer graphene. (a) Schematic diagram of a typical device. (b) Schematic drawing of the stacking order from the top view. (c) Four-probe resistance at different temperatures and carrier density for 1.16° twisted angle. Two superconducting domes are marked by dashed lines, separated by a Mott-like insulator state. (d) Four-probe resistance at different temperatures and carrier density for 1.05° twisted angle, where two superconducting domes merge.

Figure 2.5 Room-temperature exciton-based transistor. (a) Schematic diagram of the device. Variation of exciton energy in ON (b) and OFF (c) states. Exciton emission images for ON (d) and OFF (e) states corresponding to (b) and (c), respectively.

Figure 2.6 CDW phase transitions in 1T-TaS_2. (a) Top: Crystal structure of 1T-TaS_2. Bottom: Structure of a David star and a 1T-TaS_2 device. (b) Schematic drawing of lattice distortions for different CDW phases. (c) Temperature-dependent resistivity. (d) Temperature-dependent thermal conductivity. (e) In-plane electric field induced phase transition between NCCDW and ICCDW. (f) Schematic drawing of lattice potential under different in-plane electric field.

Figure 2.7 Strain-dependent bandgap of monolayer 2H TMDs. (a) Top view of crystal structure of 2H TMDs. (b) Side view of 2H TMD crystal structure and the irreducible Brillouin zone. Bandgap of monolayer 2H MoS_2 (c), WS_2 (d), $MoSe_2$ (e), WSe_2 (f), $MoTe_2$ (g), and WTe_2 (h) under various types of strain. xx: uniaxial expansion along the zigzag direction. yy: uniaxial expansion along the armchair direction. xx+yy: biaxial expansion along both zigzag and armchair direction. xx-yy: expansion along zigzag direction and suppression along armchair direction. yy-xx: suppression along zigzag direction and expansion along armchair direction. All types of strain are homogeneous.

Figure 2.8 Strain-dependent bandgap of monolayer 1T TMDs. (a) Top view of crystal structure of 1T TMDs. (b) Side view of 1T TMD crystal structure and the irreducible Brillouin zone. Bandgap of monolayer 1T ZrS_2 (c), HfS_2 (d), $ZrSe_2$ (e), $HfSe_2$ (f), $ZrTe_2$ (g), and $HfTe_2$ (h) under various types of strain. xx: homogeneous uniaxial expansion along the zigzag direction. yy: homogeneous uniaxial expansion along the armchair direction. xy: homogeneous biaxial expansion along both zigzag and armchair direction.

Figure 2.9 Electronic properties of monolayer MoS_2 under strain. (a) Strain-dependent minima of K and Q valleys. (b) Strain-dependent effective mass for different valleys. (c) Strain-dependent electron mobility. UZ, UA, and BI stand for uniaxial strain along zigzag

direction, uniaxial strain along armchair direction, and biaxial strain, respectively. The subscripts A and Z stands for mobility in the armchair and zigzag directions, respectively.

Figure 2.10 Post-synthesis doping methods. (a) Plasma immersion ion implantation of phosphorus into MoS_2. (b) Covalent doping by CH_x group. (c) Surface transfer hole doping by $AuCl_3$ solution. (d) Surface transfer electron doping by molecule $Co_6Se_8(PEt_3)_6$. (e) Surface transfer hole doping by coating a layer of MoO_3. (f) Patterning of WSe_2 P-N homojunction using the ferroelectric $BiFeO_3$ substrate.

Figure 2.11 Power-dependent PL spectra of monolayer WS_2. (a) PL spectra at different excitation laser power at room temperature. The laser wavelength is 532 nm. X_A and X_A^- peaks are emissions from excitons and negative trions, respectively. (b) Peak positions and integrated intensities of the two peaks at different excitation power at room temperature. (c) PL spectra at 4.2 K. X_AX_A is the emission from biexcitons and LS is from the localized states such as defects and impurities. (d) Power-dependent PL intensity for the four peaks at 4.2 K.

Figure 2.12 Laser writing of CDW domain walls in 1T-TaS_2 and NPN bipolar junction transistors in 2H-$MoTe_2$. (a) Bright-field transmission electron micrograph of the ultrafast laser induced CDW domain walls in 1T-TaS_2. Circles are regions of interest where selected area diffraction was performed, shown schematically at the bottom. Brown and blue areas have different CDW domain orientations. (b) Schematic diagrams showing the writing and erasing of CDW domain walls. (c) NPN bipolar junction transistor patterned by scanning laser ablation on 2H-$MoTe_2$. Two middle electrodes were ablated, and nearby regions were p-type doped.

Figure 2.13 Maximum frequency versus gate length for different transistors. (a) Comparison between graphene MOSFET and traditional transistors. (b) Comparison between graphene, phosphene, and MoS_2.

Figure 2.14 Relaxation oscillators based on RC circuits. (a) A simplest RC CMOS

oscillator formed by an inverting Schmitt trigger, a resistor, and a capacitor. (b) Left: A Schmitt trigger circuit. Right: Schmitt trigger output curve, featured by abrupt transitions of output voltage. (c) Left: CDW phase transition of 1T-TaS_2 under the bias voltage, featured by abrupt transitions of the current. Right: A TaS_2 based relaxation oscillator. (d) Output oscillation of the device shown in (c) at a frequency of about 2 MHz.

Figure 2.15 A ring oscillator based on graphene inverters. (a) Schematic circuit of the 3-stage ring oscillator with an output buffer. (b) Optical Image of the ring oscillator device. (c) Output signals of the ring oscillator for different gate lengths. (d) Oscillation tuned by the V_{DD}.

Figure 2.16 Electron mobility of 2D materials. (a) Electron mobility versus thickness for selected 2D materials and 3D semiconductors. (b) Electron mobility versus charged impurity density N_I for monolayer MoS_2 surrounded by different dielectrics. (c) Electron mobility versus electron density n_s for monolayer MoS_2 surrounded by different dielectrics.

Figure 2.17 Two types of inverters. (a) Left: Schematic diagram of a CMOS inverter. Right: Schematic circuit diagram. (b) Voltage transfer characteristics and butterfly curves of (a) under different V_{DD}. (c) Corresponding gain under different V_{DD}. (d) 3D schematic diagram of a depletion-load NMOS inverter. (e) Left: Schematic circuit diagram of (d). Right: Transfer curves of the two channels with different *W/L* ratios.

Figure 2.18 2D material based NOR gate circuits. (a) 3D schematic diagrams of a pair of nMOS transistors based on monolayer MoS_2. (b) A NOR gate circuit where two parallel MoS_2 nMOS transistors are connected to a 1 MΩ load resistor. The output voltage under different input combinations shows the logic operation of the NOR gate. (c) A similar NOR gate circuit where the load is MoS_2 FET in depletion mode. (d) Schematic diagram of a $MoTe_2$ transistor with two control gates used for the NOR gate circuit. (e) Schematic layout of planar and monolithic 3D CMOS NOR gate circuits. (f) Schematic diagram of the cross-section view and the optical image of a monolithic 3D CMOS NOR gate circuit. (g) Schematic diagrams of a doping-free WSe_2 CMOS inverter by transistor polarity control.

Each transistor consists of two polarity gates near the electrodes and one control gate at the channel center. (h) Polarity control of the WSe_2 transistor by the polarity gates.

Figure 2.19 Floating gate nonvolatile memory based on 2D materials. (a) Schematic diagram of floating gate nonvolatile memory device based on graphene, MoS_2, and HfO_2. (b) Schematic band alignment showing the operation mechanism of the nonvolatile memory device. (c) Repeatable program (P) and erase (E) operations. (d) Time stability of the erase and program states. (e) Schematic diagram of the nonvolatile memory device based on MoS_2, graphene, and hBN. (f) Time stability of the device shown in (e).

Figure 2.20 2D nonvolatile memory device based on a ferroelectric substrate. (a) Schematic diagram of the ferroelectric NVM device. (b) Diagrams of the gating effect when the PZT is up-polarized or down-polarized. (c) Retention performance of the NVM device under different storage environment.

Figure 2.21 Typical memristors and operation mechanisms. (a) *I-V* characteristics of a metal-oxide memristor based on TiO_{2-x}/Al_2O_3. Inset: Structure of the memristor. (b) Diagram showing the mechanism of the memristor in (a). Left: Oxygen vacancy defect distribution. Right: Schematic band diagram. For the off state, part of the TiO_{2-x} is depleted, which increases the resistance. (c) Graphene/$MoS_{2-x}O_x$/Graphene based memristor. (d) Top: Cross-section High-angle ADF image of the memristor at on and off states. Bottom: Atomic percentage of Mo, S, and O across the conductive channel.

Figure 3.1 Mechanical exfoliation of atomically thin 2D materials. (a) Image of thin MoS_2 crystals attached onto a silicon substrate by the Scotch tape. (b) Optical image of an exfoliated graphene sample. Regions with different thicknesses have different appearances.

Figure 3.2 Dry transfer of 2D materials. (a) Experimental setup of a transfer stage, including a microscope, an XYZ movable cantilever, and an XYθ movable substrate holder. (b) Schematic diagram for the dry transfer process. (c) Schematic diagram for the wet transfer process.

Figure 3.3 A vacuum annealing system with the pressure down to 10^{-6} Torr and the temperature up to 500 ℃.

Figure 3.4 Electron beam lithography. (a) Diagram of the setup of electron beam lithography. (b) Diagram for the lithography procedure.

Figure 3.5 Maskless photolithography. (a) A Microtech Laser Writer System. (b) An XYZ sample mounting stage whose location is precisely determined by interferometers.

Figure 3.6 Atomic force microscopy. (a) Schematic setup of an AFM. (b) Schematic diagram of the tip-sample atomic force versus the tip-sample distance. (c) Schematic diagram of the oscillation of the tip working in the tapping mode. (d) Oscillation amplitude versus tip-sample distance.

Figure 3.7 Energy levels of the sample and the tip for three cases. (a) The sample and the tip are separated in a distance. (b) The sample and tip are close enough for current tunneling, leading to the alignment of Fermi levels and the formation of the contact potential difference. (c) A DC voltage is applied to the tip with the sample grounded.

Figure 3.8 Schematic diagram of the Raman scattering. (a) Schematic energy levels involved in the Stokes scattering and anti-Stokes scattering. (b) Two dominant vibration modes in the 2H-WS_2.

Figure 3.9 Schematic diagram of the scanning electron microscopy. BSE, SE, and X stand for backscattered electrons, secondary electrons, and X-rays, respectively. SC and EBIC are the current from the specimen and electrons.

Figure 3.10 The transmission electron microscopy imaging system in two operation modes. (a) Diffraction mode: diffraction patterns (DP) are projected onto the screen. (b) Image mode: the image is projected onto the screen.

Figure 3.11 Sample stages for the device measurements. (a) A Microxact probe station with four probes and a helium pulse-tube refrigerator. (b) A Linkam temperature control stage working from -196 to 350 ℃, cooled by liquid nitrogen.

Figure 3.12 Model of Joule heating generation and dissipation in a 2D material. (a) Simplified model for heat dissipation into the substrate. The outer edge of the left contact electrode is set to $x = 0$. (b) Current crowding at the inner edge of the contact.

Figure 3.13 A TaS_2 oscillator with TaS_2 oscillates between two phases. (a) The typical current-voltage curve of the 1T-TaS_2. The hysteresis loop is between V_L and V_H. The resistance for the two phases is R_i and R_m, respectively. (b) Schematic diagram of the TaS_2 oscillator. The capacitor undergoes periodically charging and discharging. (c) Schematic curve of the output voltage oscillation.

Figure 4.1 Structure and characterization of 1T-TaS_2. (a) Side view of 1T-TaS_2 crystal structure. (b) Top view of 1T-TaS_2 crystal structure. The CDW-induced lattice distortion is featured by 12 adjacent Ta atoms shifting towards a central Ta atom, forming the so-called David star. (c) A typical optical image of exfoliated multilayer 1T-TaS_2. (d) An AFM image. (e) The height profile along the dash line in (c). (f) A Raman spectrum of 1T-TaS_2 at room temperature, with the sample at the NCCDW phase. (g) *I-V* curve of 1T-TaS_2 showing the bias-induced phase transition.

Figure 4.2 Temperature-dependent Raman spectra of 1T-TaS_2. Below 350 K, the sample is at NCCDW phase, featured by the existence of discontinuous CDW domains and the Raman peaks arising from the collective CDW modes. Above 350 K, the sample is at ICCDW phase, featured by the melt of CDW domains and disappearance of the CDW Raman peaks.

Figure 4.3 In-situ Raman measurement of the bias-induced CDW phase transition. (a) Solid line: The *I-V* curve of a 1T-TaS_2 device at 80 K, with the upper and lower threshold

marked with blue dots. Dash line: In-situ Raman signal intensity at 76 cm^{-1} under different voltage bias. The excitation wavelength is 532 nm. Inset: an optical image of the 1T-TaS_2 device. (b) Left: In-situ Raman signals of 1T-TaS_2 at 80 K. The A_{1g} peak at 76 cm^{-1} at 0 V is marked by the red arrow. Right: CDW phase under different bias. (c) Solid line: The *I-V* curve of a 1T-TaS_2 device at 220 K. Dash line: In-situ Raman intensity at 70 cm^{-1}. Inset: A height profile of the TaS_2. (d) In-situ Raman signals of 1T-TaS_2 at 220 K. The A_{1g} peak at 70 cm^{-1} at 0 V is marked by the red arrow.

Figure 4.4 Temperature-dependent *I-V* characteristic of 1T-TaS_2. (a) *I-V* curve at different temperatures. Inset: *I-V* curve at 300 K, with the upper and lower threshold (V_H and V_L) shown by red dots. (b) Joule heating rate at the upper and lower threshold under different environment temperatures.

Figure 4.5 Simulation of the Joule-heating-induced temperature change of 1T-TaS_2. (a) Top: Model of Joule heating generation and dissipation. The outer edge of the left electrode is located at $x = 0$ and the channel center is located at $x = 1.55$ μm. Bottom: Current crowding at the contact edge. (b) The temperature profile along the contact and channel when $V = V_H = 0.892$ V and $I = 0.4777$ mA at environment temperature $T = 200$ K. Three situations are considered: Joule heating (JH) without electrode contact, Joule heating with electrode and Joule heating with electrode considering the current crowding (JH+CC). (c) The temperature at the channel center under different voltages at different environment temperatures. The voltage is extracted from Figure 4.4a. Only the NCCDW part is shown. (d) Joule heating rate and temperature change at the channel center under different environment temperatures. Only data for the upper and lower threshold are shown.

Figure 4.6 Light-tuned bias-induced CDW phase transition in 1T-TaS_2 sample at room temperature. (a) Shift of the *I-V* curve of TaS_2 under a 635-nm laser illumination. (b) Change of current when the laser is turned on or off. The bias is fixed at 0.51 V.

Figure 4.7 Time constant of the current change. (a) Fitting of the current rising process for different laser intensity. (b) Fitting of the current decay process for different laser

intensity. (c) Fitted time constant for different laser intensity. (d) Joule heating rate at the upper and lower threshold voltage for different laser intensity, extracted from Figure 4.6a.

Figure 4.8 CDW oscillator based on 1T-TaS_2. (a) Schematic diagrams of the 1T-TaS_2 oscillator circuit. (b) *I-V* curve of 1T-TaS_2 at dark and the load lines of 1T-TaS_2 at different V_{DC}. (c) Oscillation curves of the output voltage at different V_{DC}.

Figure 4.9 Light-tunable TaS_2 oscillator. (a) Schematic diagrams of the light-tunable TaS_2 oscillator circuit. (b) *I-V* curves of 1T-TaS_2 under different laser intensity and the load lines of 1T-TaS_2 at V_{DC} = 3.90 and 3.82 V, respectively. (c) Light-intensity-dependent oscillation of the output voltage at V_{DC} = 3.82 V. (d) Light-intensity-dependent oscillation of the output voltage at V_{DC} = 3.90 V.

Figure 4.10 Output oscillation frequency of the TaS_2 oscillator. (a) Oscillation frequency under different V_{DC} in the dark. (b) Oscillation frequency under different laser intensity.

Figure 5.1 Structure and Characterization of 2H-WSe_2. (a) Left: Side view of the crystal structure of 2H-WSe_2. Middle: Top view of the crystal structure of 2H-WSe_2. Right: Schematic diagram of the WSe_2 FET device. (b) Raman spectrum of 2H-WSe_2. Two major peaks are labeled. (c) Transfer characteristics of pristine exfoliated 2H-WSe_2 FET devices with different thickness. All show the electron-dominant ambipolar transport behavior. Inset: A typical optical image of the WSe_2 FET device.

Figure 5.2 Optical, AFM and SKPM images of heavily ablated WSe_2. Optical images (a) before and (b) after heavy laser ablation (100 × lens, NA = 0.8, 1.55 MW/cm^2, 1.2 s per μm scan). (c) AFM image and (d) the height profile along the white line. (e) SKPM image and (f) the V_{CPD} profile along the white line.

Figure 5.3 Optical, AFM and SKPM images of moderately ablated WSe_2. Optical images of the device (a) before and (b) after a series of ablations (50 × lens, NA = 0.6,

0.54 MW/cm^2). (c) AFM image of the ablated device and (d) the height profile along the two lines. (e) SKPM image and (f) the V_{CPD} profile along the white line.

Figure 5.4 Laser-ablation-induced hole doping of WSe_2. (a) A WSe_2 FET device. (b) I_{DS}-V_{DS} curves of the pristine device. (c) I_{DS}-V_{DS} curves after ablation. Inset: Schematic illustration of laser ablation on the transistor channel. (d) Comparison of transfer characteristics of the transistor before and after ablation. (e) $I_{DS}/\sqrt{g_m}$ versus V_{GS} plot of the pristine transistor and the extraction of threshold voltage V_{th}. Inset: Linear plot of transfer curve from which the electron mobility is extracted. (f) $I_{DS}/\sqrt{g_m}$ versus V_{GS} plot of the ablated transistor and the extraction of V_{th}. Inset: Linear plot of transfer curve from which the hole mobility is extracted.

Figure 5.5 Controllable hole doping by laser ablation. (a) I_{DS}-V_{GS} transfer characteristics of a WSe_2 transistor after ablation at different ablation time from 2 to 12 s per μm. (b) Transfer characteristics of a WSe_2 transistor after ablation with increasing laser power from 0.55 to 0.74 MW/cm^2.

Figure 5.6 Temperature-dependent FET measurement for Schottky barrier height extraction. (a) Temperature-dependent I_{DS}-V_{DS} curve of a WSe_2 transistor at $V_{GS} = -40$ V after the first ablation (0.87 MW/cm^2, 6 s per μm). Inset: An optical image of the WSe_2 transistors, with the ablated channel marked by the green dash rectangle. (b) Temperature-dependent I_{DS}-V_{GS} curve of the transistor after the first ablation. (c) Arrhenius plot of $I_{DS}/T^{1.5}$ vs $1000/T$ at different V_{GS} for the transistor after the first ablation. (d) Temperature-dependent I_{DS}-V_{DS} curve at $V_{GS} = -40$ V after the second ablation (0.87 MW/cm^2, 8 s per μm). (e) Temperature-dependent I_{DS}-V_{GS} curve after the second ablation. (c) Arrhenius plot of $I_{DS}/T^{1.5}$ vs $1000/T$ at different V_{GS} after the second ablation. The activation energy is extracted from the linear fitting.

Figure 5.7 Activation energy E_A at different V_{GS} for the first (0.87 MW/cm^2, 6 s per μm scan) and second ablation (0.87 MW/cm^2, 8s per μm scan). Schottky barrier height is

extracted respectively.

Figure 5.8 Surface potential of WSe_2 in different ablation levels. (a) An optical image of the WSe_2. The marked areas were ablated in different levels. Regions 1-4 (5-8) were first ablated by a lower power (0.37 MW/cm^2, 0.5 μm/s scan) for one to four times, respectively. Then regions 5-8 were ablated by a higher power (0.44 MW/cm^2, 0.5 μm/s scan) for one to four times, respectively. (b) An SKPM image showing the surface potential of the ablated WSe_2. (c) Profiles of V_{CPD} along the two lines marked in (b).

Figure 5.9 Raman signals of WSe_2. (a) Comparation of Raman spectra between pristine WSe_2, ablated WSe_2 and WO_3. Inset: An optical image of WSe_2 after heavy ablation (100 × lens, NA = 0.8, 1.55 MW/cm^2, 1.2 s per μm scan) in the two square areas, Raman spectra at three cursors are shown. (b) Enlarged Raman spectra of the pristine and ablated WSe_2 from 50 to 420 rel. cm^{-1}. (c) Enlarged Raman spectra of the pristine and ablated WSe_2 from 450 to 850 rel. cm^{-1}.

Figure 5.10 XPS results of WSe_2. (a) Wide band XPS spectrum of WSe_2 on SiO_2 substrate. (b) Comparison of W4f peaks between pristine WSe_2 and the moderately ablated sample (50 × lens, NA = 0.6, 0.76 MW/cm^2, 2 s per μm scan). (c) XPS spectrum of the heavily ablated sample (100 × lens, NA = 0.8, 1.16 MW/cm^2, 0.6 s per μm scan).

Figure 5.11 STEM characterization of the ablated WSe_2. (a) A STEM image showing the contrast between the ablated region and the pristine WSe_2. The white line shows the growth of ablated derivatives along the zigzag direction of the pristine sample. (b) An enlarged STEM image of (a). STEM images of (c) fully pristine WSe_2 and (d) fully ablated region. (e) The enlarged image and (f) FFT image of (c), labeled with the lattice constant and Miller indices, respectively. (g) The enlarged image and (h) FFT image of (d), labeled with the lattice constants and Miller indices, respectively. Scale bar: (a, c, d) 5 nm, (b) 2 nm, (e, g) 1 nm.

Figure 5.12 EELS mapping of the ablated WSe_2 sample. (a) An ADF-STEM image of the

sample. (b) EELS mapping images of W (O edge), Se (M edge) and O (K edge).

Figure 5.13 Photocurrent mapping of a WSe_2 P-N junction built by laser ablation. (a) An optical image of the p-n junction. The device was first ablated (0.44 MW/cm^2, 8 s per μm) in the red dashed rectangle twice, followed by ablation in the yellow dashed rectangle (10 s and 12 s per μm in sequence). The green rectangle outlines the whole channel. (b) Raman mapping signal collected simultaneously to locate the channel, showing the intensity of the peak marked by the arrow in the (c) Raman spectrum. Photocurrent mapping signal after 10 s per μm ablation at (d) V_{DS} = 0 V and (e) V_{DS} = 1 V and (f) respective current profiles along the midline of channel. Photocurrent mapping signal after 12 s per μm ablation at (g) V_{DS} = 0 V and (h) V_{DS} = 1 V and (i) respective current profiles along the midline of channel. V_{GS} = -20 V.

Figure 5.14 Surface potential of the device for photocurrent mapping and diagrams showing the mechanism. (a) SKPM image of the device showing the surface contact potential difference V_{CPD}. (b) The V_{CPD} profile along the red line in (a), showing that the hole doping depends on the ablation history. (c) Schematic band diagram showing the photo response mechanism in the P-N junction with insufficient hole doping.

Figure 5.15 A NOR gate circuit based on WSe_2 by selective light-induced hole doping. (a) Left: An optical image of the device. The green region shows the two series p-channels patterned by laser ablation. Scale bar: 10 μm. Right: The logic operation of the NOR gate and a circuit diagram of the CMOS-based NOR gate. (b) A secondary electron SEM image of the device. The acceleration voltage was set to 15 kV to show the layout of input electrodes at the bottom.

Figure 5.16 Performances of the previously shown NOR gate circuit. (a) Transfer curve of the n-channel current at different input voltages. (b)Transfer curve of the p-channel current at different input voltages. (c) Transfer curve of the output voltage at different input voltages and the V_{DD} with one of the input V_A = 0 V. (d) Gain at different V_{DD} with V_A = 0 V. (e) Repeatable NOR gate operation with the reset using negative pulsed voltage at the

inputs. (f) NOR gate operation without the rest.

Figure 6.1 Basic characterization of BP. (a) Side view of the BP crystal structure. (b) A typical optical image of the BP and its thickness profile measured by AFM. Scale bar: 10 μm. (c) An HRTEM image of BP. (d) Raman spectrum of BP with three major modes. (e) Polarized Raman spectra of BP under different polarization angle. (f) Fitting of the polarization-angle-dependent intensity of A_g^2 peak.

Figure 6.2 A transmission spectrum of a 500 μm thick $SrTiO_3$ substrate, with the wavelength of the red and UV light indicated by the arrows.

Figure 6.3 BP transistor performances on the silicon substrate. (a) I_d-V_d curve of the device. (b) I_d-V_g transfer curve of the device. (c) Red light photo response of the device at V_g = 40 V and V_d = 5 V.

Figure 6.4 Light-induced nonvolatile memory in the BP/$SrTiO_3$ device at room temperature. (a) Alternating current change in BP upon red and UV light illumination. (b) I_d-V_d curve of the device in on (red) and off (black) states.

Figure 6.5 Nonvolatile change in the conductivity of BP upon light illumination with different wavelengths at 50 K. Current change by (a) red, (b) green, and (c) blue light. (d) Schematic diagram of the BP/$SrTiO_3$ heterostructure. Electron excitation and recombination in $SrTiO_3$ upon (e) UV and (f) red light illumination.

Figure 6.6 Similar persistent current in the MoS_2/$SrTiO_3$ heterostructure. Current increases upon UV light illumination and decreases upon red light illumination.

Figure 6.7 Current change of BP on $SrTiO_3$ at different temperatures for different processes. Black solid lines are for the fitting of time constant. (a) Current rising upon red light illumination. (b) Current decay after turning off red light. (c) Current rising after UV light illumination.

Figure 6.8 Temperature-dependent time constant for different processes. The time constant of current rising upon red light illumination, current decay after turning off red light, and current rising after UV light illumination is shown by black, red, and blue spheres, respectively. Fitting results are shown by solid curves.

Figure 6.9 Light-induced nonvolatile memory in the BP/$SrTiO_3$ device at 50 K. (a) Multistage nonvolatile memory tuned by red light and reset by UV light. (b) Alternating on and off switching of the device. (c) I_d-V_d curve of the device in on (red) and off (black) states. (d) The nonvolatile on (red) and off (black) states with long retention time.

Figure 7.1 Laser-ablation induced phase transition in 2H-$MoTe_2$ and formation of the ohmic contact. (a) Schematic diagram of the laser-ablation patterning of the ohmic contact. (b) Arrhenius plots for extraction of contact barrier height. (c) Comparison of mobility between two kinds of contact.

Figure 7.2 Repeat of the method proposed by Cho et al. (a) The output characteristic of the pristine fabricated 2H-$MoTe_2$ FET device, indicating high and asymmetric Schottky barriers at the two electrode contacts. (b) The output characteristic of the device after annealing, showing lower and more symmetric contact barriers.

Figure 7.3 Laser ablation on the electrodes of the 2H-WSe_2 FET device, showing a significantly enhanced hole field effect mobility without obvious shifting of the cutoff region.

Abbreviations

1D	One-Dimensional
2D	Two-Dimensional
3D	Three-Dimensional
AAAS	American Association for the Advancement of Science
ACS	American Chemical Society
ADF	Annular Dark Field
AFM	Atomic Force Microscopy
BEI	Backscatter Electron Image
BJT	Bipolar Junction Transistor
BN	Boron Nitride
BP	Black Phosphorus
BSE	Backscattered Electrons
CCD	Charge Coupled Device
CDW	Charge Density Wave
CMOS	Complementary Metal Oxide Semiconductor
CPD	Contact Potential Difference
CrL_3	Tris(diethyldithiocarbamato)chromium(III)
CsrTR	Current to Square Root of Transconductance Ratio
DCE	Dichloroethane
DEME-TSFI	N,N-Diethyl-N-methyl-N-(2-methoxyethyl)ammonium bis(trifluoromethanesulfonyl)imide
EBL	Electron Beam Lithography
EDX	Energy Dispersive X-Ray Spectroscopy
EELS	Electron Energy Loss Spectroscopy
F_4TCNQ	2,3,5,6-tetrafluoro-7,7,8,8-tetracyanoquinodimethane
FDT	1H,1H,2H,2H-Perfluorodecanethiol
FET	Field Effect Transistor
FWHM	Full Width at Half Maximum
GND	Ground

hBN	Hexagonal Boron Nitride
HEMT	High Electron Mobility Transistor
HRTEM	High Resolution Transmission Electron Microscopy
IEEE	Institute of Electrical and Electronics Engineers
IPA	Isopropyl Alcohol
MEA	Mercaptoethylamine
MIBK	Methyl Isobutyl Ketone
MoL_4	Tetrakis(diethyldithiocarbamato)molybdenum(IV)
MOSFET	Metal-Oxide-Semiconductor Field Effect Transistor
NA	Numerical Aperture
NADH	nicotinamide adenine dinucleotide
NVM	Nonvolatile Memory
PDMS	Polydimethylsiloxane
PET	Polyethylene Terephthalate
PEt_3	Triethylphosphine
PL	Photoluminescence
PMMA	Poly(methyl methacrylate)
PMN-PT	$[Pb(Mg_{1/3}Nb_{2/3})O_3]_{0.7}$-$[PbTiO_3]_{0.3}$
P(VDF-TrFE)	Poly(vinylidene fluoride-trifluoroethylene)
PZT	$Pb(Zr_{0.2}Ti_{0.8})O_3$
QD	Quantum Dot
SAD	Selected-Area Diffraction
SE	Secondary Electrons
SEI	Secondary Electron Image
SEM	Scanning Electron Microscopy
SHG	Second-Harmonic Generation
SKPM	Scanning Kelvin Probe Microscopy
SMU	Source-Measurement Unit
SRO	$SrRuO_3$
STEM	Scanning Transmission Electron Microscopy
STO	$SrTiO_3$

SWCNT	Single-Wall Carbon Nanotube
TCNQ	7,7,8,8-tetracyanoquinodimethane
TCR	Transconductance to Current Ratio
TEM	Transmission Electron Microscopy
THF	Tetrahydrofuran
TMD	Transition Metal Dichalcogenide
UV	Ultraviolet
VCO	Voltage Controlled Oscillator
vdW	van der Waals

Chapter 1

Introduction

This chapter presents a brief introduction of the thesis Firstly, the lack of studies in the light control of electronic properties of 2D materials is discussed and the importance of the light-tunable 2D electronics is addressed. Based on this, the project target is stated. Secondly, the objectives and scope are discussed. Then, the dissertation structure is summarized chapter by chapter. Finally, the outcomes and findings are summarized.

1.1 Hypothesis/Problem Statement

Two-dimensional (2D) materials have drawn great attentions since the first discovery of monolayer graphene in 2004.[1] Graphene has superior properties including the atomically thin thickness, ultrahigh strength, ultrahigh mobility and ultrahigh thermal conductivity.[2-4] The lack of bandgap in graphene limits its applications in electronics,[5] especially the logic circuits, stimulating the study of other 2D materials with large bandgaps.[6-10] There are a variety of materials in the 2D family, including graphene,[1] black phosphorus,[8] transition metal dichalcogenides,[6,7,11] Group-III chalcogenides,[12,13] hexagonal boron nitride,[14] the non-vdW 2D crystal bismuth oxide selenide[9] and MXenes.[15] From the perspective of the conductivity, there are metals,[16,17] semimetals,[1,18] semiconductors,[10] and insulators.[14] One of the major motivations for studying 2D materials is the need to fabricate sub-10 nm transistors from the semiconductor industries. For the ultrashort channel transistors, compared with traditional 3D semiconductors, 2D materials have various advantages such as the atomically thin conducting channel, enhanced gate control capability, surfaces free from dangling bonds and weak screening effect.[10,11,19-21] On the other hand, due to the wide range of bandgap[10] and strong light-matter interaction,[22-24] 2D materials have shown great potentials in the optoelectronic applications. By now, various 2D material based electronic devices have been reported, such as field effect transistors (FETs),[6,8] photo detectors,[7,25] photovoltaics,[26,27] light emitting diodes,[28,29] gas sensors,[30,31] nonvolatile memory devices,[32,33] artificial neurons,[34,35] and novel functional devices.[36,37]

In order to observe new phenomena, improve device performances and design new types of devices, various external stimuli have been studied to tune the electronic properties of 2D materials and 2D electronic devices, such as the electric field, magnetic field, strain, light, and chemical doping, among which the electric field is the most extensively studied. The electric field can tune the band structures, induce phase transitions and modulates interlayer interactions. It has been used in various applications to control the charge carrier transport, exciton transport and light-matter interactions. The strain can tune band structures and carrier mobilities, which is mainly used in flexible electronics. Chemical

doping has been widely used in optoelectronics and logic circuit applications. Although light is widely involved in the optoelectronic applications such as photo detectors, light emitters and photovoltaic devices, the light itself is less frequently used to control and tune properties of 2D materials. Light has been used in some studies to thin the materials or induce phase transitions. However, it is less used to control the functions of 2D electronic devices.

Studying the light control of 2D materials and 2D electronics is necessary and important. With the easily changeable power, size, and profile, light can be used to achieve the goals which are complex and difficult for other methods, such as the arbitrary patterning, tailoring, and surface modification of 2D materials. Moreover, in addition to the miniaturization of transistors, optical computers and optical-electronic hybrid computers are other options for the future high-speed computation, which show promising potentials for the emerging field of artificial neural networks where huge computation is required.[38-40] Therefore, it is important to study the light tunability of 2D electronic devices, which is necessary for 2D material applications in the future optical and hybrid optical-electronic computations.

This thesis demonstrates that light can be used to control and tune the electronic properties of various 2D materials and structures, and based on the tunable properties, different types of light-tunable electronic devices can be achieved.

1.2 Objectives and Scope

The objective of this PhD project is to achieve the light control of electronic properties of 2D materials and explore their applications in light-tunable 2D electronic devices. In details, the project focuses on the following three aspects:

First, control the CDW phase transition in the metallic 1T-TaS_2 using light. Study the underlying mechanism and fabricate electronic devices based on the light-tunable CDW phase transition, such as a TaS_2 based CDW oscillator.

Second, achieve the controlled hole doping in the semiconducting 2H-WSe_2 using light ablation. Study the underlying mechanism and fabricate logic circuits using selected-area light doping, such as a NOR gate circuit.

Third, study the light control of the conductivity in the heterostructure of narrow-gap black phosphorus and wide-gap strontium titanate using the photodoping effect. Study the underlying mechanism and fabricate nonvolatile devices based on the photodoping.

1.3 Dissertation Overview

The thesis addresses using light as a tool to control the electronic propertied of 2D materials and to tune the 2D electronic devices, providing more options to control 2D material properties and more strategies for 2D electronic applications.

Chapter 1 provides a rationale for the research and outlines the goals and scope.

Chapter 2 reviews the literature concerning the control of electronic properties of 2D materials and applications of 2D materials in electronic devices. Firstly, for the control of 2D material electronic properties, four major methods are discussed, which are the electric field control, strain control, chemical doping and light control. With these methods, the control of different properties such as bandgaps, electronic structures, phase transitions, carrier mobilities, carrier concentrations, carrier types and exciton dynamics are summarized. Secondly, different types of 2D electronic devices are reviewed, including 2D electronics in high frequency applications, logic circuits, and nonvolatile memory devices, which are involved in the following chapters.

Chapter 3 introduces rationales for selection of materials and experimental methods used in the whole project. For the experimental methods, the device fabrication and various types of characterization are discussed. The device fabrication includes mechanical exfoliation, sample transfer, vacuum annealing, electron beam lithography, maskless

photolithography, and metal deposition. The characterization includes atomic force microscopy, scanning Kelvin probe microscopy, Raman spectroscopy, ultraviolet-visible spectroscopy, scanning electron microscopy, transmission electron microscopy, and so on. The measurement methods of electronic devices are also discussed. The calculation and simulation methods of some key parameters are summarized.

Chapter 4 demonstrates the light control of the CDW phase transition in the metallic 1T-TaS_2 and its application in the light-tunable CDW oscillators. First, the in-situ Raman spectra was performed to provide the direct evidence of the bias-induced NCCDW-ICCDW phase transition. Then the importance of Joule heating effect on the phase transition was evaluated. Inspired by the Joule heating effect, the light heating was used to tune this NCCDW-ICCDW phase transition. And based on this light-tuned CDW phase transition, a light-tunable CDW oscillator was demonstrated, where the oscillation frequency of the output voltage could be continuously tuned by the light intensity.

Chapter 5 demonstrates the direct laser patterning of the WSe_2 logic circuits. First, the controllable light-ablation-induced hole doping of the 2H-WSe_2 was presented. Then various types of characterization were performed to understand the underlying mechanism. A further photocurrent mapping was performed on the laser patterned WSe_2 P-N junction. Finally, a NOR gate circuit was demonstrated by direct laser patterning, showing comparable performances with other logic circuit fabrication methods.

Chapter 6 demonstrates the light programmable BP/$SrTiO_3$ nonvolatile memory. First, BP transistors on the silicon substrate were tested, which showed a low photoresponsivity. Inspired by previous reports where photodoping effect could be introduced by defect states in wide-gap insulators, the BP devices on $SrTiO_3$ were studied, which showed an enhanced photoresponsivity as well as a persistent switching on the conductivity. Temperature-dependent photo switching behavior was studied under different light illuminations to understand its mechanism. Finally, the light-tunable multistage nonvolatile memory was demonstrated in the BP/$SrTiO_3$ device, which showed a very long retention time at low temperature.

Chapter 7 is the summary of the presented project. A related reconnaissance study is discussed. The strategies and opportunities of future work are discussed, which includes strategies to improve performances of the presented devices and other possible applications where light control can be used.

1.4 Findings and Outcomes/Originality

This research led to several novel outcomes by:

1. Providing the in-situ Raman evidence of the bias-induced NCCDW-ICCDW phase transition in 1T-TaS_2. Evaluating the Joule heating effect in the bias-induced CDW transition, showing that Joule heating plays a secondary role in the transition from NCCDW to ICCDW and is dominant in the transition from ICCDW to NCCDW. Demonstrating a light-tunable CDW oscillator based on the light tunability of the bias-induced CDW phase transition.
2. Demonstrating the laser-ablation-induced controlled hole doping in 2H-WSe_2, which can be used to fabricate P-N junctions with complex doping profiles. Demonstrating the direct light patterning of the WSe_2 based NOR gate logic circuit.
3. Reporting the dramatically enhanced photoresponsivity of BP in the BP/$SrTiO_3$ heterostructure. Demonstrating the wavelength-dependent persistent conductivity switching using the photodoping effect. Demonstrating a light-tunable multistage nonvolatile memory in the BP/$SrTiO_3$ heterostructure, with a very long retention time at low temperature.

References

[1] K. S. Novoselov, A. K. Geim, S. V. Morozov, D. Jiang, Y. Zhang, S. V. Dubonos, I. V. Grigorieva, and A. A. Firsov. *Science* **2004**, 306, 666-669.

[2] C. Lee, X. Wei, J. W. Kysar, and J. Hone. *Science* **2008**, 321, 385-388.

[3] K. I. Bolotin, K. J. Sikes, Z. Jiang, M. Klima, G. Fudenberg, J. Hone, P. Kim, and H. L. Stormer. *Solid State Commun.* **2008**, 146, 351-355.

[4] A. A. Balandin, S. Ghosh, W. Bao, I. Calizo, D. Teweldebrhan, F. Miao, and C. N. Lau. *Nano Lett.* **2008**, 8, 902-907.

[5] I. Meric, M. Y. Han, A. F. Young, B. Ozyilmaz, P. Kim, and K. L. Shepard. *Nat. Nanotechnol.* **2008**, 3, 654-659.

[6] B. Radisavljevic, A. Radenovic, J. Brivio, V. Giacometti, and A. Kis. *Nat. Nanotechnol.* **2011**, 6, 147-150.

[7] N. Perea-López, A. L. Elías, A. Berkdemir, A. Castro-Beltran, H. R. Gutiérrez, S. Feng, R. Lv, T. Hayashi, F. López-Urías, S. Ghosh, B. Muchharla, S. Talapatra, H. Terrones, and M. Terrones. *Adv. Funct. Mater.* **2013**, 23, 5511-5517.

[8] L. Li, Y. Yu, G. J. Ye, Q. Ge, X. Ou, H. Wu, D. Feng, X. H. Chen, and Y. Zhang. *Nat. Nanotechnol.* **2014**, 9, 372-377.

[9] J. Wu, H. Yuan, M. Meng, C. Chen, Y. Sun, Z. Chen, W. Dang, C. Tan, Y. Liu, J. Yin, Y. Zhou, S. Huang, H. Q. Xu, Y. Cui, H. Y. Hwang, Z. Liu, Y. Chen, B. Yan, and H. Peng. *Nat. Nanotechnol.* **2017**, 12, 530-534.

[10] V. K. Sangwan, and M. C. Hersam. *Annu. Rev. Phys. Chem.* **2018**, 69, 299-325.

[11] G. Fiori, F. Bonaccorso, G. Iannaccone, T. Palacios, D. Neumaier, A. Seabaugh, S. K. Banerjee, and L. Colombo. *Nat. Nanotechnol.* **2014**, 9, 768-779.

[12] D. J. Late, B. Liu, J. Luo, A. Yan, H. S. Matte, M. Grayson, C. N. Rao, and V. P. Dravid. *Adv. Mater.* **2012**, 24, 3549-3554.

[13] S. R. Tamalampudi, Y. Y. Lu, U. R. Kumar, R. Sankar, C. D. Liao, B. K. Moorthy, C. H. Cheng, F. C. Chou, and Y. T. Chen. *Nano Lett.* **2014**, 14, 2800-2806.

[14] K. Watanabe, T. Taniguchi, and H. Kanda. *Nat. Mater.* **2004**, 3, 404-409.

[15] B. Anasori, M. R. Lukatskaya, and Y. Gogotsi. *Nat. Rev. Mater.* **2017**, 2, 16098.

[16] B. Sipos, A. F. Kusmartseva, A. Akrap, H. Berger, L. Forro, and E. Tutis. *Nat. Mater.* **2008**, 7, 960-965.

[17] I. Guillamon, H. Suderow, S. Vieira, L. Cario, P. Diener, and P. Rodiere. *Phys. Rev. Lett.* **2008**, 101, 166407.

[18] P. Li, Y. Wen, X. He, Q. Zhang, C. Xia, Z. M. Yu, S. A. Yang, Z. Zhu, H. N. Alshareef, and X. X. Zhang. *Nat. Commun.* **2017**, 8, 2150.

[19] L. Xie, M. Liao, S. Wang, H. Yu, L. Du, J. Tang, J. Zhao, J. Zhang, P. Chen, X. Lu, G. Wang, G. Xie, R. Yang, D. Shi, and G. Zhang. *Adv. Mater.* **2017**, 29, 1702522.

[20] Y. Liu, X. Duan, Y. Huang, and X. Duan. *Chem. Soc. Rev.* **2018**, 47, 6388-6409.

[21] M. Y. Li, S. K. Su, H. P. Wong, and L. J. Li. *Nature* **2019**, 567, 169-170.

[22] F. Xia, H. Wang, D. Xiao, M. Dubey, and A. Ramasubramaniam. *Nat. Photon.* **2014**, 8, 899-907.

[23] X. Wang, and F. Xia. *Nat. Mater.* **2015**, 14, 264-265.

[24] Z. Sun, A. Martinez, and F. Wang. *Nat. Photon.* **2016**, 10, 227-238.

[25] X. Wang, P. Wang, J. Wang, W. Hu, X. Zhou, N. Guo, H. Huang, S. Sun, H. Shen, T. Lin, M. Tang, L. Liao, A. Jiang, J. Sun, X. Meng, X. Chen, W. Lu, and J. Chu. *Adv. Mater.* **2015**, 27, 6575-6581.

[26] M. L. Tsai, S. H. Su, J. K. Chang, D. S. Tsai, C. H. Chen, C. I. Wu, L. J. Li, L. J. Chen, and J. H. He. *ACS Nano* **2014**, 8, 8317-8322.

[27] D. Jariwala, A. R. Davoyan, J. Wong, and H. A. Atwater. *ACS Photonics* **2017**, 4, 2962-2970.

[28] P. J. Jeon, J. S. Kim, J. Y. Lim, Y. Cho, A. Pezeshki, H. S. Lee, S. Yu, S. W. Min, and S. Im. *ACS Appl. Mater. Interfaces* **2015**, 7, 22333-22340.

[29] Z. Yin, X. Zhang, Y. Cai, J. Chen, J. I. Wong, Y. Y. Tay, J. Chai, J. Wu, Z. Zeng, B. Zheng, H. Y. Yang, and H. Zhang. *Angew. Chem. Int. Ed. Engl.* **2014**, 53, 12560-12565.

[30] M. Donarelli, S. Prezioso, F. Perrozzi, F. Bisti, M. Nardone, L. Giancaterini, C. Cantalini, and L. Ottaviano. *Sens. Actuators B Chem.* **2015**, 207, 602-613.

[31] B. Cho, A. R. Kim, D. J. Kim, H. S. Chung, S. Y. Choi, J. D. Kwon, S. W. Park, Y. Kim, B. H. Lee, K. H. Lee, D. H. Kim, J. Nam, and M. G. Hahm. *ACS Appl. Mater. Interfaces* **2016**, 8, 19635-19642.

[32] D. Li, M. Chen, Z. Sun, P. Yu, Z. Liu, P. M. Ajayan, and Z. Zhang. *Nat. Nanotechnol.* **2017**, 12, 901-906.

[33] M. Wang, S. Cai, C. Pan, C. Wang, X. Lian, Y. Zhuo, K. Xu, T. Cao, X. Pan, B. Wang, S.-J. Liang, J. J. Yang, P. Wang, and F. Miao. *Nat. Electron.* **2018**, 1, 130-136.

[34] H. Kalita, A. Krishnaprasad, N. Choudhary, S. Das, D. Dev, Y. Ding, L. Tetard, H. S. Chung, Y. Jung, and T. Roy. *Sci. Rep.* **2019**, 9, 53.

[35] D. Xie, W. Hu, and J. Jiang. *Org. Electron.* **2018**, 63, 120-128.

[36] E. Guerriero, L. Polloni, M. Bianchi, A. Behnam, E. Carrion, L. G. Rizzi, E. Pop, and R. Sordan. *ACS Nano* **2013**, 7, 5588-5594.

[37] G. Liu, B. Debnath, T. R. Pope, T. T. Salguero, R. K. Lake, and A. A. Balandin. *Nat. Nanotechnol.* **2016**, 11, 845-850.

[38] Y. Shen, N. C. Harris, S. Skirlo, M. Prabhu, T. Baehr-Jones, M. Hochberg, X. Sun, S. Zhao, H. Larochelle, D. Englund, and M. Soljačić. *Nat. Photon.* **2017**, 11, 441-446.

[39] J. Chang, V. Sitzmann, X. Dun, W. Heidrich, and G. Wetzstein. *Sci. Rep.* **2018**, 8, 12324.

[40] K. Vandoorne, P. Mechet, T. Van Vaerenbergh, M. Fiers, G. Morthier, D. Verstraeten, B. Schrauwen, J. Dambre, and P. Bienstman. *Nat. Commun.* **2014**, 5, 3541.

Chapter 2

Literature Review

This chapter summarizes recent progresses in the control of electronic properties of 2D materials and the applications of 2D materials in electronic devices. Firstly, four major methods are discussed in the control of electronic properties, which are the electric field control, strain control, chemical doping and light control. With these methods, the control of properties such as bandgaps, electronic structures, phase transitions, carrier mobilities, carrier concentrations, carrier types and exciton dynamics are summarized. Secondly, different types of 2D electronic devices are reviewed, such as 2D electronics in high frequency applications, logic circuits, and nonvolatile memory devices. Finally, the PhD project in the context of the literature is discussed.

2.1 Control of Electronic Properties of 2D Materials

In traditional 3D semiconductors, as the channel length decreases, the thickness of the gate dielectric layer decreases inevitably, leading to the increased gate leakage, poor gate control efficiency and enhanced surface scattering.[1-4] Two-dimensional materials, on the other hand, provide the possibilities to solve these problems due to their atomically thin nature, fewer surface defects and weak screening effect.[3-5] The family of 2D materials includes a diversity of materials, such as graphene,[6] black phosphorus,[7] hexagonal boron nitride,[8] Group-III chalcogenides,[9,10] transition metal dichalcogenides,[11] the non-vdW 2D crystal bismuth oxide selenide (Bi_2O_2Se)[12] and metal carbides and nitrides (MXenes).[13,14] Figure 2.1 shows the lattice structures of several typical layered 2D materials. From the perspective of electronic properties, there are various 2D materials, including metals,[15-17] semiconductors,[18-20] insulators,[8] superconductors,[16,17] semi-metals,[21-23] charge density wave (CDW) materials,[24-26] ferromagnetic materials,[27-30] etc. Figure 2.2 shows the diagram of band alignment of selected 2D materials, traditional inorganic semiconductors and metals.[5] There are various methods to control the electronic properties of 2D materials. In this section, four methods will be discussed: (1) electric field control, (2) strain control, (3) chemical doping, and (4) light control.

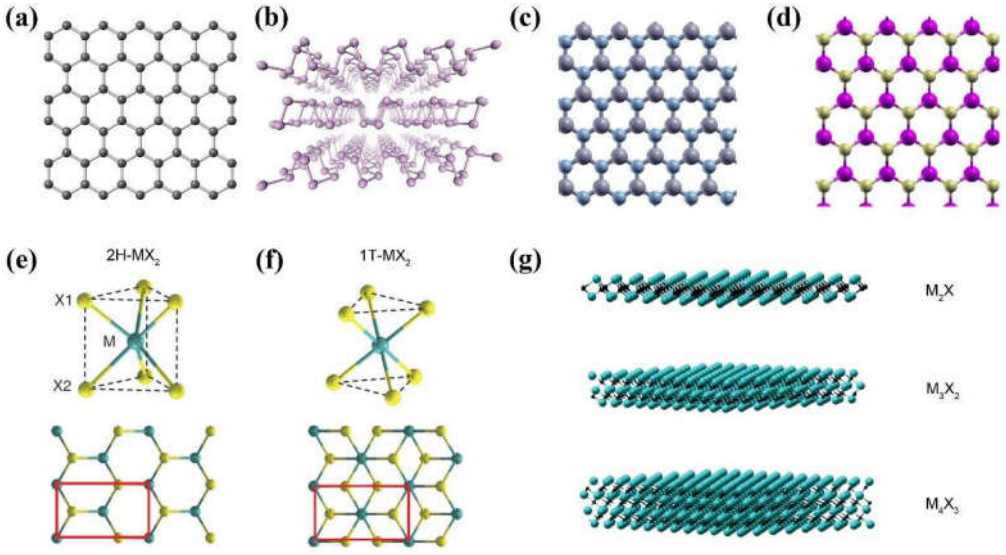

Figure 2.1 Crystal structures of typical 2D materials. (a) Graphene. (b) Black phosphorus. Reproduced with permission.[7] Copyright 2014, Macmillan Publishers Limited. (c) Boron nitride.

Grey: Boron. Blue: Nitrogen. (d) Group-III chalcogenides. Purple: Group-III element (Ga or In). Yellow: Chalcogen. (c) and (d) Reproduced with permission.[31] Copyright 2016, AAAS. Transition metal dichalcogenides in 2H (e) and 1T (f) phase. Green: Transition metal element. Yellow: Chalcogen. Reproduced with permission.[32] Copyright 2014, AAAS. (g) MXenes. Reproduced with permission.[14] Copyright 2017, Macmillan Publishers Limited.

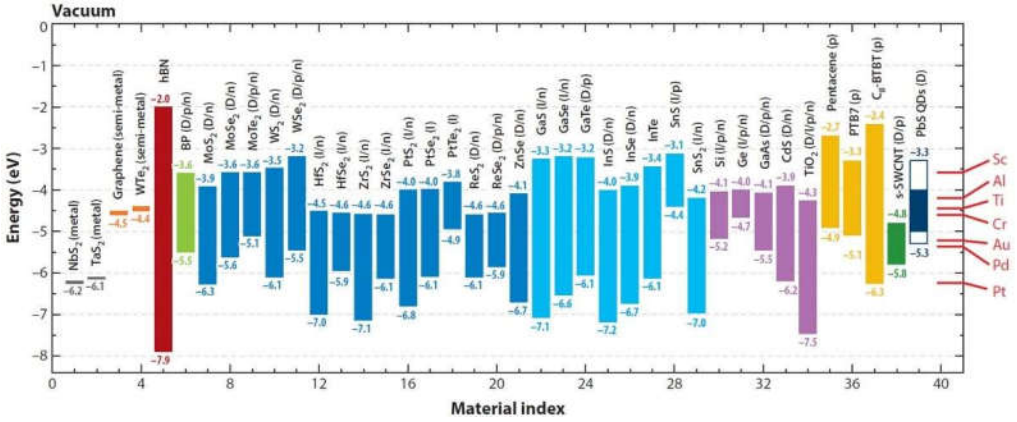

Figure 2.2 Diagram of band alignment of selected materials. From left to right: 2D metals, 2D semimetals, hBN, black phosphorus, TMDs, Group-III chalcogenides, traditional inorganic 3D semiconductors, organic semiconductors, semiconducting SWCNT, PbS quantum dots and metals used for contact electrodes. For metals and semimetals, the work function is shown. For hBN and semiconductors, the location of bandgap is shown. D/I indicates a direct or indirect bandgap. p/n indicates a hole or electron dominant transport behavior. Reproduced with permission.[5] Copyright 2018, Annual Reviews.

2.1.1 Electric Field Control

Due to the ultrathin thickness and limited carrier concentration of 2D materials, the screening effect of external electric field is reduced. As a result, external electric field has been extensively studied to tune the electrical properties of 2D materials. There are mainly two types of electric field: vertical electric field applied by gate and in-plane electric field applied by source-drain bias. While for the vertical electric field, two types of gate are mainly used, which are the gate with solid dielectrics such as oxide and hBN and the ionic liquid gate. Compared with the solid dielectric gate, the ionic liquid gate has a higher efficiency in tuning the Fermi level due to its higher capacitance.

Most studies focus on the vertical electric field applied by the gate voltage. For example, the pristine AB-stacking bilayer graphene is a semiconductor with zero bandgap. However, a vertical electric field can open the bandgap of bilayer graphene, which is tunable with increasing electric field. According to a theoretical calculation, the bandgap could be about 10 meV when the carrier concentration is tuned to 10^{12} cm^{-2} by the vertical electric field.[33] By adjusting the voltages of top gate and back gate in a dual-gate bilayer graphene FET, the resistance of the device changed for about 3 orders of magnitude compared with zero gate at 55 mK, which was related to an opened bandgap of about 10 meV.[34] A further widely tunable bandgap up to 250 meV was achieved at room temperature as the displacement field increased to 3.0 V/nm, which was confirmed by the infrared micro-spectroscopy.[35] Similarly, this gate-voltage control of the bandgap also exists in bilayer MoS_2. Different from bilayer graphene, the bandgap of bilayer MoS_2 decreases with increasing field strength. When the displacement field was zero, the direct bandgap of bilayer MoS_2 was measured to be 1.85 eV, which decreased to 1.55 eV when the field increased to 1.2 V/nm, accompanied with the red shift of the interlayer-transition-related peak in the photoluminescence (PL) spectra.[36] Although vertical electric field has little effect on monolayer MoS_2, it can tune the bandgap of rippled monolayer MoS_2 in a wide range.[37] Calculations shows that instead of applying the electric field vertically, a transverse electric field can also induce the bandgap narrowing, for both multilayer and monolayer MoS_2 armchair nanoribbons.[38,39] Under a high enough electric field, a semiconductor-metal transition can be induced.[38,39] The 2H-MoS_2 has been reported to show an insulator-metal-superconductor phase transition under the ionic liquid gate.[40] As shown in Figure 2.3a, an ionic liquid droplet (DEME-TSFI) is placed onto the MoS_2 transistor, across which a gate voltage V_{LG} is applied. Figure 2.3b shows the transfer characteristics of the transistor under the ionic liquid gate or the back gate, which shows that the ionic liquid gate has a better gate efficiency in tuning the Fermi level, due to a relatively larger capacitance. With increasing ionic liquid gate V_{LG}, MoS_2 changes from insulator to metal and finally to superconductor at the cryogenic temperature (Figure 2.3c). On the other hand, increasing back gate can only induce the phase transition from insulator to metal (Figure 2.3d). As shown in Figure 2.3e, the metal-superconductor phase transition

happens when the carrier concentration increases above 70×10^{12} cm^{-2}. And the transition temperature reaches a maximum at n~130×10^{12} cm^{-2}. Such gate-induced superconductivity has also been reported to exist in other systems, such as the pristine semiconducting 1T-$SnSe_2$ and 2H-WS_2.[41,42] Lu et al. reported that the superconducting dome only exists within certain range of gate voltage.[41] Under high ionic gate, the increased deep Coulomb traps will introduce strong localization, leading to the increased scattering of electrons and the re-entrant of insulating state at low temperature.[41] In the 1T-TaS_2 which is a Mott insulator at low temperature, the ionic liquid gate can also induce a phase transition from insulator to superconductor.[43] Furthermore, Wang et al. performed the in-situ Raman and SHG spectroscopy measurement of the ionic liquid gated $MoTe_2$, showing that the ionic liquid gate will introduce a structure change of $MoTe_2$ from 2H phase to 1T' phase.[44] This result indicates that all the above ionic liquid gate induced transitions of electronic properties may be accompanied by a transition in crystal structures, providing a possibility to tune 2D materials to phases that cannot stably exist under normal conditions. Besides, in the semi-metallic 2D topological insulator 1T'-WTe_2, a superconducting phase can also be induced by a dual gate configuration with hBN to be the dielectric layers.[45]

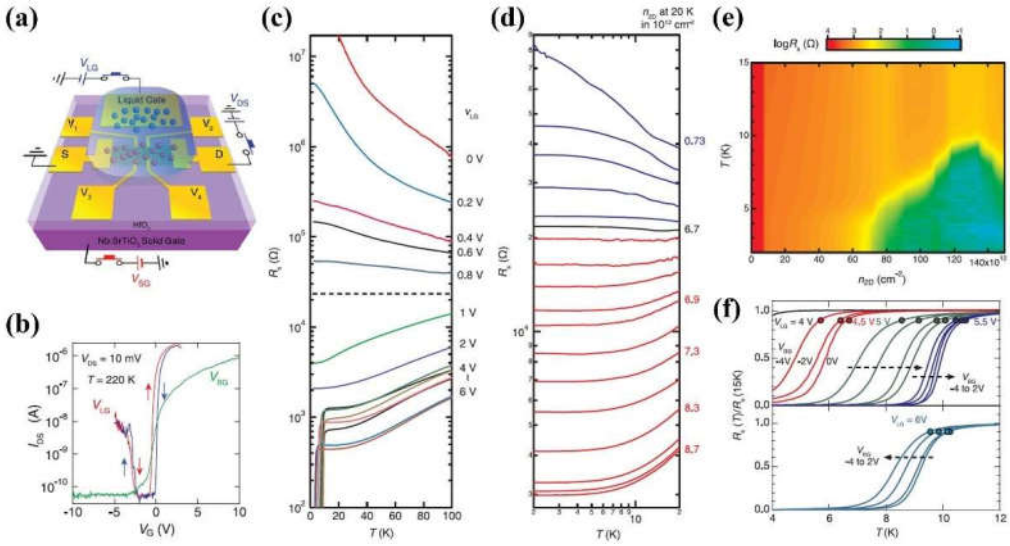

Figure 2.3 Ionic liquid gate induced superconductivity in 2H-MoS_2. (a) Schematic diagram of a 2H-MoS_2 transistor with an ionic liquid gate and an oxide back gate. (b) Transfer characteristics of the transistor under different ionic liquid gate (V_{LG}) or back gate voltage (V_{BG}). (c) Temperature-dependent sheet resistance of MoS_2 under different V_{LG}, where an insulator-metal-superconductor

phase transition exists. (d) Temperature-dependent sheet resistance of MoS_2 under different V_{BG}, where an insulator-metal phase transition exists. (e) Sheet resistance under different temperatures and carrier concentration. (f) Temperature-dependent normalized sheet resistance under different V_{LG} and V_{BG}. Reproduced with permission.[40] Copyright 2012, AAAS.

Stacking configurations can influence the response of materials to the external electric field. A theoretical study shows that bilayer MoS_2 with different stacking configurations have different decreasing rate in bandgap with the increasing electric field,[46] providing possibilities to manipulate electronic properties by changing stacking configurations. Recent works have shown that in the magic twisted bilayer graphene, electrostatic doping can induce the phase transitions between Mott insulator, metal and superconductor (Figure 2.4).[47,48] This superconductivity originates from strong electron-electron interactions rather than the electron-phonon coupling, which is different from conventional BCS superconductors.[48]

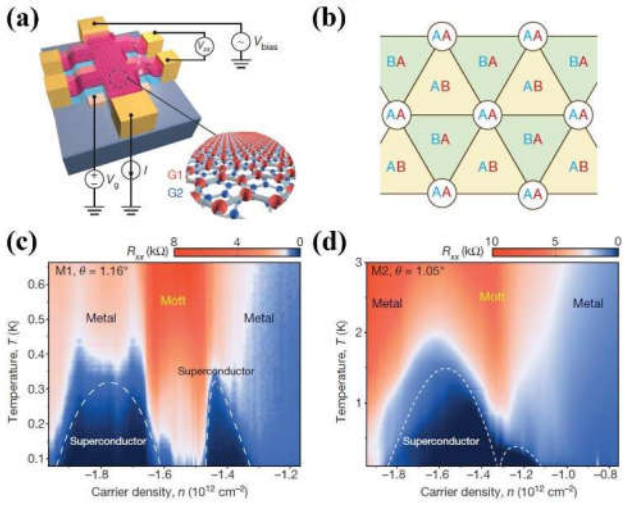

Figure 2.4 Gate-induced superconductivity in magic-angle twisted bilayer graphene. (a) Schematic diagram of a typical device. (b) Schematic drawing of the stacking order from the top view. (c) Four-probe resistance at different temperatures and carrier density for 1.16° twisted angle. Two superconducting domes are marked by dashed lines, separated by a Mott-like insulator state. (d) Four-probe resistance at different temperatures and carrier density for 1.05° twisted angle, where two superconducting domes merge. Reproduced with permission.[47,48] Copyright 2018, Macmillan Publishers Limited.

The optoelectronic properties of 2D materials and junctions can also be tuned by the external electric field. For instance, in a vertically graphene-MoS_2-graphene sandwiched heterojunction, the photo-generated carriers can be modulated by a top or back gate in such way that the polarity and amplitude of the photocurrent can be tuned, with an external quantum efficiency up to 55%.[49] The high external quantum efficiency is due to the high photo absorption efficiency by the multilayer MoS_2 and the high carrier separation efficiency by the electric field. In the type-II vdW heterojunctions formed by two different TMDs (such as MoS_2 and WSe_2), interlayer excitons will be generated by photo excitations. By applying a vertical electric field, the energy of interlayer excitons can be tuned, due to the shift of band energy level under the vertical gate bias.[50] And the lifetime of the interlayer excitons can be tuned by more than 10 times by the vertical electric field.[51,52] Due to the relatively long lifetime of the interlayer excitons (in nanosecond range), 2D exciton-based transistors can be fabricated. As shown in Figure 2.5a, interlayer excitons are generated upon light excitation and then diffuse spontaneously. After diffusion for a certain distance (several micrometers), excitons recombine with native charges, accompanied by the emission of light (Figure 2.5b and 2.5d). However, this process of exciton diffusion can be blocked by applying a high gate voltage (Figure 2.5c), as a result of which the light emission is suppressed (Figure 2.5e).[53] This provides more options to build light-electronic hybrid integrated circuits.

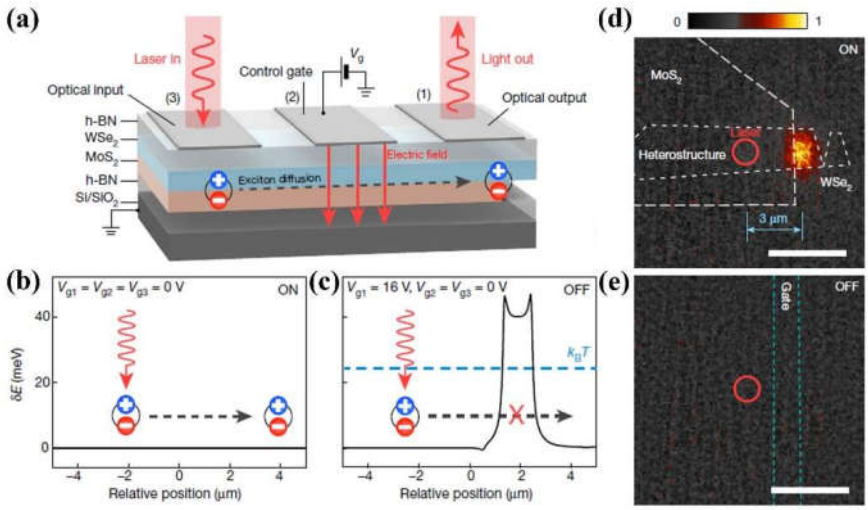

Figure 2.5 Room-temperature exciton-based transistor. (a) Schematic diagram of the device.

Variation of exciton energy in ON (b) and OFF (c) states. Exciton emission images for ON (d) and OFF (e) states corresponding to (b) and (c), respectively. Reproduced with permission.[53] Copyright 2018, Springer Nature Limited.

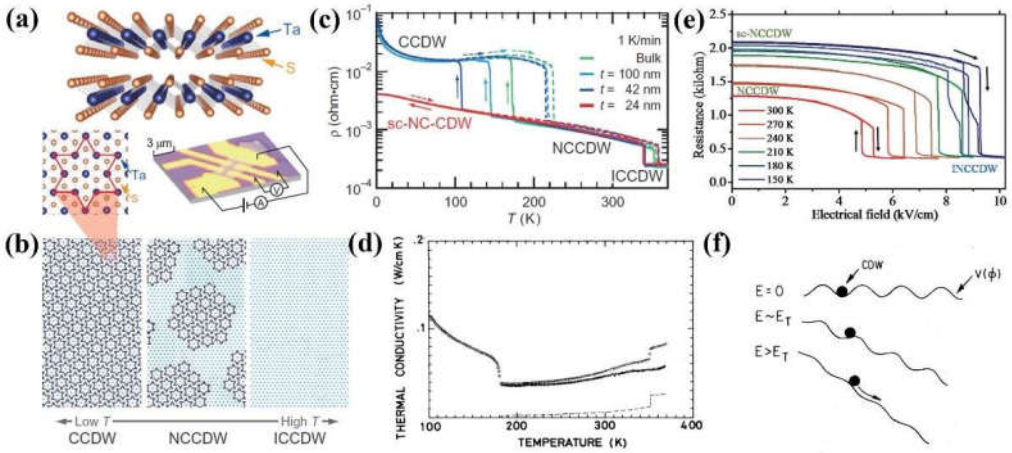

Figure 2.6 CDW phase transitions in 1T-TaS_2. (a) Top: Crystal structure of 1T-TaS_2. Bottom: Structure of a David star and a 1T-TaS_2 device. (b) Schematic drawing of lattice distortions for different CDW phases. (c) Temperature-dependent resistivity. (a-c) Reproduced with permission.[54] Copyright 2015, AAAS. (d) Temperature-dependent thermal conductivity. Reproduced with permission.[55] Copyright 1985, American Physical Society. (e) In-plane electric field induced phase transition between NCCDW and ICCDW. Reproduced with permission.[56] Copyright 2017, Royal Society of Chemistry. (f) Schematic drawing of lattice potential under different in-plane electric field. Reproduced with permission.[57] Copyright 1988, American Physical Society.

Compared with the vertical electric field, the in-plane electric field is less studied in the electronic property control of 2D materials. In-plane electric field can be used some cases such as tuning the polarizations of ferroelectric materials and the phases of CDW materials. Ferroelectric materials are spontaneously polarized without an external electric field due to different spatial distributions of net positive and net negative charges. Traditional ferroelectric materials include perovskite oxides, HfO_2, ZrO_2, etc.[58,59] For 2D materials, there are several kinds of materials showing the in-plane ferroelectrics, such as Group-IV monochalcogenides and β'-In_2Se_3.[60-62] By applying a high enough in-plane electric field, the in-plane polarization direction can be switched. CDW is a metastable collective

electronic phase featured by a periodic electron density induced by periodic lattice distortions. This usually happens in low-dimensional metals or 3D metals consisted of quasi-1D atom chains.[43,63-65] Among 2D CDW materials, 1T-TaS_2 is one of the most studied due to its enriched CDW phases. As shown in Figure 2.6, there are mainly three CDW phases, which are commensurate CDW (CCDW), nearly commensurate CDW (NCCDW) and incommensurate CDW (ICCDW) phases, with increasing temperature. The distorted lattice is formed by David stars where 12 Ta atoms move towards 1 central Ta atoms (Figure 2.6a). The three CDW phases exhibit distinguished resistivity as well as thermal properties.[54,55] The in-plane electric field can induce the transition between NCCDW and ICCDW phases (Figure 2.6e), which is usually explained by the de-pinning of CDW single particles under the in-plane bias (Figure 2.6f).[57]

2.1.2 Strain Control

The high mechanical strength of 2D materials enables the control of their electronic properties by strain. There are various ways to apply strain to 2D materials, utilizing flexible and elastic substrates, piezoelectric substrates and patterned substrates. For example, after transferring 2D materials on to the flexible substrates such as PET and elastic substrates such as PDMS, strain can be applied by bending or elongating the substrates.[66,67] Hui et al. reported the use of a piezoelectric substrate PMN-PT to apply the controllable compressive strain, which however was much smaller than that induced by flexible substrates.[68] On the other hand, the pre-patterning of nano-structures on substrates is also a method to induce strain,[69] which however has less tunability.

Calculations have shown that a high strain is required in order to induce a bandgap int the monolayer graphene. The tension along the zigzag direction is most effective with a critical strain of 23%. While no bandgap will be formed under the tension along the armchair direction.[70] For bilayer graphene, the bandgap can be opened by pulling two layers apart, which could be achieved via intercalation.[71,72] For monolayer black phosphorus, strain along the zigzag direction will induce a direct-indirect-direct bandgap transition. While strain along the armchair direction will induce a direct-indirect bandgap transition. The

maximum bandgap is achieved at around +4% strain along the zigzag direction and +8% strain along the armchair direction. A zero bandgap may be achieved at large strain beyond 12%.[73] Compared with graphene, band structures of TMDs are more easily to be tuned by the strain. There are various types of strain, such as the tensile strain (uniaxial expansion along zigzag or armchair direction and homogeneous biaxial expansion) and the shear strain (expansion in one direction and compression in the other). For monolayer 2H phase MX_2 (M = Mo or W, X = S, Se or Te) under these kinds of strain, the bandgap decreases monotonically with increasing strain and the bandgap changes from the direct to the indirect. As for the decreasing rate, MS_2 is fastest, followed by MSe_2. And homogeneous biaxial expansion can achieve the most rapid decrease in the bandgap. For MS_2 under a 10% biaxial strain, merge of d_{z^2} orbit induces a semiconductor-metal phase transition.[74] In 1T phase materials such as ZrX_2 and HfX_2 (X = S or Se), the bandgap will increase followed by decrease with increasing expansion. For 1T-MTe_2 where M = Zr or Hf, the bandgap will be opened above the critical biaxial strain and experience a metal-semiconductor phase transition.[75] The detailed changes of bandgap with strain are shown in the Figure 2.7 and Figure 2.8. From the experiment, by studying the PL spectra under strain, the direct/indirect bandgap can be extracted. Compared with results from theoretical calculations, the bandgap decreases slower with increasing strain according to the experimental results.[67,76,77] This may be due to the fact that the tensile force was not fully applied onto the samples and the actual strain was not as high as expected and not homogeneous. Due to the strain-tunable band structures, inhomogeneous local strain can be applied to 2D TMDs such as monolayer 2H-MoS_2 to tune the local bandgap and form a potential well, which can act like the artificial atom.[66,78,79]

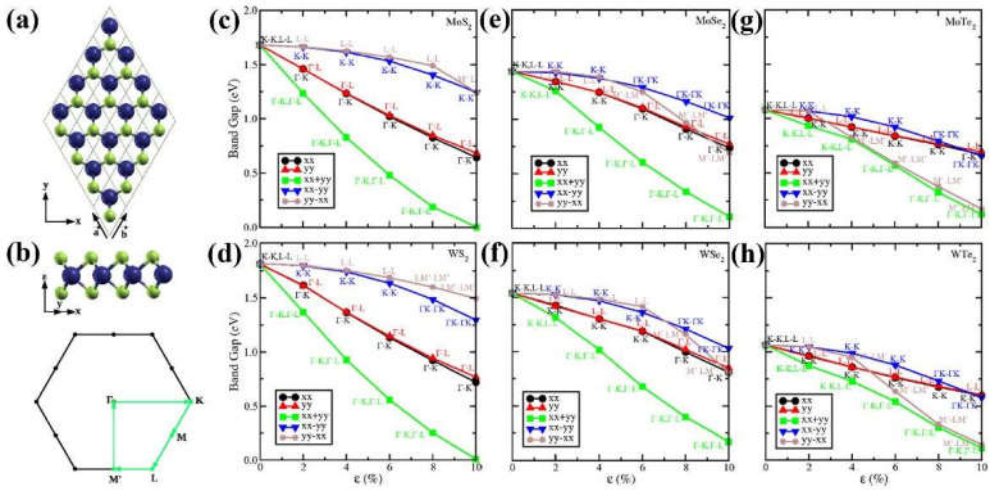

Figure 2.7 Strain-dependent bandgap of monolayer 2H TMDs. (a) Top view of crystal structure of 2H TMDs. (b) Side view of 2H TMD crystal structure and the irreducible Brillouin zone. Bandgap of monolayer 2H MoS_2 (c), WS_2 (d), $MoSe_2$ (e), WSe_2 (f), $MoTe_2$ (g), and WTe_2 (h) under various types of strain. xx: uniaxial expansion along the zigzag direction. yy: uniaxial expansion along the armchair direction. xx+yy: biaxial expansion along both zigzag and armchair direction. xx-yy: expansion along zigzag direction and suppression along armchair direction. yy-xx: suppression along zigzag direction and expansion along armchair direction. All types of strain are homogeneous. Reproduced with permission.[74] Copyright 2012, ACS.

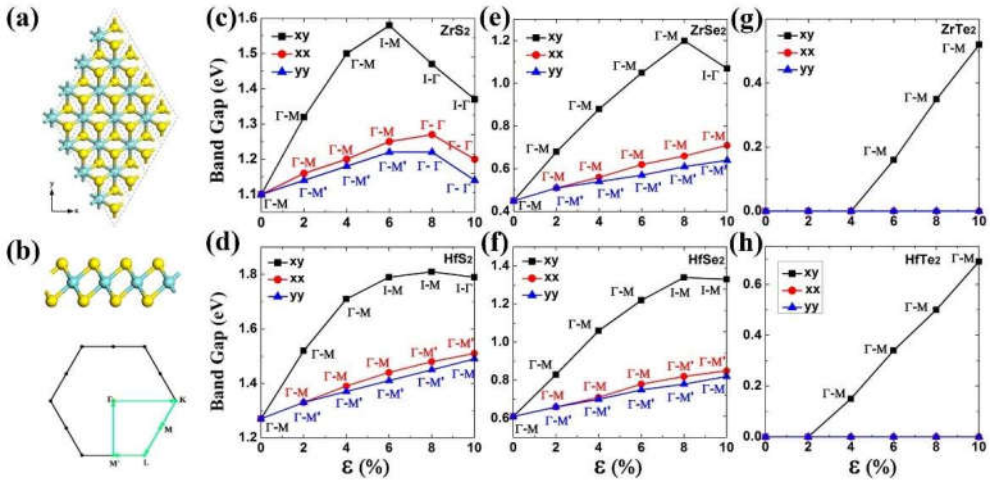

Figure 2.8 Strain-dependent bandgap of monolayer 1T TMDs. (a) Top view of crystal structure of 1T TMDs. (b) Side view of 1T TMD crystal structure and the irreducible Brillouin zone. Bandgap of monolayer 1T ZrS_2 (c), HfS_2 (d), $ZrSe_2$ (e), $HfSe_2$ (f), $ZrTe_2$ (g), and $HfTe_2$ (h) under various types of strain. xx: homogeneous uniaxial expansion along the zigzag direction. yy: homogeneous uniaxial expansion along the armchair direction. xy: homogeneous biaxial expansion along both

zigzag and armchair direction. Reproduced with permission.[75] Copyright 2014, ACS.

The Raman spectra of 2D materials can be tuned by the strain.[80-84] For monolayer graphene under uniaxial tensile stress, due to the symmetry breaking induced by strain, both G and 2D peaks split into 2 sub-peaks, noted as G^+, G^-, $2D^+$, and $2D^-$, respectively. For the non-polarized Raman spectra, G^+ and G^- peaks shift linearly with increasing strain at rates of -5.6 and -12.5 cm^{-1}/%.[80] Moreover, the shift shows strong polarization dependence. For strain along the armchair direction, the shift rates for $2D^-$ and $2D^+$ are -30.5 and -21.7 cm^{-1}/%. And the incident laser polarization will influence the peak shift and location. For the strain along the zigzag direction, shift rates are -29.7 and -16.3 cm^{-1}/%. The peak splitting is more obvious and the incident laser polarization mainly influences the relative intensities of two split peaks.[81] In monolayer MoS_2, the uniaxial strain along the zigzag direction can induce the splitting of the in-plane vibration mode $E_{2g}{}^1$ while it has no obvious influence on the out-of-plane mode A_{1g}. The shift rates of the split peaks $E_{2g}{}^{1-}$ and $E_{2g}{}^{1+}$ are -2.5 and -0.8 cm^{-1}/%, respectively, which also show the polarization dependence.[82,83]

The strain will influence the transport properties, mainly by the change in effective carrier mass and inter-valley scattering. For example, in monolayer MoS_2 under the strain in the range of $\pm$5%, the effective electron mass of the K valley will decrease with tensile strain and increase with compressive strain. While the effective mass of the Q valley will increase with tensile strain and decrease with compressive strain. For the tensile strain, the K valley minimum is much lower than the Q valley minimum, making it dominate the electron transport. While for the compressive strain, the difference between K and Q valley decreases and the intervalley scattering increases. Under the large enough compressive strain, the Q valley will be lower than the K valley and Q valley dominates the transport. As a result, the electron mobility will increase with tensile strain. For the compressive strain, the electron mobility will decrease first due to the increased K valley effective mass and inter-valley scattering, followed by an increase due to the decreased Q valley effective mass (Figure 2.9).[85] Transfer of one layer of 2D material onto another layer of 2D material is a technique often used to fabricate vdW heterostructures. During this process,

bubbles in the micro- and nano-meter scale are often observed. The random fluctuations of strain can produce the random pseudomagnetic field, which will increase the charge scattering and lower the mobility.[86]

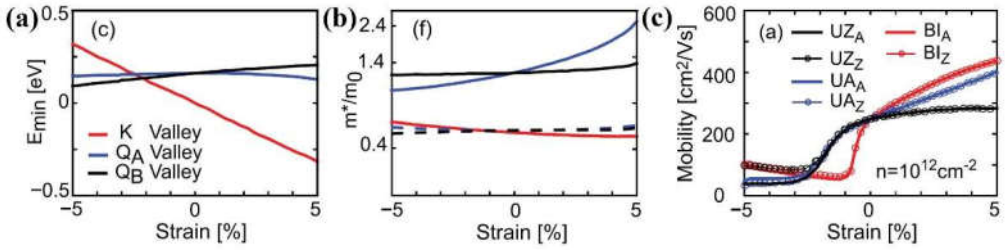

Figure 2.9 Electronic properties of monolayer MoS_2 under strain. (a) Strain-dependent minima of K and Q valleys. (b) Strain-dependent effective mass for different valleys. (c) Strain-dependent electron mobility. UZ, UA, and BI stand for uniaxial strain along zigzag direction, uniaxial strain along armchair direction, and biaxial strain, respectively. The subscripts A and Z stands for mobility in the armchair and zigzag directions, respectively. Reproduced with permission.[85] Copyright 2015, IOP Publishing.

2.1.3 Chemical Doping

Carrier doping is one of the fundamental techniques for modern semiconductor industries, which is required in the fabrication of various devices such as field effect transistors, photo detectors, light-emitting diodes and bipolar junction transistors. Controlled carrier doping is among the major concerns for the practical applications of 2D materials. There are in-situ doping and post-synthesis doping. For the in-situ doping, different synthesis methods have been used to obtain the doped materials, such as chemical vapor transport (CVT), chemical vapor deposition (CVD), aerosol-assisted CVD (AACVD) and hydrothermal synthesis. For example, by sealing powder Mo, S, and Nb precursors into an ampoule with a stoichiometric ratio of 1:2:0.005, Nb atoms could be doped into the MoS_2 using the CVT method where Mo atoms were partially substituted by Nb atoms and the p-type Nb-doped MoS_2 were obtained.[87] Similarly, instead of doping the metal atoms, chalcogen atoms can also be used for doping. Ternary $WSe_{(2-2x)}Te_{2x}$ single crystals could be synthesized using CVT method by tuning the precursor ratio, where the semiconductor-metal transition could be achieved with increasing Te doping.[88] Similar ternary materials can also be

synthesized using the CVD method, by tuning the precursor ratio or the temperature-dependent vapor pressure.[89,90] In the $WS_{2x}Se_{2-2x}$ alloy, with the increasing Se doping, the alloy gradually changed from an n-type semiconductor to a p-type semiconductor, accompanied by the decrease of bandgap from 2.0 eV to 1.6 eV.[90] Cr-doped MoS_2 has been reported to be synthesized by the aerosol-assisted CVD, where a solution of MoL_4 and CrL_3 solved in THF was used as the precursor. The precursor mist was transported by Ar gas to the heated substrates where Cr-doped MoS_2 was synthesized.[91] Compared with CVT and CVD, the hydrothermal synthesis method has a larger yield. The synthesis of Pt-doped, Co-doped, and Ni-doped MoS_2 by hydrothermal method has been reported.[92]

As for the post-synthesis doping, there are various methods, such as ion implantation, covalent functionalization, surface transfer doping by gas molecules, chemical solutions, or transition metal oxides, and doping via ferroelectric materials. Ion implantation is a method to introduce carrier doping that is extensively used in traditional silicon-based semiconductors. In 2D materials, due to their ultrathin nature, the implantation energy must be low enough in order not to induce severe sample damage. Nipane et al. reported the phosphorus implantation using the low energy plasma immersion ion implantation. MoS_2 flakes were placed in the PH_3/He plasma and the phosphorus was implanted into MoS_2 with an energy of 2 keV.[93] The implanted MoS_2 were p-type doped while the top 3-4 nm of the flakes was etched, which means that this technique may not be suitable for the doping of thin samples, especially the monolayer samples. Compared with the ion implantation, other moderate doping methods are more widely used on 2D materials, such as covalent functionalization and surface transfer doping. Covalent functionalization attaches molecules onto 2D materials via covalent bond, which can be used to introduce n-type and p-type doping. For example, Sim et al. annealed the exfoliated MoS_2 at 250 ℃ for one hour to introduce S vacancies, which was then immersed into FDT (CF_3-terminated thiol)/THF and MEA (NH_2-terminated thiol)/ethanol solution. The chemisorption of FDT and MEA by MoS_2 introduced the p-type and n-type covalent doping, respectively.[94] By chemisorption of NO_2 at a temperature of 150 ℃, the p-type doping could be induced to WSe_2 by the formation of $WSe_{2-x-y}O_xN_y$, which is irreversible at room temperature.[95] Similarly, by generating the plasma in the mixture gas of CH_4/Ar/H_2, p-type doping of WS_2

could be achieved by the substitution of S with CH_x.[96] As for the surface transfer doping, it has been reported that the n-type MoS_2 could be doped to the p-type upon immersion into the $AuCl_3$ solution. Au aggregation from $AuCl_4^-$ would take place on the surface of MoS_2, which would take electrons from MoS_2, acting as the electron acceptor and leading to the p-type doping.[97] Other solution-based dopants have also been used to achieve carrier doping of 2D materials, such as the p-type dopants TCNQ and F_4TCNQ, and the n-type dopants Dichloroethane (DCE), $Co_6Se_8(PEt_3)_6$ and NADH.[98,99] For WSe_2 and $MoSe_2$ exposed to O_3/H_2O or O_2/H_2O, the solubilization of O_2 or O_3 molecules in the water adlayer would form a redox system, whose redox potential was lower than the Fermi level of WSe_2 and $MoSe_2$, leading to the electron transfer from WSe_2 and $MoSe_2$ to the redox system.[100] This redox-induced p-type doping was non-covalent doping and reversible by dehydration upon annealing. Due to their high work function,[101] transition metal oxides are often used for the surface transfer doping. For example, by deposition a layer of MoO_3 onto the black phosphorus, a heavy hole doping could be achieved, where the hole concentration increased with increasing thickness of the MoO_3 layer.[102] Similar p-type doping could also be achieved in the ambipolar WSe_2.[103] Instead of deposition, transition metal oxides can be induced by oxidation of the TMDs. By exposure to O_3 at 100 °C for one hour, a layer of WO_{3-x} could be formed on top of the multilayer WSe_2, leading to the hole doping.[104] Notedly, the efficiency of electron transfer between WSe_2 and WO_{3-x} could be affected by surface absorption in the ambient air, which might be due to the thin thickness of the oxide layer. On the other hand, coating a layer of low work function materials such as Cs_2CO_3 will induce the electron doping.[102] Furthermore, ferroelectric materials can be used to tune the Fermi level of 2D semiconductors, leading to the tune of carrier concentration and carrier type. For example, by transferring a monolayer WSe_2 onto the ferroelectric $BiFeO_3$ substrate, the WSe_2 P-N homojunction could be formed by controlling the local polarization of the beneath $BiFeO_3$ substrate.[105]

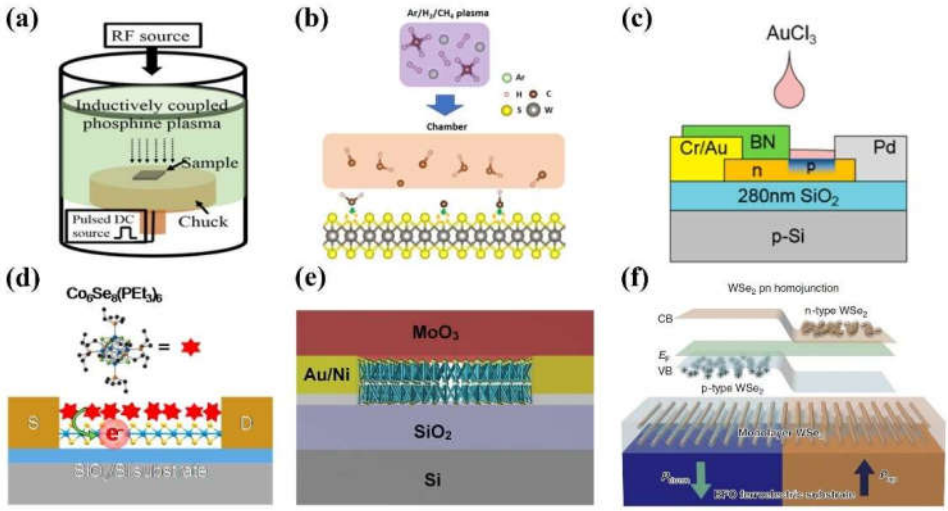

Figure 2.10 Post-synthesis doping methods. (a) Plasma immersion ion implantation of phosphorus into MoS_2. Reproduced with permission.[93] Copyright 2016, ACS. (b) Covalent doping by CH_x group. Reproduced with permission.[96] Copyright 2019, AAAS. (c) Surface transfer hole doping by $AuCl_3$ solution. Reproduced with permission.[97] Copyright 2014, ACS. (d) Surface transfer electron doping by molecule $Co_6Se_8(PEt_3)_6$. Reproduced with permission.[98] Copyright 2016, ACS. (e) Surface transfer hole doping by coating a layer of MoO_3. Reproduced with permission.[103] Copyright 2016, WILEY-VCH Verlag GmbH & Co. KGaA, Weinheim. (f) Patterning of WSe_2 P-N homojunction using the ferroelectric $BiFeO_3$ substrate. Reproduced with permission.[105] Copyright 2018, Springer Nature.

2.1.4 Light Control

The light-matter interactions of 2D materials have been extensively studied, such as photocurrent response in single materials or heterojunctions, photoluminescence and nonlinear optical properties like SHG.[44,50,90,102] In monolayer TMDs, due to the inversion symmetry breaking and strong spin-valley coupling, the spin degenerate splits and the spin and valley degrees of freedom are locked, leading to the opposite values of magnetic moments at the opposite K and K' valleys.[106] This enables the pumping of spin- and valley-polarized electrons with the circularly polarized light, which could lead to the spin-polarized current by diffusion or drifting.[107] Generation of photoluminescence involves the decay of excitons and high order excitonic quasiparticles such as trions

(charged excitons) and biexcitons. It can not only be tuned by the electric field, which is mentioned above, but also it is power-dependent. For example, as shown in Figure 2.11, two PL peaks were observed in monolayer WS_2 at room temperature, which were X_A peak (from exciton) and X_A^- peak (from negative trion). As the excitation power increased from 33 μW to 9570 μW, the X_A^- had a redshift and the X_A peak had a blueshift. Meanwhile, the X_A^-/X_A peak intensity ratio increased due to the increased negative trions by photoinduced electron doping. This power-dependent PL was more obvious at cryogenic temperature, where emission from biexcitons (X_AX_A) arose due to the longer lifetime of excitons and the easier formation of biexcitons.[108] Similar behaviours have also been observed in other materials such as monolayer phosphene and WSe_2, while the power dependence may vary.[109,110]

Apart from excitation of electrons, light can also be used to tune the structures of 2D materials. For example, for the Bi_2Se_3/MoS_2 heterostructure synthesized by CVD method, pristinely the two materials were perfectly rotational aligned and the PL of MoS_2 was almost completely quenched. After exposure to a 488-nm laser with an intensity of 76 μW/μm^2, the PL was recovered and the appearance was changed, which was attributed to the disruption of perfect rotational alignment.[111] Another example is the melting of CDW by strong photoexcitation. As mentioned previously, there are three CDW phases in 1T-TaS_2, which are ICCDW, NCCDW and CCDW phases with distinguished resistivity and splitting (Δ_{CDW}) of Ta *4f* binding energy. At the cryogenic temperature of 10 K, by the photoexcitation from an ultrafast pulsed laser (1.55 eV, 700 fs FWHM, 1.8 mJ/cm^2), the 1T-TaS_2 would experience an ultrafast melting of the long-range CCDW order, featured by the immediate drop and subsequently partial recovery of Δ_{CDW} (900 fs time constant).[112] Transport measurement has confirmed that upon a series of photoexcitation of CCDW 1T-$TaS_{2-x}Se_x$ by pulsed laser, the material would go through an insulator-to-metal transition to hidden CDW states.[113] In thin NCCDW phase 1T-TaS_2 at room temperature, a single pulsed light (1.55 eV, 90 fs, 7 mJ/cm^2) could be used to inject or remove mirror domain walls in the material, which was stable and reversible.[114]

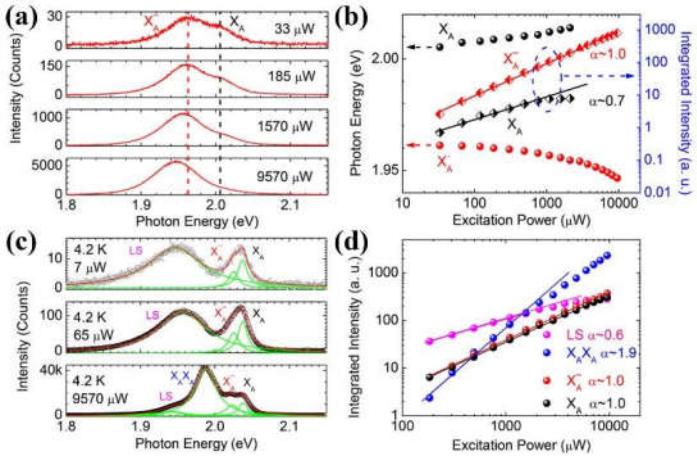

Figure 2.11 Power-dependent PL spectra of monolayer WS_2. (a) PL spectra at different excitation laser power at room temperature. The laser wavelength is 532 nm. X_A and X_A^- peaks are emissions from excitons and negative trions, respectively. (b) Peak positions and integrated intensities of the two peaks at different excitation power at room temperature. (c) PL spectra at 4.2 K. X_AX_A is the emission from biexcitons and LS is from the localized states such as defects and impurities. (d) Power-dependent PL intensity for the four peaks at 4.2 K. Reproduced with permission.[108] Copyright 2015, ACS.

Laser-ablation-induced etching and patterning of 2D materials has been studied. For example, monolayer graphene could be formed from few-layer graphene by high power laser ablation (532 nm, 0.9 NA lens, > 60 mW). Top layers of graphene were etched while the bottom monolayer preserved due to the heat transfer to the silicon substrate.[115] The laser-thinning of MoS_2 has also been reported, where the laser-thinned monolayer MoS_2 showed electronic properties comparable to those of the exfoliated monolayer MoS_2.[116] For multilayer black phosphorus, laser thinning could induce the increased bandgap and increased on/off ratio of FETs. By increasing the laser power from 20 to 180 mW, the absorption energy increased from about 2.4 to 5 eV due to the increased oxygen concentration in the BP flakes. A series of defect states were introduced during the oxidation, which could be used for multicolour display. Moreover, by the laser-ablation-induced controlled oxidation, the stability of BP in the ambient environment could be improved.[117] Cho et al. reported the phase patterning of 2H-$MoTe_2$ by laser ablation. The contact regions of the FET were ablated and thinned right before the deposition of

metal electrodes, resulting in an ohmic contact with a much lower barrier height (10 meV) compared to the pristine value (200 meV). This was attributed to the phase transition from the semiconducting 2H phase to the metallic 1T' phase.[118] However, the Raman signal of the derived material was different from other reports of 1T'-$MoTe_2$.[119,120] Seo et al. studied the direct circuit writing by selective p-type doping via the scanned laser ablation on electrodes of $MoTe_2$ transistors. And this was attributed to Mo vacancies and the subsequent absorption of oxygen clusters induced by ablation.[121]

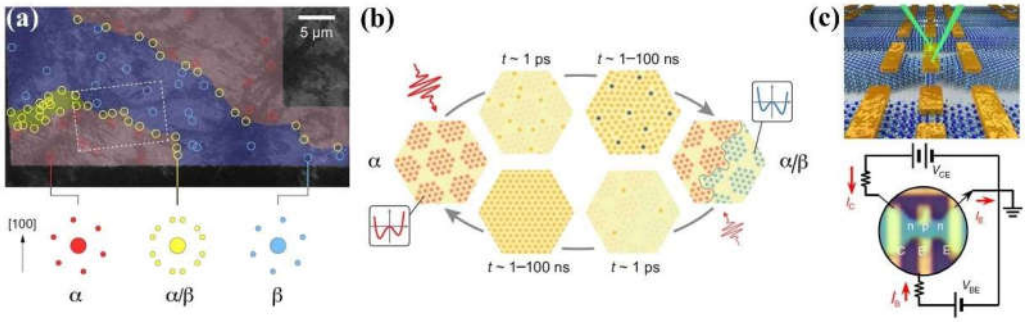

Figure 2.12 Laser writing of CDW domain walls in 1T-TaS_2 and NPN bipolar junction transistors in 2H-$MoTe_2$. (a) Bright-field transmission electron micrograph of the ultrafast laser induced CDW domain walls in 1T-TaS_2. Circles are regions of interest where selected area diffraction was performed, shown schematically at the bottom. Brown and blue areas have different CDW domain orientations. (b) Schematic diagrams showing the writing and erasing of CDW domain walls. (a) and (b) Reproduced with permission.[114] Copyright 2018, AAAS. (c) NPN bipolar junction transistor patterned by scanning laser ablation on 2H-$MoTe_2$. Two middle electrodes were ablated, and nearby regions were p-type doped. Reproduced with permission.[121] Copyright 2018, Springer Nature.

2.2 2D Electronic Devices

Due to the enriched electronic properties, 2D material based electronics devices have been demonstrated in various application fields, such as field effect transistors,[7] photo detectors,[122] solar cells,[123] gas sensors,[124] thermoelectrics,[125] spintronics,[126] and novel functional devices. This section will focus on three aspects: (1) 2D electronics for high frequency applications, (2) Logic circuits, and (3) Nonvolatile memories.

2.2.1 2D Electronics in High Frequency Applications

Due to the high intrinsic mobility and high electron saturation velocity, graphene is promising in the high frequency electronic applications.[127] For a FET, the maximum frequency f_{max} is the operating frequency where the power gain is unity (the output power equals the input power). To get a high f_{max}, the high transconductance g_m and low drain conductance g_{ds} are required.[127] Figure 2.13 shows the maximum frequency at different gate length for various materials. Generally, f_{max} decreases with increasing gate length. And the f_{max} of graphene is larger than that of phosphene and MoS_2. However, the reported f_{max} values of 2D materials are still much lower than those of traditional devices such as silicon MOSFET, GaAs HEMT and InP HEMT.[127] Instead of the high frequency responses of transistors, this section will mainly focus on the generation of high frequency signals using 2D electronic devices. Two types of oscillators will be discussed, which are relaxation oscillators based on phase transitions and ring oscillators based on logic circuits.

Relaxation oscillators are oscillators which utilize the charging and discharging of a capacitor. The capacitor is connected to an external circuit which controls the charging and discharging threshold voltages. With the alternating charging and discharging of the capacitor, an oscillated output voltage can be obtained.[128] Figure 2.14a shows the simplest RC CMOS relaxation oscillator which consists of a resistor, a capacitor, and an inverting Schmitt trigger (shown in Figure 2.14b). The oscillation is stabilized by the charging and discharging of the capacitor with the feedback from the inverting Schmitt trigger. The Schmitt trigger output behavior is shown in the right panel of Figure 2.14b, featured by a hysteresis loop with sharp changes of the output voltage. As mentioned in the previous section, the source-drain bias can induce the CDW phase transition of 1T-TaS_2, whose *I-V* characteristics shows a similar behavior. As shown in the left panel of Figure 2.14c, a reversible abrupt transition in the current can be induced by the voltage with a hysteresis. Based on this effect, Liu et al. reported a relaxation oscillator based on the CDW phase transition of 1T-TaS_2.[129] As shown in the right panel of Figure 2.14c, 1T-TaS_2 replaced the Schmitt trigger and the oscillation was controlled by the continuous transitions between two CDW phases rather than the feedback from the Schmitt trigger. The oscillator

operated at the level of 1 MHz and the frequency could be tuned by varying the connected resistor.[130] Compared with the traditional relaxation oscillators, this phase transition based oscillator had a much simpler structure and more compact. Similarly, based on voltage induced insulator-metal phase transition of the Mott insulator NbO_2, Pickett et al. demonstrated a neuristor device, by which biomimetic periodic spikes with adjustable frequencies were generated.[131]

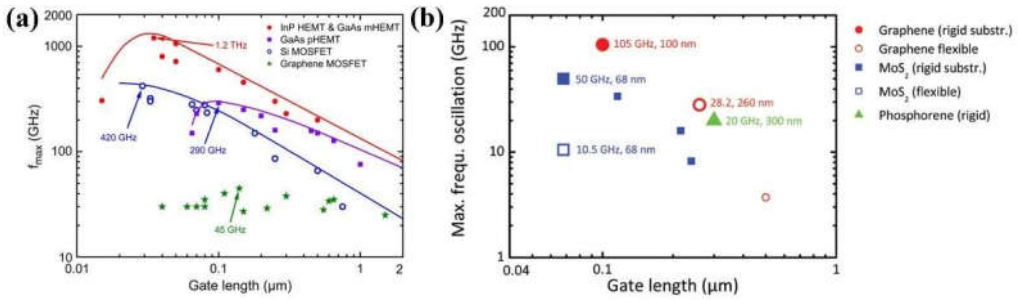

Figure 2.13 Maximum frequency versus gate length for different transistors. (a) Comparison between graphene MOSFET and traditional transistors. Reproduced with permission.[127] Copyright 2013, IEEE. (b) Comparison between graphene, phosphene, and MoS_2. Reproduced with permission.[132] Copyright 2015, The Royal Society of Chemistry.

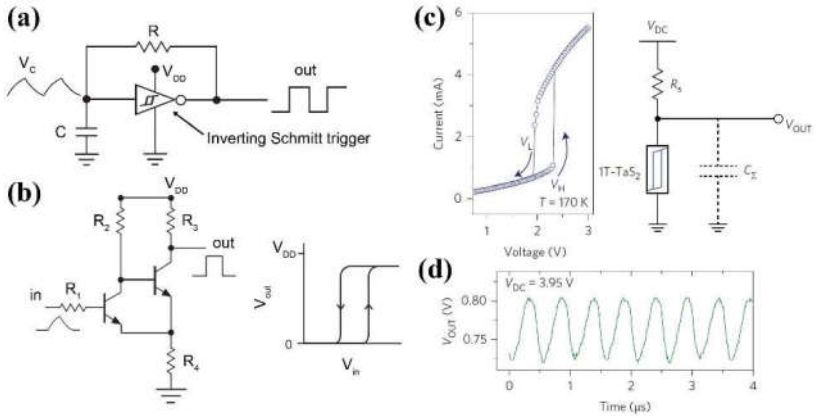

Figure 2.14 Relaxation oscillators based on RC circuits. (a) A simplest RC CMOS oscillator formed by an inverting Schmitt trigger, a resistor, and a capacitor. (b) Left: A Schmitt trigger circuit. Right: Schmitt trigger output curve, featured by abrupt transitions of output voltage. (c) Left: CDW phase transition of 1T-TaS_2 under the bias voltage, featured by abrupt transitions of the current. Right: A TaS_2 based relaxation oscillator. (d) Output oscillation of the device shown in (c) at a frequency of about 2 MHz. (c, d) Reproduced with permission.[130] Copyright 2016, Springer Nature.

Ring oscillators consist of odd number of inverters connected in a ring. As shown in Figure 2.15a, the ring oscillator was formed by the left three inverters (NOT gates, 1-3), whose gain was larger than 1. The oscillation originated from the gate delay, which was inevitable for logic gates. When an initial voltage change was applied to the input of the first inverter, it took a certain amount of time before the output responses. Since the gain was greater than 1, the output voltage would have a larger change than the input value with an opposite direction, which then acted as the input of the second inverter. The output signal of the third inverter would have an opposite change larger than the initial input with a delay, which would then propagate back to the input of the first inverter. In this way, the signal was amplified and inverted continuously until it reached a limit. And a stabilized oscillation would arise at the output of the third inverter, whose frequency was double of the whole delay time of the three inverters.[133] The fourth inverter in Figure 2.15a was used as a buffer to minimize the influence of the output load on the ring oscillator. The output oscillation frequency increased with decreasing gate length L, which was 1.22 GHz when L = 1 μm, V_{DD} = 3.5 V and V_{BG} = 50 V. The frequency could also be tuned by the V_{DD} but the variation was small (5.6%/V).[134] Similar device has been demonstrated on bilayer MoS_2, with a maximum frequency of 1.6 MHz and the V_{DD} tunability of 240%/V.[135]

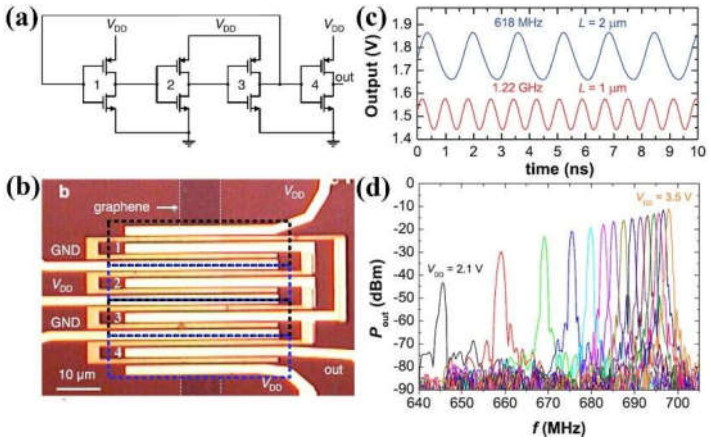

Figure 2.15 A ring oscillator based on graphene inverters. (a) Schematic circuit of the 3-stage ring oscillator with an output buffer. (b) Optical Image of the ring oscillator device. (c) Output signals of the ring oscillator for different gate lengths. (d) Oscillation tuned by the V_{DD}. Reproduced with permission.[134] Copyright 2013, ACS.

2.2.2 Logic Circuits Based on 2D Materials

Field effect transistors form the basis of logic circuits. Two important figures of merit of FETs are the field-effect mobility and the intrinsic gain, which are essential for the performances of the built logic circuits, such as the switching speed and the power consumption. The field-effect mobility can be influenced by factors including the effective mass and various scattering sources of the semiconductor, dielectrics, and the contact barrier height at the source and drain. Figure 2.16a shows the electron mobility of selected typical 2D materials and traditional 3D materials, where graphene shows the highest mobility due to its smallest electron effective mass.[136] Theoretical calculations have shown that the electron mobility of 2D materials is mainly dominated by the charge impurity scattering as well as the dielectric environment (Figure 2.16b). Increased charged impurity density will decrease the mobility while the mobility will increase with increasing electron density. For very low impurity density, surface-optical phonon scattering will dominant the scattering which will be influenced by the surrounding dielectrics, where low-κ dielectrics are preferred. For high impurity density, high-κ dielectrics offer a higher mobility.[137] Besides, compared with the Schottky contacts, ohmic contacts provide a higher field-effect mobility, which can be achieved by introducing metallic 1T phase or degenerate doping at contact regions.[138,139] On the other hand, the intrinsic gain is defined by the equation $A_i = g_m/g_{ds}$, where the transconductance g_m and drain conductance g_{ds} are defined as $g_m = dI_D/dV_{GS}$ and $g_{ds} = dI_D/dV_{DS}$, respectively.[140] A good drain current saturation is required to get a high intrinsic gain.

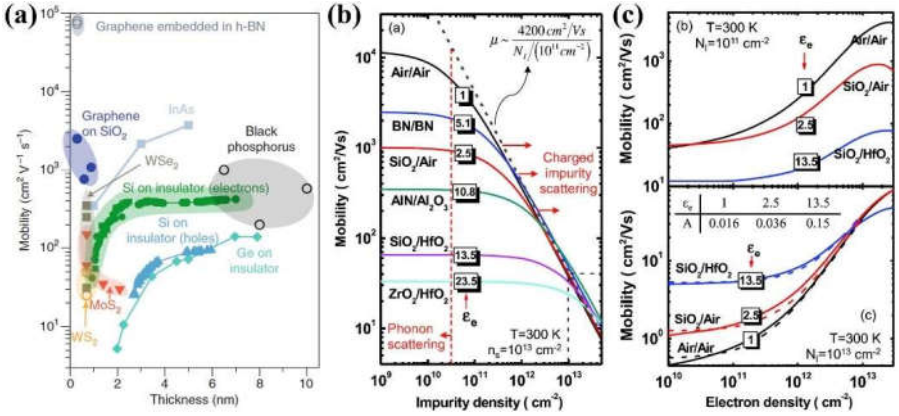

Figure 2.16 Electron mobility of 2D materials. (a) Electron mobility versus thickness for

selected 2D materials and 3D semiconductors. Reproduced with permission.[136] Copyright 2018, Springer Nature. (b) Electron mobility versus charged impurity density N_I for monolayer MoS_2 surrounded by different dielectrics. (c) Electron mobility versus electron density n_s for monolayer MoS_2 surrounded by different dielectrics. (b, c) Reproduced with permission.[137] Copyright 2014, American Physical Society.

Various logic devices have been demonstrated based on 2D materials, such as inverters, NOR gates, and NAND gates.[140-152] An inverter (NOT gate) is a logic circuit whose output level is logically opposite to the input. Figure 2.17 shows two types of inverters. One is the CMOS inverter which is composed of a pMOS and an nMOS (Figure 2.17a). When the input level is low, the pMOS is on and the nMOS is off, leading to the high level of output voltage ($V_{OUT} = V_{DD}$). While when the input level is high, the pMOS is off and the nMOS is on, leading to the low level of the output ($V_{OUT} = 0$). The noise margins (NM_L and NM_H) are ranges of input within which the output level is not altered. The switching voltage is the voltage where $V_{IN} = V_{OUT}$, which can be described by $V_M \approx rV_{DD}/(1 + r)$ with $r = \upsilon_{satp}W_p/(\upsilon_{satn}W_n)$. The $\upsilon_{satn,p}$ is the saturation velocity and $W_{n,p}$ is the channel width. By adjusting the width ratio W_p/W_n, V_M can be tuned, leading to the change in the symmetry of voltage transfer characteristics (VTC). Increasing the pMOS channel width moves the transition region towards V_{DD} while increasing the nMOS channel width moves the transition region towards GND. For an inverter, a high gain is desired, which can be descried using a small signal model by the equation:

$$A_v = (g_{mn} + g_{mp})(r_{on}||r_{op}) \quad (2.1)$$

where $g_{mn,p}$ is the transconductance, and $r_{on,p} = 1/g_{dsn,p}$ is output resistance.[144] Large output resistances, which means good drain current saturations, are required for a high gain inverter (Figure 2.17c). Meanwhile, the threshold voltages of the nMOS and pMOS should be well matched to form a narrow switching region. For inverters operating in the saturation region, decreasing V_{DD} leads to increasing gain. However, the lower V_{DD} leads to lower current at the switching region, which means a lower operation speed.[153] Another type of inverter is the depletion-load NMOS inverter shown in Figure 2.17d, which consists of a nonlinear depletion MOSFET as the load and a MOSFET as the driver.[147] The driver FET is connected to the GND and driven by the input voltage. The load FET is

connected to the V_{DD}. And the output is wired to the gate of the load FET as well. The load FET is wider and shorter in channel in order to have a lower threshold voltage than the driver FET.

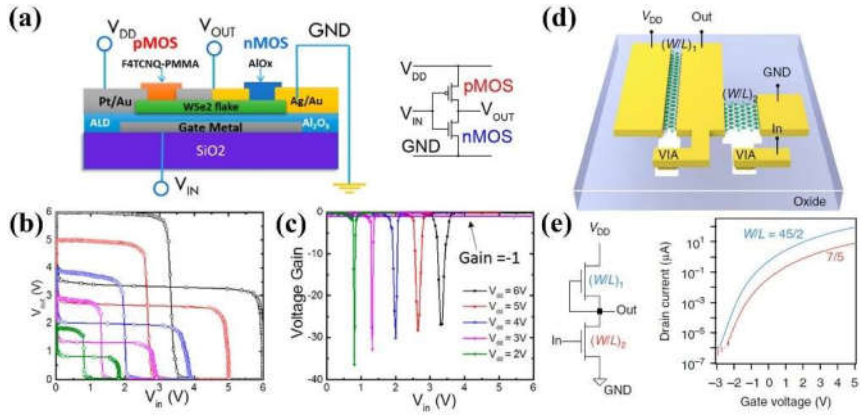

Figure 2.17 Two types of inverters. (a) Left: Schematic diagram of a CMOS inverter. Right: Schematic circuit diagram. (b) Voltage transfer characteristics and butterfly curves of (a) under different V_{DD}. (c) Corresponding gain under different V_{DD}. (a-c) Reproduced with permission.[144] Copyright 2015, ACS. (d) 3D schematic diagram of a depletion-load NMOS inverter. (e) Left: Schematic circuit diagram of (d). Right: Transfer curves of the two channels with different *W/L* ratios. (d, e) Reproduced with permission.[147] Copyright 2017, Springer Nature.

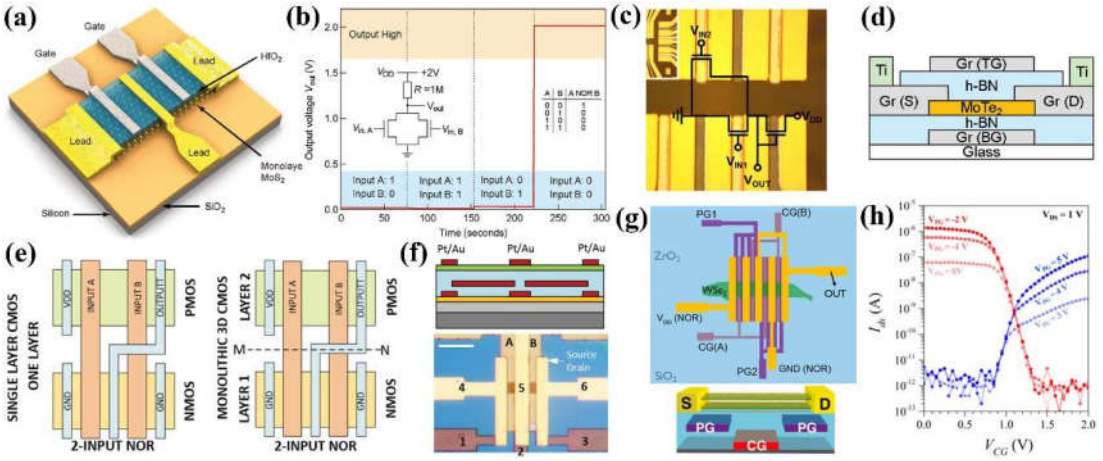

Figure 2.18 2D material based NOR gate circuits. (a) 3D schematic diagrams of a pair of nMOS transistors based on monolayer MoS_2. (b) A NOR gate circuit where two parallel MoS_2 nMOS transistors are connected to a 1 MΩ load resistor. The output voltage under different input combinations shows the logic operation of the NOR gate. (a, b) Reproduced with permission.[148] Copyright 2011, ACS. (c) A similar NOR gate circuit where the load is MoS_2 FET in depletion mode. Reproduced with permission.[150] Copyright 2016, IOP Publishing Ltd. (d) Schematic

diagram of a $MoTe_2$ transistor with two control gates used for the NOR gate circuit. Reproduced with permission.[149] Copyright 2016, WILEY-VCH Verlag GmbH & Co. KGaA, Weinheim. (e) Schematic layout of planar and monolithic 3D CMOS NOR gate circuits. (f) Schematic diagram of the cross-section view and the optical image of a monolithic 3D CMOS NOR gate circuit. (e, f) Reproduced with permission.[151] Copyright 2016, WILEY-VCH Verlag GmbH & Co. KGaA, Weinheim. (g) Schematic diagrams of a doping-free WSe_2 CMOS inverter by transistor polarity control. Each transistor consists of two polarity gates near the electrodes and one control gate at the channel center. (h) Polarity control of the WSe_2 transistor by the polarity gates. Reproduced with permission.[152] Copyright 2018, ACS.

The NOR and NAND gate are the only two kinds of gate from which all other logic gates can be built. Different structures have been studied to build these two gates. Figure 2.18 shows several reported 2D material based NOR gate circuits with different configurations. A simple way to build an NOR gate is to connect two parallel nMOS transistors to a suitable resistor (Figure 2.18a). Logic operations of the NOR gate are shown in Figure 2.18b.[148] When both inputs were at low level, both nMOS transistors were high resistive and the output voltage was high. In other cases where at least one input was high, the overall resistance of the parallel nMOS transistors was low and the output was low. A variation is shown in Figure 2.18c where the load resistor is replaced by a depletion-mode nMOS transistor.[150] Choi et al. reported an NOR gate circuit based on the $MoTe_2$ dual-gate transistor, which replaced the two parallel nMOS transistors in Figure 2.18a.[149] Planar CMOS NOR gate has a layout similar to the one shown in Figure 2.18e. A positive V_{DD} is applied to an electrode on one side of a pMOS, which is then connected to another pMOS, followed by two parallel nMOS channels. The end side of the two nMOS transistors are connected to the ground. When both inputs are at low level, the series pMOS channel is low resistive and the parallel nMOS channel is high resistive, leading to the high-level output. In other cases, the series pMOS channel is turned off while the parallel nMOS channel is on, leading to the low-level output. Sachid et al. reported the monolithic 3D CMOS NOR gate where the n-channel material was MoS_2 and the p-channel material was WSe_2 (Figure 2.18e,f).[151] Compared with the planar CMOS NOR gate, the 3D monolithic CMOS NOR gate required less areas but more fabrication steps. Resta et al. reported a doping-free CMOS NOR gate by controlling the transistor polarity.[152] There

were three gates for each channel of the CMOS NOR gate, among which two were polarity gates (V_{PG}) located beneath the source and drain electrode contacts and one was the control gate (V_{CG}) located at the channel center (Figure 2.18g). The channel material was WSe_2, which was pristinely ambipolar. As shown in Figure 2.18h, the channel was p-type (n-type) under the negative (positive) V_{PG}. This NOR gate only used one kind of channel material and the p-type channels were induced by the polarity gates rather than doping. The main advantage was that the polarity of the channels was tunable and different logic circuits could be achieved using the same device.[152] The disadvantage was the complexity of the device fabrication.

2.2.3 Nonvolatile Memory Devices Based on 2D Materials

The key difference between volatile and nonvolatile memory is whether the power is required to retain the data. For volatile memory, data will be lost after the power is off. While for nonvolatile memory (NVM), data will be preserved. For 2D material based nonvolatile memory, various strategies have been explored, such as floating gate, charge trapping dielectric, ferroelectric layer, memristor, etc. Figure 2.19 shows the structures and operations of typical floating gate NVM devices.[154,155] As shown in Figure 2.19a, apart from the conductive channel (MoS_2) and the back gate (p++ Si), there are floating gate (few-layer graphene) and control gate. The floating gate is used to store charges, which is controlled by the control gate. Under a positive control gate $V_{cg} \gg 0$, electrons in MoS_2 will tunnel through the dielectric HfO_2 into the graphene floating gate. After remove the control gate ($V_{cg} = 0$), electrons will be trapped in the floating gate due to the large barrier. These extra electrons then act as a negative gate which will turn off the MoS_2 channel. While applying a negative control gate ($V_{cg} \ll 0$), electrons will tunnel out of the floating gate into the MoS_2, leaving holes in the floating gate. And the holes will act as a positive gate, which will then turn on the MoS_2 channel. As shown in Figure 2.19c, by applying a series of positive and negative pulsed control gate, the MoS_2 channel can be tuned to the low conductive (program, P) and high conductive (erase, E) states, respectively. Due to the large tunnel barrier of the HfO_2, charges trapped in the floating gate can retain for a long time without the external power supply, leading to the nonvolatile memory. However, due

to the finite barrier height and existence of defects, processes such as charge redistribution in defects and charge loss by back tunneling will happen, leading to the finite charge retention time (Figure 2.19d). The bandgap of HfO_2 is high (up to 5.9 eV, depending on the growth substrate).[156] However, there are defects inevitably locating in the bandgap of HfO_2, lowering the retention time of the nonvolatile memory device.[157] On the other hand, hexagonal boron nitride (hBN) has a similar bandgap as HfO_2 and has few defects. Based on this, Choi et al. used hBN as the tunneling barrier layer (Figure 2.19e) and achieved a much stable data storage and longer retention time (Figure 2.19f).[155] A WSe_2-hBN-Graphene based semi-floating gate device has been reported, where only half of the channel was controlled by the floating gate. Based on this device, the nonvolatile P-N junction memory could be achieved, with a much higher on/off ratio and the nonvolatile photovoltaic behavior.[158]

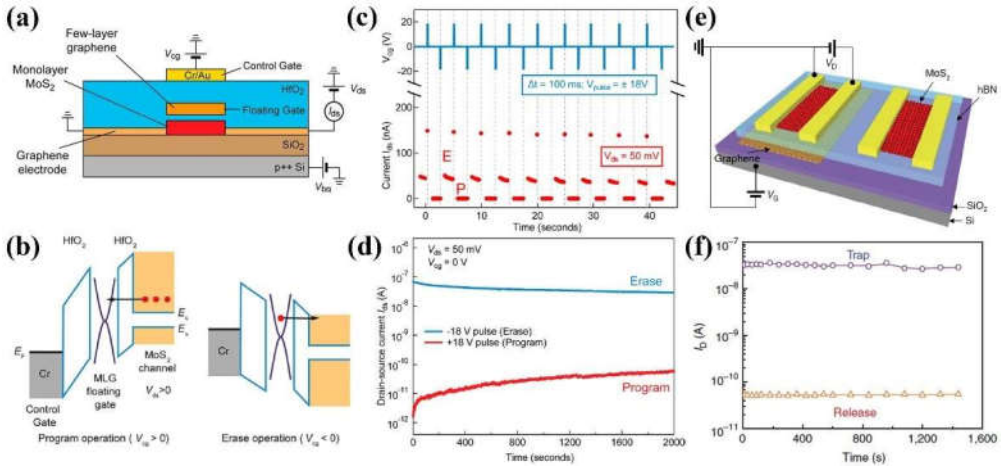

Figure 2.19 Floating gate nonvolatile memory based on 2D materials. (a) Schematic diagram of floating gate nonvolatile memory device based on graphene, MoS_2, and HfO_2. (b) Schematic band alignment showing the operation mechanism of the nonvolatile memory device. (c) Repeatable program (P) and erase (E) operations. (d) Time stability of the erase and program states. (a-d) Reproduced with permission.[154] Copyright 2013, ACS. (e) Schematic diagram of the nonvolatile memory device based on MoS_2, graphene, and hBN. (f) Time stability of the device shown in (e). (e, f) Reproduced with permission.[155] Copyright 2013, Macmillan Publishers Limited.

Unlike the floating gate NVM where a conductive charge trapping layer (usually graphene) is used, defects in the insulating dielectrics can also be used to trap charges. For example,

Al_2O_3 can be used to trap charges in its native defects, which however has problems in charge retention due to reasons as mentioned previously.[159] Lee et al. reported the $Al_2O_3/AlO_x/Al_2O_3$/graphene NVM device, where the oxygen ion bombardment induced defects in AlO_x acted as charge traps and the Al_2O_3 was used to reduce the back tunneling of trapped charges.[160] Xiang et al. used hBN as the charge trapping material with a WSe_2/hBN/SiO_2/Gate configuration, where the programming and erasing were done under both gate control and 3 eV light excitation. In this way, electrons in the mid-gap defect states could be photoexcited into the conduction band and then transferred into WSe_2 under the negative control gate, leaving positive holes in the middle of hBN bandgap. The erasing process used a positive control gate as well as the light excitation. Electrons in the valence band of hBN would be excited into the mid-band states and neutralize the previous positive charges. And the holes in the valence band of hBN would then transfer into the WSe_2 under the positive control gate. Due to the large barrier height of mid-gap states, this NVM device showed much stable storage (half of the programmed current would be retained after 10 years).[161] Ferroelectric materials have also been used to achieve the 2D material based nonvolatile memory, such as P(VDF-TrFE), PZT, and PMN-PT.[162-164] For example, Ko et al. reported the NVM based on WSe_2 exfoliated on the PZT/SRO/STO substrate. By applying a large enough positive or negative gate voltage, the polarization of the ferroelectric PZT could be tuned upward or downward (Figure 2.20b), which would then act like a gate to tune the off/on state of the 2D channel. The retention time would be influenced by the storage environment, where the nitrogen environment was better than the ambient environment.[163]

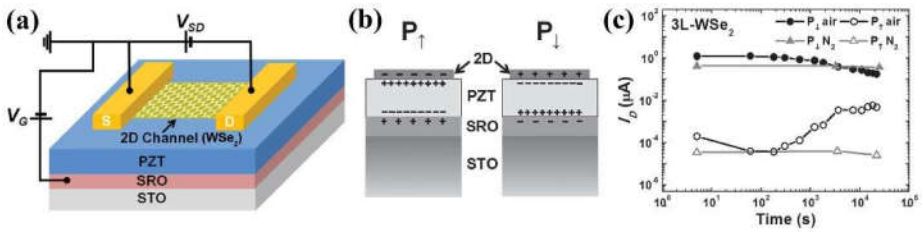

Figure 2.20 2D nonvolatile memory device based on a ferroelectric substrate. (a) Schematic diagram of the ferroelectric NVM device. (b) Diagrams of the gating effect when the PZT is up-polarized or down-polarized. (c) Retention performance of the NVM device under different storage environment. Reproduced with permission.[163] Copyright 2016, WILEY-VCH Verlag GmbH & Co. KGaA, Weinheim.

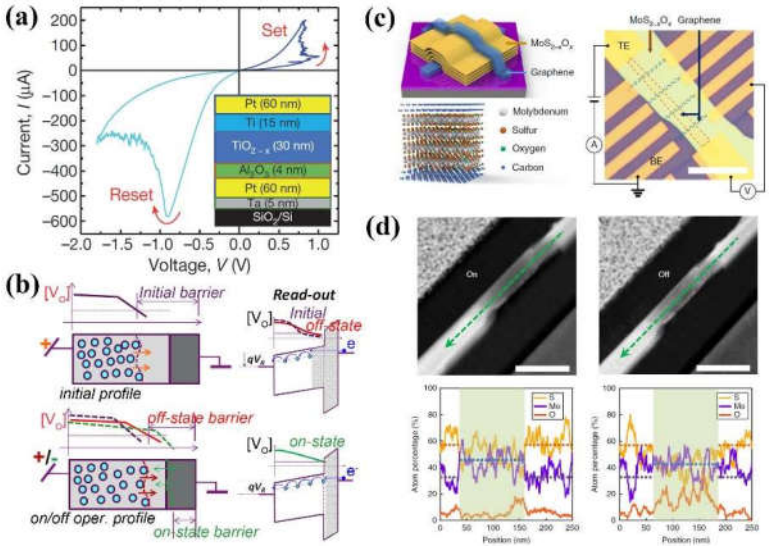

Figure 2.21 Typical memristors and operation mechanisms. (a) *I-V* characteristics of a metal-oxide memristor based on TiO_{2-x}/Al_2O_3. Inset: Structure of the memristor. Reproduced with permission.[165] Copyright 2015, Macmillan Publishers Limited. (b) Diagram showing the mechanism of the memristor in (a). Left: Oxygen vacancy defect distribution. Right: Schematic band diagram. For the off state, part of the TiO_{2-x} is depleted, which increases the resistance. Reproduced with permission.[166] Copyright 2013, IEEE. (c) Graphene/$MoS_{2-x}O_x$/Graphene based memristor. (d) Top: Cross-section High-angle ADF image of the memristor at on and off states. Bottom: Atomic percentage of Mo, S, and O across the conductive channel. Reproduced with permission.[167] Copyright 2018, Springer Nature.

The above mentioned NVM devices are all controlled by the gate voltage. On the other hand, there is a category of NVM called memristor, which is controlled by the source-drain bias and whose resistivity is determined by the bias history. A traditional metal-oxide memristor is shown in Figure 2.21a, which exhibits two states with distinguished resistance. To form a memristor, first a forward current was applied to the top electrode, making the positive charged oxygen vacancies in TiO_{2-x} move towards the Al_2O_3. When the current increased to about 50 μA, oxygen vacancies spread through the whole TiO_{2-x}, leading to the low resistance and onset of the memristor, featured by an abrupt increase in current with little change in voltage. The set current reached the maximum of 200 μA, which set the memristor to the on state. The reset process was achieved by applying a backward voltage. When the reset voltage reached about -0.8 V, the oxygen vacancies moved far away from the interface of TiO_{2-x} and Al_2O_3, leading to the decrease in the current. The

reset voltage reached a maximum value of -1.75 V, resetting the memristor back to the off state. After the memristor was formed, a pulsed voltage ($+1.3$ V or -1.3 V) could be used to set or reset the memristor.[165,166] Wang et al. reported a Graphene/$MoS_{2-x}O_x$/Graphene based memristor, whose on and off states were controlled by the migration of oxygen ions. The device showed a high temperature stability (up to 340℃).[167] Besides, there are reports of memristors based on QDs of 2D materials.[168,169] Different from typical memristors which utilize the formation of conductive filaments or migration of charged ions, memristors based on the phase transition of Mott insulators have been demonstrated.[170,171] As mentioned in the previous section, a source-drain bias can induce the CDW phase transition of 1T-TaS_2. For thick 1T-TaS_2 at low temperature, a short pulsed current (< 200 ms) could induce the phase transition from high resistive Mott insulator phase to a low resistive metallic hidden CDW phase. This hidden state was stable at low temperature (< 40 K) and could be reversed by a long pulsed current (> 200 ms).[171]

2.3 Research Gaps

To push 2D electronics into practical applications, exploring the ways to tune electronic properties of 2D materials is fundamentally necessary. As discussed in the previous sections, there are various methods to tune the electronic properties of 2D materials, such as electric field, strain and light. Among these methods, the electric field control is the most extensively studied, where in most cases a gate electrode is used to apply a vertical electric field. Solid dielectrics such as HfO_2 and hBN are often used. However, the ionic liquid is more frequently used in cases where a strong control of the electron density is required, which makes it not suitable for large-scale applications. On the other hand, strain control requires pre-patterned substrates or the flexible substrates, where the former is limited in applications while the latter is not compatible with traditional silicon-based semiconductors. Compared with the electric field control and strain control, light control provides a more direct way to tune the properties of 2D electronics, without patterning of the gate electrode or the substrate. Moreover, due to the parallel nature and the high bandwidth, light shows great potentials in the high-speed communications and computing, such as hybrid opto-electronic integrated circuits. However, the studies on the light-tunable

2D electronic devices are insufficient at the moment.

In order to provide more options and possibilities for the practical electronic applications of 2D materials, further studies are required to explore the role of light in tuning electronic properties of 2D materials and the integration of light into 2D electronics. Specifically, the research gaps and questions are as follows:

1. For the metallic CDW materials such as 1T-TaS_2, previous studies focused on the ultrafast laser excitation at the cryogenic temperature. The light tuned CDW phase transition at room temperature is insufficiently studied. On the other hand, for the bias-induced phase transition in TaS_2, evidence from in-situ characterizations is lacking and the role of Joule heating effect is unclear.
2. For the building of 2D logic circuits, current strategies include using two kinds of materials (one is n-type and the other is p-type), polarity control of a single material using additional gates, and selective carrier doping of a single material. For these strategies, the device fabrication procedures are complex, which requires multiple channel materials, multiple steps to deposit dielectrics and pattern additional gates, and additional steps to pattern and remove passive layers. It is necessary to find more simple ways of selective carrier doping and circuit patterning for the large-scale applications of 2D electronics. On the other hand, for the strong laser ablation, previous studies mainly focused on the thinning effect of 2D materials. The laser-ablation induced tune of other electronic properties such as carrier density is less studied.
3. For the nonvolatile memory, current studies are mainly focused on the charge trapping and releasing controlled by the electric field. Light-based nonvolatile memories are also an important for future optoelectronics.

2.4 Scope of PhD Thesis

Regarding the problems mentioned above, the light control of 2D electronics was studied in materials with different bandgaps, including the metallic 1T-TaS_2, the semiconductor 2H-WSe_2, and the semiconductor/insulator heterostructure of narrow-gap black

phosphorus and wide-gap strontium titanate ($SrTiO_3$). For example, *Chapter 4* demonstrates the light control of the CDW phase transition in 1T-TaS_2 at room temperature, showing that the light could be used to tune the CDW phase transition between NCCDW and ICCDW phases. And a light-tunable oscillator based on the CDW phase transition was demonstrated, showing potentials in the high frequency applications. *Chapter 5* shows the tune of carrier type in the semiconducting 2H-WSe_2 using light. By light ablation, controlled p-type doping was achieved in the atomically thin 2H-WSe_2 films, based on which the direct writing of logic circuits was demonstrated without the patterning of additional gate electrodes or passive layers. Chapter 6 demonstrates the wavelength dependent persistent tuning of the conductivity of BP flakes in the BP/$SrTiO_3$ heterostructure, where the visible light could be used to tune the BP to the conductive state while the ultraviolet light could tune the BP to the non-conductive state. The relatively long retention time made it possible for the nonvolatile memory applications.

References

[1] P. S. Peercy. *Nature* **2000**, 406, 1023-1026.

[2] H. Proc Natl Acad Sci U S AWong, and H. Iwai. *Physics World* **2005**, 18, 40-44.

[3] G. Fiori, F. Bonaccorso, G. Iannaccone, T. Palacios, D. Neumaier, A. Seabaugh, S. K. Banerjee, and L. Colombo. *Nat. Nanotechnol.* **2014**, 9, 768-779.

[4] M. Y. Li, S. K. Su, H. P. Wong, and L. J. Li. *Nature* **2019**, 567, 169-170.

[5] V. K. Sangwan, and M. C. Hersam. *Annu. Rev. Phys. Chem.* **2018**, 69, 299-325.

[6] K. S. Novoselov, A. K. Geim, S. V. Morozov, D. Jiang, Y. Zhang, S. V. Dubonos, I. V. Grigorieva, and A. A. Firsov. *Science* **2004**, 306, 666-669.

[7] L. Li, Y. Yu, G. J. Ye, Q. Ge, X. Ou, H. Wu, D. Feng, X. H. Chen, and Y. Zhang. *Nat. Nanotechnol.* **2014**, 9, 372-377.

[8] K. Watanabe, T. Taniguchi, and H. Kanda. *Nat. Mater.* **2004**, 3, 404-409.

[9] S. R. Tamalampudi, Y. Y. Lu, U. R. Kumar, R. Sankar, C. D. Liao, B. K. Moorthy, C. H. Cheng, F. C. Chou, and Y. T. Chen. *Nano Lett.* **2014**, 14, 2800-2806.

[10] D. J. Late, B. Liu, J. Luo, A. Yan, H. S. Matte, M. Grayson, C. N. Rao, and V. P. Dravid. *Adv. Mater.* **2012**, 24, 3549-3554.

[11] Q. H. Wang, K. Kalantar-Zadeh, A. Kis, J. N. Coleman, and M. S. Strano. *Nat. Nanotechnol.* **2012**, 7, 699-712.

[12] J. Wu, H. Yuan, M. Meng, C. Chen, Y. Sun, Z. Chen, W. Dang, C. Tan, Y. Liu, J. Yin, Y. Zhou, S. Huang, H. Q. Xu, Y. Cui, H. Y. Hwang, Z. Liu, Y. Chen, B. Yan, and H. Peng. *Nat. Nanotechnol.* **2017**, 12, 530-534.

[13] Z. Ling, C. E. Ren, M. Q. Zhao, J. Yang, J. M. Giammarco, J. Qiu, M. W. Barsoum, and Y. Gogotsi. *Proc. Natl. Acad. Sci. U.S.A.* **2014**, 111, 16676-16681.

[14] B. Anasori, M. R. Lukatskaya, and Y. Gogotsi. *Nat. Rev. Mater.* **2017**, 2, 16098.

[15] M. Acerce, D. Voiry, and M. Chhowalla. *Nat. Nanotechnol.* **2015**, 10, 313-318.

[16] T. Yokoya, T. Kiss, A. Chainani, S. Shin, M. Nohara, and H. Takagi. *Science* **2001**, 294, 2518-2520.

[17] X. Xi, Z. Wang, W. Zhao, J.-H. Park, K. T. Law, H. Berger, L. Forró, J. Shan, and K. F. Mak. *Nat. Phys.* **2015**, 12, 139-143.

[18] Z. Yin, H. Li, H. Li, L. Jiang, Y. Shi, Y. Sun, G. Lu, Q. Zhang, X. Chen, and H. Zhang. *ACS Nano* **2012**, 6, 74-80.

[19] W. Zhao, Z. Ghorannevis, L. Chu, M. Toh, C. Kloc, P. H. Tan, and G. Eda. *ACS Nano* **2013**, 7, 791-797.

[20] H. S. Matte, A. Gomathi, A. K. Manna, D. J. Late, R. Datta, S. K. Pati, and C. N. Rao. *Angew. Chem. Int. Ed. Engl.* **2010**, 49, 4059-4062.

[21] Y. C. Jiang, J. Gao, and L. Wang. *Sci. Rep.* **2016**, 6, 19624.

[22] J. Jiang, Z. K. Liu, Y. Sun, H. F. Yang, C. R. Rajamathi, Y. P. Qi, L. X. Yang, C. Chen, H. Peng, C. C. Hwang, S. Z. Sun, S. K. Mo, I. Vobornik, J. Fujii, S. S. Parkin, C. Felser, B. H. Yan, and Y. L. Chen. *Nat. Commun.* **2017**, 8, 13973.

[23] Y. Qi, P. G. Naumov, M. N. Ali, C. R. Rajamathi, W. Schnelle, O. Barkalov, M. Hanfland, S. C. Wu, C. Shekhar, Y. Sun, V. Suss, M. Schmidt, U. Schwarz, E. Pippel, P. Werner, R. Hillebrand, T. Forster, E. Kampert, S. Parkin, R. J. Cava, C. Felser, B. Yan, and S. A. Medvedev. *Nat. Commun.* **2016**, 7, 11038.

[24] B. Sipos, A. F. Kusmartseva, A. Akrap, H. Berger, L. Forro, and E. Tutis. *Nat. Mater.* **2008**, 7, 960-965.

[25] W. Z. Hu, G. Li, J. Yan, H. H. Wen, G. Wu, X. H. Chen, and N. L. Wang. *Phys. Rev. B* **2007**, 76, 045103.

[26] L. J. Li, E. C. O'Farrell, K. P. Loh, G. Eda, B. Ozyilmaz, and A. H. Castro Neto. *Nature* **2016**, 529, 185-189.

[27] B. Huang, G. Clark, E. Navarro-Moratalla, D. R. Klein, R. Cheng, K. L. Seyler, D. Zhong, E. Schmidgall, M. A. McGuire, D. H. Cobden, W. Yao, D. Xiao, P. Jarillo-Herrero, and X. Xu. *Nature* **2017**, 546, 270-273.

[28] C. Gong, L. Li, Z. Li, H. Ji, A. Stern, Y. Xia, T. Cao, W. Bao, C. Wang, Y. Wang, Z. Q. Qiu, R. J. Cava, S. G. Louie, J. Xia, and X. Zhang. *Nature* **2017**, 546, 265-269.

[29] D. Ghazaryan, M. T. Greenaway, Z. Wang, V. H. Guarochico-Moreira, I. J. Vera-Marun, J. Yin, Y. Liao, S. V. Morozov, O. Kristanovski, A. I. Lichtenstein, M. I. Katsnelson, F. Withers, A. Mishchenko, L. Eaves, A. K. Geim, K. S. Novoselov, and A. Misra. *Nat. Electron.* **2018**, 1, 344-349.

[30] B. Huang, G. Clark, D. R. Klein, D. MacNeill, E. Navarro-Moratalla, K. L. Seyler, N. Wilson, M. A. McGuire, D. H. Cobden, D. Xiao, W. Yao, P. Jarillo-Herrero, and X. Xu. *Nat. Nanotechnol.* **2018**, 13, 544-548.

[31] K. S. Novoselov, A. Mishchenko, A. Carvalho, and A. H. Castro Neto. *Science* **2016**, 353, aac9439.

[32] X. Qian, J. Liu, L. Fu, and J. Li. *Science* **2014**, 346, 1344-1347.

[33] E. McCann. *Phys. Rev. B* **2006**, 74, 161403.

[34] J. B. Oostinga, H. B. Heersche, X. Liu, A. F. Morpurgo, and L. M. Vandersypen. *Nat. Mater.* **2008**, 7, 151-157.

[35] Y. Zhang, T. T. Tang, C. Girit, Z. Hao, M. C. Martin, A. Zettl, M. F. Crommie, Y. R. Shen, and F. Wang. *Nature* **2009**, 459, 820-823.

[36] T. Chu, H. Ilatikhameneh, G. Klimeck, R. Rahman, and Z. Chen. *Nano Lett.* **2015**, 15, 8000-8007.

[37] J. Qi, X. Li, X. Qian, and J. Feng. *Appl. Phys. Lett.* **2013**, 102, 173112.

[38] Q. Yue, S. Chang, J. Kang, X. Zhang, Z. Shao, S. Qin, and J. Li. *J. Phys. Condens. Matter* **2012**, 24, 335501.

[39] K. Dolui, C. D. Pemmaraju, and S. Sanvito. *ACS Nano* **2012**, 6, 4823-4834.

[40] J. T. Ye, Y. J. Zhang, R. Akashi, M. S. Bahramy, R. Arita, and Y. Iwasa. *Science* **2012**, 338, 1193-1196.

[41] J. Lu, O. Zheliuk, Q. Chen, I. Leermakers, N. E. Hussey, U. Zeitler, and J. Ye. *Proc. Natl. Acad. Sci. U.S.A.* **2018**, 115, 3551-3556.

[42] J. Zeng, E. Liu, Y. Fu, Z. Chen, C. Pan, C. Wang, M. Wang, Y. Wang, K. Xu, S. Cai, X. Yan, Y. Wang, X. Liu, P. Wang, S. J. Liang, Y. Cui, H. Y. Hwang, H. Yuan, and F. Miao. *Nano Lett.* **2018**, 18, 1410-1415.

[43] Y. Yu, F. Yang, X. F. Lu, Y. J. Yan, Y. H. Cho, L. Ma, X. Niu, S. Kim, Y. W. Son, D. Feng, S. Li, S. W. Cheong, X. H. Chen, and Y. Zhang. *Nat. Nanotechnol.* **2015**, 10, 270-276.

[44] Y. Wang, J. Xiao, H. Zhu, Y. Li, Y. Alsaid, K. Y. Fong, Y. Zhou, S. Wang, W. Shi, Y. Wang, A. Zettl, E. J. Reed, and X. Zhang. *Nature* **2017**, 550, 487-491.

[45] E. Sajadi, T. Palomaki, Z. Fei, W. Zhao, P. Bement, C. Olsen, S. Luescher, X. Xu, J. A. Folk, and D. H. Cobden. *Science* **2018**, 362, 922-925.

[46] Q. Liu, L. Li, Y. Li, Z. Gao, Z. Chen, and J. Lu. *J. Phys. Chem. C* **2012**, 116, 21556-21562.

[47] Y. Cao, V. Fatemi, A. Demir, S. Fang, S. L. Tomarken, J. Y. Luo, J. D. Sanchez-Yamagishi, K. Watanabe, T. Taniguchi, E. Kaxiras, R. C. Ashoori, and P. Jarillo-Herrero. *Nature* **2018**, 556, 80-84.

[48] Y. Cao, V. Fatemi, S. Fang, K. Watanabe, T. Taniguchi, E. Kaxiras, and P. Jarillo-Herrero. *Nature* **2018**, 556, 43-50.

[49] W. J. Yu, Y. Liu, H. Zhou, A. Yin, Z. Li, Y. Huang, and X. Duan. *Nat. Nanotechnol.* **2013**, 8, 952-958.

[50] P. Rivera, J. R. Schaibley, A. M. Jones, J. S. Ross, S. Wu, G. Aivazian, P. Klement, K. Seyler, G. Clark, N. J. Ghimire, J. Yan, D. G. Mandrus, W. Yao, and X. Xu. *Nat. Commun.* **2015**, 6, 6242.

[51] S. Gao, L. Yang, and C. D. Spataru. *Nano Lett.* **2017**, 17, 7809-7813.

[52] Z. Wang, Y. H. Chiu, K. Honz, K. F. Mak, and J. Shan. *Nano Lett.* **2018**, 18, 137-143.

[53] D. Unuchek, A. Ciarrocchi, A. Avsar, K. Watanabe, T. Taniguchi, and A. Kis. *Nature* **2018**, 560, 340-344.

[54] M. Yoshida, R. Suzuki, Y. Zhang, M. Nakano, and Y. Iwasa. *Sci. Adv.* **2015**, 1, e1500606.

[55] M. D. Nuez-Regueiro, J. M. Lopez-Castillo, and C. Ayache. *Phys. Rev. Lett.* **1985**, 55, 1931-1934.

[56] S. Zheng, F. Liu, C. Zhu, Z. Liu, and H. J. Fan. *Nanoscale* **2017**, 9, 2436-2441.

[57] G. Grüner. *Rev. Mod. Phys.* **1988**, 60, 1129-1181.

[58] J. Muller, T. S. Boscke, U. Schroder, S. Mueller, D. Brauhaus, U. Bottger, L. Frey, and T. Mikolajick. *Nano Lett.* **2012**, 12, 4318-4323.

[59] R. E. Cohen. *Nature* **1992**, 358, 136-138.

[60] C. Cui, F. Xue, W.-J. Hu, and L.-J. Li. *NPJ 2D Mater. Appl.* **2018**, 2, 18.

[61] C. Zheng, L. Yu, L. Zhu, J. L. Collins, D. Kim, Y. Lou, C. Xu, M. Li, Z. Wei, Y. Zhang, M. T. Edmonds, S. Li, J. Seidel, Y. Zhu, J. Z. Liu, W. X. Tang, and M. S. Fuhrer. *Sci. Adv.* **2018**, 4, eaar7720.

[62] R. Fei, W. Kang, and L. Yang. *Phys. Rev. Lett.* **2016**, 117, 097601.

[63] A. Zettl, G. Grüner, and A. H. Thompson. *Phys. Rev. B* **1982**, 26, 5760-5772.

[64] S. G. Zybtsev, V. Y. Pokrovskii, V. F. Nasretdinova, S. V. Zaitsev-Zotov, V. V. Pavlovskiy, A. B. Odobesco, W. W. Pai, M. W. Chu, Y. G. Lin, E. Zupanič, H. J. P. van Midden, S. Šturm, E. Tchernychova, A. Prodan, J. C. Bennett, I. R. Mukhamedshin, O. V. Chernysheva, A. P. Menushenkov, V. B. Loginov, B. A. Loginov, A. N. Titov, and M. Abdel-Hafiez. *Phys. Rev. B* **2017**, 95, 035110.

[65] P. Chen, Y. H. Chan, X. Y. Fang, Y. Zhang, M. Y. Chou, S. K. Mo, Z. Hussain, A. V. Fedorov, and T. C. Chiang. *Nat. Commun.* **2015**, 6, 8943.

[66] A. Castellanos-Gomez, R. Roldan, E. Cappelluti, M. Buscema, F. Guinea, H. S. van der Zant, and G. A. Steele. *Nano Lett.* **2013**, 13, 5361-5366.

[67] C. R. Zhu, G. Wang, B. L. Liu, X. Marie, X. F. Qiao, X. Zhang, X. X. Wu, H. Fan, P. H. Tan, T. Amand, and B. Urbaszek. *Phys. Rev. B* **2013**, 88, 121301.

[68] Y. Y. Hui, X. Liu, W. Jie, N. Y. Chan, J. Hao, Y. T. Hsu, L. J. Li, W. Guo, and S. P. Lau. *ACS Nano* **2013**, 7, 7126-7131.

[69] H. Li, A. W. Contryman, X. Qian, S. M. Ardakani, Y. Gong, X. Wang, J. M. Weisse, C. H. Lee, J. Zhao, P. M. Ajayan, J. Li, H. C. Manoharan, and X. Zheng. *Nat. Commun.* **2015**, 6, 7381.

[70] V. M. Pereira, A. H. Castro Neto, and N. M. R. Peres. *Phys. Rev. B* **2009**, 80, 045401.

[71] B. Verberck, B. Partoens, F. M. Peeters, and B. Trauzettel. *Phys. Rev. B* **2012**, 85, 125403.

[72] K. Sugawara, K. Kanetani, T. Sato, and T. Takahashi. *AIP Adv.* **2011**, 1, 022103.

[73] X. Peng, Q. Wei, and A. Copple. *Phys. Rev. B* **2014**, 90, 085402.

[74] P. Johari, and V. B. Shenoy. *ACS Nano* **2012**, 6, 5449-5456.

[75] H. Guo, N. Lu, L. Wang, X. Wu, and X. C. Zeng. *J. Phys. Chem. C* **2014**, 118, 7242-7249.

[76] H. J. Conley, B. Wang, J. I. Ziegler, R. F. Haglund, Jr., S. T. Pantelides, and K. I. Bolotin. *Nano Lett.* **2013**, 13, 3626-3630.

[77] K. He, C. Poole, K. F. Mak, and J. Shan. *Nano Lett.* **2013**, 13, 2931-2936.

[78] J. Feng, X. Qian, C.-W. Huang, and J. Li. *Nat. Photon.* **2012**, 6, 866-872.

[79] S. Manzeli, A. Allain, A. Ghadimi, and A. Kis. *Nano Lett.* **2015**, 15, 5330-5335.

[80] M. Proc Natl Acad Sci U S AHuang, H. Yan, C. Chen, D. Song, T. F. Heinz, and J. Hone. *Proc. Natl. Acad. Sci. U.S.A.* **2009**, 106, 7304-7308.

[81] M. Huang, H. Yan, T. F. Heinz, and J. Hone. *Nano Lett.* **2010**, 10, 4074-4079.

[82] C. Rice, R. J. Young, R. Zan, U. Bangert, D. Wolverson, T. Georgiou, R. Jalil, and K. S. Novoselov. *Phys. Rev. B* **2013**, 87, 081307.

[83] Y. Wang, C. Cong, C. Qiu, and T. Yu. *Small* **2013**, 9, 2857-2861.

[84] Y. Li, Z. Hu, S. Lin, S. K. Lai, W. Ji, and S. P. Lau. *Adv. Funct. Mater.* **2017**, 27, 1600986.

[85] M. Hosseini, M. Elahi, M. Pourfath, and D. Esseni. *J. Phys. D: Appl. Phys.* **2015**, 48, 375104.

[86] N. J. G. Couto, D. Costanzo, S. Engels, D.-K. Ki, K. Watanabe, T. Taniguchi, C. Stampfer, F. Guinea, and A. F. Morpurgo. *Phys. Rev. X* **2014**, 4, 041019.

[87] J. Suh, T. E. Park, D. Y. Lin, D. Fu, J. Park, H. J. Jung, Y. Chen, C. Ko, C. Jang, Y. Sun, R. Sinclair, J. Chang, S. Tongay, and J. Wu. *Nano Lett.* **2014**, 14, 6976-6982.

[88] P. Yu, J. Lin, L. Sun, Q. L. Le, X. Yu, G. Gao, C.-H. Hsu, D. Wu, T.-R. Chang, Q. Zeng, F. Liu, Q. J. Wang, H.-T. Jeng, H. Lin, A. Trampert, Z. Shen, K. Suenaga, and Z. Liu. *Adv. Mater.* **2017**, 29, 1603991.

[89] B. Tang, J. Zhou, P. Sun, X. Wang, L. Bai, J. Dan, J. Yang, K. Zhou, X. Zhao, S. J. Pennycook, and Z. Liu. *Adv. Mater.* **2019**, 31, e1900862.

[90] X. Duan, C. Wang, Z. Fan, G. Hao, L. Kou, U. Halim, H. Li, X. Wu, Y. Wang, J. Jiang, A. Pan, Y. Huang, R. Yu, and X. Duan. *Nano Lett.* **2016**, 16, 264-269.

[91] D. J. Lewis, A. A. Tedstone, X. L. Zhong, E. A. Lewis, A. Rooney, N. Savjani, J. R. Brent, S. J. Haigh, M. G. Burke, C. A. Muryn, J. M. Raftery, C. Warrens, K. West, S. Gaemers, and P. O'Brien. *Chem. Mater.* **2015**, 27, 1367-1374.

[92] J. Deng, H. Li, J. Xiao, Y. Tu, D. Deng, H. Yang, H. Tian, J. Li, P. Ren, and X. Bao. *Energy Environ. Sci.* **2015**, 8, 1594-1601.

[93] A. Nipane, D. Karmakar, N. Kaushik, S. Karande, and S. Lodha. *ACS Nano* **2016**, 10, 2128-2137.

[94] D. M. Sim, M. Kim, S. Yim, M. J. Choi, J. Choi, S. Yoo, and Y. S. Jung. *ACS Nano* **2015**, 9, 12115-12123.

[95] P. Zhao, D. Kiriya, A. Azcatl, C. Zhang, M. Tosun, Y. S. Liu, M. Hettick, J. S. Kang, S. McDonnell, K. C. Santosh, J. Guo, K. Cho, R. M. Wallace, and A. Javey. *ACS Nano* **2014**, 8, 10808-10814.

[96] F. Zhang, Y. Lu, D. S. Schulman, T. Zhang, K. Fujisawa, Z. Lin, Y. Lei, A. L. Elias, S. Das, S. B. Sinnott, and M. Terrones. *Sci. Adv.* **2019**, 5, eaav5003.

[97] M. S. Choi, D. Qu, D. Lee, X. Liu, K. Watanabe, T. Taniguchi, and W. J. Yoo. *ACS Nano* **2014**, 8, 9332-9340.

[98] J. Yu, C. H. Lee, D. Bouilly, M. Han, P. Kim, M. L. Steigerwald, X. Roy, and C. Nuckolls. *Nano Lett.* **2016**, 16, 3385-3389.

[99] S. Mouri, Y. Miyauchi, and K. Matsuda. *Nano Lett.* **2013**, 13, 5944-5948.

[100] S. Wang, W. Zhao, F. Giustiniano, and G. Eda. *Phys. Chem. Chem. Phys.* **2016**, 18, 4304-4309.

[101] M. T. Greiner, L. Chai, M. G. Helander, W.-M. Tang, and Z.-H. Lu. *Adv. Funct. Mater.* **2012**, 22, 4557-4568.

[102] D. Xiang, C. Han, J. Wu, S. Zhong, Y. Liu, J. Lin, X. A. Zhang, W. Ping Hu, B. Ozyilmaz, A. H. Neto, A. T. Wee, and W. Chen. *Nat. Commun.* **2015**, 6, 6485.

[103] C. Zhou, Y. Zhao, S. Raju, Y. Wang, Z. Lin, M. Chan, and Y. Chai. *Adv. Funct. Mater.* **2016**, 26, 4223-4230.

[104] M. Yamamoto, S. Nakaharai, K. Ueno, and K. Tsukagoshi. *Nano Lett.* **2016**, 16, 2720-2727.

[105] J. W. Chen, S. T. Lo, S. C. Ho, S. S. Wong, T. H. Vu, X. Q. Zhang, Y. D. Liu, Y. Y. Chiou, Y. X. Chen, J. C. Yang, Y. C. Chen, Y. H. Chu, Y. H. Lee, C. J. Chung, T. M. Chen, C. H. Chen, and C. L. Wu. *Nat. Commun.* **2018**, 9, 3143.

[106] K. F. Mak, and J. Shan. *Nat. Photon.* **2016**, 10, 216-226.

[107] Y. K. Luo, J. Xu, T. Zhu, G. Wu, E. J. McCormick, W. Zhan, M. R. Neupane, and R. K. Kawakami. *Nano Lett.* **2017**, 17, 3877-3883.

[108] J. Shang, X. Shen, C. Cong, N. Peimyoo, B. Cao, M. Eginligil, and T. Yu. *ACS Nano* **2015**, 9, 647-655.

[109] J. Yang, R. Xu, J. Pei, Y. W. Myint, F. Wang, Z. Wang, S. Zhang, Z. Yu, and Y. Lu. *Light Sci. Appl.* **2015**, 4, e312.

[110] Y. You, X.-X. Zhang, T. C. Berkelbach, M. S. Hybertsen, D. R. Reichman, and T. F. Heinz. *Nat. Phys.* **2015**, 11, 477-481.

[111] A. Vargas, F. Liu, C. Lane, D. Rubin, I. Bilgin, Z. Hennighausen, M. DeCapua, A. Bansil, and S. Kar. *Sci. Adv.* **2017**, 3, e1601741.

[112] S. Hellmann, M. Beye, C. Sohrt, T. Rohwer, F. Sorgenfrei, H. Redlin, M. Kallane, M. Marczynski-Buhlow, F. Hennies, M. Bauer, A. Fohlisch, L. Kipp, W. Wurth, and K. Rossnagel. *Phys. Rev. Lett.* **2010**, 105, 187401.

[113] K. Sun, S. Sun, C. Zhu, H. Tian, H. Yang, and J. Li. *Sci. Adv.* **2018**, 4, eaas9660.

[114] A. Zong, X. Shen, A. Kogar, L. Ye, C. Marks, D. Chowdhury, T. Rohwer, B. Freelon, S. Weathersby, R. Li, J. Yang, J. Checkelsky, X. Wang, and N. Gedik. *Sci. Adv.* **2018**, 4, eaau5501.

[115] G. H. Han, S. J. Chae, E. S. Kim, F. Gunes, I. H. Lee, S. W. Lee, S. Y. Lee, S. C. Lim, H. K. Jeong, M. S. Jeong, and Y. H. Lee. *ACS Nano* **2011**, 5, 263-268.

[116] A. Castellanos-Gomez, M. Barkelid, A. M. Goossens, V. E. Calado, H. S. van der Zant, and G. A. Steele. *Nano Lett.* **2012**, 12, 3187-3192.

[117] J. Lu, J. Wu, A. Carvalho, A. Ziletti, H. Liu, J. Tan, Y. Chen, A. H. Castro Neto, B. Ozyilmaz, and C. H. Sow. *ACS Nano* **2015**, 9, 10411-10421.

[118] S. Cho, S. Kim, J. H. Kim, J. Zhao, J. Seok, D. H. Keum, J. Baik, D. H. Choe, K. J. Chang, K. Suenaga, S. W. Kim, Y. H. Lee, and H. Yang. *Science* **2015**, 349, 625-628.

[119] M. Kan, H. G. Nam, Y. H. Lee, and Q. Sun. *Phys. Chem. Chem. Phys.* **2015**, 17, 14866-14871.

[120] R. Beams, L. G. Cancado, S. Krylyuk, I. Kalish, B. Kalanyan, A. K. Singh, K. Choudhary, A. Bruma, P. M. Vora, F. Tavazza, A. V. Davydov, and S. J. Stranick. *ACS Nano* **2016**, 10, 9626-9636.

[121] S.-Y. Seo, J. Park, J. Park, K. Song, S. Cha, S. Sim, S.-Y. Choi, H. W. Yeom, H. Choi, and M.-H. Jo. *Nat. Electron.* **2018**, 1, 512-517.

[122] F. H. Koppens, T. Mueller, P. Avouris, A. C. Ferrari, M. S. Vitiello, and M. Polini. *Nat. Nanotechnol.* **2014**, 9, 780-793.

[123] M. L. Tsai, S. H. Su, J. K. Chang, D. S. Tsai, C. H. Chen, C. I. Wu, L. J. Li, L. J. Chen, and J. H. He. *ACS Nano* **2014**, 8, 8317-8322.

[124] W. Yuan, and G. Shi. *J. Mater. Chem. A* **2013**, 1, 10078.

[125] M. J. Lee, J. H. Ahn, J. H. Sung, H. Heo, S. G. Jeon, W. Lee, J. Y. Song, K. H. Hong, B. Choi, S. H. Lee, and M. H. Jo. *Nat. Commun.* **2016**, 7, 12011.

[126] A. Dankert, and S. P. Dash. *Nat. Commun.* **2017**, 8, 16093.

[127] F. Schwierz. *Proc. IEEE* **2013**, 101, 1567-1584.

[128] P. Horowitz, and W. Hill, *The art of electronics*, Cambridge Univ. Press, **1989**.

[129] L. Chua. *IEEE Trans. Circuit Theory* **1971**, 18, 507-519.

[130] G. Liu, B. Debnath, T. R. Pope, T. T. Salguero, R. K. Lake, and A. A. Balandin. *Nat. Nanotechnol.* **2016**, 11, 845-850.

[131] M. D. Pickett, G. Medeiros-Ribeiro, and R. S. Williams. *Nat. Mater.* **2013**, 12, 114-117.

[132] F. Schwierz, J. Pezoldt, and R. Granzner. *Nanoscale* **2015**, 7, 8261-8283.

[133] G. Gonzalez, *Foundations of oscillator circuit design*, Artech House Norwood, **2007**.

[134] E. Guerriero, L. Polloni, M. Bianchi, A. Behnam, E. Carrion, L. G. Rizzi, E. Pop, and R. Sordan. *ACS Nano* **2013**, 7, 5588-5594.

[135] H. Wang, L. Yu, Y. H. Lee, Y. Shi, A. Hsu, M. L. Chin, L. J. Li, M. Dubey, J. Kong, and T. Palacios. *Nano Lett.* **2012**, 12, 4674-4680.

[136] G. Iannaccone, F. Bonaccorso, L. Colombo, and G. Fiori. *Nat. Nanotechnol.* **2018**, 13, 183-191.

[137] N. Ma, and D. Jena. *Phys. Rev. X* **2014**, 4, 011043.

[138] R. Kappera, D. Voiry, S. E. Yalcin, B. Branch, G. Gupta, A. D. Mohite, and M. Chhowalla. *Nat. Mater.* **2014**, 13, 1128-1134.

[139] H. J. Chuang, B. Chamlagain, M. Koehler, M. M. Perera, J. Yan, D. Mandrus, D. Tomanek, and Z. Zhou. *Nano Lett.* **2016**, 16, 1896-1902.

[140] F. Schwierz. *Nat. Nanotechnol.* **2010**, 5, 487-496.

[141] F. Traversi, V. Russo, and R. Sordan. *Appl. Phys. Lett.* **2009**, 94, 223312.

[142] W. Kim, J. Riikonen, C. Li, Y. Chen, and H. Lipsanen. *Nanotechnology* **2013**, 24, 395202.

[143] P. J. Jeon, J. S. Kim, J. Y. Lim, Y. Cho, A. Pezeshki, H. S. Lee, S. Yu, S. W. Min, and S. Im. *ACS Appl. Mater. Interfaces* **2015**, 7, 22333-22340.

[144] L. Yu, A. Zubair, E. J. Santos, X. Zhang, Y. Lin, Y. Zhang, and T. Palacios. *Nano Lett.* **2015**, 15, 4928-4934.

[145] Y. Su, C. U. Kshirsagar, M. C. Robbins, N. Haratipour, and S. J. Koester. *2D Mater.* **2016**, 3, 011006.

[146] Y. Liu, and K. W. Ang. *ACS Nano* **2017**, 11, 7416-7423.

[147] S. Wachter, D. K. Polyushkin, O. Bethge, and T. Mueller. *Nat. Commun.* **2017**, 8, 14948.

[148] B. Radisavljevic, M. B. Whitwick, and A. Kis. *ACS Nano* **2011**, 5, 9934-9938.

[149] K. Choi, Y. T. Lee, J. S. Kim, S.-W. Min, Y. Cho, A. Pezeshki, D. K. Hwang, and S. Im. *Adv. Funct. Mater.* **2016**, 26, 3146-3153.

[150] H. Kwon, P. J. Jeon, J. S. Kim, T.-Y. Kim, H. Yun, S. W. Lee, T. Lee, and S. Im. *2D Mater.* **2016**, 3, 044001.

[151] A. B. Sachid, M. Tosun, S. B. Desai, C. Y. Hsu, D. H. Lien, S. R. Madhvapathy, Y. Z. Chen, M. Hettick, J. S. Kang, Y. Zeng, J. H. He, E. Y. Chang, Y. L. Chueh, A. Javey, and C. Hu. *Adv. Mater.* **2016**, 28, 2547-2554.

[152] G. V. Resta, Y. Balaji, D. Lin, I. P. Radu, F. Catthoor, P. E. Gaillardon, and G. De Micheli. *ACS Nano* **2018**, 12, 7039-7047.

[153] J. M. Rabaey, A. P. Chandrakasan, and B. Nikolic, *Digital integrated circuits*, Prentice hall Englewood Cliffs, **2002**.

[154] S. Bertolazzi, D. Krasnozhon, and A. Kis. *ACS Nano* **2013**, 7, 3246-3252.

[155] M. S. Choi, G. H. Lee, Y. J. Yu, D. Y. Lee, S. H. Lee, P. Kim, J. Hone, and W. J. Yoo. *Nat. Commun.* **2013**, 4, 1624.

[156] M. C. Cheynet, S. Pokrant, F. D. Tichelaar, and J.-L. Rouvière. *J. Appl. Phys.* **2007**, 101, 054101.

[157] A. S. Foster, F. Lopez Gejo, A. L. Shluger, and R. M. Nieminen. *Phys. Rev. B* **2002**, 65, 174117.

[158] D. Li, M. Chen, Z. Sun, P. Yu, Z. Liu, P. M. Ajayan, and Z. Zhang. *Nat. Nanotechnol.* **2017**, 12, 901-906.

[159] H. Tian, B. Deng, M. L. Chin, X. Yan, H. Jiang, S. J. Han, V. Sun, Q. Xia, M. Dubey, F. Xia, and H. Wang. *ACS Nano* **2016**, 10, 10428-10435.

[160] S. Lee, E. B. Song, S. Min Kim, Y. Lee, D. H. Seo, S. Seo, and K. L. Wang. *Appl. Phys. Lett.* **2012**, 101, 243109.

[161] D. Xiang, T. Liu, J. Xu, J. Y. Tan, Z. Hu, B. Lei, Y. Zheng, J. Wu, A. H. C. Neto, L. Liu, and W. Chen. *Nat. Commun.* **2018**, 9, 2966.

[162] Y. T. Lee, H. Kwon, J. S. Kim, H. H. Kim, Y. J. Lee, J. A. Lim, Y. W. Song, Y. Yi, W. K. Choi, D. K. Hwang, and S. Im. *ACS Nano* **2015**, 9, 10394-10401.

[163] C. Ko, Y. Lee, Y. Chen, J. Suh, D. Fu, A. Suslu, S. Lee, J. D. Clarkson, H. S. Choe, S. Tongay, R. Ramesh, and J. Wu. *Adv. Mater.* **2016**, 28, 2923-2930.

[164] W. Hou, A. Azizimanesh, A. Sewaket, T. Pena, C. Watson, M. Liu, H. Askari, and S. M. Wu. *Nat. Nanotechnol.* **2019**, 14, 668–673.

[165] M. Prezioso, F. Merrikh-Bayat, B. D. Hoskins, G. C. Adam, K. K. Likharev, and D. B. Strukov. *Nature* **2015**, 521, 61-64.

[166] B. Govoreanu, A. Redolfi, L. Zhang, C. Adelmann, M. Popovici, S. Clima, H. Hody, V. Paraschiv, I. P. Radu, A. Franquet, J. C. Liu, J. Swerts, O. Richard, H. Bender, L. Altimime, and M. Jurczak. **2013**, DOI: 10.1109/iedm.2013.672459910.12.11-10.12.14.

[167] M. Wang, S. Cai, C. Pan, C. Wang, X. Lian, Y. Zhuo, K. Xu, T. Cao, X. Pan, B. Wang, S.-J. Liang, J. J. Yang, P. Wang, and F. Miao. *Nat. Electron.* **2018**, 1, 130-136.

[168] C. Tan, Z. Liu, W. Huang, and H. Zhang. *Chem. Soc. Rev.* **2015**, 44, 2615-2628.

[169] S. T. Han, L. Hu, X. Wang, Y. Zhou, Y. J. Zeng, S. Ruan, C. Pan, and Z. Peng. *Adv. Sci.* **2017**, 4, 1600435.

[170] S. Kumar, J. P. Strachan, and R. S. Williams. *Nature* **2017**, 548, 318-321.

[171] D. Svetin, I. Vaskivskyi, S. Brazovskii, and D. Mihailovic. *Sci. Rep.* **2017**, 7, 46048.

Chapter 3

Experimental Methodology

This chapter summarizes the experimental methods used in the whole project. Firstly, the rational for material selection is discussed. Secondly, the methods for device fabrication are described, which includes the mechanical exfoliation, sample transfer, vacuum annealing, electron beam lithography, maskless photolithography, and metal deposition. Thirdly, the characterization methods are summarized, such as the atomic force microscopy, scanning Kelvin probe microscopy, Raman spectroscopy, ultraviolet-visible spectroscopy, scanning electron microscopy, transmission electron microscopy, electron energy loss spectroscopy, and X-ray Photoelectron Spectroscopy. The measurement methods of electronic devices are also discussed. Finally, simulation and calculation methods of some key parameters are summarized.

3.1 Rationale for Selection of Materials

To study the light tune of electronic properties of 2D materials with different bandgaps, three systems were selected. The first was the metallic 1T-TaS_2. 1T-TaS_2 has three main CDW phases, which are CCDW phase below 180 K, NCCDW phase from 180 K to 350 K, and ICCDW above 350 K.[1] It has been reported that ultrafast pulsed laser could induce CDW phase transition of 1T-TaS_2 at the cryogenic temperature,[2] which suggests the possibility to tune the CDW phase by light at room temperature as well as its possible applications in high frequency electronics. The second was the semiconducting 2H-WSe_2. 2H-WSe_2 has a bandgap of 1.65 eV for the monolayer and 1.2 eV for the bulk.[3,4] Pristine WSe_2 is ambipolar whose carrier type and carrier density are easily to be influenced by factors such as thickness, surface absorption and contact metal work function.[5-7] Laser ablation, which could lead to the thinning of 2D materials, should also be able to tune the carrier type of 2H-WSe_2. The third was the heterostructure of the narrow bandgap semiconductor black phosphorus and the wide bandgap strontium titanate ($SrTiO_3$). The selection of this system was mainly based on two concerns. One was that $SrTiO_3$ is a wide bandgap material (3.25 eV) with oxygen vacancy states in the bandgap, which could be used as charge traps.[8,9] On the other hand, the black phosphorus is one of the few p-type 2D materials. Compared with graphene and TMD materials such as MoS_2 and WSe_2, the black phosphorus has both high mobility and high current on/off ratio.[10,11] Moreover, unlike other 2D semiconductors such as MoS_2 and WSe_2, black phosphorus has a direct bandgap, which decreases with increasing thickness. The bandgap of monolayer, trilayer and bulk black phosphorus is 1.73, 0.83, and 0.35 eV, respectively, which makes multilayer black phosphorus a good candidate for the infrared photodetection.[12]

3.2 Device Fabrication

3.2.1 Mechanical Exfoliation

Mechanical exfoliation is one of the methods to obtain atomic thin 2D materials. Compared with other methods such as CVD synthesis and liquid exfoliation, mechanical exfoliation

can be used to get cleaner samples with fewer defects. The major disadvantage of mechanical exfoliation is the low yield. For the mechanical exfoliation, bulk single crystals of 2D materials are required, which are mainly synthesized by the chemical vapor transport method. First, two sides of a bulk single crystal are attached by two pieces of Scotch tape, which are then peeled off from the single crystal. Due to the weak van der Waals interlayer interaction of 2D materials, thin films will be attached onto the Scotch tape. This is called exfoliation. After several times of exfoliation, samples on the tape will become much thinner. Then the tape together with the samples on it will be attached onto a silicon substrate with a 285 nm SiO_2 layer. Certain amount of force is then applied to the top of the tape to increase the adherence of the samples to the substrate. Then the tape is peeled off from the substrate. Since the interaction between the samples and the substrate is like the interlayer interaction of the samples, there is a certain probability that atomically thin 2D films will be left on the substrate. With the existence of the 285 nm SiO_2, samples with different layers can be differentiated in the optical image due to the difference in light absorption and interference. The thickness is first estimated by appearance in the optical image and then confirmed by AFM and Raman spectroscopy. Samples with suitable thickness are then selected for experiments.

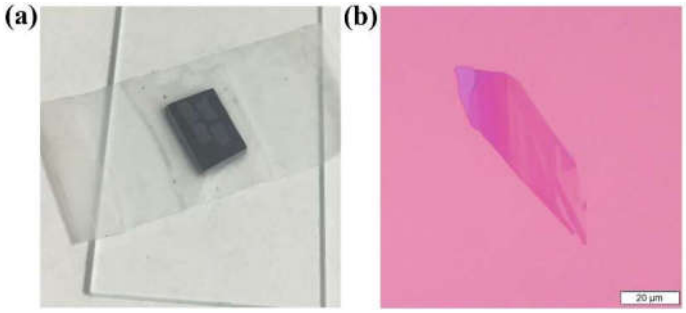

Figure 3.1 Mechanical exfoliation of atomically thin 2D materials. (a) Image of thin MoS_2 crystals attached onto a silicon substrate by the Scotch tape. (b) Optical image of an exfoliated graphene sample. Regions with different thicknesses have different appearances.

3.2.2 Sample Transfer

There are mainly two methods for the transfer of 2D materials, which are the dry transfer and wet transfer. The major difference of these two methods is whether the liquid is used

during the transfer process. Figure 3.2a shows a setup for the dry transfer, which consists of a microscope, an XYZ movable cantilever for the transferred sample, and an XYθ movable stage to mount the target stage. The dry transfer procedure is shown in Figure 3.2b. First the sample is exfoliated onto a PDMS stamp placed on a glass slide, which is then turned upside down and fixed onto the cantilever. By tuning the XY position of the transferred sample and the XY position and the angular orientation of the target substrate, the transferred sample and the substrate are well aligned. Then the cantilever is lowered down to press the sample onto the target substrate. After a while, the cantilever is lifted together with the PDMS stamp. Since the interaction between the sample and the target substrate is close to the interaction between the sample and the PDMS, there is a high probability that the sample will stick on the target substrate. In this way, the sample is dry transferred onto the target substrate. It needs to be mentioned that for the PDMS assisted dry transfer, the bubbles beneath the transferred sample seem to be inevitable. In order to minimize the bubbles, the approach and retraction of the cantilever should be as slow as possible. Besides, successful dry transfer depends highly on how firmly the sample adheres to the target substrate. Large height variation or severe particle absorption in the substrate will make it difficult to transfer the sample successfully. Another transfer method is the wet transfer, which is often used for the CVD synthesized samples and samples for the TEM characterization. For samples on a substrate such as the SiO_2/Si substrate, a layer of polymer (usually PMMA) is spin-coated on the top. After removing the solution in the coating layer by baking or vacuum pumping, the wafer is placed into the etchant, which is KOH for the silicon wafer. The SiO_2 will react with KOH and water-soluble K_2SiO_3 will be produced. The dissolve of SiO_2 will separate the silicon substrate with the PMMA film, with the samples sticking to the PMMA. Then the PMMA film is rinsed in the deionized water for several times to remove the KOH. Then the PMMA film is picked up by the target substrate (such as a TEM grid), followed by drying. At last, the PMMA is removed by a solvent such as the acetone. In this way, the samples are wet transferred from the original substrate to the target substrate. Since PMMA is very flexible, a piece of tape or PDMS stamp is usually attached on top of PMMA to avoid the bending of the PMMA film. And to avoid the KOH corrosion of the target substrate, enough rinse in deionized water is required.

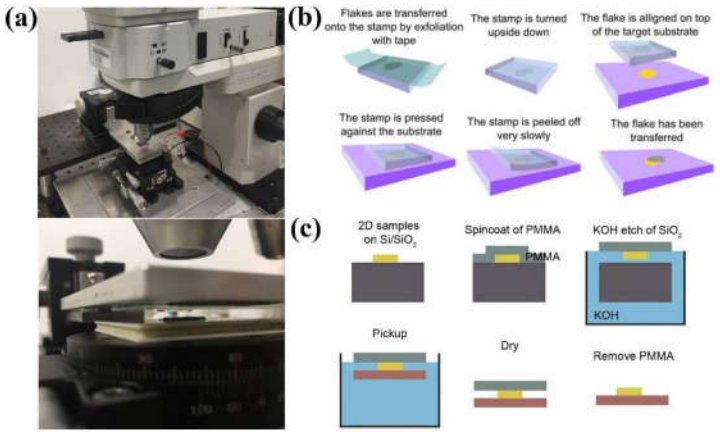

Figure 3.2 Dry transfer of 2D materials. (a) Experimental setup of a transfer stage, including a microscope, an XYZ movable cantilever, and an XYθ movable substrate holder. (b) Schematic diagram for the dry transfer process. Reproduced with permission.[13] Copyright 2014, IOP Publishing Ltd. (c) Schematic diagram for the wet transfer process. Reproduced with permission.[14] Copyright 2018, The Royal Society of Chemistry.

3.2.3 Vacuum Annealing

Annealing is a process where the sample is heated up to a high temperature for a duration of time and then cooled down to the room temperature, which can be used for the phase transition, sample re-crystallization, defect removing, surface absorption removing, and improving the interlayer contact. For dry-transferred materials, the contact between different samples and the substrate is often loose. After stacking two pieces of flakes and spin-coating PMMA onto the sample, PMMA is very likely to enter between the two flakes and ruin the sample. This problem can be solved by vacuum annealing.

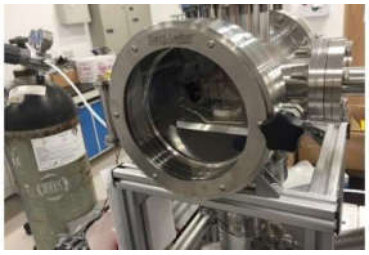

Figure 3.3 A vacuum annealing system with the pressure down to 10^{-6} Torr and the temperature up to 500 ℃.

3.2.4 Electron Beam Lithography

Electron beam lithography (EBL) is a way to fabricate mesoscopic and nanoscopic electronic devices with the help of a scanning focused beam of electrons. For the scanning electron microscope (SEM), sample images are obtained by scanning the sample with a focused electron beam, which will be discussed later. The EBL is based on the SEM with some adjustments. For SEM, the whole field of view is scanned continuously by the electrons. While for EBL, only regions of interest are scanned (exposed) by the electron beam. This is achieved by the integration of a pattern generation system. In the Figure 3.4a, the beam blanking and electrostatic deflector are controlled by a pattern generator. The beam blanking is used to control the pass of the electron beam by a transverse voltage. When the voltage is zero, the electrons pass through a series of lenses to the sample. While when a high transverse voltage (100 V) is applied in the beam blanking, the trajectory of the electron beam is bent. Since the location of the beam blanking is far away from the sample, finally the electron beam will totally miss the sample. The electrostatic deflector is used to control the electron trajectory by the electric field. Continuous deflection in X and Y directions defines the field of view, which is related to the magnification and working distance. In general, a small magnification and a large working distance lead to a large field of view. The selected exposure of electrons in the regions of interest is achieved by collaboration of the beam blanking and deflector. The deflector bends electrons to regions of interest while the voltage at the beam blanking is zero. For other regions where electron exposure is unwanted, the high voltage is applied at the beam blanking so that no electrons will reach the sample. The standard procedure of EBL is shown in Figure 3.4b. First the electron sensitive resist PMMA is spin-coated onto the substrate, which is then put into the EBL system for the electron exposure in regions of interest. Upon electron exposure, the large molecule PMMA will break into small molecules, which can be dissolved by the developer (MIBK), leading to the patterned regions exposed. After the development, the sample is then placed in an evaporator to deposit a layer of metal onto the surface. Then the sample is placed in the acetone to dissolve the remaining PMMA. The metal on the PMMA will be detached while the metal on the exposed area will stick onto the substrate. In this way, metal electrodes are patterned onto the sample. There are various types of metal

deposition methods, such as magnetron sputtering, electron beam evaporation, and thermal evaporation. The energy of sputtering is high, which is likely to damage 2D materials. Thus, for 2D materials, the electron beam evaporation and thermal evaporation are often used. The former uses high speed electrons to evaporate the metal sources while the latter uses Joule heating to evaporate the metal. Both are done under high vacuum.

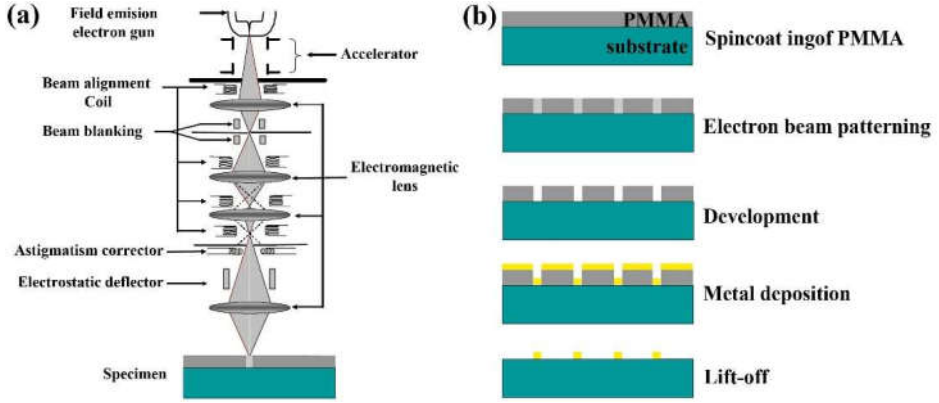

Figure 3.4 Electron beam lithography. (a) Diagram of the setup of electron beam lithography. (b) Diagram for the lithography procedure. Reproduced with permission.[15] Copyright 2010, IntechOpen.

3.2.5 Maskless Photolithography

Photolithography is extensively used in semiconductor industries to create patterned microstructures with the help of the ultraviolet light. A photomask contains pre-designed microscopic patterns which allow light to pass through. With the help of the photomask, the patterns on it is projected by light to the photoresist on the substrate, which then undergoes etching or metal deposition to pattern microstructures on the substrate. However, the photomask is pre-designed, and its patterns are fixed, which is suitable for standard fabrications in the large scale yet not suitable for most laboratory experiments. For 2D materials, there are still problems for the large-scale electronic applications due to the difficulty in synthesis of large-scale high-quality uniform thin films. Samples for 2D prototype electronic devices are often small with random structures and randomly located on the substrates, which are more obvious for the exfoliated samples. In this case, the maskless photolithography is more convenient, which directly writes patterns by the light

without the photomask. Figure 3.5 shows a maskless Laser Writer system from Microtech. The maskless photolithography is achieved by a pattern generator with an XYZ sample stage. The pattern generator determines sample locations where the light exposure is required according to patterns designed in the software. And the sample location is precisely controlled by the infrared interferometers. In this way, arbitrary electrode patterns based on specific samples can be written. Unlike the EBL where prepatterned marks are required for the location of the sample, in the Laser Writer, the sample location is in situ determined using the infrared light microscopy, making it less time-consumable than the EBL. On the other hand, for the EBL, a conductive layer (metal or conductive polymer) needs to be coated on the insulating substrate. While the maskless photolithography has no requirement on the conductivity of the substrate, making it more convenient for the device fabrication on the insulating substrate. There are some issues which need to be kept in mind. Since the photoresists are sensitive to the ultraviolet light, the yellow-light room is often used to avoid unnecessary exposure of the photoresists. And during the development, the samples are often rinsed in the deionized water to remove the developer. As a result, this method is not suitable for 2D materials which will degrade in water.

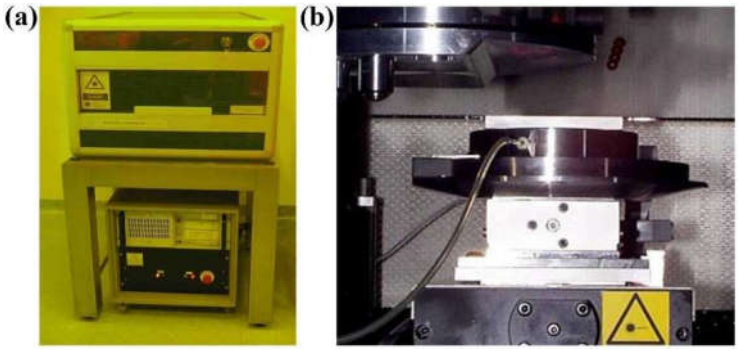

Figure 3.5 Maskless photolithography. (a) A Microtech Laser Writer System. (b) An XYZ sample mounting stage whose location is precisely determined by interferometers.

3.3 Characterization

3.3.1 Atomic Force Microscopy

The atomic force microscopy is used to measure the topology of samples by the distance-

dependent atomic forces. There are both attractive and repulsive forces between the top and the sample, such as the attractive van der Waals interaction and the repulsive electron-electron Coulomb interaction. Both the vdW interaction and the electron-electron Coulomb interaction decrease with increasing tip-sample distance. However, the repulsive Coulomb interaction decreases much faster than the vdW interaction and has a shorter range. As a result, at the large distance, the vdW force is dominant and the overall force is attractive. At the short distance, the Coulomb interaction is dominant and the overall force is repulsive. The distance-dependent net force is shown in Figure 3.6a, where the attractive region and repulsive region marked. Apart from the force, the tip oscillation frequency and the oscillation amplitude are also dependent on the tip-sample distance. A schematic setup of AFM is shown in Figure 3.6b, which includes a piezoelectric controlled sharp tip (usually with a diameter below 50 nm), a piezoelectric x-y-z scanner for sample mounting, a laser, a photo diode, a lock-in amplifier, a PID feedback system, and so on. A beam of laser is shone onto the tip and then reflected to the photo diode, which records the location information of the tip. As the tip scans along the sample surface, the change of the sample height will induce the change of the tip-sample interaction force, leading to the change of the tip deflection, tip oscillation frequency and amplitude. By controlling relative parameters, the sample topology can be recorded. For the AFM, there are mainly three operation modes, which are non-contact mode, tapping mode, and contact mode. For the non-contact mode, the tip operates at the attractive region. In order to control the resonant frequency at a constant value, a fixed tip-sample distance is required. This is done by adjusting the z value of the x-y-z scanner according to the sample height, from which the sample topology can be recorded. For the contact mode, the tip operates at the repulsive region. The sample topology is recorded by controlling the tip deflection at a constant. Non-contact mode is often used for soft materials and the recorded topology at the sample border is not very sharp. While the contact mode is often used for rigid samples and is easy to break materials. For 2D materials, the tapping mode is most used, which can obtain a sharp sample topology without destroying the sample. As shown in Figure 3.6c, before engagement, the tip oscillates at a free constant amplitude. After engagement, the oscillation amplitude is limited and decreases with decreasing distance. By controlling the amplitude at a constant value (the setpoint), the sample topology can be measured.

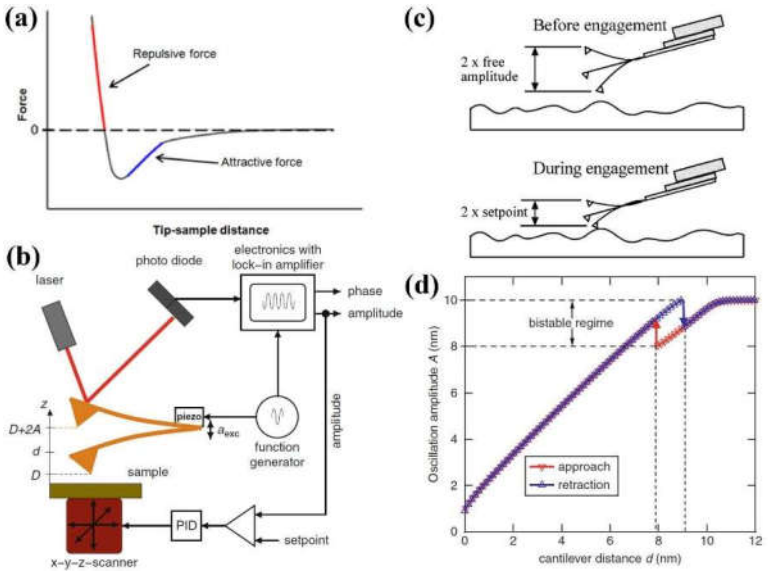

Figure 3.6 Atomic force microscopy. (a) Schematic setup of an AFM. (b) Schematic diagram of the tip-sample atomic force versus the tip-sample distance. (c) Schematic diagram of the oscillation of the tip working in the tapping mode. (d) Oscillation amplitude versus tip-sample distance. Reproduced with permission.[16] Copyright 2012, Springer Science Business Media B.V.

The scanning Kelvin probe microscopy is a derivative of the basic AFM, which is used to measure the surface potential of samples. When materials with different potentials are enough, the alignment of the Fermi levels will induce a potential difference in their vacuum levels, which is the contact potential difference (CPD). CPD is defined by the equation $V_{CPD} = -(\Phi_{tip} - \Phi_s)/e$, where Φ_{tip} and Φ_s is the work function of the metal-coated tip and the sample. The existence of CPD will introduce the electrostatic force between the tip and the sample, which will then influence the tip oscillation. By applying a DC voltage (V_{DC}) to the tip and connecting the sample to the ground, the electrostatic force can be nullified when $V_{DC} = V_{CPD}$. If the work function of the tip is known, then the work function (surface potential) of the sample can be obtained. It needs to be noted that the work function of tips varies from one to another, even when the same metal is coated. For the SKPM measurement, the tip first scans the sample surface to determine the topology then it scans for the second time at a fixed tip-surface distance to measure the V_{CPD}.

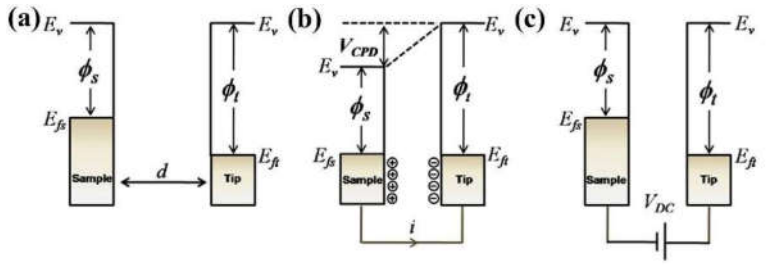

Figure 3.7 Energy levels of the sample and the tip for three cases. (a) The sample and the tip are separated in a distance. (b) The sample and tip are close enough for current tunneling, leading to the alignment of Fermi levels and the formation of the contact potential difference. (c) A DC voltage is applied to the tip with the sample grounded.

3.3.2 Raman Spectroscopy

When the light travels through a material such as crystals and molecules, it will be scattered by the crystal atoms or molecules. There are two types of light scattering, where are the elastic Rayleigh scattering and the inelastic Raman scattering. For the Rayleigh scattering, the photon energy will not change after the scattering. While the Raman scattering will change the photon energy due to the energy transfer between the photon and the material. As shown in Figure 3.8a, there are multiple energy states above the base state due to the different vibration modes of the crystal lattice or the molecule. The incident photons excite the lattice from a lower vibrational state to a virtual state, which then falls back to a higher vibrational state, accompanied by the emission of photons with lower energies than the incident photons. This is called the Stokes Raman scattering. On the other hand, if the lattice transits from a higher vibration state to a lower vibration state and the emitted photons have higher energies than the incident photons, the scattering is called the anti-Stokes Raman scattering. The shifts of photon energies during the Raman scattering depend highly on the lattice structures and the element compositions. As a result, the Raman scattering provides a way to identify the material types and structures. Figure 3.8b shows the two dominant vibration modes in the 2H-WS_2 crystal, where the E_{2g}^1 and A_{1g} are in-plane and out-of-plane vibration modes, respectively. The *A* and *E* stand for the degeneracy, where *A* is for the non-degenerate mode and *E* is for the doubly degenerate mode. The subscript g means that the vibration is centrosymmetric. The subscript number 1 means

symmetric with respect to the XY plane (with Z axis as the principal axis). And the subscript number 2 means anti-symmetric with respect to the XY plane. The superscript number 1 is used to distinguish it from another E_{2g} mode (labeled as E_{2g}^1) at low frequency.[17] For a confocal Raman spectroscopy, a beam of laser focused by an objective lens is shone onto the sample and the scattered light is collected by the same lens, which then travels through an optical fiber into a spectrometer. In the spectrometer, the light shines on a diffraction grating, leading to the dispersion of light. The dispersed light then shines onto a CCD. According to the relative angles between the incident light, dispersed light, and the diffraction grating, the light intensity of different wavelengths can be determined. The light dispersion capacity is dependent on the groove density of the grating. A higher groove density leads to a higher dispersion capability, which means light with different wavelengths can be more separated. A higher groove density means a higher spectral resolution but a lower spectral intensity.

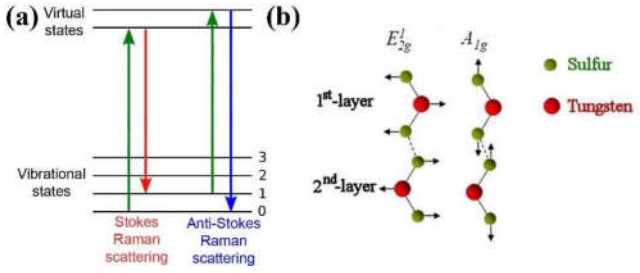

Figure 3.8 Schematic diagram of the Raman scattering. (a) Schematic energy levels involved in the Stokes scattering and anti-Stokes scattering. (b) Two dominant vibration modes in the 2H-WS_2. Reproduced with permission.[18] Copyright 2013, Springer Nature.

3.3.3 Ultraviolet-Visible Spectroscopy

Ultraviolet-visible spectroscopy is a kind of absorption spectroscopy working in the ultraviolet-visible range, which can be used to measure the bandgap of wide bandgap semiconductors and insulators. Electrons in the valence band will jump into the conduction band upon excitations from the light with the photon energy larger than the bandgap. In this case, the light will be absorbed by the sample. If the photon energy is smaller than the bandgap, the light will travel through the sample without absorption. In an ultraviolet-visible spectrometer, continuous light is first generated by the light source and then travels

through the monochromator, after which the monochromic light can be obtained. Then the monochromic light is split into two beams. One travels through the sample and the other travels through the reference. Then the two beams are both collected by the photo detector. By comparing the intensity of these two beams, the transmission of the sample can be determined. After measuring the transmission over a wavelength range, the transmission spectrum of the sample can be obtained, from which the bandgap of the sample can be determined.

3.3.4 Scanning Electron Microscopy

In the traditional optical microscopy, the system resolution is limited by the light diffraction. The resolution of an optical microscope is given by the Rayleigh criterion $r = 0.61\lambda/NA$, where λ is the light wavelength and *NA* is the numerical aperture of the objective lens. The above equation shows that a higher resolution can be achieved with a shorter light wavelength, but it still cannot reach the atomic level due to the limitations of the wavelength and the numerical aperture. On the other hand, the wave-particle duality of the electron can be described by the de Broglie equation $\lambda = h/p = h/\sqrt{2meV}$, where *h* is the Planck constant, *m* is the electron mass, *e* is the elementary charge, and *V* is the acceleration voltage. This shows that when the electrons are accelerated to a high speed by a high acceleration voltage, the wavelength of the electrons can be very small. For example, when the acceleration voltage is 100 keV, the electron wavelength is calculated to be about 3.7 pm, which is much smaller than the wavelength of visible light. In the practice, due to the imperfection of the electromagnetic lenses and the environmental noises, the resolution of electron microscopy is much higher than the electron wavelength.

Figure 3.9 is a schematic diagram showing the principles of the SEM. The main column of the microscope is in high vacuum to avoid scattering of electrons by air molecules. High-speed electrons are emitted and accelerated by an electron gun with a high acceleration voltage. There are various types of electron guns, such as the thermionic electron guns, Schottky-emission guns, and field-emission guns. For thermal emitters such as the tungsten filament, due to the Joule heating by the high current, electrons in the filament cathode are

thermally excited to overcome the metal work function. Since the cathode is negatively biased with respect to the surroundings, the thermally excited electrons are emitted from the filament surface, which are then accelerated by a high voltage between the filament and the anode. For Schottky emitters, the cathode has an emission tip with a smaller radius (1 μm), leading to the high electric field at the metal surface, which lowers the local work function. Besides, the surface work function can be further lowered by specific coatings on the surface, such as ZrO on the W(100). In this way, electrons can be emitted in the thermo-field region with a lower temperature and a higher emission current density. For the field-emission guns, the emitters have a smallest tip radius (0.1 μm) and highest negative bias. The field emission guns work at a low cathode temperature and the produced electron beam has a smaller diameter, smaller energy spread, and higher brightness than that from thermionic guns or Schottky-emission guns. High-speed electrons from the gun are then focused by a series of electromagnetic lenses under the Lorentz force and then reach the specimen. The interactions between high-speed electrons and the specimen will produce various signals, which are then collected by detectors. By the deflection of electrons under electrostatic forces controlled by the scan generator, the specimen is raster-scattered by electrons and the SEM images are obtained.

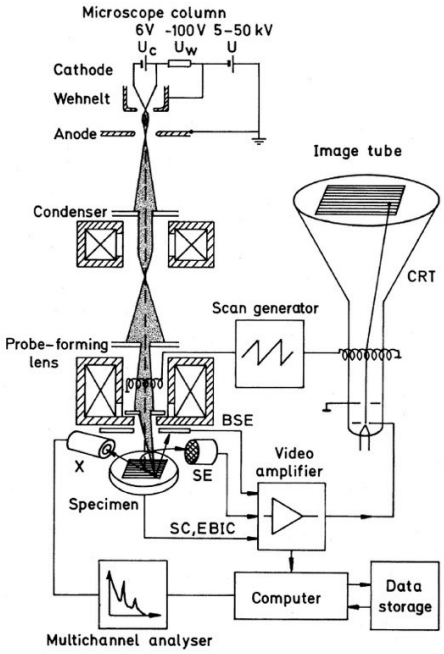

Figure 3.9 Schematic diagram of the scanning electron microscopy. BSE, SE, and X stand for backscattered electrons, secondary electrons, and X-rays, respectively. SC and EBIC are the current

from the specimen and electrons. Reproduced with permission.[19] Copyright 1998, Springer.

The SEM signals include backscattered electrons, secondary electrons, and X-rays. The backscattered electrons (BSE) have a wide energy range from 50 eV to the energy of primary electrons, which are mainly from deceleration of primary electrons after elastic collisions as well as multiple inelastic collisions. Due to their high energy, the BSE travel on straight trajectories which are less likely to be affected by the signal collection fields. Although the specimen surface topology can influence BSE signals, the intensity of BSE is mostly affected by the atomic number. The backscattering coefficient is the ratio of BSE intensity to the primary electron intensity. In general, when the normal incident electrons have energy higher than 5 keV, the backscattering coefficient increases with increasing atomic number. And for light atoms such as C, Al, and Si, the backscattering coefficient decreases with increasing primary electron energy. While for heavy atoms such as Mo, In, and W, the coefficient increases with increasing primary energy. The BSE detector has a large ring-shaped structure, which is placed below the polepiece at a high take-off angle in order to suppress the contrast from the topology. In this way, the contrast of the BSE images mainly arises from differences in the mean atomic number, which can be used to identify the composition information. Different from the BSE which have a large and wide range of energy, the energy of secondary electrons (SE) is much lower (below 50 eV). SE are mainly excited electrons from the specimen, which are generated by the inelastic interactions between primary electrons and the specimen or the BSE and the specimen. Due to their low energy, the trajectories of SE can be easily affected by a small collection voltage. As a result, a positively biased collector is placed at the side of the specimen to collect the SE. The intensity of SE signal can be influenced by both the surface topology and the composition. Only SE generated within a small depth beneath the surface can leave the specimen. This depth, which is called the exit depth, is of the order of several nanometers. The SE yield increases with increasing specimen tilt angle. With a larger tilt angle, the primary electrons travel through a longer distance within the exit depth, generating more SE. The SE also increases slightly with increasing atomic number, due to the increased excitation of SE by the increased BSE. Two types of X-rays can be generated during the scattering between high-speed electrons and the specimen. One is the X-ray

continuum due to the deceleration of high-energy primary electrons. The other is the characteristic X-ray spectra. When an electron at the inner shell is ionized by the primary electrons, an inner-shell vacancy will be produced. Then the vacancy will be filled by an electron from the outer shell, accompanied by the emission of an X-ray photon. The X-ray photon energy is equal to the energy difference of the two shells. The specimens for SEM should be conductive to prevent the accumulation of electrons. For insulating specimens, a conductive layer needs to be coated on top of the specimen surface.

3.3.5 Transmission Electron Microscopy

Transmission electron microscopy (TEM) is one of the most power techniques to obtain sub-nanometer images of materials. In the TEM, high-speed electrons are transmitted through the specimen, when the interactions between electrons and specimen atoms take place. The transmitted electrons then form an image, which is then recorded after the magnification by a series of electron lenses. The specimen needs to be thinner than 100 nm, which makes 2D materials naturally suitable for the TEM imaging. TEM operates at an acceleration voltage much higher than the SEM. And with the help of aberration correctors which eliminate the spherical and chromatic aberrations of the electron lenses, atomic resolution below 0.05 nm can be achieved.[20] Figure 3.10 shows the simplified schematic diagrams of two basic operation modes of the TEM imaging, which are the diffraction mode and the image mode. After several electron lenses, high-speed electrons emitted from the electron gun are turned into a parallel electron beam, which is then shone onto the specimen in the region of interest. The transmitted electrons are then focused by the objective lens. For the diffraction mode, a selected-area diffraction (SAD) aperture is inserted at the image plane, which is used to block the electrons from the unwanted region of the specimen. By changing the intermediate lens to a suitable strength, diffraction patterns of the specimen are projected onto the viewing screen (or detector) by the projector lens. For the image mode, the SAD aperture is removed. While the objective aperture is inserted at the back-focal plane of the objective lens, which is used to control the collection angle of the transmitted electrons. The strength of the intermediate lens is changed to a value such that the spatial image of the specimen is projected onto the viewing screen. If

the center of the objective aperture locates at the optical axis, a bright-field image is obtained. If the center of the objective aperture is displaced from the optical axis, a dark-field image is obtained. On the other hand, by adding a deflector in the electron path before the specimen, the incident electron beam can scan the specimen over a wider region. This leads to the scanning transmission electron microscopy (STEM).

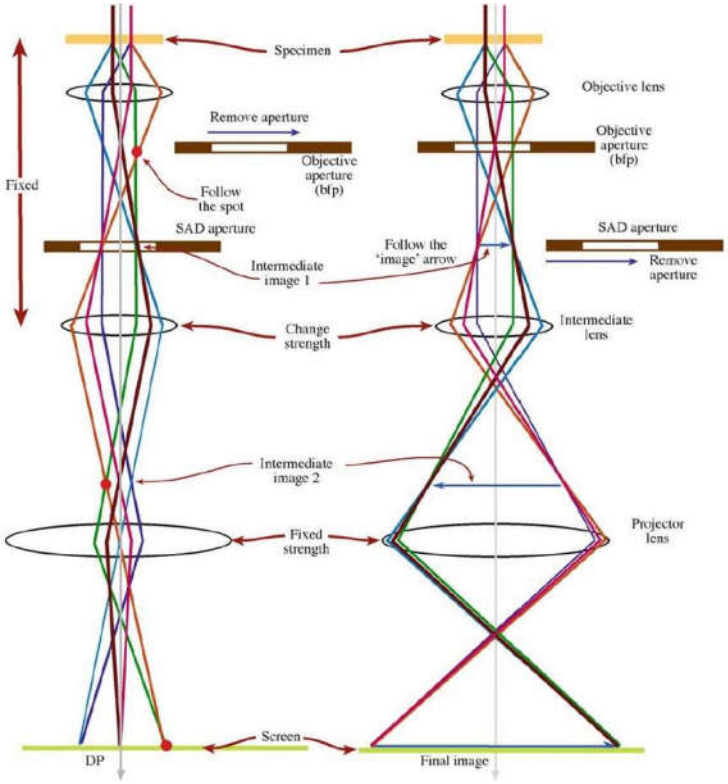

Figure 3.10 The transmission electron microscopy imaging system in two operation modes. (a) Diffraction mode: diffraction patterns (DP) are projected onto the screen. (b) Image mode: the image is projected onto the screen. Reproduced with permission.[21] Copyright 2009, Springer-Verlag US.

3.3.6 Electron Energy Loss Spectroscopy

Electron energy loss spectroscopy (EELS) is often used in the TEM to measure the energy loss of primary electrons due to the inelastic interactions with the specimen, such as inter-band transitions and inner-shell ionizations. To obtain the EELS signal, the transmitted electrons are collected by an electron spectrometer, which counts the number of electrons

at different electron energy. From the electron energy loss spectrum, various peaks can be observed, including the zero-loss peak, plasmon excitation peaks and the peaks due to inner-shell ionizations. The energy loss from the inner-shell ionizations can be used to determine the elemental components of the specimen, like the EDX.

3.3.7 X-Ray Photoelectron Spectroscopy

The X-ray photoelectron spectroscopy is a technology used to measure the electron binding energies of materials. The X-ray is a kind of electromagnetic wave with high photon energies. When a beam of X-rays is shining onto the sample, electrons in the sample can obtain energies by absorption of the X-ray photons. When the absorbed energy is high enough, electrons will overcome the binding from the sample atoms and molecules and escape from the surface of the sample, which are then collected by the detectors. The intensity of the emitted photoelectrons will reach a maximum when the energy of the X-ray is equal to the binding energy of the electrons. In this way, the binding energies of electrons in the material can be obtained from the positions of XPS peaks. Since the electron binding energy is different for different kinds of elements and different electronic states of the same element, the XPS can be used to measure the elemental composition of the sample as well as the electronic states of the elements.

3.3.8 Electronic Device Characterization

Most characterizations on the performances of electronic devices have been done by the source-measurement units with the devices mounted in a Microxact probe station or a Linkam temperature control stage. A source-measurement unit (SMU) can provide electric source (voltage or current) and make electric measurement (current or voltage) at the same time. There are four types of source-measurement options, which are forcing voltage and measuring current (2-probe or 4-probe) and forcing current and measuring voltage (2-probe or 4-probe). For the 2-probe measurement, only two electrodes are involved, which are the source and the drain. The current flows out of the Force High terminal, through the drain electrode into the device channel, and then through the source electrode back to the Force

Low terminal. The current is the actual value flowing through the device channel. While the voltage is the total voltage drop between the two force terminals, which is contributed by the drop in the device channel, electrode/channel contacts, electrodes, and the wires. So the calculated 2-probe resistance is the total resistance between the two force terminals. The 4-probe measurement involves four parallel electrodes across the channel. The current flows in and out of the channel via two outer electrodes. While the voltage is measured across two inner electrodes. Since ideally there is no current flow in the loop of voltage measurement, the measured voltage is indeed the voltage drop between the two inner electrodes without the influence from contacts and wires, from which the resistance of the channel between two inner electrodes can be precisely determined. The noise level of the measurement system is influenced by various factors such as the environmental electromagnetic noise, the temperature variation, and the measurement range and speed. Several methods can be used to lower the noise level, such as mounting the sample in an anti-vibration stage under vacuum, covering the device with metal shielding, and connecting the SMU and devices by coaxial cables. A coaxial cable usually contains an inner conductor, an insulating middle layer, and a conductive shield at the outside. Due to the insulating layer is not infinite insulating, there is current leakage from the inner conductor to the outside shield. To reduce this effect, a triaxial cable can be used, which has an additional conductive guard between the inner conductor and the shield. During the measurement, the guard is sourced with the same voltage as the inner conductor. Thus no current leakage between the inner conductor and the guard, leading to a lower noise level than the biaxial cables. In addition, the measurement range and speed can also influence the noise level. A small measurement range leads to a low noise level. A slow measurement speed and a long integration time lead to a low noise level.

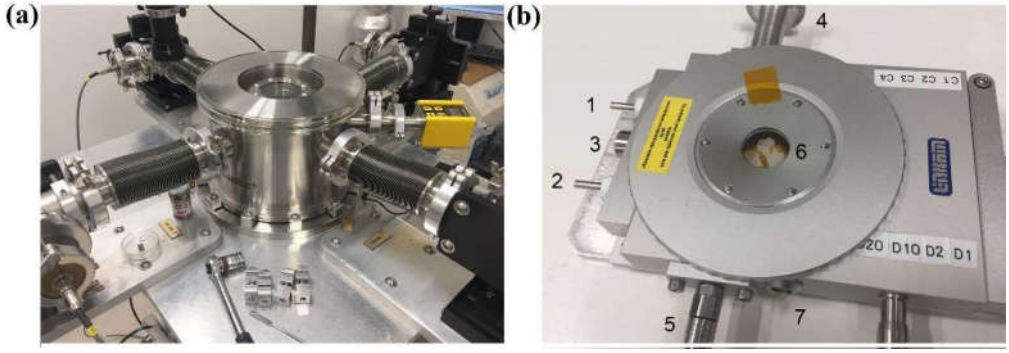

Figure 3.11 Sample stages for the device measurements. (a) A Microxact probe station with four probes and a helium pulse-tube refrigerator. (b) A Linkam temperature control stage working from -196 to 350 ℃, cooled by liquid nitrogen.

The Microxact probe station is equipped with a helium pulse-tube refrigerator. The pulse-tube refrigerator works by periodic compression and expansion of the helium inside the pulse tube. The pulse tube has two ends, which are the hot end and the cold end. The hot end is a closed end where the heat is dissipated to the environment. The cold end is an open end which connects to a helium regeneration tube whose warm end is connected to a compressor. At the beginning, the compressor compresses the helium in the pulse tube to the hot end. Due to the adiabatic compression of helium, its temperature will increase. Then the heat dissipation occurs at the heat end, leading to the decrease of the internal energy of the helium in the pulse tube. Then the compressor retracts, and the helium undergoes the adiabatic expansion with the temperature decreasing to a lower value than the initial. Then the heat exchange between the helium and the cold end leads to the temperature decrease of the cold end. In this way, after one compression expansion cycle, the heat at the cold end is transferred to the hot end, leading to the cooling of the cold end. The Linkam stage is cooled by the liquid nitrogen. As shown in Figure 3.11b, the inlet 1 is connected to a liquid nitrogen tank. Liquid nitrogen flows through sample stage with the help of a nitrogen pump connected to the outlet 2. The terminal 3 is connected to a temperature controller which controls the heating power and nitrogen pumping speed. The connector 4 and 5 are for vacuum pumping. The window 6 is for the light excitation of the sample. The terminal 7 is for the electrical measurement.

3.4 Simulation and Calculation

3.4.1 Simulation of Temperature Change by Joule Heating

According to the report by Bae et al., the temperature change of 2D devices induced by the Joule heating can be described by a 1D heat dissipation model with internal heat generation.[22] The heat equation can be written as:

$$A\frac{\partial}{\partial x}\left(k\frac{\partial T}{\partial x}\right)+P-g(\mathrm{T}-T_0)=0 \tag{3.1}$$

where $A=WH$ is the cross-section of the channel, k is the thermal conductivity of the 2D material, $P=I^2R_{ch}/L_{ch}$ is Joule heating rate per unit length, $g\approx 1/[(R_{SiO2}+R_{Si})L_{ch}]$ is the thermal conductance to the substrate per unit length, $R_{SiO2}=t_{SiO2}/(WL_{ch}k_{SiO2})$ is the thermal resistance of SiO_2 underneath the TaS_2 channel, $R_{Si}\approx 1/\left(2k_{Si}\sqrt{WL_{ch}}\right)$ is the thermal spreading resistance into the silicon wafer. For simplification, here the Joule heating rate is taken as a uniform value along the channel between the two electrodes. In the contact areas under the source and drain electrodes, due to the current crowding effect, the current density under the electrodes is not uniform. The current is most likely to flow into or out of an electrode near the side close to the conducting channel. As a result, the voltage in the sample beneath the contact electrode decreases near-exponentially, which can be described by:

$$V(x)=\frac{I}{W}\sqrt{\rho_c R_{sh}}\frac{cosh(x/L_T)}{sinh(L_c/L_T)} \tag{3.2}$$

where $\rho_c=R_cA_c$ is the contact resistivity (R_c is the contact resistance and A_c is the contact area), $R_{sh}=R_{ch}W/L_{ch}$ is the sheet resistance of the sample, L_c is the contact length, $L_T=\sqrt{\rho_c/R_{sh}}$ is the contact transfer length (over which distance the voltage drops to $1/e$) and $x<L_c$ is the location with respect to the outer side of the contact (Figure 3.12). The heat generation under the contact is defined by $P=I\,dV(x)/dx$. Since the metal electrode has a much higher thermal conductivity and diffusivity than the sample and the substrate, the sample temperature beneath the electrode is mainly determined by the heat dissipation to the electrode, which follows the Equation 3.1, where $P=I\,dV(x)/dx$, $g=Wk_{Cr}/t_{Cr}$, and T_0 is replaced by T_{Au}, which is the electrode temperature heated by the

Joule heating from the sample. On the other hand, the temperature of the electrode can be described by an equation like the Equation 3.1, where the Joule heating within the electrode is neglected due to its low resistance and the heat dissipation is the heat transferred from the beneath sample. By combining the heat equation of both the sample channel and the electrode, the temperature profile along the channel can be calculated using the finite element methods. The initial condition is the environment temperature. And the boundary conditions are: (1) the temperature gradient at the channel center is set to zero, and (2) the temperature of the sample and electrode far away from the conducting channel is set to the environment temperature.

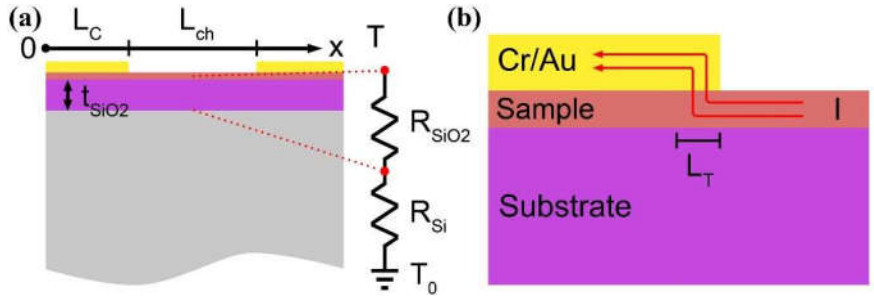

Figure 3.12 Model of Joule heating generation and dissipation in a 2D material. (a) Simplified model for heat dissipation into the substrate. The outer edge of the left contact electrode is set to $x = 0$. (b) Current crowding at the inner edge of the contact.

3.4.2 Calculation of Oscillation Frequency of a TaS_2 Oscillator

For the TaS_2 based oscillator shown in Figure 3.13b, the output oscillation frequency can be derived from the total charging and discharging time of the capacitor.[23] The output voltage is equal to the voltage across the capacitor as well as the TaS_2. For the charging process, the output voltage increases from V_L to V_H, with the TaS_2 resistance at R_i. This follows the equation by:

$$C\frac{dV_{OUT}}{dt} = \frac{V_{DC} - V_{OUT}}{R_s} - \frac{V_{OUT}}{R_i} \tag{3.3}$$

While for the discharging process, the output voltage decreases from V_H to V_L, with the TaS_2 resistance at R_m. This follows the equation by:

$$C\frac{dV_{OUT}}{dt} = \frac{V_{DC} - V_{OUT}}{R_s} - \frac{V_{OUT}}{R_m} \tag{3.4}$$

From Equation 3.3 and 3.4, the output voltage can be described by:

$$V_{OUT} = ae^{-t/(R_s||R_{i,m})C} + V_{DC}R_{i,m}/(R_{i,m} + R_s) \tag{3.5}$$

where a is a constant. Then the rising and falling time for the charging and discharging processes is given by:

$$t_{rise} = C(R_s||R_i)ln\left[\frac{V_{DC} - (1 + R_s/R_i)V_L}{V_{DC} - (1 + R_s/R_i)V_H}\right] \tag{3.6}$$

$$t_{fall} = C(R_s||R_m)ln\left[\frac{V_{DC} - (1 + R_s/R_m)V_H}{V_{DC} - (1 + R_s/R_m)V_L}\right] \tag{3.7}$$

Then the oscillation frequency can be obtained by:

$$f = 1/(t_{rise} + t_{fall}) \tag{3.8}$$

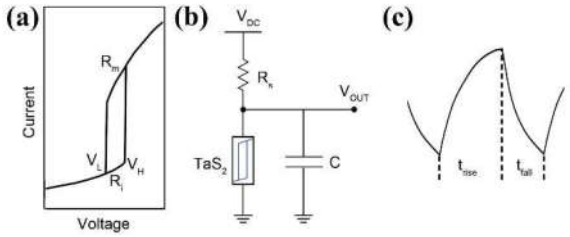

Figure 3.13 A TaS_2 oscillator with TaS_2 oscillates between two phases. (a) The typical current-voltage curve of the 1T-TaS_2. The hysteresis loop is between V_L and V_H. The resistance for the two phases is R_i and R_m, respectively. (b) Schematic diagram of the TaS_2 oscillator. The capacitor undergoes periodically charging and discharging. (c) Schematic curve of the output voltage oscillation.

3.4.3 Calculation of Mobility, Threshold Voltage and Carrier Density

The field-effect mobility μ can be obtained from measuring the I_{DS}-V_{GS} transfer characteristic of the FET, from which the transconductance can be calculated by $g_m = dI_{DS}/dV_{GS}$. Then the field-effect mobility can be determined by:

$$\mu = \frac{L}{C_{ox}V_{DS}W}\frac{dI_{DS}}{dV_{GS}} \tag{3.9}$$

where L is the channel length, W is the channel width, and C_{ox} is the thickness of the dielectric.

The threshold voltage V_{th} is the gate voltage at which the FET is turned on. The traditional method to extract the V_{th} is the linear extrapolation (LE) method. By the linear extrapolation of the linear region of the I_{DS}-V_{GS} curve, the V_{th} is obtained at the intercept of the extrapolation at the V_{GS} axis. The parasitic resistance and mobility degradation can seriously influence the extracted value of V_{th}. Other methods have been proposed to reduce the influence from these effects, such as the second derivative (SD) method, $I_{DS}/\sqrt{g_m}$ (CsrTR) method, and g_m/I_{DS} (TCR) method.[24] For the SD method, d^2I_{DS}/dV_{GS}^2 is plotted against V_{GS}, and the V_{th} equals to the V_{GS} where the d^2I_{DS}/dV_{GS}^2 reaches the maximum. For the CsrTR method, $I_{DS}/\sqrt{g_m}$ is plotted against V_{GS} and the V_{th} can be extracted from linear extrapolation. For the TCR method, the TCR g_m/I_{DS} versus V_{GS} is plotted and the V_{th} locates at the point where the TCR shows the maximum negative slope. The CsrTR method is weakly dependent on the parasitic resistance. While the SD and TCR methods are nearly independent of parasitic resistance. Besides, the TCR method has a smaller variation with the V_{DS}. Since the SD and TCR methods involve the high-order derivative of the transfer curve, a lower experimental noise is required and the smoothing of relative curves is needed.[24]

The carrier concentration can be measured by the Hall effect. On the other hand, it can be estimated from the FET characteristics. According to a previous report, a 12 nm thick WSe_2 has a capacitance of about 500 nF/cm^2, which increases linearly with decreasing thickness.[25] The capacitance of WSe_2 is much larger than that of a 285 nm SiO_2 (12 nF/cm^2). Thus the carrier concentration can be estimated by the equation as:

$$n = -\frac{C_{ox}(V_{GS} - V_{th})}{e} \tag{3.10}$$

where C_{ox} is the capacitance of the gate dielectric layer.[26] This estimation of carrier concentration is based on the assumption that the gate capacitance is constant for different V_{GS} and the carrier concentration below the V_{th} is zero.

3.4.4 Calculation of Schottky Barrier Height

The Schottky barrier height can be extracted from the activation energy E_A. For Schottky

transistors working in the subthreshold regime and $qV_{DS} \gg k_B T$, the source-drain current can be described by:

$$I_{DS} = AA^* T^{1.5} exp\left(-\frac{E_A}{k_B T}\right) \tag{3.11}$$

where A is the contact area, A^* is Richardson constant, T is the temperature and k_B is Boltzmann constant.[27] According to Equation 3.11, the activation energy can be obtained by:

$$E_A = -2.303 k_B \, d[\log(I_{DS}/T^{1.5})]/d(1/T) \tag{3.12}$$

which can be extracted from the measurement of the temperature-dependent source-drain current. For p-type transistors at $V_{GS} > V_{FB}$, the activation energy changes linearly with the V_{GS}, which is described by:

$$E_A = q\Phi_{B0} + (1 + C_{it}/C_{ox})^{-1}(V_{GS} - V_{FB}) \tag{3.13}$$

where C_{it} is the capacitance due to interface traps and the V_{FB} is the flat-band voltage. The Schottky barrier height $q\Phi_{B0}$ is equal to the activation energy at the point where the gate-dependent linearity stops.

3.4.5 Calculation of Inverter Gain

To calculate the gain of an inverter, the output transfer characteristic needs to be measured first. By changing the input voltage gradually from a low level to a high level, the output voltage of the inverter will change from a high level to a low level, as shown in Figure 2.20b. A sharp transition of the output voltage is preferred, which is evaluated by the gain. The gain of an inverter is defined by $A_v = dV_{OUT}/dV_{IN}$, which can be extracted from the first-order derivative of the output transfer curve.

3.4.6 Calculation of Photoresponsivity and Time Constant

For the photo response measurement of semiconducting devices, the source-drain current is measured when the light illumination is off and on, which is taken as I_d and I_{on}, respectively. The photocurrent is the difference between the on current and dark current, which can be obtained by $I_{ph} = I_{on} - I_d$. Then the photoresponsivity R can be calculated

by $R = I_{ph}/P$, where P is the incident light power.

When the light is turned on and off repeatedly, the source-drain current changes between the on and off states. And the switch of the current can be fitted exponentially by $I = a\left(1 - e^{-t/t_0}\right) + b$ for the switch-on process and $I = ae^{-t/t_0} + b$ for the switch-off process, where a and b are constant and t_0 is the time constant.

3.5 Overview of Methodologies

In this thesis, the light-tunable electronic devices based on 2D materials have been studied. First thin films were mechanical exfoliated from single crystals of 2D materials or dry-transferred onto substrates. Then electronic devices were fabricated by photolithography or EBL. And the light was used to tune the properties of these devices, including the TaS_2 based oscillator, WSe_2 based logic circuit, and the BP/$SrTiO_3$ based nonvolatile memory device. Besides, the AFM was used to determine the sample thickness. The SKPM was used to measure the device surface potential. The Raman spectroscopy was used to confirm the materials and to study the in-situ CDW phase transition of TaS_2. The ultraviolet-visible spectroscopy was used to determine the bandgap of $SrTiO_3$. The SEM was used to check the morphology of samples and devices. The TEM was used to characterize the BP atomic structure as well as the WSe_2. The EELS was used to study the laser induced change in WSe_2.

References

[1] B. Sipos, A. F. Kusmartseva, A. Akrap, H. Berger, L. Forro, and E. Tutis. *Nat. Mater.* **2008**, 7, 960-965.

[2] S. Hellmann, M. Beye, C. Sohrt, T. Rohwer, F. Sorgenfrei, H. Redlin, M. Kallane, M. Marczynski-Buhlow, F. Hennies, M. Bauer, A. Fohlisch, L. Kipp, W. Wurth, and K. Rossnagel. *Phys. Rev. Lett.* **2010**, 105, 187401.

[3] W. Zhao, Z. Ghorannevis, L. Chu, M. Toh, C. Kloc, P. H. Tan, and G. Eda. *ACS Nano* **2013**, 7, 791-797.

[4] K. K. Kam, and B. A. Parkinson. *J. Phys. Chem.* **1982**, 86, 463-467.

[5] S. Wang, W. Zhao, F. Giustiniano, and G. Eda. *Phys. Chem. Chem. Phys.* **2016**, 18, 4304-4309.

[6] M. Yamamoto, S. Nakaharai, K. Ueno, and K. Tsukagoshi. *Nano Lett.* **2016**, 16, 2720-2727.

[7] C. Zhou, Y. Zhao, S. Raju, Y. Wang, Z. Lin, M. Chan, and Y. Chai. *Adv. Funct. Mater.* **2016**, 26, 4223-4230.

[8] K. van Benthem, C. Elsässer, and R. H. French. *J. Appl. Phys.* **2001**, 90, 6156-6164.

[9] C. Mitra, C. Lin, J. Robertson, and A. A. Demkov. *Phys. Rev. B* **2012**, 86, 155105.

[10] G. Iannaccone, F. Bonaccorso, L. Colombo, and G. Fiori. *Nat. Nanotechnol.* **2018**, 13, 183-191.

[11] L. Li, Y. Yu, G. J. Ye, Q. Ge, X. Ou, H. Wu, D. Feng, X. H. Chen, and Y. Zhang. *Nat. Nanotechnol.* **2014**, 9, 372-377.

[12] L. Li, J. Kim, C. Jin, G. J. Ye, D. Y. Qiu, F. H. da Jornada, Z. Shi, L. Chen, Z. Zhang, F. Yang, K. Watanabe, T. Taniguchi, W. Ren, S. G. Louie, X. H. Chen, Y. Zhang, and F. Wang. *Nat. Nanotechnol.* **2017**, 12, 21-25.

[13] A. Castellanos-Gomez, M. Buscema, R. Molenaar, V. Singh, L. Janssen, H. S. J. van der Zant, and G. A. Steele. *2D Mater.* **2014**, 1, 011002.

[14] R. Frisenda, E. Navarro-Moratalla, P. Gant, D. Perez De Lara, P. Jarillo-Herrero, R. V. Gorbachev, and A. Castellanos-Gomez. *Chem. Soc. Rev.* **2018**, 47, 53-68.

[15] C. Shawn, Y. Makiuchi, and C. Che. **2010**, DOI: 10.5772/8179.

[16] H. Hölscher, in *Encyclopedia of Nanotechnology*, DOI: 10.1007/978-90-481-9751-4_33 (Ed: B. Bhushan), Springer Netherlands, **2012**, p. 99-99.

[17] J. L. Verble, and T. J. Wieting. *Phys. Rev. Lett.* **1970**, 25, 362-365.

[18] A. Berkdemir, H. R. Gutiérrez, A. R. Botello-Méndez, N. Perea-López, A. L. Elías, C.-I. Chia, B. Wang, V. H. Crespi, F. López-Urías, J.-C. Charlier, H. Terrones, and M. Terrones. *Sci. Rep.* **2013**, 3, 1755.

[19] L. Reimer, *Scanning electron microscopy: physics of image formation and microanalysis*, Springer, **2013**.

[20] R. Erni, M. D. Rossell, C. Kisielowski, and U. Dahmen. *Phys. Rev. Lett.* **2009**, 102, 096101.

[21] D. B. Williams, and C. B. Carter, in *Transmission electron microscopy*, Springer, **1996**, p. 3-17.

[22] M. H. Bae, Z. Y. Ong, D. Estrada, and E. Pop. *Nano Lett.* **2010**, 10, 4787-4793.

[23] G. Liu, B. Debnath, T. R. Pope, T. T. Salguero, R. K. Lake, and A. A. Balandin. *Nat. Nanotechnol.* **2016**, 11, 845-850.

[24] A. Ortiz-Conde, F. J. García-Sánchez, J. Muci, A. Terán Barrios, J. J. Liou, and C.-S. Ho. *Microelectron. Reliab.* **2013**, 53, 90-104.

[25] K. Kim, S. Larentis, B. Fallahazad, K. Lee, J. Xue, D. C. Dillen, C. M. Corbet, and E. Tutuc. *ACS Nano* **2015**, 9, 4527-4532.

[26] N. Ma, and D. Jena. *2D Mater.* **2015**, 2, 015003.

[27] A. Allain, J. Kang, K. Banerjee, and A. Kis. *Nat. Mater.* **2015**, 14, 1195-1205.

Chapter 4*

Light-Tunable Oscillators Based on Metallic 1T-TaS_2

In this chapter, the light control of the bias-induced CDW phase transition in the metallic 1T-TaS_2 at room temperature is presented, and a light-tunable CDW oscillators is demonstrated. Firstly, the in-situ Raman spectra was performed to provide the direct evidence of the bias-induced NCCDW-ICCDW phase transition. Then temperature-dependent bias-induced phase transition was measured, based on which the Joule heating effect was evaluated. Inspired by the Joule heating effect, the light heating was used to tune the bias-induced CDW phase transition. Based on this light-tuned CDW phase transition, a light-tunable CDW oscillator was demonstrated, where the oscillation frequency of the output voltage could be tuned continuously by the light intensity.

---

*This section has been published substantially as "**Chao Zhu**, Yu Chen, Fucai Liu, Shoujun Zheng, Xiaobao Li, Apoorva Chaturvedi, Jiadong Zhou, Qundong Fu, Yongmin He, Qingsheng Zeng, Hong Jin Fan, Hua Zhang, Wen-Jun Liu, Ting Yu, and Zheng Liu. Light-Tunable 1T-TaS_2 Charge-Density-Wave Oscillators. *ACS Nano*, **2018**, 12, 11203-11210."

4.1 Introduction

Periodic lattice distortion is often observed in low-dimensional metals such as TMDs[1-7] and cuprates.[8-10] At low temperature, interactions such as the electron-electron interaction[11] and electron-phonon interaction[12] become significant that a periodic lattice distortion is preferred in energy, leading to a periodic modulation of electron densities and the formation of the charge density wave (CDW). In recent years, 1T-TaS_2 has been one of the most extensively studied 2D CDW materials due to its enriched CDW phases.[13-24] Three major CDW phases exist in 1T-TaS_2, which are the commensurate CDW (CCDW) phase below 180 K, nearly commensurate CDW (NCCDW) phase from 180 K to 350 K, and the incommensurate CDW (ICCDW) phase above 350 K. In the low temperature CCDW 1T-TaS_2, a Mott insulating state also exists.[2] With these phases, 1T-TaS_2 becomes a good platform for control of phases. The CDW phase of 1T-TaS_2 can be influenced by various factors such as the gate voltage,[19] the source drain bias,[13-17] ultrafast current and photo excitation,[18,22] thickness,[17,19] temperature changing rate,[14] and the substrate.[24] For instance, the CCDW phase is absent in thin 1T-TaS_2 films below 10 nm.[19] And the ultrafast current and photoexcitation can induce the melting of the CCDW phase at low temperature.[18,22] For the source-drain bias induced CDW phase transition in 1T-TaS_2, although there are many studies,[13-17] the in-situ characterization of the bias-induced phase transition is insufficiently studied. For the underlying mechanism, most research attributed the phase transition to the bias-induced depinning of CDW single particles. The contribution from the Joule heating is insufficiently studied. Although there are studies to induce CDW phase transition at low temperature,[25] the use of light to control CDW phase at room temperature is insufficiently studied. In addition, novel devices can be designed utilizing the bias-induced CDW phase transition.[15,26,27] For example, a TaS_2-graphene based voltage-controlled oscillator (VCO) has been demonstrated,[15] based on which a neural network for pattern recognition has been proposed.[26] Achieving the light manipulation of such devices is fundamentally important for optoelectronic device applications.

In this work, the light-tunable bias-induced CDW phase transition was systematically studied in 1T-TaS_2. The in-situ Raman spectroscopy was performed to study the bias-induced CDW phase transition, providing a direct evidence of the bias-induced NCCDW-ICCDW phase transition. Temperature-dependent *I-V* measurement was performed to evaluate the role of Joule heating (JH) effect in the phase transition. Inspired by the effect of Joule heating, the light tunable bias-induced phase transition was demonstrated, which was then used to control the oscillation frequency of the CDW oscillator based on TaS_2. It was found that the oscillation frequency could be well tuned by the light power, where the frequency could be tuned up to 30%. Light tunability of the CDW oscillator provides more possibilities for the high-frequency and optoelectronic applications of CDW materials.

4.2 Experimental Methods

4.2.1 Crystal Synthesis and Device Fabrication

1T-TaS_2 single crystals were synthesized by the CVT method with quenching First, the sulphur pieces (99.9995%) and tantalum powder (99.97%) in a stoichiometric amount and a small amount (2 mg/cc) of iodine spheres were sealed in an evacuated ampoule with the pressure below 10^{-5} Torr, which was then placed into a two-zone furnace tube. The temperature profile was set at 950 to 900 ℃. After heating for 168 hours, the ampoule was taken out quickly and placed into the ice for quenching. The quenching was necessary to obtain the 1T-TaS_2 single crystals. Otherwise, the synthesized single crystals would be in the 2H phase without the quenching. From the synthesized 1T-TaS_2 single crystals, thin 1T-TaS_2 flakes were mechanically exfoliated onto the silicon substrate with a 285-nm SIO_2 layer. Then the electrodes (5/50 nm Cr/Au) were patterned by the standard EBL process and the thermal evaporation.

4.2.2 Raman Spectra Test

The in-situ Raman measurement was performed by a WITec Confocal Raman system with a Linkam temperature control stage. The device was placed on the stage in the vacuum and

the source-drain bias was applied by a Keithley 4200 semiconductor analyser. A laser beam was shined onto the device through a 50 × long working distance objective lens. The excitation wavelength was 532 nm and the laser power was set at 1 mW.

4.2.3 Temperature-Dependent *I-V* Characterization

The temperature-dependent *I-V* measurement was performed by placing the device in the Linkam temperature control stage under vacuum and applying the source-drain bias by a Keithley 2450 source-measurement unit.

4.2.4 Joule Heating Simulation

The simulation of Joule heating was performed using a simplified 1D model by the finite element method. The heat equation is given by:

$$A\frac{\partial}{\partial x}\left(k\frac{\partial T}{\partial x}\right) + P - g(\mathrm{T} - T_0) = 0 \tag{4.1}$$

where A is the channel cross section, k is the channel thermal conductivity, P is Joule heating rate in the channel, g is the thermal conductance to the heat sink, and T_0 is the environmental temperature. The details of the method are discussed previously in the Section 3.4.1.

4.2.5 Light-Tuned TaS_2 Oscillator Measurement

Samples were placed under vacuum with the pressure below 10^{-5} Torr inside a MicroXact probe station. The light-tunable bias-induced CDW phase transition was measured by an Agilent B1500A semiconductor analyser. For the oscillator measurement, a DC voltage was applied by a Keithley 2450 source-measurement unit to a constant resistor, which was then connected to the TaS_2 device. The other side of the TaS_2 device was connected to the ground. The excitation light wavelength is 635 nm. And the output voltage was measured by a Tektronix MDO3052 oscilloscope.

4.3 Principle Outcomes

4.3.1 Structure and Characterization of 1T-TaS_2

Figure 4.1a shows the side view of the crystal structure of 1T-TaS_2 with an interlayer distance of 5.85 Å. As shown in Figure 4.1b, according to Peierls' theory,[12,28] lattice distortions will arise due to the Peierls instability. Twelve adjacent Ta atoms will shift towards the central Ta atom. And an atom cluster called the David star will be formed. In the CCDW phase, all areas of the lattice are distorted, and the lattice is fully filled by David star formed CDW domains. In the NCCDW phase, the lattice is partially filled by CDW domains, between which are undistorted areas. In the ICCDW phase, there is no CDW domains. Figure 4.1c shows an optical image of exfoliated 1T-TaS_2 thin films. And the AFM image is shown in Figure 4.1d. Figure 4.1e is the height profile along the dash line in Figure 4.1c. Figure 4.1f shows a typical Raman spectrum of 1T-TaS_2 at room temperature, when the material is at the NCCDW phase. Figure 4.1g is a typical *I-V* curve of 1T-TaS_2 measured at room temperature, which shows sharp change in the conductivity at certain threshold bias. The bias-induced change in conductivity is attributed to the phase transition between NCCDW and ICCDW phases.[13-15,17] However, direct evidence of the phase transition from in-situ characterizations is insufficiently reported.

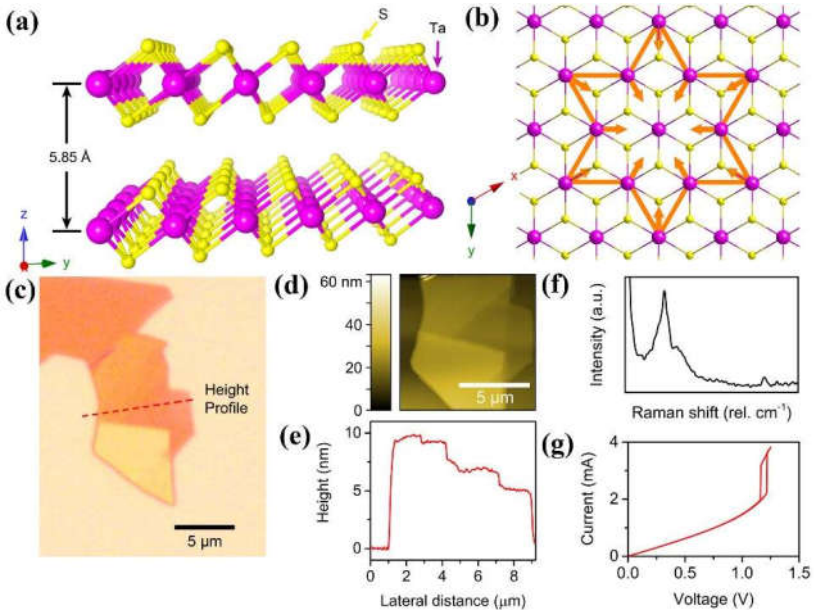

Figure 4.1 Structure and characterization of 1T-TaS_2. (a) Side view of 1T-TaS_2 crystal structure.

(b) Top view of 1T-TaS_2 crystal structure. The CDW-induced lattice distortion is featured by 12 adjacent Ta atoms shifting towards a central Ta atom, forming the so-called David star. (c) A typical optical image of exfoliated multilayer 1T-TaS_2. (d) An AFM image. (e) The height profile along the dash line in (c). (f) A Raman spectrum of 1T-TaS_2 at room temperature, with the sample at the NCCDW phase. (g) *I-V* curve of 1T-TaS_2 showing the bias-induced phase transition.

4.3.2 In-Situ Raman Test for Bias-Induced CDW Transition in 1T-TaS_2

4.3.2.1 Temperature-Dependent Raman Measurement

Before performing the in-situ Raman test of the bias-induced CDW transition of 1T-TaS_2, the temperature-dependent Raman measurement was first performed to obtain the Raman spectra of 1T-TaS_2 at different CDW phases. Figure 4.2 shows the Raman signals of a 1T-TaS_2 with a 9.4-nm thickness. The excitation wavelength is 532 nm. The laser intensity is 1 mW. The Raman signal collection time is 90 s, due to the relatively weak signals. The lattice distortion gives rise to the CDW peaks , such as A_{1g} (70 and 76 cm^{-1}) and E_g (60 and 93 cm^{-1}) peaks, which is consistent with previous reports.[20,21,29] The increase in temperature leads to the decrease in the CDW peak intensities, indicating the relaxation of the lattice distortions and the melting of the CDW domains. At the temperature above 350 K, an NCCDW-ICCDW phase transition occurs, leading to the vanishing of the CDW peaks. This temperature-dependent Raman spectrum confirms the CDW phase transition, providing the possibility for the in-situ monitor of the CDW phase transition.

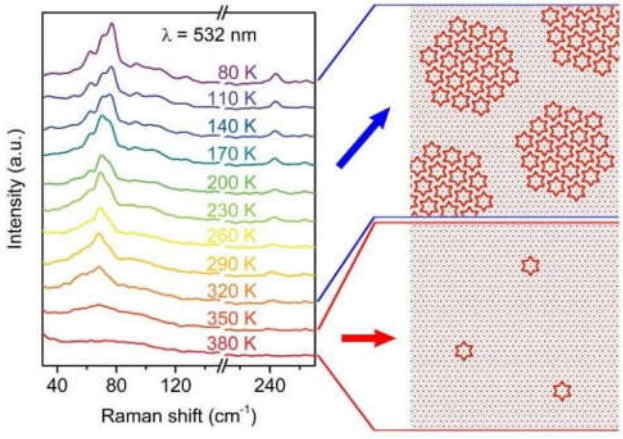

Figure 4.2 Temperature-dependent Raman spectra of 1T-TaS_2. Below 350 K, the sample is at

NCCDW phase, featured by the existence of discontinuous CDW domains and the Raman peaks arising from the collective CDW modes. Above 350 K, the sample is at ICCDW phase, featured by the melt of CDW domains and disappearance of the CDW Raman peaks.

4.3.2.2 In-Situ Raman Measurement

In-situ Raman measurement was performed to provide the direct evidence of the bias-induced CDW transition in 1T-TaS_2. As shown in Figure 4.2, Raman signals of 1T-TaS_2 are weak at high temperature, thus the in-situ measurement was performed at low temperatures (80 K and 220 K). As shown in Figure 4.3a, to determine the threshold voltage (upper threshold V_H and lower threshold V_L, marked by blue dots), the bidirectional *I-V* curve was first measured at 80 K, which showed that V_H = 2.43 V at the forward sweeping and V_L = 2.22 V at the backward sweeping. Then in-situ Raman measurement was performed. A source-drain bias was applied to the device while shining with a low power laser for Raman measurement. To simplify the case, the bias was set to certain key values in sequence, which are 0 , 2.00 and 2.25 V before the forward transition at V_H, 2.50 V after the forward transition at V_H, 2.25 V before the backward transition at V_L, and 2.00 V after the backward transition at V_L. In this way, the sample could go through the whole process, where it changed from the low conductive state to the high conductive state and then changed back to the low conductive state, which was confirmed by the in-situ measurement of the current. As shown in Figure 4.3b, 1T-TaS_2 is in the NCCDW phase at 0 V since the Raman spectrum is the same with the obtained NCCDW Raman spectrum from the temperature-dependent Raman test. As the bias increases to 2.25 V, though the peak intensity decrease, the CDW peaks still exist, showing that the device is still in the NCCDW phase. When the bias increases to 2.50 V, the CDW peaks disappear, indicating that the phase of the sample changes from NCCDW to ICCDW. When the voltage decreases back to 2.25 V, which is higher than the lower threshold, the CDW peaks are still not presented, indicating that the sample is still in the ICCDW phase. Then the bias drops back further to 2.00 V. The CDW peaks reappears, indicating that the sample changes from the ICCDW phase back to the NCCDW phase. The red dash line in Figure 4.3a shows the Raman signal intensity of the peak at 76 cm^{-1} (marked by the red arrow in Figure 4.3b),

which decreases along the NCCDW-ICCDW transition and increases along the ICCDW-NCCDW transition. At 2.00 V before and after the phase transitions, the Raman intensity changes little, meaning that the in-situ Raman test is non-destructive. In-situ Raman spectrum was also measured at 220 K, which showed the same behaviour (Figure 4.3c and 4.3d). At 220 K, V_H and V_L were 1.69 V and 1.60 V, respectively. And the voltage was set in sequence to 0 V, 1.51 V, 1.61 V, 1.71 V, 1.61 V and 1.51 V during the in-situ measurement. The bias-dependent intensity of A_{1g} peak at 70 cm^{-1} is shown in Figure 4.3c by the red dash line. This in-situ Raman measurement of 1T-TaS_2 provides the direct evidence of the bias-induced CDW phase transition in 1T-TaS_2.

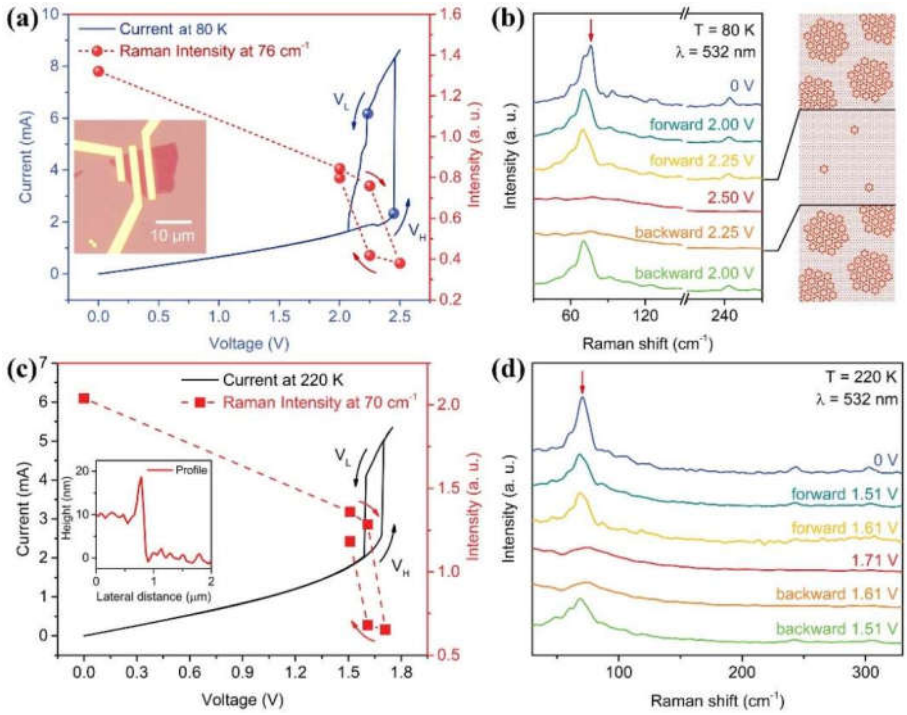

Figure 4.3 In-situ Raman measurement of the bias-induced CDW phase transition. (a) Solid line: The *I-V* curve of a 1T-TaS_2 device at 80 K, with the upper and lower threshold marked with blue dots. Dash line: In-situ Raman signal intensity at 76 cm^{-1} under different voltage bias. The excitation wavelength is 532 nm. Inset: an optical image of the 1T-TaS_2 device. (b) Left: In-situ Raman signals of 1T-TaS_2 at 80 K. The A_{1g} peak at 76 cm^{-1} at 0 V is marked by the red arrow. Right: CDW phase under different bias. (c) Solid line: The *I-V* curve of a 1T-TaS_2 device at 220 K. Dash line: In-situ Raman intensity at 70 cm^{-1}. Inset: A height profile of the TaS_2. (d) In-situ Raman signals of 1T-TaS_2 at 220 K. The A_{1g} peak at 70 cm^{-1} at 0 V is marked by the red arrow.

4.3.3 Joule Heating Effect in the Bias-Induced CDW Phase Transition

4.3.3.1 Temperature-Dependent CDW Phase Transition

The local temperature change of the sample due to the current-induced Joule heating effect may play a role in the bias-induced CDW phase transition. It has been mentioned that the bias-induced CDW transition is attributed to both the CDW single particle depinning by the electric field and the Joule heating by the current.[12,14,16] The importance of the Joule heating effect is still not clearly evaluated. Here, the Joule heating effect was studied quantitatively. An *I-V* test was performed to characterize the bias-induced CDW transition at different temperatures (Figure 4.4a). With temperature increasing from 200 K to 330 K, V_H decreases from 0.89 V to 0.40 V, and V_L decreases from 0.82 V to 0.40 V. According to the *I-V* data at V_H and V_L, the corresponding Joule heating (JH) rate is calculated, showing a linear decrease with increasing temperature (Figure 4.4b).

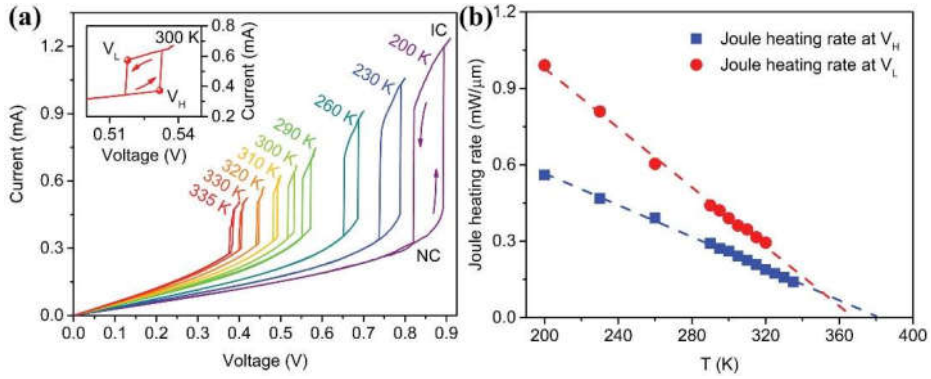

Figure 4.4 Temperature-dependent *I-V* characteristic of 1T-TaS_2. (a) *I-V* curve at different temperatures. Inset: *I-V* curve at 300 K, with the upper and lower threshold (V_H and V_L) shown by red dots. (b) Joule heating rate at the upper and lower threshold under different environment temperatures.

4.3.3.2 Evaluation of Joule Heating Effect

To evaluate the Joule heating induced heat generation and dissipation in 1T-TaS_2 devices on the silicon substrate, a simplified 1D model is used.[30,31] For simplification, the Joule heating is assumed to be uniform within the channel and the thermal conductivity is

assumed to be a temperature-independent constant. As discussed in the previous chapter, in the TaS_2 channel, the temperature along the channel is described by the heat equation as:

$$A\frac{\partial}{\partial x}\left(k\frac{\partial T_{JH}}{\partial x}\right)+P-g\left(T_{JH}-T\right)=0 \tag{4.2}$$

where the cross section $A = WH = 1.2\ \mu m \times 11.8\ nm$ and the thermal conductivity k of TaS_2 is 5 $Wm^{-1}K^{-1}$ for NCCDW phase and 8 $Wm^{-1}K^{-1}$ for ICCDW phase.[32] The Joule heating rate per unit length is calculated by $P = I^2R_{ch}/L_{ch}$. According to a previous work,[17] the contact resistance is estimated to be 8% of the total resistance ($R_{ch} = 0.92 \times R_{tot} = 0.92\,V/I$).In the channel where the heat dissipates into the beneath substrate, the thermal conductance is estimated by $g \approx 1/[(R_{SiO2}+R_{Si})L_{ch}] \approx 5.8\ Wm^{-1}K^{-1}$,[30] where the thermal resistance of the 285-nm SiO_2 layer is $R_{SiO2} = t_{SiO2}/(WL_{ch}k_{SiO2}) \approx 2.4\times10^5$ K/W and the thermal spreading resistance into the p-doped Si is estimated by $R_{Si} \approx 1/\left(2k_{Si}\sqrt{WL_{ch}}\right) \approx 3.9\times10^3$ K/W. Basic parameters for the simulation are shown in Table 4.1.

At the contact area under the electrode, due to the existence of current crowding,[31,33] most current flows into or out of the electrode at the inner edge of the contact (Figure 4.5a), leading to the voltage in TaS_2 dropping near-exponentially along the contact. The voltage profile under the electrode is defined by:

$$V(x)=\frac{I}{W}\sqrt{\rho_c R_{sh}}\frac{cosh(x/L_T)}{sinh(L_c/L_T)} \tag{4.3}$$

where $\rho_c = R_cL_cW$ is the contact resistivity, $R_{sh} = R_{ch}W/L_{ch}$ is the sheet resistance, x is the location defined in Figure 4.5a, $L_T = \sqrt{\rho_c/R_{sh}}$ is the contact transfer length, and L_c is the contact length. Here, $R_c = 0.08 \times R_{tot}/2 = 0.04R_{tot}$. The heat generation rate in TaS_2 beneath the contact is then defined by $P = I\,dV(x)/dx$. Since the gold electrode has a much higher thermal conductivity and diffusivity than the underlying TaS_2 and SiO_2,[8] the temperature of TaS_2 beneath the electrode is dominant by the heat dissipation in the electrode, which is described by $g_c\left(T_{JH}-T_{Au}\right)$. The thermal conductance from TaS_2 to the gold is estimated by $g_c = Wk_{Cr}/t_{Cr} \approx 1800\ Wm^{-1}K^{-1}$, where t_{Cr} is the thickness of Cr layer between TaS_2 and gold, and k_{Cr} is the thermal conductivity of the evaporated Cr layer. T_{Au} is the gold temperature. According to the Wiedemann-Franz Law, $k_{Cr} = L_{Cr}T/\rho_{Cr} \approx$

7.5 $Wm^{-1}K^{-1}$.[34-36] On the other hand, the heat dissipation inside the gold electrode can be described by an equation similar to the Equation 4.2, where $k_{Au} \approx 127$ $Wm^{-1}K^{-1}$ for 50-nm-thick gold[37] and $A = Wt_{Au}$. The Joule heating within the electrode is neglected. And the heat dissipation from the underlying TaS_2 is considered.

By combining the heat dissipation in the TaS_2 and the electrode, the temperature profile along the TaS_2 can be calculated. As shown in Figure 4.5b, the red curve shows the case when both the Joule heating (JH) in the channel and the heating from current crowding (CC) under the contact are considered. The contact region is also heated up. If the heating from the current crowding under the contact is ignored, the temperature in the contact region will be much lower. But the temperature changes little for about 2 K at the channel center (the green curve). If the temperature change under the contact is ignored and the temperature of the channel edge is set to the environment temperature, the temperature at the channel center does not show much difference (the blue curve). This is consistent with the previous report.[31] Figure 4.5c shows the temperature at the channel center under different voltages in the TaS_2 at the NCCDW phase. Figure 4.5d shows the Joule heating induced temperature change ($T_{JH} - T$) at the upper and lower threshold, which decreases linearly with increasing temperature.

Two conclusions can be inferred from the temperature simulation. First, for the bias-induced transition from NCCDW to ICCDW, the Joule heating is not the dominant factor. As shown in Figure 4.5c, for the NCCDW-ICCDW transition at the upper threshold V_H, as the environment temperature varies from 200 to 330 K, Joule heating induced local temperature of the sample varies from 290 to 355 K, most of which is below the transition temperature (about 350 K).[19] For the lower environment temperature, the difference between the local sample temperature and the transition temperature is larger and meanwhile the upper threshold bias is larger. This means that for the bias-induced transition from NCCDW to ICCDW, the field-induced depinning dominates the transition while the Joule heating has a secondary role. This is consistent with the fact that the sample resistance at V_H is different for different environment temperatures.[17] Second, for the bias-induced transition from ICCDW to NCCDW, the Joule heating is the dominant factor.

For the ICCDW-NCCDW transition at the lower threshold V_L, as the environment temperature varies from 200 K to 320 K, Joule heating induced local temperature varies from 350 K to 365 K, which is close to the reported transition temperature[19] and varies little with the environment temperature. Decrease in bias and current results in the decrease in the Joule heating. When the bias decreases further below V_L, the decrease in the Joule heating leads to the decrease of local sample temperature below the transition temperature, giving rise to the ICCDW-NCCDW transition. This is consistent with the fact that at different environment temperatures, the sample resistance is almost the same at V_L.[17] Moreover, by the linear extrapolation of the $T_{JH} - T$ versus T data to the temperature axis, the intercept points are 382 K and 368 K for the upper and lower threshold, respectively. This is consistent with the fact that $T_{NC-IC} > T_{IC-NC}$.[19] The two extracted temperatures are a little bit higher than the reported phase transition temperatures, which might be due to the estimation of thermal conductivity,[32] contact resistance and thermal resistance to the substrate and the electrode.

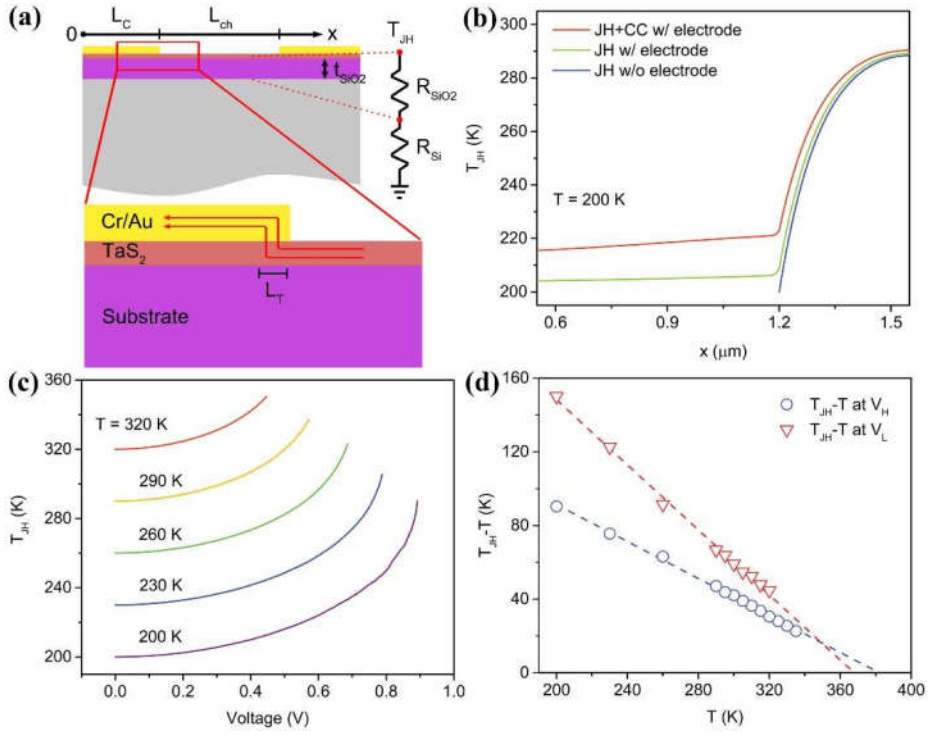

Figure 4.5 Simulation of the Joule-heating-induced temperature change of 1T-TaS_2. (a) Top: Model of Joule heating generation and dissipation. The outer edge of the left electrode is located at $x = 0$ and the channel center is located at $x = 1.55$ μm. Bottom: Current crowding at the contact

edge. (b) The temperature profile along the contact and channel when $V = V_H = 0.892$ V and $I = 0.4777$ mA at environment temperature $T = 200$ K. Three situations are considered: Joule heating (JH) without electrode contact, Joule heating with electrode and Joule heating with electrode considering the current crowding (JH+CC). (c) The temperature at the channel center under different voltages at different environment temperatures. The voltage is extracted from Figure 4.4a. Only the NCCDW part is shown. (d) Joule heating rate and temperature change at the channel center under different environment temperatures. Only data for the upper and lower threshold are shown.

Table 4.1 Parameters for the simulation of the temperature change induced by Joule heating. Thermal conductivity values are referred to Refs [32,34-39].

Parameter	Value	Parameter	Value
W	1.2 μm	t_{SiO2}	285 nm
H	11.8 nm	k_{SiO2}	1.4 $Wm^{-1}K^{-1}$
L_{ch}	0.7 μm	k_{Si}	140 $Wm^{-1}K^{-1}$
$k_{TaS2,NC}$	5 $Wm^{-1}K^{-1}$	k_{Cr}	7.5 $Wm^{-1}K^{-1}$
$k_{TaS2,IC}$	8 $Wm^{-1}K^{-1}$	k_{Au}	127 $Wm^{-1}K^{-1}$

4.3.4 Light-Tunable CDW Oscillators

4.3.4.1 Light-Tuned CDW Phase Transition

Inspired by the Joule heating effect, laser heating effect can provide another option for tuning the bias-induced CDW phase transition. As shown in Figure 4.6a, with the illumination by a 635-nm laser, the hysteresis *I-V* curve can shift to the left. A higher laser intensity induces a larger *I-V* curve shift. The *I-V* curves in the dark repeats well before and after laser shining, meaning that no obvious degradation occurs. The time-dependent current changing was studied, to understand the mechanism of light-tuned phase transition. A fixed source-drain bias at 0.51 V was applied on the sample. By turning the laser on and off, the current changing was recorded. As shown in Figure 4.6b, the laser is turned on at 10 s and turned off at 130 s. Overall, the current increases slowly upon turning on the laser illumination and decreases slowly upon turning off the laser. For the laser intensity at 40,

80 and 120 mW/cm^2, the absence of sharp change in current means the absence of the phase transition. For the intensity at 160 mW/cm^2, the sharp current change happens at about 90 s, indicating an NCCDW-ICCDW phase transition. This also supports the previous conclusion that the Joule heating plays an important role in the bias-induced CDW phase transition. When the laser is off, the current decreases slowly with several steps of abrupt current drop before it finally falls back to the initial value at 250 s. This is consistent with the fact that there are multiple stages for the transition from ICCDW to NCCDW (Figure 4.6a).

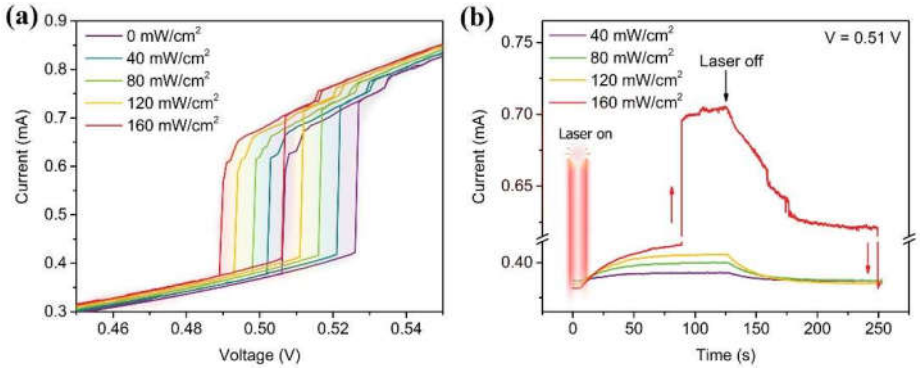

Figure 4.6 Light-tuned bias-induced CDW phase transition in 1T-TaS_2 sample at room temperature. (a) Shift of the *I-V* curve of TaS_2 under a 635-nm laser illumination. (b) Change of current when the laser is turned on or off. The bias is fixed at 0.51 V.

The current evolution with time can be well fitted exponentially (Figure 4.7a and 4.7b). The rising process can be fitted by $I = a\left(1 - e^{-t/t_0}\right) + b$ and the decay process can be fitted by $I = ae^{-t/t_0} + b$, where a and b are constant and t_0 is the time constant. For the decay process of 160 mW/cm^2, the curve is fitted with an offset for each of the three parts. The time constant for both the rising and decay processes is shown in Figure 4.7c. The light-tunable bias-induced CDW phase transition is attributed to the thermal effect due to the large time constant. The Joule heating rate at the upper and lower threshold is shown in Figure 4.7d, which shows a linear dependence on the laser intensity. When the laser intensity increases from 0 mW/cm^2 to 160 mW/cm^2, the Joule heating rate at V_H decreases for about 0.019 mW/μm. A comparison with Figure 4.4b shows that the change induced by laser heating is close to the effect from 6 K change in the environment temperature.

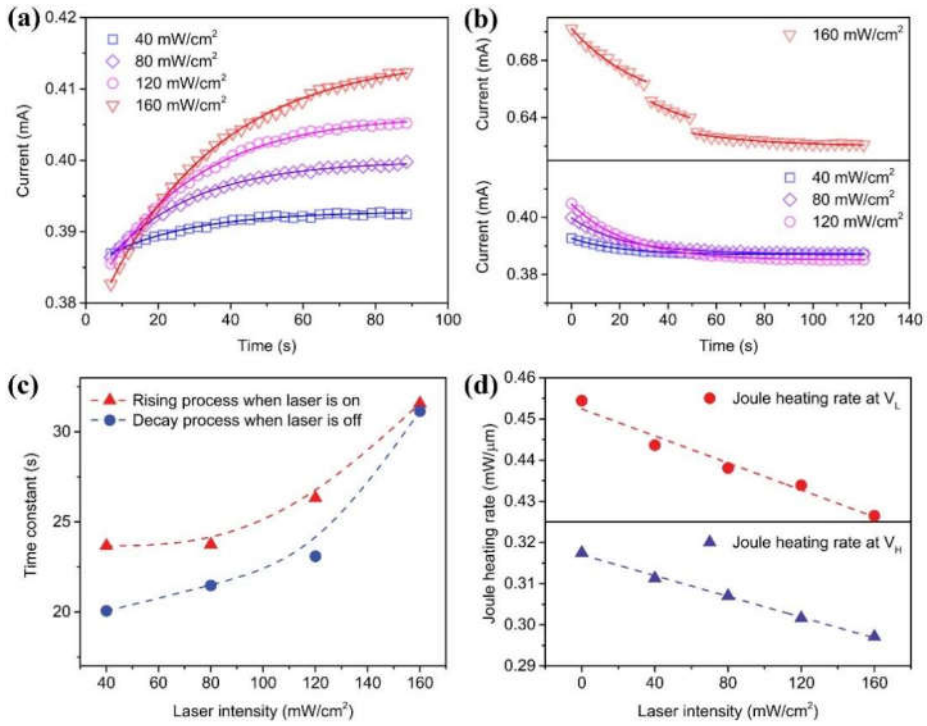

Figure 4.7 Time constant of the current change. (a) Fitting of the current rising process for different laser intensity. (b) Fitting of the current decay process for different laser intensity. (c) Fitted time constant for different laser intensity. (d) Joule heating rate at the upper and lower threshold voltage for different laser intensity, extracted from Figure 4.6a.

4.3.4.2 CDW Oscillator Based on 1T-TaS_2

Based on the bias-induced CDW phase transition, a TaS_2 oscillator can be constructed. As shown in Figure 4.8a, a constant resistor is connected on one side to the 1T-TaS_2 with the input voltage V_{DC} applied on the other side of the resistor and the ground connected to the other side of 1T-TaS_2. The output signal is the voltage across the 1T-TaS_2. Figure 4.8b demonstrates the oscillation mechanism. Supposing that the 1T-TaS_2 is at the large resistive NCCDW phase at the beginning, by increasing the input voltage gradually, the voltage loaded on the 1T-TaS_2 will increase accordingly. At the point when the voltage bias on TaS_2 reaches the upper threshold, the TaS_2 will change from the NCCDW to the ICCDW phase. Since ICCDW phase is a low resistive phase and the connected resistor is constant, the voltage loaded on the TaS_2 will decrease subsequently. Once the loaded voltage

decreases below the lower threshold, the TaS_2 will change from the ICCDW to the NCCDW phase. And the increased resistance of TaS_2 will lead to the increase of load voltage above the upper threshold, causing the NCCDW to ICCDW phase transition again. In this way, the TaS_2 will continuously change between the two phases, leading to the oscillation of the voltage loaded on it. This enables the TaS_2 based CDW oscillators. As shown in Figure 4.8c, there is a range of the input voltage V_{DC} for the output voltage oscillation. With increasing input voltage, the frequency of the output signal (V_{OUT}) increases first and then decreases, which reaches a maximum at about V_{DC} = 3.82 V. As shown in Figure 4.8b, the load line for 3.82 V locates at the center of the hysteresis *I-V* loop. With increasing V_{DC}, the load line will shift upward such that the TaS_2 will tend to stay longer time in the ICCDW phase. According to Figure 4.6b, current evolution within the ICCDW or NCCDW phase is much slower than the current change at transition points. As a result, it will take a longer time for the TaS_2 to reach the transition points, leading to a lower frequency. The output voltage frequency is determined by the charging and discharging time of the capacitor between the output and the ground, which is related to various factors such as the threshold voltage and channel resistance.[15]

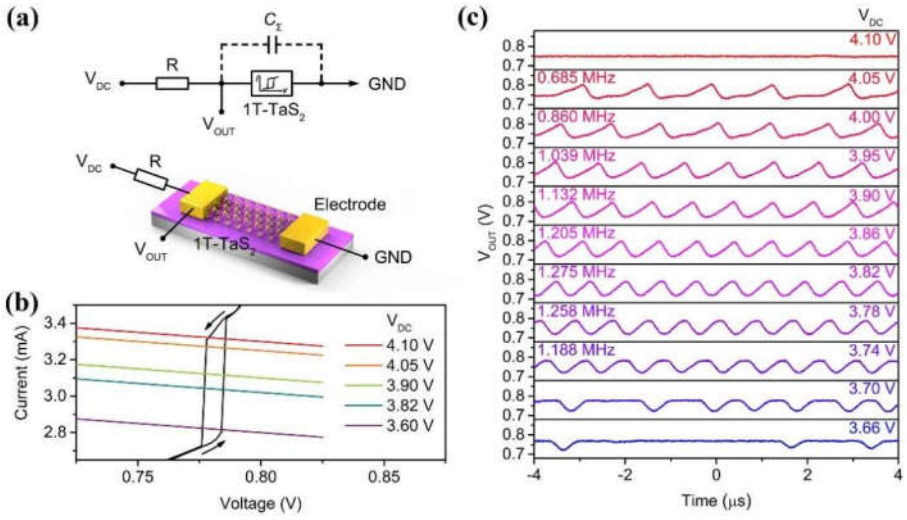

Figure 4.8 CDW oscillator based on 1T-TaS_2. (a) Schematic diagrams of the 1T-TaS_2 oscillator circuit. (b) *I-V* curve of 1T-TaS_2 at dark and the load lines of 1T-TaS_2 at different V_{DC}. (c) Oscillation curves of the output voltage at different V_{DC}.

4.3.4.3 Light-Tuned CDW Oscillators

The light tunability of the bias-induced CDW phase transition provides the possibility to tune the oscillator frequency by light. Based on this, a light-tunable CDW oscillator is demonstrated. In this case, the input voltage is set to a fixed value and the light is shined onto the device. As shown in Figure 4.9c and 4.9d, with the light intensity increasing, the output frequency could be tuned up to about 30% with the maintaining of the high-quality periodicity. On the other hand, as the laser intensity increases, the oscillation waveforms becomes asymmetric, which may be attributed to the asymmetric status of TaS_2 set by V_{DC}. As shown in Figure 4.9b, the load line is not located exactly at the middle of the hysteresis *I-V* loop, which will shift upward as the light intensity increases. Therefore, TaS_2 will stay at the ICCDW phase for a longer time, leading to a longer time for the ICCDW-NCCDW transition. The load line for V_{DC} = 3.90 V locates higher than the load line for 3.82 V. As a result, the asymmetry of the oscillation for 3.90 V is severe than that for 3.82 V.

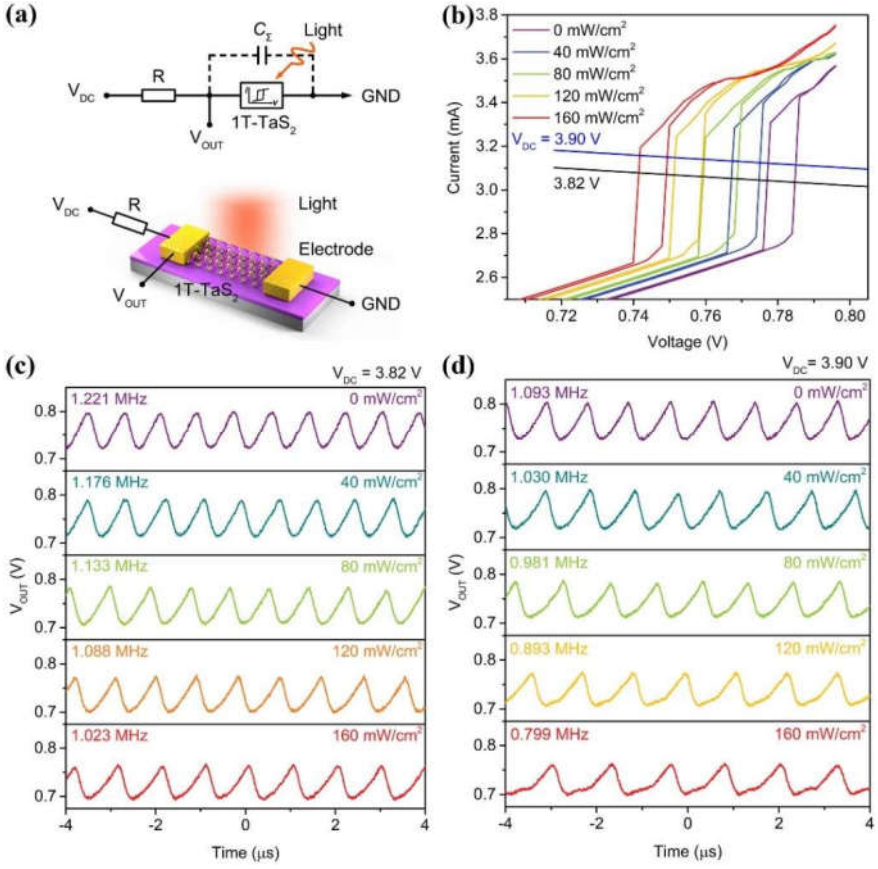

Figure 4.9 Light-tunable TaS_2 oscillator. (a) Schematic diagrams of the light-tunable TaS_2

oscillator circuit. (b) *I-V* curves of 1T-TaS_2 under different laser intensity and the load lines of 1T-TaS_2 at V_{DC} = 3.90 and 3.82 V, respectively. (c) Light-intensity-dependent oscillation of the output voltage at V_{DC} = 3.82 V. (d) Light-intensity-dependent oscillation of the output voltage at V_{DC} = 3.90 V.

Figure 4.10 shows the oscillation frequency at different input voltage and light intensity. On the other hand, as previously mentioned in the Section 3.4.2, the oscillation frequency can be estimated using the *I-V* characteristics,[15] which is depicted with dash lines in Figure 4.10b. Is shows that with the light illumination, the output oscillation frequency can be tuned up to 30%. The tunability should be larger in a device with a narrower and higher hysteresis transition loop, which could be achieved by optimizing the channel size and sample thickness.[17,40] Light-tunable CDW phase transitions provide more options for the applications of CDW materials. And the tunable oscillation frequency and waveform may be useful for high-frequency applications, such as the neural spiking generation[41,42] and pattern recognition[26,43] and fast neural spiking generation. In addition, other local heating techniques[30,44] can also be used to tune the CDW based oscillators.

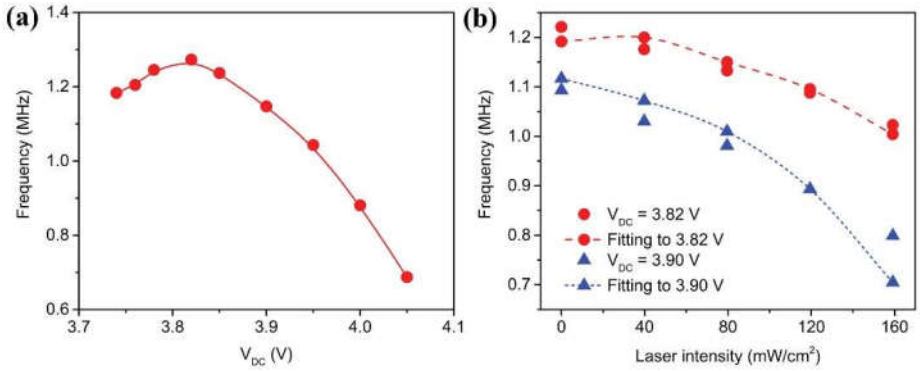

Figure 4.10 Output oscillation frequency of the TaS_2 oscillator. (a) Oscillation frequency under different V_{DC} in the dark. (b) Oscillation frequency under different laser intensity.

4.4 Conclusions

In this chapter, the non-destructive in-situ Raman measurement is demonstrated, which provides the direct evidence of the bias-induced CDW phase transition in 1T-TaS_2.

Temperature-depend *I-V* measurement is demonstrated and the effect of Joule heating on the bias-induced CDW transition is studied, which shows that Joule heating plays a secondary role in the NCCDW-ICCDW transition while the ICCDW-NCCDW transition is mainly determined by the change in the sample local temperature due to Joule heating. Furthermore, the light tunability of the bias-induced CDW transition is demonstrated, based on which a light-tunable TaS_2 oscillator is constructed. With the laser illumination, the output frequency of the oscillator can be tuned by 30%. And the output waveform can be tuned as well. The results will be of much help for understanding the mechanism of the bias-induced CDW phase transition and will provide more options for the device applications of CDW materials.

References

[1] T. L. Adelman, S. V. Zaitsev-Zotov, and R. E. Thorne. *Phys. Rev. Lett.* **1995**, 74, 5264-5267.

[2] B. Sipos, A. F. Kusmartseva, A. Akrap, H. Berger, L. Forro, and E. Tutis. *Nat. Mater.* **2008**, 7, 960-965.

[3] J. H. Miller, Jr., A. I. Wijesinghe, Z. Tang, and A. M. Guloy. *Phys. Rev. Lett.* **2012**, 108, 036404.

[4] R. Samnakay, D. Wickramaratne, T. R. Pope, R. K. Lake, T. T. Salguero, and A. A. Balandin. *Nano Lett.* **2015**, 15, 2965-2973.

[5] L. J. Li, E. C. O'Farrell, K. P. Loh, G. Eda, B. Ozyilmaz, and A. H. Castro Neto. *Nature* **2016**, 529, 185-189.

[6] J. A. Wilson, F. J. Di Salvo, and S. Mahajan. *Phys. Rev. Lett.* **1974**, 32, 882-885.

[7] D. E. Moncton, J. D. Axe, and F. J. DiSalvo. *Phys. Rev. B* **1977**, 16, 801-819.

[8] A. J. Achkar, F. He, R. Sutarto, C. McMahon, M. Zwiebler, M. Hucker, G. D. Gu, R. Liang, D. A. Bonn, W. N. Hardy, J. Geck, and D. G. Hawthorn. *Nat. Mater.* **2016**, 15, 616-620.

[9] J. Chang, E. Blackburn, O. Ivashko, A. T. Holmes, N. B. Christensen, M. Hucker, R. Liang, D. A. Bonn, W. N. Hardy, U. Rutt, M. V. Zimmermann, E. M. Forgan, and S. M. Hayden. *Nat. Commun.* **2016**, 7, 11494.

[10] A. Frano, S. Blanco-Canosa, E. Schierle, Y. Lu, M. Wu, M. Bluschke, M. Minola, G. Christiani, H. U. Habermeier, G. Logvenov, Y. Wang, P. A. van Aken, E. Benckiser, E. Weschke, M. Le Tacon, and B. Keimer. *Nat. Mater.* **2016**, 15, 831-834.

[11] B. I. Halperin, and T. M. Rice. *Rev. Mod. Phys.* **1968**, 40, 755-766.

[12] G. Grüner. *Rev. Mod. Phys.* **1988**, 60, 1129-1181.

[13] A. W. Tsen, R. Hovden, D. Wang, Y. D. Kim, J. Okamoto, K. A. Spoth, Y. Liu, W. Lu, Y. Sun, J. C. Hone, L. F. Kourkoutis, P. Kim, and A. N. Pasupathy. *Proc. Natl. Acad. Sci. U.S.A.* **2015**, 112, 15054-15059.

[14] M. Yoshida, R. Suzuki, Y. Zhang, M. Nakano, and Y. Iwasa. *Sci. Adv.* **2015**, 1, e1500606.

[15] G. Liu, B. Debnath, T. R. Pope, T. T. Salguero, R. K. Lake, and A. A. Balandin. *Nat. Nanotechnol.* **2016**, 11, 845-850.

[16] M. Yoshida, T. Gokuden, R. Suzuki, M. Nakano, and Y. Iwasa. *Phys. Rev. B* **2017**, 95, 121405.

[17] S. Zheng, F. Liu, C. Zhu, Z. Liu, and H. J. Fan. *Nanoscale* **2017**, 9, 2436-2441.

[18] I. Vaskivskyi, J. Gospodaric, S. Brazovskii, D. Svetin, P. Sutar, E. Goreshnik, I. A. Mihailovic, T. Mertelj, and D. Mihailovic. *Sci. Adv.* **2015**, 1, e1500168.

[19] Y. Yu, F. Yang, X. F. Lu, Y. J. Yan, Y. H. Cho, L. Ma, X. Niu, S. Kim, Y. W. Son, D. Feng, S. Li, S. W. Cheong, X. H. Chen, and Y. Zhang. *Nat. Nanotechnol.* **2015**, 10, 270-276.

[20] O. R. Albertini, R. Zhao, R. L. McCann, S. Feng, M. Terrones, J. K. Freericks, J. A. Robinson, and A. Y. Liu. *Phys. Rev. B* **2016**, 93, 214109.

[21] W. Fu, Y. Chen, J. Lin, X. Wang, Q. Zeng, J. Zhou, L. Zheng, H. Wang, Y. He, H. He, Q. Fu, K. Suenaga, T. Yu, and Z. Liu. *Chem. Mater.* **2016**, 28, 7613-7618.

[22] I. Vaskivskyi, I. A. Mihailovic, S. Brazovskii, J. Gospodaric, T. Mertelj, D. Svetin, P. Sutar, and D. Mihailovic. *Nat. Commun.* **2016**, 7, 11442.

[23] G. Liu, S. Rumyantsev, M. A. Bloodgood, T. T. Salguero, and A. A. Balandin. *Nano Lett.* **2018**, 18, 3630-3636.

[24] R. Zhao, Y. Wang, D. Deng, X. Luo, W. J. Lu, Y. P. Sun, Z. K. Liu, L. Q. Chen, and J. Robinson. *Nano Lett.* **2017**, 17, 3471-3477.

[25] A. Zong, X. Shen, A. Kogar, L. Ye, C. Marks, D. Chowdhury, T. Rohwer, B. Freelon, S. Weathersby, R. Li, J. Yang, J. Checkelsky, X. Wang, and N. Gedik. *Sci. Adv.* **2018**, 4, eaau5501.

[26] A. Khitun, G. Liu, and A. A. Balandin. *IEEE Trans. Nanotechnol.* **2017**, 16, 860-867.

[27] G. Liu, E. X. Zhang, C. D. Liang, M. A. Bloodgood, T. T. Salguero, D. M. Fleetwood, and A. A. Balandin. *IEEE Electron Device Lett.* **2017**, 38, 1724-1727.

[28] R. E. Peierls, *Quantum theory of solids*, Oxford University Press, **1955**.

[29] R. He, J. Okamoto, Z. Ye, G. Ye, H. Anderson, X. Dai, X. Wu, J. Hu, Y. Liu, W. Lu, Y. Sun, A. N. Pasupathy, and A. W. Tsen. *Phys. Rev. B* **2016**, 94, 201108.

[30] M. H. Bae, Z. Y. Ong, D. Estrada, and E. Pop. *Nano Lett.* **2010**, 10, 4787-4793.

[31] K. L. Grosse, M. H. Bae, F. Lian, E. Pop, and W. P. King. *Nat. Nanotechnol.* **2011**, 6, 287-290.

[32] M. D. Nuez-Regueiro, J. M. Lopez-Castillo, and C. Ayache. *Phys. Rev. Lett.* **1985**, 55, 1931-1934.

[33] D. K. Schroder, *Semiconductor material and device characterization*, John Wiley & Sons, **2015**.

[34] S. P. Gurrum, W. P. King, Y. K. Joshi, and K. Ramakrishna. *J. Heat Transfer* **2008**, 130, 082403.

[35] J. F. Goff. *Phys. Rev. B* **1970**, 1, 1351-1362.

[36] K. V. Rajani, S. Daniels, P. J. McNally, F. O. Lucas, and M. M. Alam. *Phys. Status Solidi A* **2010**, 207, 1586-1589.

[37] G. Chen, and P. Hui. *Appl. Phys. Lett.* **1999**, 74, 2942-2944.

[38] S. M. Lee, and D. G. Cahill. *J. Appl. Phys.* **1997**, 81, 2590-2595.

[39] M. Asheghi, K. Kurabayashi, R. Kasnavi, and K. E. Goodson. *J. Appl. Phys.* **2002**, 91, 5079-5088.

[40] G. Liu, B. Debnath, T. R. Pope, T. T. Salguero, R. K. Lake, and A. A. Balandin. *Nat. Nanotechnol.* **2016**, 11, 845-850.

[41] X. Liu, and D. L. Wang. *IEEE Trans. Neural Netw.* **1999**, 10, 564-573.

[42] J. H. Wijekoon, and P. Dudek. *Neural Netw.* **2008**, 21, 524-534.

[43] F. C. Hoppensteadt, and E. M. Izhikevich. *IEEE Trans. Neural Netw.* **2000**, 11, 734-738.

[44] J. Moser, A. Barreiro, and A. Bachtold. *Appl. Phys. Lett.* **2007**, 91, 163513.

Chapter 5

Light-Patterned Logic Circuits Based on Semiconducting WSe_2

This chapter demonstrates the direct laser patterning of the WSe_2 logic circuits. First, by moderate ablation with carefully controlled laser intensity, the 2H-WSe_2 could be uniformly thinned at a very low rate, accompanied by a uniform increase in its surface potential. Secondly, FET measurement showed that by moderate laser ablation on the WSe_2 channel, the hole doping could be induced. Further ablation tests showed that by control of the laser power and ablation time, controllable hole doping of 2H-WSe_2 could be achieved. Various types of characterization were performed to understand the underlying mechanism, which showed that the ablation-induced reduction of Se and the resulting oxidation could account for the hole doping. A further photocurrent mapping was performed on the laser patterned WSe_2 P-N junction, showing that a vertical-lateral hybrid P-N junction was performed upon a small amount of ablation. Finally, a NOR gate circuit was demonstrated by direct laser patterning, showing comparable performances with other logic circuit fabrication methods.

5.1 Introduction

TMDs have been studied in various fields such as field effect transistors,[1-3] photo detectors,[4-6] gas sensors[7,8] and nonvolatile memory devices.[9-11] To push forward their applications in next generation electronics, great efforts have been put into controlling and improving device properties, such as good metal-semiconductor contact quality,[12-16] fast on/off switching speed[17-19] and controlled doping.[20-29] 2H-WSe_2 is a semiconductor with a bandgap of 1.65 eV for monolayer[30] and 1.2 eV for bulk.[31] For CVD synthesized monolayer or few layer WSe_2, it is often reported to be a p-type semiconductor, which may be due to high valence band maximum position,[32] tungsten vacancy[33] and absorption of oxygen and H_2O in the air.[34] On the other hand, the fresh mechanical exfoliated multilayer WSe_2 is usually ambipolar,[34-37] whose carrier type and concentration can be easily affected by surface doping[34,36-40] and the work function of metal contacts.[37,38,41] For instance, ambipolar WSe_2 can be p-type doped by O_3 exposure, which is reversible by annealing in nitrogen.[34] Metal contacts with high work function lead to a p-type transistor behavior while low work function metal contacts result in an n-type transistor.[37] A kind of electron-rich superatom has been used to achieve the n-type doping of WSe_2.[40] However, selective doping using these techniques requires patterning of passive layers, which introduces more process steps, especially for complicated circuits. Recently, Seo et al. reported the p-type doping of $MoTe_2$ by laser scanning on the electrodes, which provides an optional way to control the carrier type.[42] However, the laser ablation must be done upon the electrodes, which requires high laser intensity and limits its applications.

Here in this work, the controllable hole doping of 2H-WSe_2 by simple direct laser ablation on the channel was demonstrated, without pre-patterning of passive layers or metals. By controlling the laser power and ablation time, controllable levels of hole doping could be achieved. As proved by the STEM characterizations, formation of tungsten oxide within the ablated region was responsible for the induced doping. Photocurrent mapping test showed that moderate ablation could form a vertical-lateral hybrid p-n junction within the channel, which could be tuned to a lateral p-n junction by further ablation. Finally, a WSe_2-

based light-patterned NOR gate circuit was demonstrated, which showed potentials in the scale-up applications of integrated logic circuits.

5.2 Experimental Methods

5.2.1 Device Fabrication

Thin WSe_2 samples were mechanically exfoliated onto the silicon substrate (with a 285 nm SiO_2 on top) from WSe_2 single crystals synthesized by chemical vapor transport method. Then standard EBL process was performed to pattern the electrodes, which were then followed by the deposition of 4/50 nm Cr/Au film using the electron beam evaporator. For the device of NOR gate circuit, input gate electrodes were first patterned onto the silicon substrate using the standard EBL method. Then BN and WSe_2 were transferred subsequently using the PDMS-assisted dry transfer method. Electrodes for V_{DD}, V_{OUT} and ground were patterned subsequently by the standard EBL process.

5.2.2 Hole Doping by Laser Ablation

Heavy ablation was performed by a beam of 532 nm laser focused by a 100× objective lens (NA = 0.80). Moderate ablation was performed by the 532 nm laser focused by a 50× objective lens (NA = 0.60). Samples were placed on a piezoelectric stage of WITec alpha 300R Raman system for laser scanning. For both types of ablations, the sample moved continuously with the help of a scan stage, so that the ablation dose was uniform throughout the whole ablated area. The laser power was measured by Thorlabs PM100D optical power and energy meter with an S130C sensor (500 mW range).

5.2.3 Raman and Photocurrent Mapping

The photocurrent mapping test was performed by a WITec alpha 300R Raman system in the Raman and photocurrent mapping module, which could measure the Raman and photocurrent signals simultaneously. The excitation 532 nm laser was set to 0.1 mW to

avoid unnecessary ablation. The laser was focused by a 100× objective lens (NA = 0.80). The drain electrode was connected to a Keithley 2450 source-measurement unit while the source electrode was connected to the input of a Femto DLPCA-200 low noise current amplifier, whose output voltage was then collected by the WITec system. Raman mapping signals were collected at the same time with a 600 g/mm grating. The integration time is set to 0.2 s.

5.2.4 SKPM Measurement

SKPM measurement was performed by an Asylum Research MFP-3D atomic force microscope integrated with a Stanford Research 830 lock-in amplifier. The tip was platinum coated. One electrode of the device was connected to the ground using the silver paste while the other electrode was connected to the lock-in amplifier. The tip-sample distance was set to 5 nm.

5.2.5 SEM Imaging

The SEM image of the NOR gate circuit device was collected in the secondary electron imaging mode by a Jeol 7600F field-emission SEM system. The working distance was set to 8.0 mm. The acceleration voltage was set to 15 kV in order to show the layout of the bottom electrodes.

5.2.6 STEM and EELS Measurement

Exfoliated WSe_2 flakes were transferred onto a TEM grid by the PMMA-assisted wet transfer method, which were then ablated by a 2.5 mW laser focused by a 100 × objective lens (NA = 0.95, power density = 0.68 MW/cm^2). STEM imaging was performed by an aberration-corrected JEOL ARM-200F equipped with a cold field emission gun (60 kV) and an Advanced STEM Corrector (ASCOR). EELS mapping was conducted by a low voltage modified Gatan GIF Quantum spectrometer integrated in the STEM system.

5.2.7 FET and Logic Circuit Measurement

Room temperature FET and NOR gate circuit performances were characterized by Keysight B1500A semiconductor device analyzer with devices placed in an MicroXact vacuum probe station. For the temperature dependent tests, devices were placed on a vacuumed Linkam THMS350V stage, which used liquid nitrogen for cooling.

5.3 Principle Outcomes

5.3.1 Characterization and Laser Ablation of 2H-WSe_2

5.3.1.1 Structure and Characterization

The crystal structures of 2H-WSe_2 are shown in Figure 5.1a. The left panel is the side view of the crystal structure, where the interlayer distance is about 6.51 Å. The middle panel is the top view of the crystal, showing a honeycomb lattice structure. The right panel is a 3D schematic diagram of the two-electrode WSe_2 FET device on the silicon substrate. A typical Raman spectrum of 2H-WSe_2 is shown in Figure 5.1b, where two major peaks locate at around 250 cm^{-1}. One peak is for the E^1_{2g} and A_{1g} modes, which are degenerate in thin WSe_2 films. The other peak is from the longitudinal acoustic mode at the M point in the Brillouin zone, which is labeled as 2LA(M).[43] The other small peaks on the two sides of the two major peaks are mainly from secondary order vibration modes. Figure 5.1c shows typical transfer characteristics of the pristine WSe_2 devices based on the exfoliated samples. Devices of four thicknesses are shown, which are 2.6, 6.1, 8.8, and 13.0 nm, respectively. The inset is an optical image of the WSe_2 FET device, with the thickness of 6.1 nm. A shown by the transfer curves, all the devices show a slightly ambipolar transport behavior, where the electron transport is dominant. The four FET devices have a similar off region. With the increasing thickness, the on current increases.

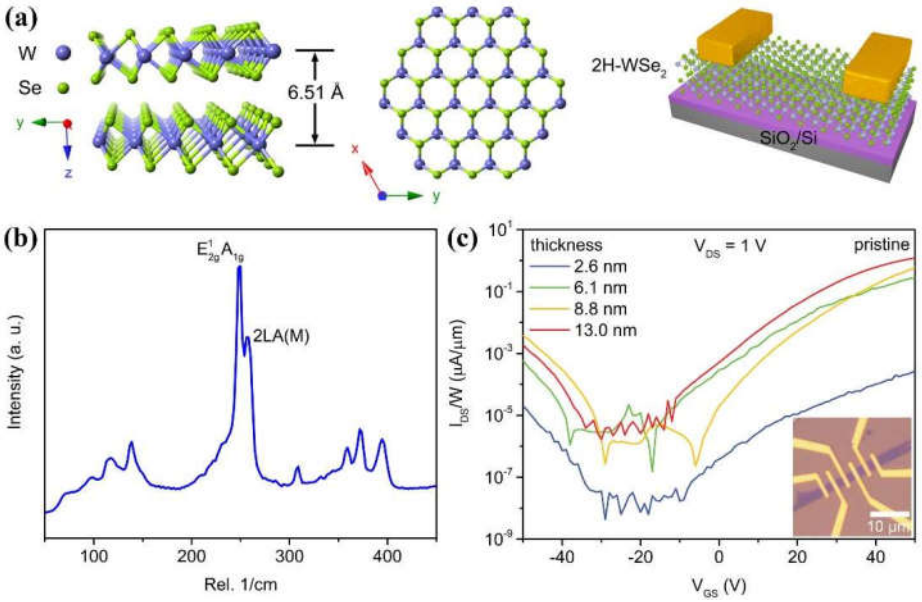

Figure 5.1 Structure and Characterization of 2H-WSe_2. (a) Left: Side view of the crystal structure of 2H-WSe_2. Middle: Top view of the crystal structure of 2H-WSe_2. Right: Schematic diagram of the WSe_2 FET device. (b) Raman spectrum of 2H-WSe_2. Two major peaks are labeled. (c) Transfer characteristics of pristine exfoliated 2H-WSe_2 FET devices with different thickness. All show the electron-dominant ambipolar transport behavior. Inset: A typical optical image of the WSe_2 FET device.

5.3.1.2 Laser Ablation

First, heavy laser ablation was applied onto the WSe_2. The ablation was done with an 8-mW laser focused by a 100 × objective lens (NA = 0.80, power density = 1.55 MW/cm^2) with an ablation time of 1.2 s per μm. Then AFM and SKPM tests were performed on the heavily ablated sample, which are shown in Figure 5.2. According to the SKPM results, the ablated region shows a low V_{CPD}, which means a higher surface potential and a hole doping. However, according to the AFM height results, deep holes are generated in the ablation region, which means that the heavy laser ablation will damage the conducting channel and is not suitable for the controlled hole doping.

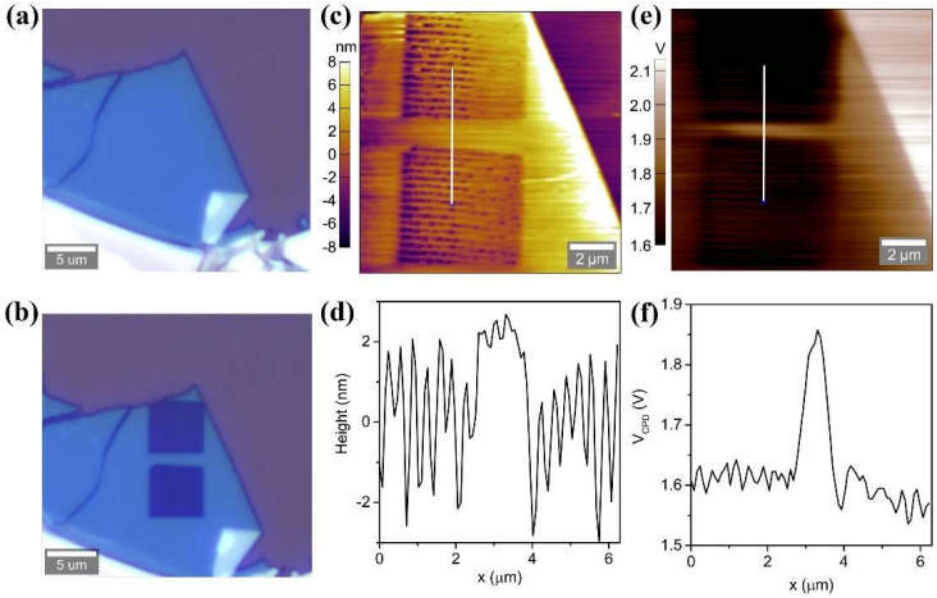

Figure 5.2 Optical, AFM and SKPM images of heavily ablated WSe_2. Optical images (a) before and (b) after heavy laser ablation (100 × lens, NA = 0.8, 1.55 MW/cm^2, 1.2 s per μm scan). (c) AFM image and (d) the height profile along the white line. (e) SKPM image and (f) the V_{CPD} profile along the white line.

Then the moderate ablation was studied, which was achieved by scanning the sample with a laser focused by a 50 × objective lens (NA = 0.60). By using a relatively moderate power and careful controlling of ablation conditions, severe damage on the channel can be avoided and different hole doping levels can be achieved by using different laser power and ablation time. Figure 5.3a and 5.3b show the optical images of a device before and after a series of moderate ablations (0.54 MW/cm^2), which show that the moderate ablation can thin the sample uniformly without introducing deep holes. The AFM measurement confirms the uniformity of the moderate ablation. Note that bubbles exist beneath the WSe_2, which were introduced by the PMDS-assisted dry transfer of the sample onto the silicon substrate. Height profiles along the red and black lines show that the pristine WSe_2 is 8.3 nm thick while the ablated WSe_2 is 2.6 nm thick (Figure 5.3d). Figure 5.3e shows a near uniform decrease in the contact potential difference, which means a uniform increase in the sample surface potential as well as the uniform hole doping. The V_{CPD} profile along the white line is shown in Figure 5.3f. The presented results show that the moderate laser

ablation under the 50 × objective lens can uniformly introduce the hole doping without producing severe damage to the conducting channel, which makes it suitable for the controlled hole doping of the WSe_2 FET devices.

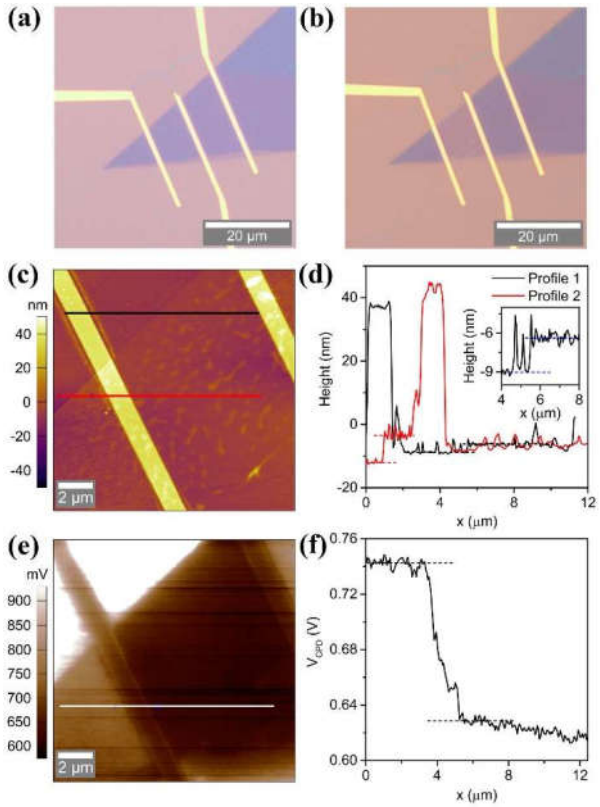

Figure 5.3 Optical, AFM and SKPM images of moderately ablated WSe_2. Optical images of the device (a) before and (b) after a series of ablations (50 × lens, NA = 0.6, 0.54 MW/cm^2). (c) AFM image of the ablated device and (d) the height profile along the two lines. (e) SKPM image and (f) the V_{CPD} profile along the white line.

5.3.2 Laser-Induced Controlled Hole Doping in 2H-WSe_2

5.3.2.1 FET Performances

2H-WSe_2 thin films were mechanically exfoliated onto silicon substrates with a 285 nm SiO_2 layer, on which field effect transistors were then fabricated. In this study, most pristine multilayer WSe_2 transistors showed an electron-dominated transport behavior as shown in

Figure 5.1c, which were then moderately ablated by a scanning focused laser ($50\times$ lens, NA = 0.6) to introduce the hole doping (inset of Figure 5.4c). Figure 5.4a show a typical optical image of the WSe_2 FET device, where the ablated region is marked by the green dash rectangle. Figure 5.4b shows typical source-drain output characteristics of a pristine WSe_2 transistor, which exhibits an n-type behavior. While after the channel is ablated by a 0.74 MW/cm^2 laser for 2 s per μm, the transistor becomes p-type doped (Figure 5.4c). Figure 5.4d shows the transfer characteristics of the transistor along both positive and negative sweeping directions before and after laser ablation. The on/off ratio of the transistor is about 10^8 before ablation and 10^6 after ablation. In order to extract the threshold voltage V_{th}, $I_{DS}/\sqrt{g_m}$ versus V_{GS} is plotted to minimize the influence from parasitic resistance,[44] where $g_m = dI_{DS}/dV_{GS}$. As shown in Figure 5.4e, the extrapolation of the linear region gives $V_{th} = 22.3$ V. Given that thick WSe_2 has a much larger capacitance[45] than 285 nm SiO_2 ($C_{ox} = 1.2 \times 10^{-8}$ F $\cdot$ cm^{-2}), the gate-induced carrier concentration n can be estimated by:[24,46,47]

$$n = -\frac{C_{ox}(V_{GS} - V_{th})}{e} \tag{5.1}$$

From the Equation 5.1, the electron concentration of the pristine transistor can be calculated to 1.3×10^{12} cm^{-2} at $V_{GS} = 40$ V. For the ablated transistor, the threshold voltage $V_{th} = -25.0$ V (Figure 5.4f) and the hole concentration is estimated to 1.1×10^{12} cm^{-2} at $V_{GS} = -40$ V. Field effect mobility μ can be calculated by the equation:[24]

$$\mu = \frac{L}{C_{ox}V_{DS}W}\frac{dI_{DS}}{dV_{GS}} \tag{5.2}$$

where L and W are the channel length and width. According to the linear extrapolation of the transfer characteristic curve (inset of Figure 5.4e), the electron mobility is calculated to 11.3 cm^{2}V^{-1}s^{-1} for the pristine transistor. While the hole mobility of the ablated transistor is 7.02 cm^{2}V^{-1}s^{-1} (inset of Figure 5.4f).

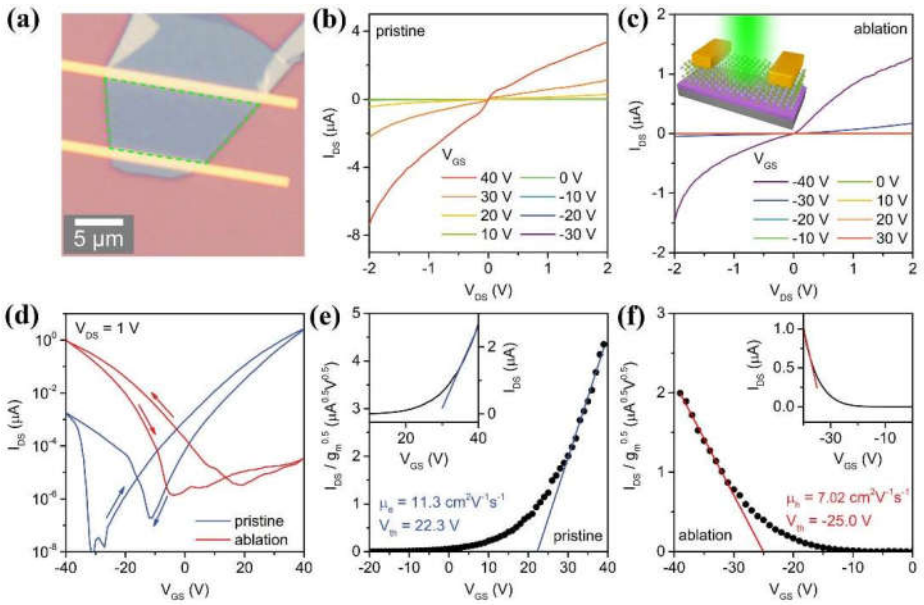

Figure 5.4 Laser-ablation-induced hole doping of WSe_2. (a) A WSe_2 FET device. (b) I_{DS}-V_{DS} curves of the pristine device. (c) I_{DS}-V_{DS} curves after ablation. Inset: Schematic illustration of laser ablation on the transistor channel. (d) Comparison of transfer characteristics of the transistor before and after ablation. (e) $I_{DS}/\sqrt{g_m}$ versus V_{GS} plot of the pristine transistor and the extraction of threshold voltage V_{th}. Inset: Linear plot of transfer curve from which the electron mobility is extracted. (f) $I_{DS}/\sqrt{g_m}$ versus V_{GS} plot of the ablated transistor and the extraction of V_{th}. Inset: Linear plot of transfer curve from which the hole mobility is extracted.

By simply tuning the ablation time, the hole doping level in WSe_2 channel can be controlled. As shown in Figure 5.5a, under the same laser power of 0.54 MW/cm^2, by gradually changing the ablation time from 2 s to 12 s per μm, the transistor changes from electron-dominant transport to hole-dominant transport. During this process, the electron current decreases by 6 orders of magnitude at $V_{GS} = 30$ V while the hole current increased by 6 orders of magnitude at $V_{GS} = -30$ V. In the pristine transistor, the electron and hole field effect mobility are 0.67 and 0.0046 $cm^2V^{-1}s^{-1}$, respectively. After a series of ablation, the transistor reaches a hole mobility of 7.8 $cm^2V^{-1}s^{-1}$. On the other hand, the hole doping level can also be adjusted by changing the laser power. Figure 5.5b exhibits the shift of transfer characteristics with the power increasing, where the electron current decreases by about 5

orders of magnitude at $V_{GS} = 30$ V and hole current increases by 7 orders of magnitude at $V_{GS} = -30$ V.

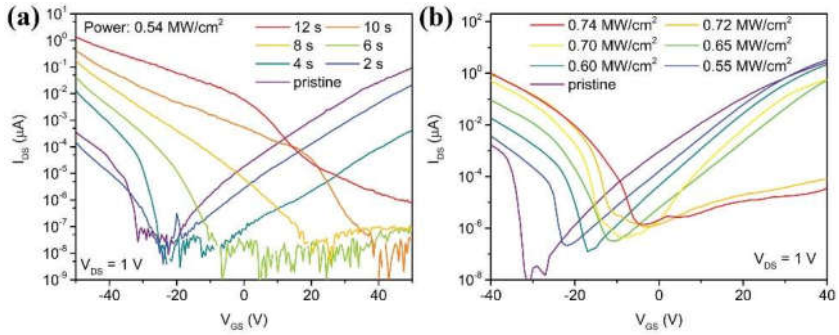

Figure 5.5 Controllable hole doping by laser ablation. (a) I_{DS}-V_{GS} transfer characteristics of a WSe_2 transistor after ablation at different ablation time from 2 to 12 s per μm. (b) Transfer characteristics of a WSe_2 transistor after ablation with increasing laser power from 0.55 to 0.74 MW/cm^2.

5.3.2.2 Schottky Barrier Height Measurement

Temperature dependent *I-V* characterization was performed to study the influence of p-type doping on the Schottky barrier height (SBH) at the metal/WSe_2 interface. In the thermionic emission regime, the charge injection is mainly dependent on the SBH $q\Phi_{B0}$, which can be extracted from the activation energy (E_A). For transistors in the sub-threshold regime and $qV_{DS} \gg k_BT$, the source-drain current can be described by the following equation:[48,49]

$$I_{DS} = AA^*T^{1.5}exp\left(-\frac{E_A}{k_BT}\right) \tag{5.3}$$

where A is the contact area, A^* is Richardson constant, T is the temperature and k_B is Boltzmann constant. From Equation 5.3, E_A is given by:

$$E_A = -2.303k_B\, d[\log(I_{DS}/T^{1.5})]/d(1/T) \tag{5.4}$$

For p-type FETs, when the V_{GS} is larger than the flat-band voltage V_{FB}, E_A is linearly dependent on V_{GS} by:[48,49]

$$E_A = q\Phi_{B0} + (1 + C_{it}/C_{ox})^{-1}(V_{GS} - V_{FB}) \tag{5.5}$$

where C_{it} is the capacitance per unit area of interface traps. The linearity stops at $V_{B0} = V_{FB}$, where $E_A = q\Phi_{B0}$. As a result, by measuring the temperature-dependent current of

the FET device and plotting relative curves, the SBH can be extracted. Figure 5.6 shows the results of temperature-dependent current measurement after two times of ablations (Figure 5.6a-c and 5.6d-f, respectively). The condition of the first ablation is 0.87 MW/cm^2, and 6 s per μm. And the condition of the second ablation is 0.87 MW/cm^2, and 8 s per μm. As shown in Figure 5.6c, the semi-log plot of $I_{DS}/T^{1.5}$ versus $1000/T$ is linearly fitted for different V_{GS}, from which the activation energy E_A can be extracted. By comparison between the results of the first (Figure 5.6a-c) and the second (Figure 5.6d-f) ablations, it shows that after the second ablation, the hole current is increased and the barrier height is decreased, featured by the increased linearity of the I_{DS}-V_{DS} curves.

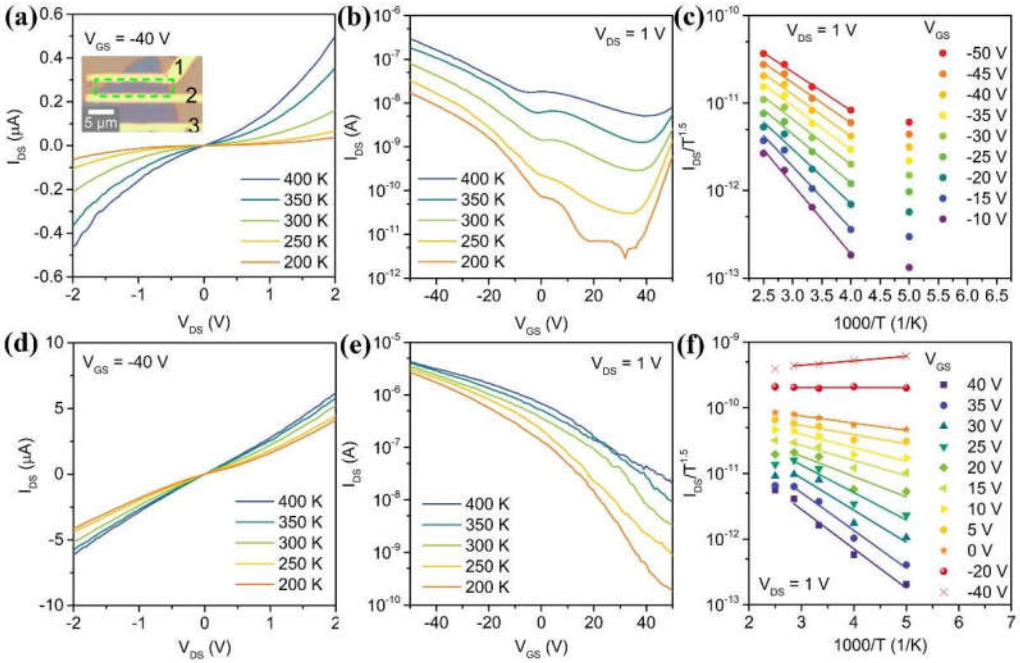

Figure 5.6 Temperature-dependent FET measurement for Schottky barrier height extraction. (a) Temperature-dependent I_{DS}-V_{DS} curve of a WSe_2 transistor at $V_{GS} = -40$ V after the first ablation (0.87 MW/cm^2, 6 s per μm). Inset: An optical image of the WSe_2 transistors, with the ablated channel marked by the green dash rectangle. (b) Temperature-dependent I_{DS}-V_{GS} curve of the transistor after the first ablation. (c) Arrhenius plot of $I_{DS}/T^{1.5}$ vs $1000/T$ at different V_{GS} for the transistor after the first ablation. (d) Temperature-dependent I_{DS}-V_{DS} curve at $V_{GS} = -40$ V after the second ablation (0.87 MW/cm^2, 8 s per μm). (e) Temperature-dependent I_{DS}-V_{GS} curve after the second ablation. (c) Arrhenius plot of $I_{DS}/T^{1.5}$ vs $1000/T$ at different V_{GS} after the second ablation. The activation energy is extracted from the linear fitting.

As shown in Figure 5.7, E_A is then plotted versus V_{GS} to extract the value of Schottky barrier height, which is the value of E_A at the point where the linear dependence of V_{GS} ends. After the first ablation (0.87 MW/cm^2, 6 s per µm), the SBH is extracted as 127 meV. While after the second ablation (0.87 MW/cm^2, 8 s per µm), the SBH decreases to 60 meV. This shows that the ablation-induced p-type doping of the channel will influence the contacts as well.

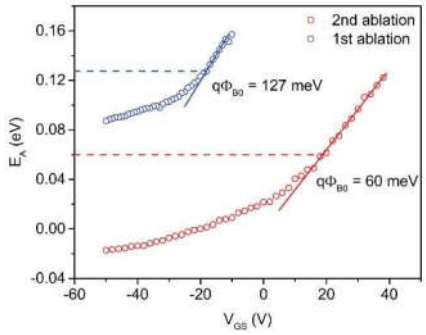

Figure 5.7 Activation energy E_A at different V_{GS} for the first (0.87 MW/cm^2, 6 s per µm scan) and second ablation (0.87 MW/cm^2, 8s per µm scan). Schottky barrier height is extracted respectively.

5.3.2.3 SKPM Characterization

A stepped increased ablation and correspondent SKPM measurement were also performed to confirm the increased hole doping by increasing the laser power and ablation time. As shown in Figure 5.8a, the exfoliated sample was ablated within the red rectangles. First, regions 1-4 (and 5-8) were ablated by a lower power of 0.37 MW/cm^2 with a scan speed of 0.5 µm/s for one to four times, respectively. Then the regions 5-8 were further ablated by a higher power of 0.44 MW/cm^2 with a scan speed of 0.5 µm/s for one to four times, respectively. Then the SKPM image was measured as shown in Figure 5.8b. The profiles of contact potential difference along the red and blue lines are shown in Figure 5.8c, which shows a stepped decrease of V_{CPD} with the stepped increase of ablation time and laser power. And the change between two regions is quite sharp.

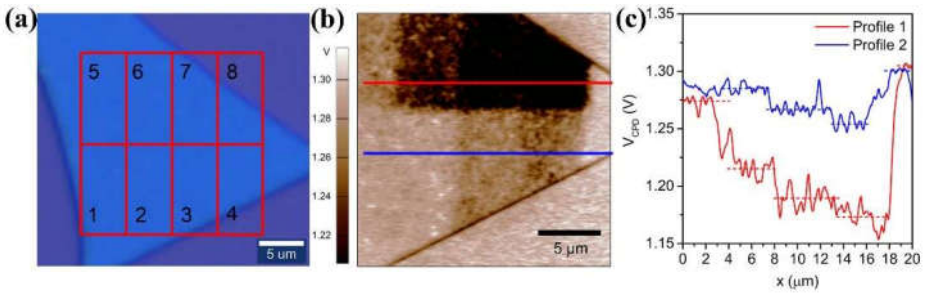

Figure 5.8 Surface potential of WSe_2 in different ablation levels. (a) An optical image of the WSe_2. The marked areas were ablated in different levels. Regions 1-4 (5-8) were first ablated by a lower power (0.37 MW/cm^2, 0.5 µm/s scan) for one to four times, respectively. Then regions 5-8 were ablated by a higher power (0.44 MW/cm^2, 0.5 µm/s scan) for one to four times, respectively. (b) An SKPM image showing the surface potential of the ablated WSe_2. (c) Profiles of V_{CPD} along the two lines marked in (b).

5.3.3 Mechanism of Laser-Induced Hole Doping

5.3.3.1 Raman Signals

Raman spectroscopy was performed to study the mechanism of the laser-induced hole doping of 2H-WSe_2. For the severe ablation (1.55 MW/cm^2, 1.2 s per µm) previously shown in Figure 5.2, the Raman spectra of three spots were collected (Figure 5.9a). Two spectra were collected from the ablated area (the red and blue spots, inset of Figure 5.9a) and one spectrum was collected from the pristine area (the green spot). Figure 5.9a also shows the Raman spectrum of WO_3 (the black curve). Enlarged Raman spectra are shown in Figure 5.9b and 5.9c. It shows that for ablated WSe_2 the signal intensity of E^1_{2g} and A_{1g} peak increases while the intensity of 2LA(M) peak decreases, which is consistent with previous reports when WSe_2 decreases in thickness.[43,50] The broad signals between 600 to 800 rel. cm^{-1} are second order Raman signals of WSe_2.[43] No obvious signal from tungsten oxide is observed.[51-53] This might be due to insufficient amount of tungsten oxide and the poor crystallization in a large scale.[54] Although there is a previous report where the signals of tungsten oxide were observed from the intense laser illuminated WSe_2, the signal collection time was very long (up to 600 s).[54]

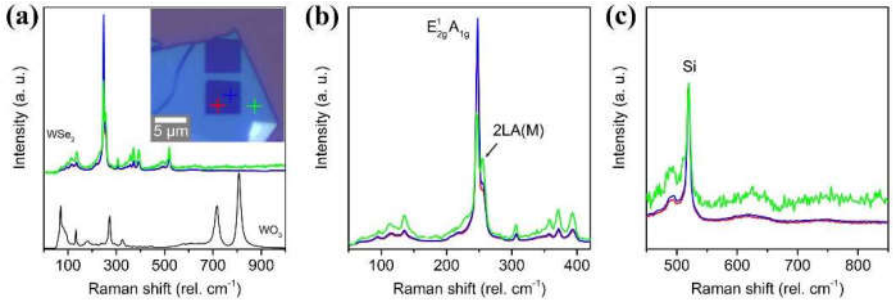

Figure 5.9 Raman signals of WSe_2. (a) Comparation of Raman spectra between pristine WSe_2, ablated WSe_2 and WO_3. Inset: An optical image of WSe_2 after heavy ablation (100 × lens, NA = 0.8, 1.55 MW/cm^2, 1.2 s per μm scan) in the two square areas, Raman spectra at three cursors are shown. (b) Enlarged Raman spectra of the pristine and ablated WSe_2 from 50 to 420 rel. cm^{-1}. (c) Enlarged Raman spectra of the pristine and ablated WSe_2 from 450 to 850 rel. cm^{-1}.

5.3.3.2 XPS Results

The XPS characterization was also performed to study the elemental composition and electronic state of elements in the ablated materials. Figure 5.10a and 5.10b show the XPS spectra of the pristine WSe_2 and the moderately ablated WSe_2 (50 × lens, NA = 0.6, 0.76 MW/cm^2, 2 s per μm) and Figure 5.10c shows the spectra of heavily ablated WSe_2 (100 × lens, NA = 0.8, 1.16 MW/cm^2, 0.6 s per μm). For the moderately ablated sample, the XPS spectrum shows no obvious change with respect to the pristine sample. As shown in Figure 5.10b, the two peaks of tungsten ($W4f_{7/2}$ and $W4f_{5/2}$) show little difference and no peaks from the tungsten oxide is observed. However, for the heavily ablated sample, the peaks from the tungsten oxide are observed (Figure 5.10c). The parameters for fitting of W4f peaks are listed in the Table 5.1. The results indicate that in the moderately ablated WSe_2, the amount of oxide is at a low level.

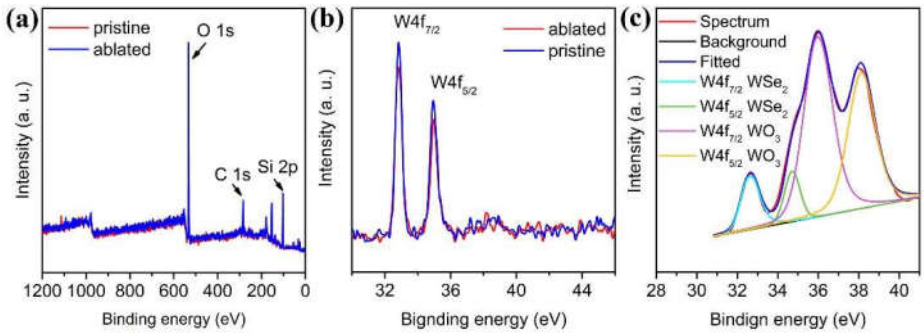

Figure 5.10 XPS results of WSe_2. (a) Wide band XPS spectrum of WSe_2 on SiO_2 substrate. (b) Comparison of W4f peaks between pristine WSe_2 and the moderately ablated sample (50 × lens, NA = 0.6, 0.76 MW/cm^2, 2 s per μm scan). (c) XPS spectrum of the heavily ablated sample (100 × lens, NA = 0.8, 1.16 MW/cm^2, 0.6 s per μm scan).

Table 5.1 Parameters for the XPS peak fitting of the heavily ablated sample (100 × lens, NA = 0.8, 1.16 MW/cm^2, 0.6 s per μm scan).

Bonding	Binding energy (eV)	FWHM (eV)	Area %
$W4f_{7/2}$ WSe_2	32.53	0.84	9.28
$W4f_{5/2}$ WSe_2	34.71	0.84	6.96
$W4f_{7/2}$ WO_3	35.94	1.51	47.87
$W4f_{5/2}$ WO_3	38.12	1.51	35.9

5.3.3.3 STEM and EELS Results

To better understand the underlying mechanism of the laser-induced hole doping, scanning transmission electron microscopy (STEM) characterizations were performed. As shown in Figure 5.11a, the left region is ablated while the right is pristine. As marked by the white line, the ablated derivatives grow along the zigzag direction of the WSe_2 crystal. There are some brighter areas in the pristine WSe_2, which may be attributed to bare W atoms. Figure 5.11b shows the enlarged image of Figure 5.11a. The left is the ablated lattice and the right is the pristine WSe_2 hexagonal lattice, between which are thinned WSe_2 and amorphous areas. Figure 5.11c and 5.11d show the STEM images of fully pristine and fully ablated regions, respectively. Figure 5.11e shows the enlarged STEM image of Figure 5.11c, where the lattice constant is determined to be $d_{(010)} = 0.33$ nm, which is consistent with previous

reports.[55,56] The FFT image of Figure 5.11c is shown by Figure 5.11f labeled with the Miller indices, which confirms the $P6_3/mmc$ space group of WSe_2. Figure 5.11g is the enlarged STEM image of Figure 5.11d, showing a nearly square lattice with a lattice constant $d_{001} = 0.38$ nm and $d_{100} = 0.37$ nm, which is close to distances of adjacent W atoms in the reported WO_3.[57] Figure 5.11h shows the corresponding FFT image labeled with Miller indices.

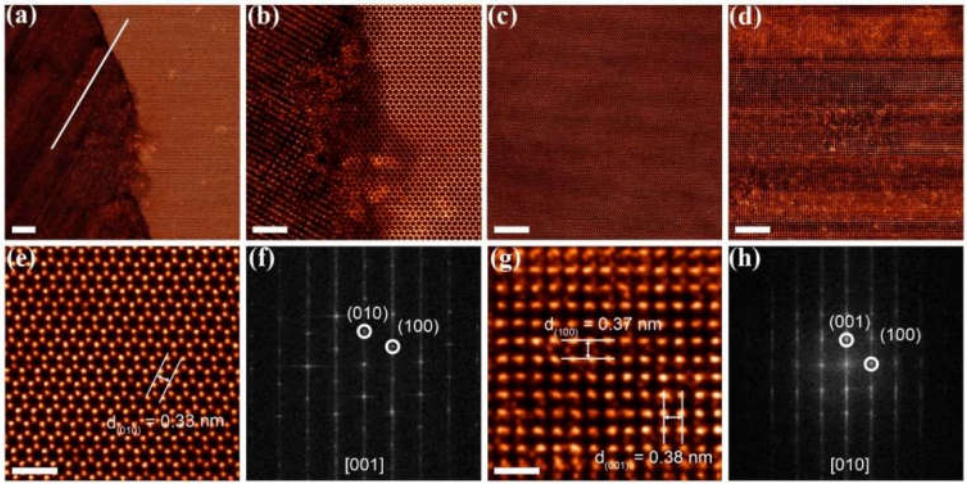

Figure 5.11 STEM characterization of the ablated WSe_2. (a) A STEM image showing the contrast between the ablated region and the pristine WSe_2. The white line shows the growth of ablated derivatives along the zigzag direction of the pristine sample. (b) An enlarged STEM image of (a). STEM images of (c) fully pristine WSe_2 and (d) fully ablated region. (e) The enlarged image and (f) FFT image of (c), labeled with the lattice constant and Miller indices, respectively. (g) The enlarged image and (h) FFT image of (d), labeled with the lattice constants and Miller indices, respectively. Scale bar: (a, c, d) 5 nm, (b) 2 nm, (e, g) 1 nm.

Figure 5.12a shows the annular dark-field STEM (ADF-STEM) image of the ablated sample showing in Figure 5.11. The corresponding EELS mapping signals of W (O edge), Se (M edge) and O (K edge) are shown in Figure 5.12b, showing the decrease of Se and increase of O in the ablated region. Since WO_3 is a 3D crystal while the oxide derivatives here is 2D, the laser-induced square-lattice-structured oxide is simply labeled as WO_{3-x}. During the oxidation of WSe_2, electrons are transferred from WSe_2 to the oxide, leading to the p-type doping of WSe_2.

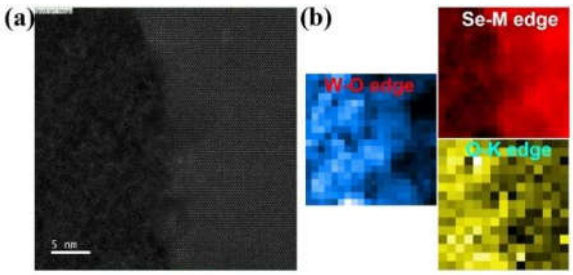

Figure 5.12 EELS mapping of the ablated WSe_2 sample. (a) An ADF-STEM image of the sample. (b) EELS mapping images of W (O edge), Se (M edge) and O (K edge).

5.3.4 Photocurrent Mapping Test of Laser-Written P-N Junctions

5.3.4.1 Photocurrent Mapping Results

To further understand the ablation-induced p-type doping, photocurrent mapping tests were performed on a 12-nm-thick sample shown in Figure 5.13a. The ablation power density was set to 0.44 MW/cm^2. A small power of 0.1 mW was used for photocurrent mapping. To determine the location of channel and electrodes, Raman spectral mapping was also performed simultaneously. Figure 5.13b is a typical Raman mapping image showing the intensity of the E^1_{2g} and A_{1g} peak, which is marked by the arrow in Figure 5.13c. At the beginning, region 1 (Figure 5.13a, marked by the red dashed rectangle) were ablated twice for 8 s per μm. The photo response was strongest at the contacts, which means that the hole doping was not high enough and the charge separation was dominated by the Schottky barrier induced built-in field. Then region 1 and 2 (marked by the yellow dashed rectangle) were ablated for 10 s per μm. Figure 5.13d shows the mapping of the short-circuit current at $V_{DS} = 0$ V and $V_{GS} = -20$ V, while Figure 5.13e shows the current at $V_{DS} = 1$ V and $V_{GS} = -20$ V. For $V_{DS} = 0$ V, the maximum photo response locates at the center of the ablated region. While for $V_{DS} = 1$ V, the maximum response exists near the border of ablated and unablated regions. Cross-section photocurrent profiles along the longitudinal midline of the channel from the drain to the source are shown in Figure 5.13f, where the extrema show a spatial mismatch between $V_{DS} = 0$ V and $V_{DS} = 1$ V. Then the region 1 and 2 were further ablated for 12 s per μm. Figure 5.13g and 5.13h show the corresponding

photocurrent for $V_{DS} = 0$ V and 1 V and the maximum response locates at the border of the ablated region. According to the cross-section profiles in Figure 5.13i, the extrema of photocurrent is coincident for $V_{DS} = 0$ V and 1 V.

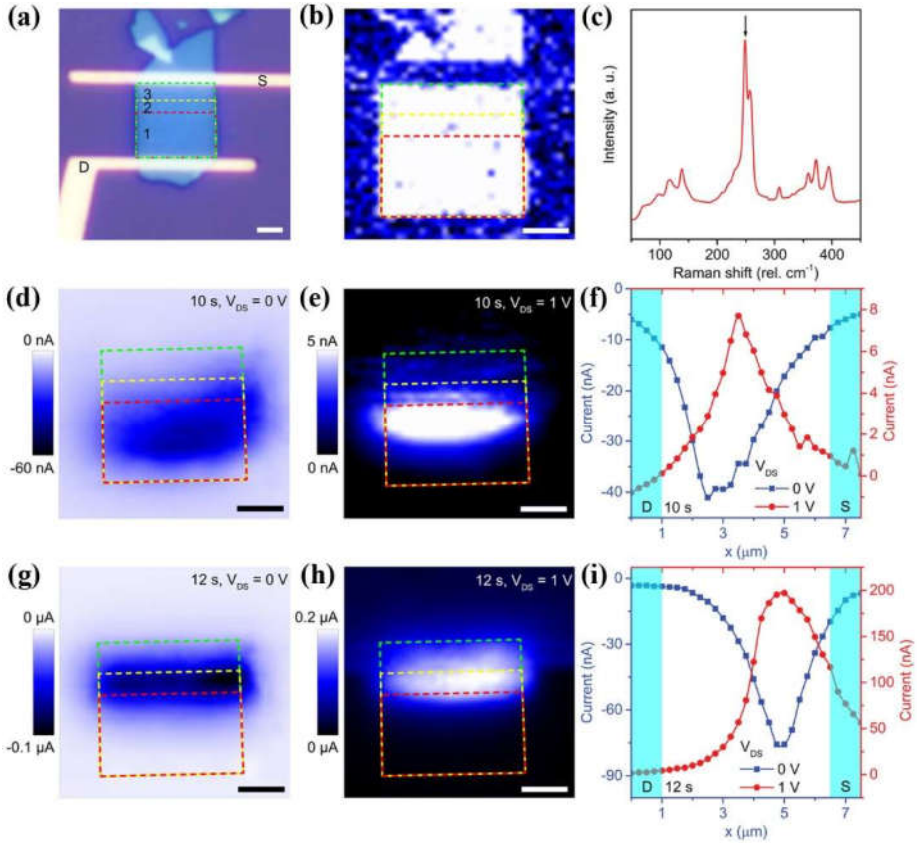

Figure 5.13 Photocurrent mapping of a WSe_2 P-N junction built by laser ablation. (a) An optical image of the p-n junction. The device was first ablated (0.44 MW/cm^2, 8 s per μm) in the red dashed rectangle twice, followed by ablation in the yellow dashed rectangle (10 s and 12 s per μm in sequence). The green rectangle outlines the whole channel. (b) Raman mapping signal collected simultaneously to locate the channel, showing the intensity of the peak marked by the arrow in the (c) Raman spectrum. Photocurrent mapping signal after 10 s per μm ablation at (d) V_{DS} = 0 V and (e) V_{DS} = 1 V and (f) respective current profiles along the midline of channel. Photocurrent mapping signal after 12 s per μm ablation at (g) V_{DS} = 0 V and (h) V_{DS} = 1 V and (i) respective current profiles along the midline of channel. V_{GS} = -20 V.

5.3.4.2 SKPM Results and Discussion

A further scanning Kelvin probe microscopy (SKPM) was performed to obtain the profile of the ablation-induced hole doping. Figure 5.14a shows the contact potential difference V_{CPD} between the tip and sample surface. V_{CPD} profile along the red line (upward) is shown in Figure 5.14b, from which we can see that surface potential in region 1 is quite uniform. Compared with region 2, region 1 has a lower V_{CPD}, i.e., a higher surface potential and a higher p-type doping level, which means that the p-type doping level depends on the ablation history.

Now the situation can be described as the following. After the 10 s per μm ablation, a vertical-lateral hybrid p-n junction is formed (left-top panel of Figure 5.14c), in which only top layers of the ablated region are p-type doped. As shown in the left-bottom panel of Figure 5.14c, when $V_{DS} = 0$ V, the built-in field in the depletion region will accelerate the separation of photoexcited carriers, leading to the electron flow to the source and the hole flow to the drain. This process is the same for both the vertical and lateral depletion regions of the p-n junction, which is the reason why the maximum photo response locates near the center of the ablated region. When $V_{DS} = 1$ V, in the lateral depletion region of p-n junction, the net electric field is reduced (right-top panel of Figure 5.14c), leading to easier carrier diffusion across the lateral depletion region. Light excitation will produce more holes and electrons on two sides of the depletion region, which will then diffuse across the depletion region and form an increased forward current under the forward bias. However, in the vertical depletion region (right-bottom panel of Figure 5.14c), where the built-in field is normal to the external field, the net field is not reduced as much as that in the lateral depletion region, making it contribute little to the forward current. As a result, for $V_{DS} = 1$ V, the maximum photo response locates near the border of the ablated region. After the 12 s per μm ablation, region 1 is fully p-type doped and the maximum photo response locates near the border of the ablated region for both $V_{DS} = 0$ V and 1 V.

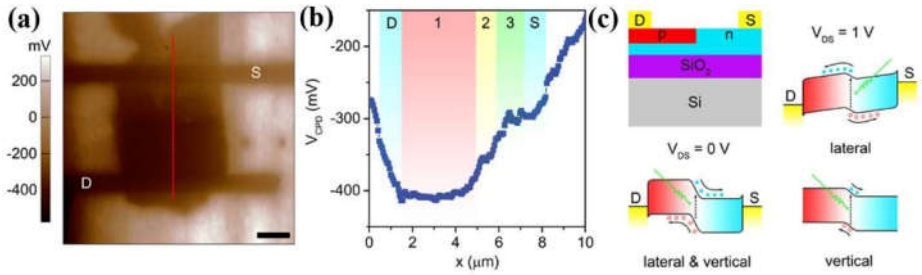

Figure 5.14 Surface potential of the device for photocurrent mapping and diagrams showing the mechanism. (a) SKPM image of the device showing the surface contact potential difference V_{CPD}. (b) The V_{CPD} profile along the red line in (a), showing that the hole doping depends on the ablation history. (c) Schematic band diagram showing the photo response mechanism in the P-N junction with insufficient hole doping.

5.3.5 Direct Logic Circuit Writing

5.3.5.1 Direct Patterning of a NOR Gate Circuit

Controllable doping in WSe_2 enables the fabrication of circuit elements. Utilizing the light-ablation-induced p-type doping, NOR logic circuits were patterned directly without the passive layer. NOR gate circuit operates in such way that the output V_{OUT} is at high level only when both of two inputs V_A and V_B are at low level, and it could be used to build all other logical gates. Figure 5.15a shows a typical NOR gate circuit built by WSe_2 (left panel). First, input gate electrodes A and B were patterned on the SiO_2/Si substrate. Then BN and WSe_2 were transferred on top of gate electrodes subsequently, followed by the pattern of top electrodes for V_{DD}, V_{OUT} and ground (GND). The pristine WSe_2 exhibited the enhancement mode. Then the green region was ablated to build two series p-type channels in the depletion mode. The right-bottom panel shows a schematic drawing of the NOR gate circuit in the left panel, where two series p-type FETs are serially connected to two parallel n-type FETs. The logic operations of the NOR gate are shown in the right-top panel of Figure 5.15a. Figure 5.15b shows an SEM image of the WSe_2-based NOR gate circuit. The bright electrodes are two input gates V_A and V_B at the bottom, which are covered by a layer of BN (exists in the whole field of view). WSe_2 is on top of BN. The dark electrodes are at the top-most, which are for V_{DD}, V_{OUT} and the ground (GND).

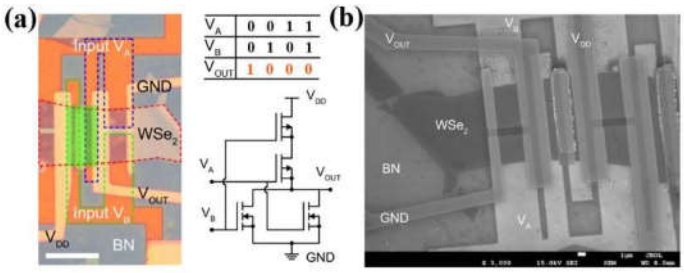

Figure 5.15 A NOR gate circuit based on WSe_2 by selective light-induced hole doping. (a) Left: An optical image of the device. The green region shows the two series p-channels patterned by laser ablation. Scale bar: 10 μm. Right: The logic operation of the NOR gate and a circuit diagram of the CMOS-based NOR gate. (b) A secondary electron SEM image of the device. The acceleration voltage was set to 15 kV to show the layout of input electrodes at the bottom.

5.3.5.2 NOR Gate Circuit Performances

Transfer characteristics of the current flowing through the parallel n-type FETs (Figure 5.16a) show that the parallel n-channels are off when both V_A and V_B are zero and are on when either V_A or V_B is 5 V. Figure 5.16b exhibits the transfer characteristics of the current flowing through the series p-type FETs. The series p-channels are on only when both of V_A and V_B are zero. Compared to the parallel n-channels, the series p-channels are off when either V_A or V_B is 5 V. Figure 5.16c plots transfer characteristics of V_{OUT} versus V_B at different V_{DD} with V_A = 0 V. And Figure 5.16d shows the corresponding gain value at different V_B and V_{DD} with V_A = 0 V, where the maximum gain is about 4 at V_{DD} = 5 V. The output curve of the NOR gate circuit is shown in Figure 5.16e, which shows a good repeatability with varying inputs. Compared with previous reports on 2D material based complementary NOR gates,[58-60] the laser-ablation method requires a much simpler structure as well as a simpler device fabrication procedure, while the gain and output characteristics are retained in a reasonable range. It needs to be mentioned that the gain of the demonstrated NOR gate circuit is not as high as values of WSe_2 based inverters in some previous reports,[41,61,62] which is because p-channels are not so well doped as to match with n channels perfectly. Another issue is that a reset with pulsed $-10\ V$ input is required to maintain a good low- level output (Figure 5.16e). Without the reset, the low-level output performance is not very good (Figure 5.16f), which should be due to the accumulation of

charges in the interface traps under high input gate voltages. Nevertheless, there is still much room to improve the device performances, such as a better-matched p-type doping and cleaner interfaces with fewer traps.

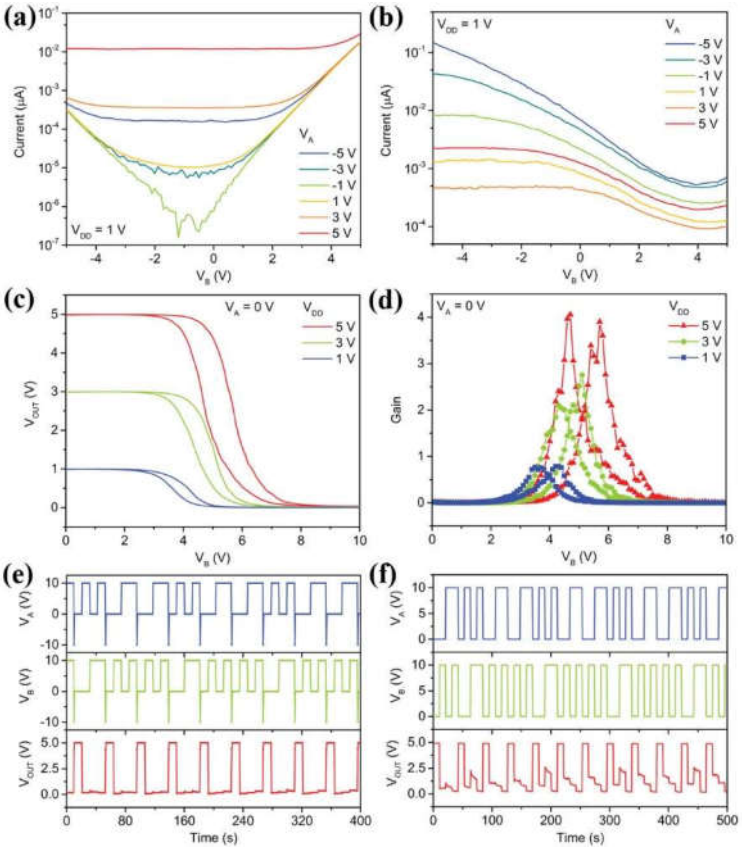

Figure 5.16 Performances of the previously shown NOR gate circuit. (a) Transfer curve of the n-channel current at different input voltages. (b)Transfer curve of the p-channel current at different input voltages. (c) Transfer curve of the output voltage at different input voltages and the V_{DD} with one of the input $V_A = 0$ V. (d) Gain at different V_{DD} with $V_A = 0$ V. (e) Repeatable NOR gate operation with the reset using negative pulsed voltage at the inputs. (f) NOR gate operation without the rest.

5.4 Conclusions

In this article, laser-ablation-induced controllable p-type doping of WSe_2 is reported. As the ablation on the channel increases, a gradually increased hole doping can be achieved. The electron current can decrease by larger than 6 orders of magnitude. Meanwhile the hole current can increase by up to 7 orders of magnitude. STEM characterizations show

the oxidation of WSe_2 under laser ablation, which accounts for the p-type doping. Photocurrent mapping shows that for multilayer WSe_2, a small amount of ablation can only convert top layers to the p-type doped, which will then form a vertical-lateral hybrid p-n junction. As the ablation increases, all layers are p-type doped and a pure lateral p-n junction is formed. The ability of adjusting the p-type doping profile in the vertical direction gives more possibilities to construct complex junction structures in the layered quasi-2D materials. Moreover, a NOR gate circuit is demonstrated by selective laser ablation of WSe_2, which shows the ability to perform reliable NOR operations. Laser ablation needs no passive layer which is required by other carrier doping techniques.[20,22,38-40] Without processes for patterning and removing passive layers, different doping levels can be achieved in different devices on a same wafer, which provides a much simpler and more flexible way for device fabrications. Although scanning focused light is used in this report, with the help of a higher power but less focused light and photomasks, multiple channels can be ablated at the same time, which makes it possible for large scale circuit fabrications. Considering the previous report of $MoTe_2$,[42] this laser-ablation method should be available for other TMD materials with a relatively small band gap. The demonstrated results provide more opportunities for applications of TMD materials in optoelectronic devices, logic circuits and other functional devices.

References

[1] H. Wang, L. Yu, Y. H. Lee, Y. Shi, A. Hsu, M. L. Chin, L. J. Li, M. Dubey, J. Kong, and T. Palacios. *Nano Lett.* **2012**, 12, 4674-4680.

[2] Y. Du, H. Liu, Y. Deng, and P. D. Ye. *ACS Nano* **2014**, 8, 10035-10042.

[3] W. L. Chow, P. Yu, F. Liu, J. Hong, X. Wang, Q. Zeng, C. H. Hsu, C. Zhu, J. Zhou, X. Wang, J. Xia, J. Yan, Y. Chen, D. Wu, T. Yu, Z. Shen, H. Lin, C. Jin, B. K. Tay, and Z. Liu. *Adv. Mater.* **2017**, 29.

[4] O. Lopez-Sanchez, D. Lembke, M. Kayci, A. Radenovic, and A. Kis. *Nat. Nanotechnol.* **2013**, 8, 497-501.

[5] Y. Q. Bie, G. Grosso, M. Heuck, M. M. Furchi, Y. Cao, J. Zheng, D. Bunandar, E. Navarro-Moratalla, L. Zhou, D. K. Efetov, T. Taniguchi, K. Watanabe, J. Kong, D. Englund, and P. Jarillo-Herrero. *Nat. Nanotechnol.* **2017**, 12, 1124-1129.

[6] X. Yu, P. Yu, D. Wu, B. Singh, Q. Zeng, H. Lin, W. Zhou, J. Lin, K. Suenaga, Z. Liu, and Q. J. Wang. *Nat. Commun.* **2018**, 9, 1545.

[7] Q. He, Z. Zeng, Z. Yin, H. Li, S. Wu, X. Huang, and H. Zhang. *Small* **2012**, 8, 2994-2999.

[8] Y. Zhao, J. G. Song, G. H. Ryu, K. Y. Ko, W. J. Woo, Y. Kim, D. Kim, J. H. Lim, S. Lee, Z. Lee, J. Park, and H. Kim. *Nanoscale* **2018**, 10, 9338-9345.

[9] F. Liu, C. Zhu, L. You, S. J. Liang, S. Zheng, J. Zhou, Q. Fu, Y. He, Q. Zeng, H. J. Fan, L. K. Ang, J. Wang, and Z. Liu. *Adv. Mater.* **2016**, 28, 7768-7773.

[10] J. Lee, S. Pak, Y. W. Lee, Y. Cho, J. Hong, P. Giraud, H. S. Shin, S. M. Morris, J. I. Sohn, S. Cha, and J. M. Kim. *Nat. Commun.* **2017**, 8, 14734.

[11] D. Xiang, T. Liu, J. Xu, J. Y. Tan, Z. Hu, B. Lei, Y. Zheng, J. Wu, A. H. C. Neto, L. Liu, and W. Chen. *Nat. Commun.* **2018**, 9, 2966.

[12] L. Wang, I. Meric, P. Y. Huang, Q. Gao, Y. Gao, H. Tran, T. Taniguchi, K. Watanabe, L. M. Campos, D. A. Muller, J. Guo, P. Kim, J. Hone, K. L. Shepard, and C. R. Dean. *Science* **2013**, 342, 614-617.

[13] H. J. Chuang, X. Tan, N. J. Ghimire, M. M. Perera, B. Chamlagain, M. M. Cheng, J. Yan, D. Mandrus, D. Tomanek, and Z. Zhou. *Nano Lett.* **2014**, 14, 3594-3601.

[14] Y. Du, L. Yang, J. Zhang, H. Liu, K. Majumdar, P. D. Kirsch, and P. D. Ye. *IEEE Electron Device Lett.* **2014**, 35, 599-601.

[15] S. Cho, S. Kim, J. H. Kim, J. Zhao, J. Seok, D. H. Keum, J. Baik, D. H. Choe, K. J. Chang, K. Suenaga, S. W. Kim, Y. H. Lee, and H. Yang. *Science* **2015**, 349, 625-628.

[16] Y. Liu, J. Guo, E. Zhu, L. Liao, S. J. Lee, M. Ding, I. Shakir, V. Gambin, Y. Huang, and X. Duan. *Nature* **2018**, 557, 696-700.

[17] A. Nourbakhsh, A. Zubair, S. Joglekar, M. Dresselhaus, and T. Palacios. *Nanoscale* **2017**, 9, 6122-6127.

[18] X. Yan, C. Liu, C. Li, W. Bao, S. Ding, D. W. Zhang, and P. Zhou. *Small* **2017**, 13.

[19] Q. A. Vu, S. Fan, S. H. Lee, M.-K. Joo, W. J. Yu, and Y. H. Lee. *2D Mater.* **2018**, 5, 031001.

[20] T. Lohmann, K. von Klitzing, and J. H. Smet. *Nano Lett.* **2009**, 9, 1973-1979.

[21] S. Mouri, Y. Miyauchi, and K. Matsuda. *Nano Lett.* **2013**, 13, 5944-5948.

[22] M. S. Choi, D. Qu, D. Lee, X. Liu, K. Watanabe, T. Taniguchi, and W. J. Yoo. *ACS Nano* **2014**, 8, 9332-9340.

[23] J. Suh, T. E. Park, D. Y. Lin, D. Fu, J. Park, H. J. Jung, Y. Chen, C. Ko, C. Jang, Y. Sun, R. Sinclair, J. Chang, S. Tongay, and J. Wu. *Nano Lett.* **2014**, 14, 6976-6982.

[24] D. Xiang, C. Han, J. Wu, S. Zhong, Y. Liu, J. Lin, X. A. Zhang, W. Ping Hu, B. Ozyilmaz, A. H. Neto, A. T. Wee, and W. Chen. *Nat. Commun.* **2015**, 6, 6485.

[25] A. Azcatl, X. Qin, A. Prakash, C. Zhang, L. Cheng, Q. Wang, N. Lu, M. J. Kim, J. Kim, K. Cho, R. Addou, C. L. Hinkle, J. Appenzeller, and R. M. Wallace. *Nano Lett.* **2016**, 16, 5437-5443.

[26] X. Duan, C. Wang, Z. Fan, G. Hao, L. Kou, U. Halim, H. Li, X. Wu, Y. Wang, J. Jiang, A. Pan, Y. Huang, R. Yu, and X. Duan. *Nano Lett.* **2016**, 16, 264-269.

[27] D. Pierucci, H. Henck, Z. Ben Aziza, C. H. Naylor, A. Balan, J. E. Rault, M. G. Silly, Y. J. Dappe, F. Bertran, P. Le Fevre, F. Sirotti, A. T. Johnson, and A. Ouerghi. *ACS Nano* **2017**, 11, 1755-1761.

[28] Z. Xiao, J. Song, D. K. Ferry, S. Ducharme, and X. Hong. *Phys. Rev. Lett.* **2017**, 118, 236801.

[29] J. W. Chen, S. T. Lo, S. C. Ho, S. S. Wong, T. H. Vu, X. Q. Zhang, Y. D. Liu, Y. Y. Chiou, Y. X. Chen, J. C. Yang, Y. C. Chen, Y. H. Chu, Y. H. Lee, C. J. Chung, T. M. Chen, C. H. Chen, and C. L. Wu. *Nat. Commun.* **2018**, 9, 3143.

[30] W. Zhao, Z. Ghorannevis, L. Chu, M. Toh, C. Kloc, P. H. Tan, and G. Eda. *ACS Nano* **2013**, 7, 791-797.

[31] K. K. Kam, and B. A. Parkinson. *J. Phys. Chem.* **1982**, 86, 463-467.

[32] A. Eftekhari. *J. Mater. Chem. A* **2017**, 5, 18299-18325.

[33] S. Zhang, C. G. Wang, M. Y. Li, D. Huang, L. J. Li, W. Ji, and S. Wu. *Phys. Rev. Lett.* **2017**, 119, 046101.

[34] S. Wang, W. Zhao, F. Giustiniano, and G. Eda. *Phys. Chem. Chem. Phys.* **2016**, 18, 4304-4309.

[35] S. Das, and J. Appenzeller. *Appl. Phys. Lett.* **2013**, 103, 103501.

[36] M. Yamamoto, S. Nakaharai, K. Ueno, and K. Tsukagoshi. *Nano Lett.* **2016**, 16, 2720-2727.

[37] C. Zhou, Y. Zhao, S. Raju, Y. Wang, Z. Lin, M. Chan, and Y. Chai. *Adv. Funct. Mater.* **2016**, 26, 4223-4230.

[38] H. Fang, S. Chuang, T. C. Chang, K. Takei, T. Takahashi, and A. Javey. *Nano Lett.* **2012**, 12, 3788-3792.

[39] P. Zhao, D. Kiriya, A. Azcatl, C. Zhang, M. Tosun, Y. S. Liu, M. Hettick, J. S. Kang, S. McDonnell, K. C. Santosh, J. Guo, K. Cho, R. M. Wallace, and A. Javey. *ACS Nano* **2014**, 8, 10808-10814.

[40] J. Yu, C. H. Lee, D. Bouilly, M. Han, P. Kim, M. L. Steigerwald, X. Roy, and C. Nuckolls. *Nano Lett.* **2016**, 16, 3385-3389.

[41] S. Das, M. Dubey, and A. Roelofs. *Appl. Phys. Lett.* **2014**, 105, 083511.

[42] S.-Y. Seo, J. Park, J. Park, K. Song, S. Cha, S. Sim, S.-Y. Choi, H. W. Yeom, H. Choi, and M.-H. Jo. *Nat. Electron.* **2018**, 1, 512-517.

[43] X. Zhang, X. F. Qiao, W. Shi, J. B. Wu, D. S. Jiang, and P. H. Tan. *Chem. Soc. Rev.* **2015**, 44, 2757-2785.

[44] A. Ortiz-Conde, F. J. García-Sánchez, J. Muci, A. Terán Barrios, J. J. Liou, and C.-S. Ho. *Microelectron. Reliab.* **2013**, 53, 90-104.

[45] K. Kim, S. Larentis, B. Fallahazad, K. Lee, J. Xue, D. C. Dillen, C. M. Corbet, and E. Tutuc. *ACS Nano* **2015**, 9, 4527-4532.

[46] N. Ma, and D. Jena. *2D Mater.* **2015**, 2, 015003.

[47] M. K. Bera, R. Kharb, N. Sharma, A. K. Sharma, R. Sehrawat, S. P. Pandey, R. Mittal, and D. K. Tyagi. *J. Electron. Mater.* **2019**, 48, 3504-3513.

[48] A. Allain, J. Kang, K. Banerjee, and A. Kis. *Nat. Mater.* **2015**, 14, 1195-1205.

[49] H.-M. Chang, K.-L. Fan, A. Charnas, P. D. Ye, Y.-M. Lin, C.-I. Wu, and C.-H. Wu. *J. Phys. D: Appl. Phys.* **2018**, 51, 135306.

[50] W. Zhao, Z. Ghorannevis, K. K. Amara, J. R. Pang, M. Toh, X. Zhang, C. Kloc, P. H. Tan, and G. Eda. *Nanoscale* **2013**, 5, 9677-9683.

[51] M. F. Daniel, B. Desbat, J. C. Lassegues, B. Gerand, and M. Figlarz. *J. Solid State Chem.* **1987**, 67, 235-247.

[52] F. S. Manciu, J. L. Enriquez, W. G. Durrer, Y. Yun, C. V. Ramana, and S. K. Gullapalli. *J. Mater. Res.* **2011**, 25, 2401-2406.

[53] K. Thummavichai, N. Wang, F. Xu, G. Rance, Y. Xia, and Y. Zhu. *R. Soc. Open Sci.* **2018**, 5, 171932.

[54] H. Li, G. Lu, Y. Wang, Z. Yin, C. Cong, Q. He, L. Wang, F. Ding, T. Yu, and H. Zhang. *Small* **2013**, 9, 1974-1981.

[55] R. Coehoorn, C. Haas, J. Dijkstra, C. J. F. Flipse, R. A. de Groot, and A. Wold. *Phys. Rev. B* **1987**, 35, 6195-6202.

[56] J. K. Huang, J. Pu, C. L. Hsu, M. H. Chiu, Z. Y. Juang, Y. H. Chang, W. H. Chang, Y. Iwasa, T. Takenobu, and L. J. Li. *ACS Nano* **2014**, 8, 923-930.

[57] T. Vogt, P. M. Woodward, and B. A. Hunter. *J. Solid State Chem.* **1999**, 144, 209-215.

[58] S. L. Li, H. Miyazaki, M. V. Lee, C. Liu, A. Kanda, and K. Tsukagoshi. *Small* **2011**, 7, 1552-1556.

[59] A. B. Sachid, M. Tosun, S. B. Desai, C. Y. Hsu, D. H. Lien, S. R. Madhvapathy, Y. Z. Chen, M. Hettick, J. S. Kang, Y. Zeng, J. H. He, E. Y. Chang, Y. L. Chueh, A. Javey, and C. Hu. *Adv. Mater.* **2016**, 28, 2547-2554.

[60] G. V. Resta, Y. Balaji, D. Lin, I. P. Radu, F. Catthoor, P. E. Gaillardon, and G. De Micheli. *ACS Nano* **2018**, 12, 7039-7047.

[61] M. Tosun, S. Chuang, H. Fang, A. B. Sachid, M. Hettick, Y. Lin, Y. Zeng, and A. Javey. *ACS Nano* **2014**, 8, 4948-4953.

[62] L. Yu, A. Zubair, E. J. Santos, X. Zhang, Y. Lin, Y. Zhang, and T. Palacios. *Nano Lett.* **2015**, 15, 4928-4934.

Chapter 6*

Light-Programmable Nonvolatile Memory in the $BP/SrTiO_3$ Semiconductor/Insulator Heterostructure

In this chapter, a light programmable nonvolatile memory based on $BP/SrTiO_3$ was demonstrated. First, BP transistors on the silicon substrate were tested, which showed a p-type transport behavior in the depletion mode and a low photoresponsivity. Inspired by the photodoping effect in wide-gap insulators, BP devices on $SrTiO_3$ were then studied, which showed an enhanced photoresponsivity as well as a persistent switching on the conductivity. Then, the temperature-dependent photo switching behavior was studied under different light illuminations to understand its mechanism. Finally, the light-tunable multistage nonvolatile memory was demonstrated in the $BP/SrTiO_3$ heterostructure, which showed a very long retention time at low temperature.

---

*This section has been published substantially as "Fucai Liu, **Chao Zhu**, Lu You, Shi-Jun Liang, Shoujun Zheng, Jiadong Zhou, Qundong Fu, Yongmin He, Qingsheng Zeng, Hong Jin Fan, Lay Kee Ang, Junling Wang, and Zheng Liu. 2D Black Phosphorus/$SrTiO_3$-Based Programmable Photoconductive Switch. *Advanced Materials*, **2016**, 28, 7768-7773."

6.1 Introduction

Heterostructures integrated by different functional materials with novel properties and external-stimuli-tunable functions are of great interest and have attracted wide attentions, among which the transition metal oxides are extensively studied.[1-10] Since the properties of transition metal oxide are very sensitive to structural distortions and crystal chemistry, heterostructures formed by transition metal oxides provide a good platform to study the interface induced novel phenomena and the external manipulation of heterostructure properties.[6] A variety of interface induced phenomena have been reported, such as the superconductivity and ferromagnetism at the interface of two dielectrics,[4,5] ferromagnetic metallic states in the antiferromagnetic insulator formed superlattice,[1] and the interface-induced high temperature superconductor in FeSe/$SrTiO_3$.[3] $SrTiO_3$ is one of the most extensively used materials in the study of oxide interface physics and novel oxide electronics. For example, the lanthanum aluminate ($LaAlO_3$) is an insulator with a large bandgap above 6 eV[11] and the strontium titanate ($SrTiO_3$) is a wide-band semiconductor with an indirect bandgap of 3.25 eV,[12] both of which are insulating normally. However, in the $LaAlO_3$/$SrTiO_3$ superlattice, the interface shows the conductivity,[2] superconductivity and ferromagnetism.[4,5] For the monolayer FeSe grown on $SrTiO_3$, a high-temperature superconductivity has been observed, with the transition temperature above 100 K.[9] Light induced magnetism and photodoping effect have also been reported in the $SrTiO_3$ based heterostructures.[7,8,10]

2D/3D heterostructures have been widely studied, especially for the light-based applications such as photo detectors and solar cells.[13-20] For example, by transferring monolayer MoS_2 onto the p-type doped Si to form a type-II heterojunction, a photovoltaic device was demonstrated with a power conversion efficiency of 5.23%, which was higher than the pure monolayer TMD-based solar cells.[13] A theoretical study has shown that the two-junction tandem device formed by 2D materials on silicon will show a much higher power conversion efficiency than the single-junction device based on 2D materials.[14] On the other hand, inspired by the novel properties discovered in the interfaces of transition metal oxides, stacking functional 2D materials with strongly correlated oxide substrate will

provide a new way to fabricate devices with novel phenomena and unique properties. The black phosphorus (BP) is a 2D material which shows excellent electronic properties, such as a high hole mobility up to 1000 $cm^2 V^{-1}s^{-1}$,[21] an on/off ratio up to 10^5,[21-23] the strong in-plane anisotropy,[24-26] and a direct bandgap ranging from 0.3 V to 1.8 V with decreasing thickness.[27,28] Such a wide range of layer-dependent bandgap makes BP a very promising 2D material for broadband optoelectronic applications.[29-31] In this work, a mixed 2D/3D heterostructure is demonstrated, which is based on the narrow-band multilayer BP and the wide-band $SrTiO_3$. In contrast to the BP devices fabricated on SiO_2 substrate, remarkable optoelectronic functionalities have been observed, with a significantly enhanced photocurrent on/off ratio of up to 10^6 and the light-tunable persistent switching on the conductivity. Based on these results, a light-tunable multistage nonvolatile memory is demonstrated, providing a new strategy for the light-controlled 2D nonvolatile memory.

6.2 Experimental Methods

6.2.1 Device Fabrication

BP flakes were first mechanically exfoliated on to the silicon or $SrTiO_3$ substrates from the single crystals synthesized by the CVT method. Then samples with suitable thickness (above 10 nm) were selected for the device fabrication. The thickness was estimated from the color of the sample, which was finally confirmed using the AFM after all the optoelectronic measurements were finished. Since the $SrTiO_3$ was non-conductive, the standard EBL process was not suitable in this case. For simplification, the maskless photolithography was used to fabricate the BP/$SrTiO_3$ two-electrode devices. The sample was coated with a layer of the photoresist S1805. Electrode patterns were then exposed by the UV light in a Microtech Laserwriter system and developed by the developer MF319. The photoresist coating, the electrode patterning and the development were all performed inside a yellow-light room to avoid unnecessary exposures. The metal deposition (5 /50 nm Ti/Au) was performed using the electron beam evaporation.

6.2.2 TEM Characterization

For the HRTEM characterization, BP thin films were directly transferred onto an amorphous holey SiN TEM grids (Norcada, Inc.). Then a suitable suspended sample was characterized by an FEI Tecnai G2-F20 TEM, with an accelerating voltage at 200 kV. The electron dose was reduced to minimize the radiation damage.

6.2.3 Raman Characterization

Raman spectra were measured by a WITec confocal Raman system, with an excitation laser wavelength of 532 nm. The laser was focused by a 100 × objective lens (NA = 0.95). To avoid laser-induced ablation of samples, Raman signals were measured at low power levels. For the polarized Raman measurement, the angle between polarization direction of the excitation light and the *b*-axis of the BP sample was tuned by rotating the crystal. An analyzer was used to detect the parallel polarized Raman signals or the perpendicular polarized Raman signals.

6.2.4 Transmission Spectrum Characterization

The transmission spectrum of the $SrTiO_3$ single crystal was measured by the Shimadzu UV-3600 UV-VIS-NIR Spectrophotometer with double beams. The thickness of the $SrTiO_3$ was around 500 μm.

6.2.5 Optoelectronic Measurement

All the electronic and optoelectronic measurements were performed by an Agilent B1500A semiconductor analyzer with the devices placed in a MicroXact probe station under vacuum, with the temperature ranging from room temperature to 50 K. The light excitation was provided by solid state laser diodes with different wavelengths of 405 nm, 532 nm, and 633 nm, respectively. A 365 nm lamp was used for the UV illumination.

6.3 Principle Outcomes

6.3.1 Basic Characterization of BP and $SrTiO_3$

6.3.1.1 Basic Characterization of BP

Figure 6.1a shows the side view of the crystal structure of BP. And Figure 6.1b shows a typical optical image and the corresponding height profile of the BP flake. In this work, samples with thickness larger than 10 nm were studied, due to the degradation of ultrathin BP films in the ambient environment. Figure 6.1c shows the HRTEM image of BP, which shows an orthorhombic structure with the lattice constants of 3.37 Å and 4.42 Å in the (100) (zigzag) and (001) (armchair) direction, respectively. A Raman spectrum of BP is shown in Figure 6.1d, where three peaks exist. The three Raman peaks at around 365, 440 and 470 cm^{-1} are corresponding to the A_g^1, B_{2g} and A_g^2 modes, respectively, which are consistent with previous reports.[32] Figure 6.1e shows the Raman spectra of BP at different angles under the parallel configurations, which shows a strong angle dependence. The angle is tuned by rotating the BP sample in the xy plane. The intensity of the A_g^2 peak under parallel configuration is plotted as a function of the angle (Figure 6.1f), from which the crystal orientation can be determined. According the previous reports,[33] the armchair direction of the BP is nearly parallel to the polarization direction of the incident laser when the sample angle is 0°.

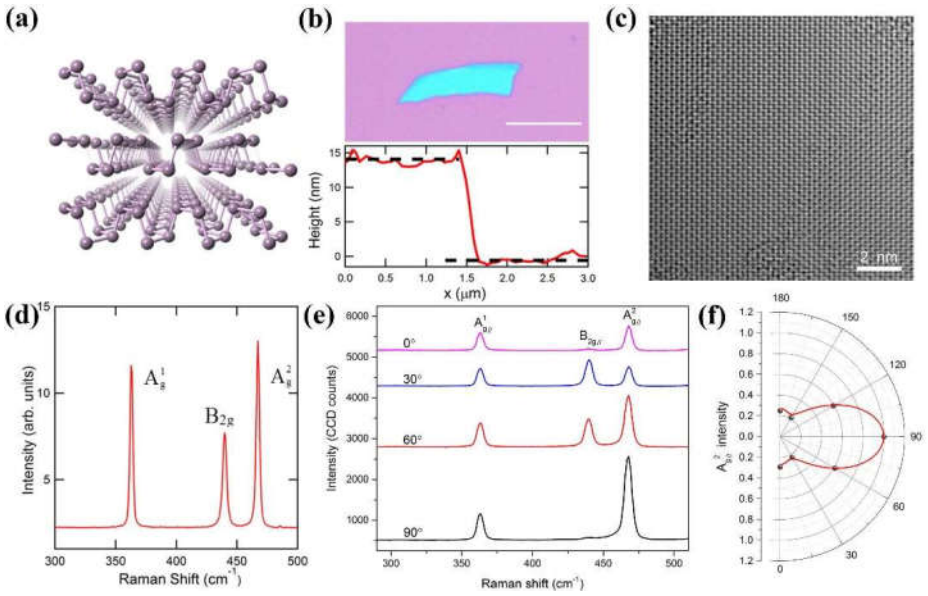

Figure 6.1 Basic characterization of BP. (a) Side view of the BP crystal structure. (b) A typical optical image of the BP and its thickness profile measured by AFM. Scale bar: 10 μm. (c) An HRTEM image of BP. (d) Raman spectrum of BP with three major modes. (e) Polarized Raman spectra of BP under different polarization angle. (f) Fitting of the polarization-angle-dependent intensity of A_g^2 peak.

6.3.1.2 Transmission Spectrum of $SrTiO_3$

The transmission spectrum of the $SrTiO_3$ substrate (0.5 mm thick) is shown in Figure 6.2. The locations of the red light (633 nm) and the UV light (365 nm) are marked by the arrows. As shown from the transmission spectrum, more than 50% light can go through the $SrTiO_3$ substrate at the wavelength of 633 nm, while at 365 nm, almost no light could transmit through the substrate.

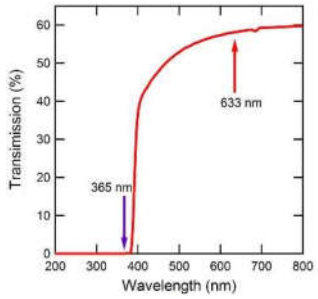

Figure 6.2 A transmission spectrum of a 500 μm thick $SrTiO_3$ substrate, with the wavelength

of the red and UV light indicated by the arrows.

6.3.2 Optoelectronic Measurement of BP on Silicon Substrate

The BP transistor on the silicon substrate was measured first for comparison. Its FET and photo response performances were measured chamber under vacuum at room temperature. Figure 6.3a shows the I_d-V_d output curve. The almost linear I_d-V_d curve at low voltage bias indicates the low Schottky barrier height at the electrode contacts. The I_d-V_g transfer curve is shown in Figure 6.3b, showing a p-type transport behavior with an FET on/off ratio of up to 10^5. By fitting the curve in the linear region from -10 V to -30 V, the mobility of the channel is extracted to be 149 $cm^2V^{-1}s^{-1}$, which is comparable to the values in previous reports.[21,22] The photo response measurement was performed by alternately turning on and off the 633 nm excitation light, with V_d = 5 V and V_g = 40 V. The photo response at other gate voltages was also measured, but the response under V_g = 40 V was higher. Figure 6.3c shows the current variation with and without light illumination. The photoresponsivity can be calculated by $R = I_{ph}/P$ (I_{ph} is generated photocurrent, P is the light power absorbed by the channel). The photoresponsivity is calculated to be 2.5 A/W, similar to the reported value of 0.66 A/W.[31] This might be due to the difference of the applied gate voltage and drain voltage, leading to the different Schottky barrier height and charge separation rate. 2D semiconductors have a strong photon-electron coupling, which is due to the band nesting.[34] For MoS_2, the gap between the nested conduction and valence bands is about 2 ~ 3 eV.[34] While for BP, it is about 3 ~ 4 eV.[35] As a result, the photoresponsivity of BP in the visible regime is much smaller than that of MoS_2, whose photoresponsivity can reach up to 2200 A/W.[13] This limits the applications of BP in photo detectors.

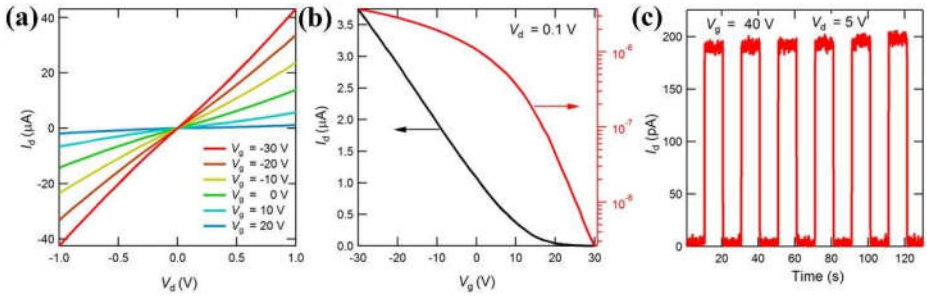

Figure 6.3 BP transistor performances on the silicon substrate. (a) I_d-V_d curve of the device. (b)

I_d-V_g transfer curve of the device. (c) Red light photo response of the device at V_g = 40 V and V_d = 5 V.

6.3.3 Light-Tuned BP/$SrTiO_3$ Nonvolatile Memory

6.3.3.1 Light-Tuned Persistent Switching of BP/$SrTiO_3$

For the BP devices on the $SrTiO_3$ substrates, dramatic different behavior can be observed due to the strong interaction from the substrate. When the device was alternately shined by the red and UV light, significant drain current change was observed. As shown in Figure 6.4a, at the room temperature, when the device is illuminated by the red light (120 s), the drain current increases gradually. When the red light is turned off, the current keeps almost constant (the on state). Then a pulse (2 s) of UV light shines onto the device, leading to the sharp drop of the current. After the UV light is turned off, the current increases slowly (the off state). The current change is well repeatable under the alternating illumination states. Figure 6.4b shows the I_d-V_d curves of the device under the on state (immediately after turning off red light) and the off state (immediately after turning off the UV light), respectively. By subtracting the off current from the on current, the light induced responsivity of current change is calculated to be 1.1×10^5 A/W, which is about 10^5 times larger than that for the BP transistor on the silicon substrate.[31]

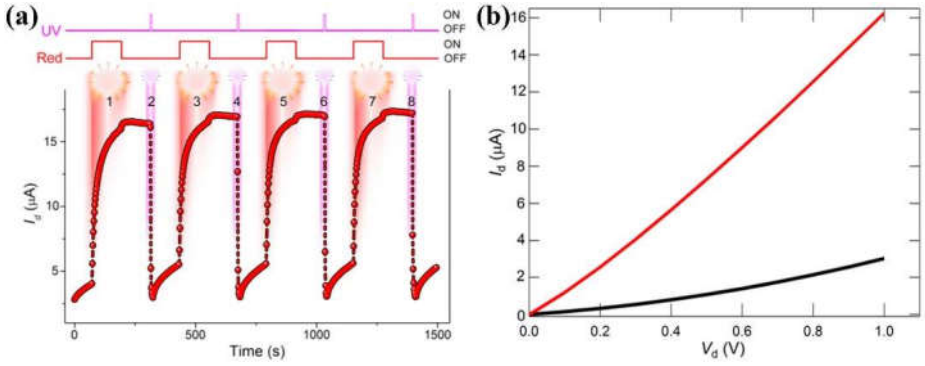

Figure 6.4 Light-induced nonvolatile memory in the BP/$SrTiO_3$ device at room temperature. (a) Alternating current change in BP upon red and UV light illumination. (b) I_d-V_d curve of the device in on (red) and off (black) states.

6.3.3.2 Wavelength-Dependent Photo Response

To understand mechanism of the light-induced persistent photocurrent in the BP/$SrTiO_3$ heterostructure, the wavelength dependent photo response measurement was performed with the fixed laser intensity and illumination time. The temperature was set at 50 K. The source-drain bias was set at 1 V. And 633, 532, and 455 nm laser sources were used. As shown in Figure 6.5, the current after 633 nm illumination is about 1.8 μA. While the current after 532 nm illumination is about 125 nA. And for 455 nm, the current decreases to about 40 nA. This indicates that the wavelength plays an important role in the persistent photoconductivity. The results can be explained by a model based on electron-hole generation and recombination process related to light absorption of defects in $SrTiO_3$.[10] In the bandgap of the $SrTiO_3$, there are lots of defect states.[36,37] Due to the wavelength-dependent light absorption, light with different wavelengths can excite electrons in different defect states and will be absorbed differently throughout the $SrTiO_3$ substrate. As previously shown in Figure 6.2, the 365 nm UV light shows almost zero transmission through the $SrTiO_3$ substrate where the 633 nm red light shows a transmission larger than 50%. As a result, UV light can only travel for a very limited distance beneath the BP/$SrTiO_3$ interface. Since the 365 nm UV light has a higher photon energy than the bandgap, electrons in all defect states can be excited, which will then diffuse into the deep regions of $SrTiO_3$ and be trapped by various defects. In this way, as shown in Figure 6.5e, net positive charges will be produced in $SrTiO_3$ near the BP/$SrTiO_3$ interface, which will then act like a positive gate and turn off the BP channel. While red light can travel through the entire sample and excite electrons trapped in the shallow defects in the deep regions. The excited electrons will then diffuse back to the surface region of $SrTiO_3$ and recombine with the previously produced positive charges (Figure 6.5f). The UV light induced positive charges near the BP/$SrTiO_3$ interface will be neutralized and the UV light induced gate effect will be erased. This light-tunable gating effect at the BP/$SrTiO_3$ interface enables the high photoresponsivity and the persistent conductivity of the BP.

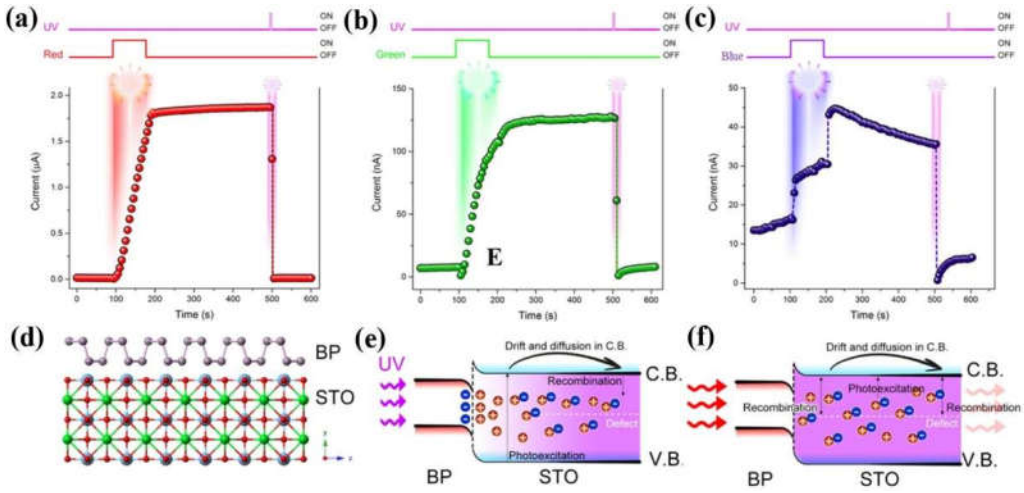

Figure 6.5 Nonvolatile change in the conductivity of BP upon light illumination with different wavelengths at 50 K. Current change by (a) red, (b) green, and (c) blue light. (d) Schematic diagram of the BP/$SrTiO_3$ heterostructure. Electron excitation and recombination in $SrTiO_3$ upon (e) UV and (f) red light illumination.

The heterostructure of MoS_2 and $SrTiO_3$ was also fabricated to confirm the previous explanations. Its photo response is shown in Figure 6.6, which also exhibits the persistent change in conductivity under different light illumination. Different from the BP/$SrTiO_3$ device, the conductivity of the MoS_2 increases upon UV light illumination and decreases upon red light illumination. This is because that the MoS_2 is n-type. Under the UV light induced positive gating effect, MoS_2 will be further turned on. This is consistent with the previous explanations.

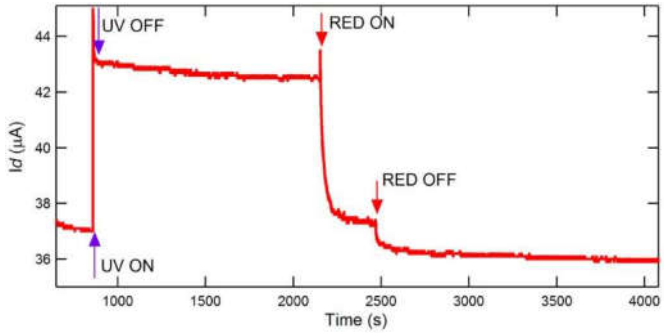

Figure 6.6 Similar persistent current in the MoS_2/$SrTiO_3$ heterostructure. Current increases upon UV light illumination and decreases upon red light illumination.

6.3.3.3 Temperature-Dependent Time Constant

To further explore the optical gating effect induced persistent current, the temperature-dependent photo response was studied from 50 K to room temperature (300 K). The time resolved response of the current upon and after light illumination was measured at different temperatures. Three processes were studied, including the current rising process upon red light illumination, the current decaying process after red light illumination (the on state), and the current rising process after the UV light illumination (the off state). The normalized time resolved current change of each process is shown in Figure 6.7. The time constant can be obtained by fitting the time resolved curve using exponential functions, which are $I = a\left(1 - e^{-t/t_0}\right) + b$ for the current rising and $I = ae^{-t/t_0} + b$ for the current decay. The t_0 is the time constant.

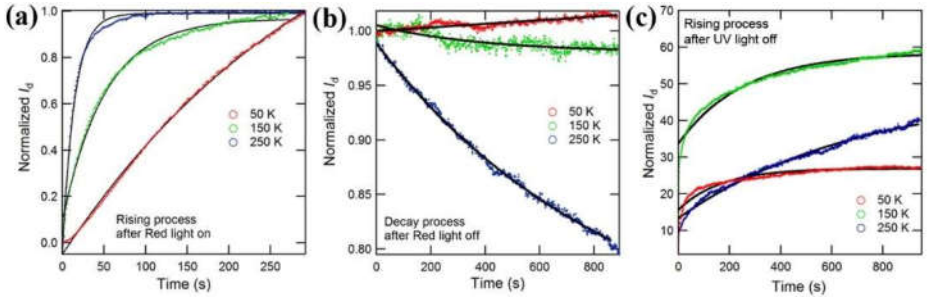

Figure 6.7 Current change of BP on $SrTiO_3$ at different temperatures for different processes. Black solid lines are for the fitting of time constant. (a) Current rising upon red light illumination. (b) Current decay after turning off red light. (c) Current rising after UV light illumination.

The temperature-dependent time constant is plotted in Figure 6.8. As previously discussed, the current rising upon red light illumination is due to the diffusion of photoexcited electrons in the conduction band and the subsequent recombination with positively charged defects. This process is mainly influenced by the scattering of the excited electrons by phonon scattering from the lattice and impurity scattering from the defects. When there is no defect, the electron relaxation time τ can be solely determined by the phonon time τ_0 at different temperatures. With the existence of defects, τ will also be affected by the scattering from the defects in the $SrTiO_3$. Then the overall time constant can be described by $\tau_t = \tau_0 e^{E_0/k_B T}$, where E_0 is the activation energy of traps and k_B is the Boltzmann

constant. For the current decaying process after red light illumination, it is related to the electron redistribution in various defect states, where the relaxation time is mainly determined by the electron energy and given by $\tau \propto T^{\frac{3}{2}}$. For the current rising after UV light illumination, both of two mechanisms are considered, where the overall relaxation time is defined by $\tau^{-1} = \sum_j \tau_j{}^{-1}$ and j represents different relaxation mechanism.

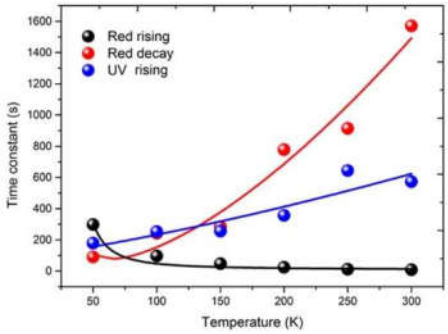

Figure 6.8 Temperature-dependent time constant for different processes. The time constant of current rising upon red light illumination, current decay after turning off red light, and current rising after UV light illumination is shown by black, red, and blue spheres, respectively. Fitting results are shown by solid curves.

6.3.3.4 Light-Tunable Multistage Nonvolatile Memory

The light-induced persistent switching of conductivity can be used for nonvolatile memory devices. As shown in Figure 6.9a, at 50 K, by shining the device with red light step by step, multiple persistent current stages can be achieved, which can be erased by a short UV light (2 s). Figure 6.9b shows the photocurrent change under alternating red and UV light illuminations, with V_d = 1 V. By alternately shining the red and UV light onto the device, the device can be tuned between the high-conductive (on) and low-conductive (off) states, which shows good repeatability and high stability. Figure 6.9c shows the I_d-V_d curves under the on and off states, which shows a current on/off ratio of up to 10^6. Apart from the high photosensitivity, the light-induced current change has a very long retention time. As shown in Figure 6.9d, after turning off the light, the on and off current keeps almost constant for more than 10^4 s. The highly distinguished on and off states and their long retention time

make the BP/$SrTiO_3$ heterojunction device a good candidate for the multistage nonvolatile memory at low temperature.

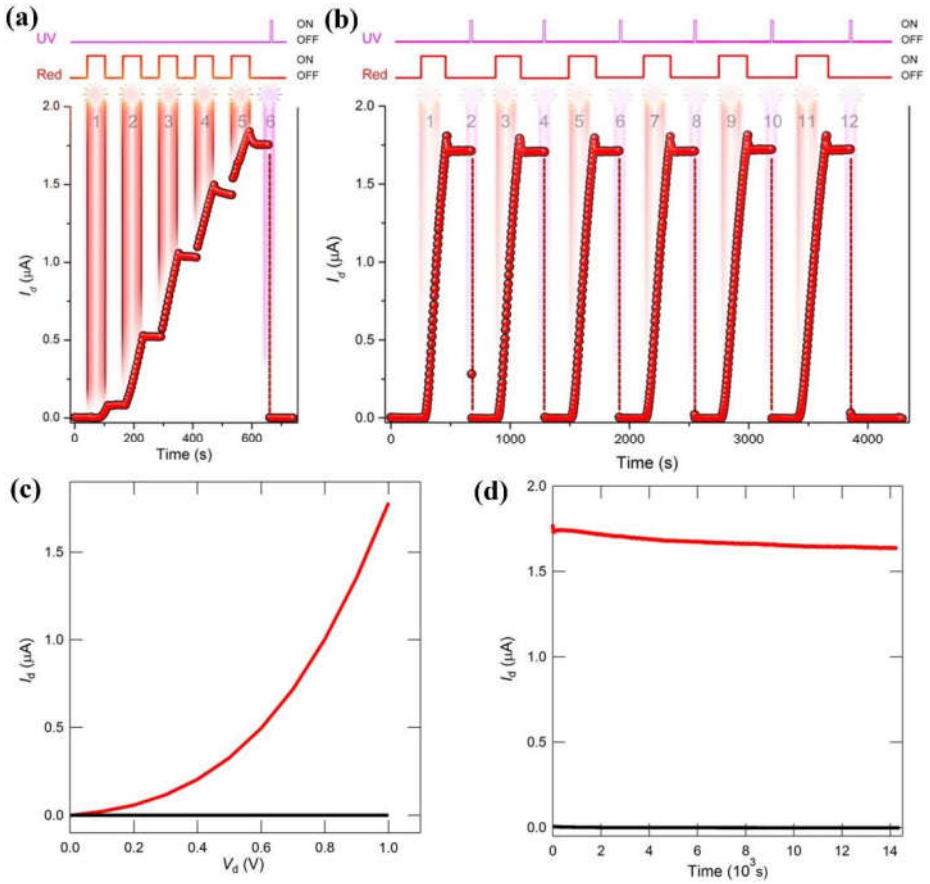

Figure 6.9 Light-induced nonvolatile memory in the BP/$SrTiO_3$ device at 50 K. (a) Multistage nonvolatile memory tuned by red light and reset by UV light. (b) Alternating on and off switching of the device. (c) I_d-V_d curve of the device in on (red) and off (black) states. (d) The nonvolatile on (red) and off (black) states with long retention time.

6.4 Conclusions

In conclusion, the giant photoresponsivity has been observed in the BP/$SrTiO_3$ heterostructure devices. The responsivity of light induced current change reaches above 10^5 A/W. The light-induced persistent current is observed, which shows a retention time longer than 10^4 s at low temperature. Based on this, the light-tunable multistage nonvolatile memory is demonstrated, where the conductivity of BP can be tuned to a series of stepped

levels by repeated red light illuminations and can be reset by the UV light illumination. Wavelength-dependent light-induced persistent current measurement shows that among 455, 532, and 633 nm light illumination, the 633 nm light illumination can induce the most significant photocurrent with an on/off ratio up to 10^6. The light-induced persistent switching on the conductivity is explained by the light-induced gating effect in the BP/$SrTiO_3$ interface. This light-induced gating effect provides a new strategy to enhance the photoresponsivity of materials. And the light-induced persistent switching on the conductivity adds more options for the light-controlled nonvolatile memory devices.

References

[1] T. Koida, M. Lippmaa, T. Fukumura, K. Itaka, Y. Matsumoto, M. Kawasaki, and H. Koinuma. *Phys. Rev. B* **2002**, 66, 144418.

[2] A. Ohtomo, and H. Y. Hwang. *Nature* **2004**, 427, 423-426.

[3] A. Gozar, G. Logvenov, L. F. Kourkoutis, A. T. Bollinger, L. A. Giannuzzi, D. A. Muller, and I. Bozovic. *Nature* **2008**, 455, 782-785.

[4] D. A. Dikin, M. Mehta, C. W. Bark, C. M. Folkman, C. B. Eom, and V. Chandrasekhar. *Phys. Rev. Lett.* **2011**, 107, 056802.

[5] L. Li, C. Richter, J. Mannhart, and R. C. Ashoori. *Nat. Phys.* **2011**, 7, 762-766.

[6] H. Y. Hwang, Y. Iwasa, M. Kawasaki, B. Keimer, N. Nagaosa, and Y. Tokura. *Nat. Mater.* **2012**, 11, 103-113.

[7] Y. Lei, Y. Li, Y. Z. Chen, Y. W. Xie, Y. S. Chen, S. H. Wang, J. Wang, B. G. Shen, N. Pryds, H. Y. Hwang, and J. R. Sun. *Nat. Commun.* **2014**, 5, 5554.

[8] W. D. Rice, P. Ambwani, M. Bombeck, J. D. Thompson, G. Haugstad, C. Leighton, and S. A. Crooker. *Nat. Mater.* **2014**, 13, 481-487.

[9] J. F. Ge, Z. L. Liu, C. Liu, C. L. Gao, D. Qian, Q. K. Xue, Y. Liu, and J. F. Jia. *Nat. Mater.* **2015**, 14, 285-289.

[10] A. L. Yeats, Y. Pan, A. Richardella, P. J. Mintun, N. Samarth, and D. D. Awschalom. *Sci. Adv.* **2015**, 1, e1500640.

[11] G. Murtaza, and I. Ahmad. *J. Appl. Phys.* **2012**, 111, 123116.

[12] K. van Benthem, C. Elsässer, and R. H. French. *J. Appl. Phys.* **2001**, 90, 6156-6164.

[13] M. L. Tsai, S. H. Su, J. K. Chang, D. S. Tsai, C. H. Chen, C. I. Wu, L. J. Li, L. J. Chen, and J. H. He. *ACS Nano* **2014**, 8, 8317-8322.

[14] D. Jariwala, A. R. Davoyan, J. Wong, and H. A. Atwater. *ACS Photonics* **2017**, 4, 2962-2970.

[15] H. Choi, K. A. Min, J. Cha, and S. Hong. *Phys. Chem. Chem. Phys.* **2018**, 20, 25240-25245.

[16] R. K. Chowdhury, R. Maiti, A. Ghorai, A. Midya, and S. K. Ray. *Nanoscale* **2016**, 8, 13429-13436.

[17] D. Li, Z. Xiao, H. R. Golgir, L. Jiang, V. R. Singh, K. Keramatnejad, K. E. Smith, X. Hong, L. Jiang, J.-F. Silvain, and Y. Lu. *Adv. Electon. Mater.* **2017**, 3, 1600335.

[18] R. K. Chowdhury, T. K. Sinha, A. K. Katiyar, and S. K. Ray. *Nanoscale* **2017**, 9, 15591-15597.

[19] H. Henck, Z. Ben Aziza, O. Zill, D. Pierucci, C. H. Naylor, M. G. Silly, N. Gogneau, F. Oehler, S. Collin, J. Brault, F. Sirotti, F. Bertran, P. Le Fèvre, S. Berciaud, A. T. C. Johnson, E. Lhuillier, J. E. Rault, and A. Ouerghi. *Phys. Rev. B* **2017**, 96, 115312.

[20] O. Lopez-Sanchez, E. Alarcon Llado, V. Koman, A. Fontcuberta i Morral, A. Radenovic, and A. Kis. *ACS Nano* **2014**, 8, 3042-3048.

[21] A. Chernikov, T. C. Berkelbach, H. M. Hill, A. Rigosi, Y. Li, O. B. Aslan, D. R. Reichman, M. S. Hybertsen, and T. F. Heinz. *Phys. Rev. Lett.* **2014**, 113, 076802.

[22] H. Liu, A. T. Neal, Z. Zhu, Z. Luo, X. Xu, D. Tomanek, and P. D. Ye. *ACS Nano* **2014**, 8, 4033-4041.

[23] J. Qiao, X. Kong, Z. X. Hu, F. Yang, and W. Ji. *Nat. Commun.* **2014**, 5, 4475.

[24] Z. Luo, J. Maassen, Y. Deng, Y. Du, R. P. Garrelts, M. S. Lundstrom, P. D. Ye, and X. Xu. *Nat. Commun.* **2015**, 6, 8572.

[25] X. Wang, A. M. Jones, K. L. Seyler, V. Tran, Y. Jia, H. Zhao, H. Wang, L. Yang, X. Xu, and F. Xia. *Nat. Nanotechnol.* **2015**, 10, 517-521.

[26] H. Yuan, X. Liu, F. Afshinmanesh, W. Li, G. Xu, J. Sun, B. Lian, A. G. Curto, G. Ye, Y. Hikita, Z. Shen, S. C. Zhang, X. Chen, M. Brongersma, H. Y. Hwang, and Y. Cui. *Nat. Nanotechnol.* **2015**, 10, 707-713.

[27] V. Tran, R. Soklaski, Y. Liang, and L. Yang. *Phys. Rev. B* **2014**, 89, 235319.

[28] J. Pei, X. Gai, J. Yang, X. Wang, Z. Yu, D. Y. Choi, B. Luther-Davies, and Y. Lu. *Nat. Commun.* **2016**, 7, 10450.

[29] M. Buscema, D. J. Groenendijk, S. I. Blanter, G. A. Steele, H. S. van der Zant, and A. Castellanos-Gomez. *Nano Lett.* **2014**, 14, 3347-3352.

[30] M. Buscema, D. J. Groenendijk, G. A. Steele, H. S. van der Zant, and A. Castellanos-Gomez. *Nat. Commun.* **2014**, 5, 4651.

[31] N. Youngblood, C. Chen, S. J. Koester, and M. Li. *Nat. Photon.* **2015**, 9, 247-252.

[32] H. B. Ribeiro, M. A. Pimenta, C. J. de Matos, R. L. Moreira, A. S. Rodin, J. D. Zapata, E. A. de Souza, and A. H. Castro Neto. *ACS Nano* **2015**, 9, 4270-4276.

[33] J. Wu, N. Mao, L. Xie, H. Xu, and J. Zhang. *Angew. Chem. Int. Ed. Engl.* **2015**, 54, 2366-2369.

[34] A. Carvalho, R. M. Ribeiro, and A. H. Castro Neto. *Phys. Rev. B* **2013**, 88, 115205.

[35] J. Wu, G. K. Koon, D. Xiang, C. Han, C. T. Toh, E. S. Kulkarni, I. Verzhbitskiy, A. Carvalho, A. S. Rodin, S. P. Koenig, G. Eda, W. Chen, A. H. Neto, and B. Ozyilmaz. *ACS Nano* **2015**, 9, 8070-8077.

[36] H. Yamada, and G. R. Miller. *J. Solid State Chem.* **1973**, 6, 169-177.

[37] C. Lee, J. Destry, and J. L. Brebner. *Phys. Rev. B* **1975**, 11, 2299-2310.

Chapter 7

Discussion and Future Work

This chapter first summarizes the findings and outcomes of the thesis project. Three types of 2D systems were studied for the light control of electronic properties, based on which light-tunable 2D electronic devices were demonstrated, including a light-tunable TaS_2 CDW oscillator, a WSe_2 NOR gate circuit directly patterned by laser ablation, and a light-tunable multistage nonvolatile memory based on BP/$SrTiO_3$. Then, a reconnaissance study is discussed. And the strategies and opportunities of future work are discussed, which includes strategies to improve performances of the presented devices and other possible applications where light control can be used.

7.1 General Discussion

In this thesis, the light-tunable two-dimensional electronic devices have been discussed. The light tunability has been studied in systems including the metal, the semiconductor, and the narrow-gap/wide-gap semiconductor heterostructure, showing that the light can be widely used as a tool to tune the electronic properties of 2D materials and 2D electronic devices. Specifically, the light tunability has been explored in details in the following three aspects: (1) the CDW phase transitions in the metallic 1T-TaS_2, (2) the hole doping in the semiconducting 2H-WSe_2, and (3) the persistent conductivity switching in the narrow-gap BP and wide-gap $SrTiO_3$ heterostructure.

First, the light tunability of the CDW transitions in metallic 1T-TaS_2 at room temperature has been studied. First the Joule heating induced local temperature change of the sample was evaluated according to the temperature-dependent *I-V* behaviors. The simulation of the Joule heating induced temperature change indicated that for the bias-induced phase transition between NCCDW and ICCDW, the Joule heating effect cannot be neglected. In details, for the NCCDW-ICCDW transition, the field-induced depinning effect dominates the transition and the Joule heating effect is secondary important. While for the transition from ICCDW back to NCCDW, the Joule heating effect is dominant. Inspired by this, the light heating effect was demonstrated to be able to tune the bias-induced CDW phase transition at the room temperature. This light tunability enabled the use of light to tune the CDW oscillators based on 1T-TaS_2. It was shown that under light illumination, the output frequency of the TaS_2 oscillator could be tuned continuously up to 30% from 1.093 to 0.799 MHz. This light tunability of CDW phases provides more options for controlling the properties of CDW materials and their applications in high frequency electronics.

Second, light-induced controlled hole doping was studied in the semiconducting 2H-WSe_2. It was shown that under moderate laser ablation of the WSe_2 conducting channel, hole doping could be induced to the WSe_2 FET devices. By controlling the laser power and ablation time, different levels of hole doping could be achieved. The light-induced hole doping was attributed to the ablation-induced reduction in Se and the subsequent

oxidization, which was confirmed by XPS, STEM, and EELS characterization of heavily ablated WSe_2. No signals of the oxidation were observed in the moderately ablated sample, which might be due to the insufficient amount of the tungsten oxide. According to the photocurrent mapping results, under a small amount of ablation, a vertical-lateral hybrid P-N junction could be formed. While under enough ablation, the ablated area would be p-type doped throughout the whole thickness and a pure lateral P-N junction could be formed. Based on the light-induced controlled hole doping, the direct patterning of the WSe_2 logic circuit was demonstrated. A WSe_2 based NOR gate circuit was fabricated, which showed a comparable performance with previously reported NOR gates using other fabrication methods. This light-induced doping method enables the selective area doping and the direct writing of 2D logic circuits, avoiding the complex procedures to pattern and remove passive layers. Besides, using this method, P-N junctions with complex profiles can be constructed by carefully controlling the ablation conditions.

Third, the light-tunable persistent switching of the conductivity has been studied in the narrow-band BP and wide-band $SrTiO_3$ heterostructure. It was shown that the red-light illumination could switch the BP channel to an on state and the UV-light illumination could switch the BP channel to an off state. With a series of red-light illumination, the conductivity of BP could be tuned to a series of stages, which could be reset with the UV-light illumination. At low temperature, the light-induced conductivity switching could be retained for a very long time (no significant change over 10^4 seconds). The mechanism of this persistent switching was attributed to the light-induced gating effect due to the electron redistribution in the defect states. After UV-light illumination, net positively charged defects would be produced near the BP/$SrTiO_3$ interface, which would act like a positive gate. After red-light illumination, electrons trapped in the shallow defect states could be excited to the conduction band and then diffuse and recombine with positively charged defects, in which way the charged defects near the BP/$SrTiO_3$ interface would be neutralized and the optical gating effect would be erased. This light-induced persistent switching on conductivity adds more possibilities for the light-controlled multistage nonvolatile memories.

7.2 Reconnaissance Work Not Included in Main Chapters

As previously reported by Cho et al.,[1] by laser ablation of 2H-$MoTe_2$, the semiconducting 2H-$MoTe_2$ could be changed to the metallic 1T'-$MoTe_2$. During the transistor fabrication process, before the deposition of the electrodes, the contact areas could be patterned to the 1T' phase by laser ablation. Then after the electrodes were deposited, the 1T' ohmic contact would be achieved in the $MoTe_2$ transistor, leading to the enhancement of the mobility (Figure 7.1). However, during repeating this method, it was found that the method could not be well repeated. The fabricated $MoTe_2$ devices usually showed poor performances, featured by a relatively high Schottky barrier and the asymmetric barrier height at source and drain electrodes. The output characteristic of the transistors was often shown as Figure 7.2a, with a large difference in the current for the opposite bias and very nonlinear I_d-V_d curves. The device performance could be greatly improved by vacuum annealing. As shown in Figure 7.2b, after annealing, the I_d-V_d curves became much more linear within -2 to 2 V drain bias, the linearity of the output characteristic suggested the low contact barrier. Besides, before annealing the device was ambipolar and the current was below 20 nA at V_g = 50 V. While after annealing, the device was n-type and the current increased to above 5 μA at V_g = 60 V. This change in the device performance might be due to the improved contact quality during the annealing. For some other devices, the device performance was not improved much even after the annealing. And for almost all the pristine fabricated devices (above 10 devices), the performance was much inferior than the reported results. This might be due to that the contact areas were not fully changed to the 1T' phase and the metallic 1T' phase was somehow oxidized before deposition of the metal electrodes.

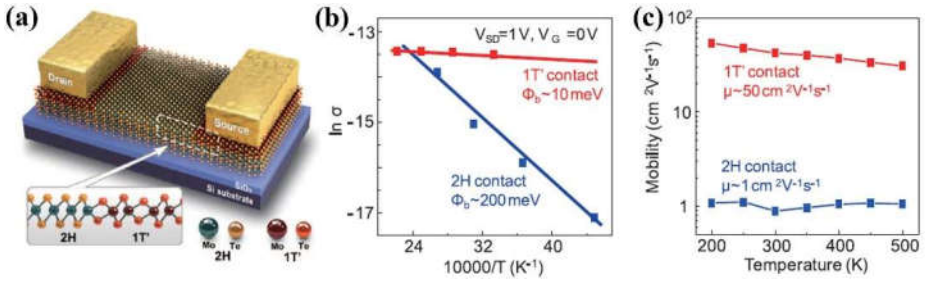

Figure 7.1 Laser-ablation induced phase transition in 2H-$MoTe_2$ and formation of the ohmic contact. (a) Schematic diagram of the laser-ablation patterning of the ohmic contact. (b) Arrhenius

plots for extraction of contact barrier height. (c) Comparison of mobility between two kinds of contact. Reproduced with permission.[1] Copyright 2015, AAAS.

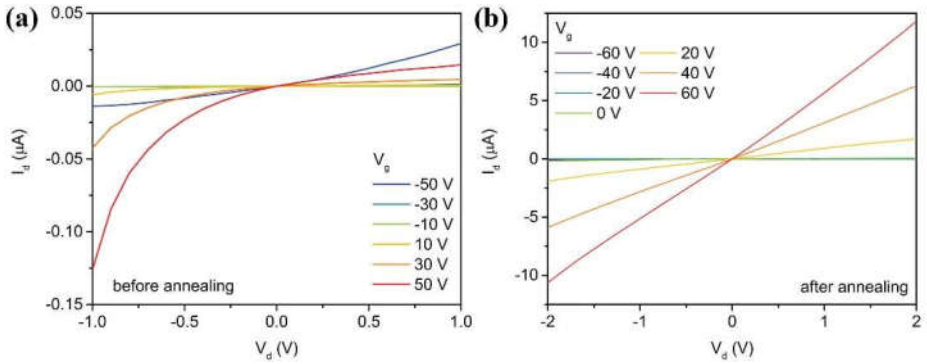

Figure 7.2 Repeat of the method proposed Cho et al.[1] (a) The output characteristic of the pristine fabricated 2H-$MoTe_2$ FET device, indicating high and asymmetric Schottky barriers at the two electrode contacts. (b) The output characteristic of the device after annealing, showing lower and more symmetric contact barriers.

Since laser ablation of the contact areas before the metal deposition of electrodes might be influenced by unwanted oxidation, the laser ablation of the contacts after the metal deposition was studied. First the 2H-WSe_2 FET device was fabricated. Then high-power laser was scanning along the source and drain electrodes. As shown in Figure 7.3, the device performance changes significantly. Before ablation, the device is ambipolar, with an electron mobility of 9.4 $cm^2V^{-1}s^{-1}$ and a hole mobility of 4.6 $cm^2V^{-1}s^{-1}$. After ablation, the device is ambipolar with a hole-dominant transport behavior, where the electron mobility decreases to 0.4 $cm^2V^{-1}s^{-1}$ and the hole mobility dramatically increases to 213.5 $cm^2V^{-1}s^{-1}$, which is among the highest reported values.[2-5] In the previous report by Seo et al.,[6] laser ablation on the electrodes would induce an increased p-type doping in the 2H-$MoTe_2$ accompanied by the shift of the cutoff region to the positive V_g. However, in the results presented in Figure 7.3, significant p-type doping is induced without obvious shift of the cutoff region. It needs further studies on the mechanisms of the huge enhancement in the hole mobility by laser ablation on electrodes and the difference in the cutoff region shift compared with the reported results.

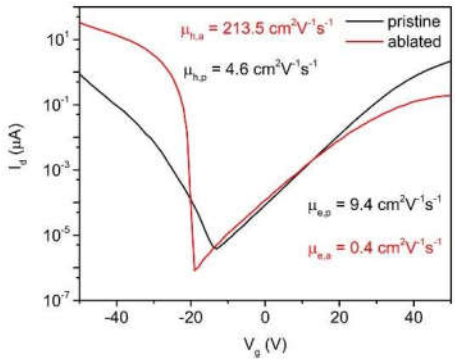

Figure 7.3 Laser ablation on the electrodes of the 2H-WSe_2 FET device, showing a significantly enhanced hole field effect mobility without obvious shifting of the cutoff region.

7.3 Outstanding Questions

For the light-tunable devices reported in the Chapter 4-6, there is still much room for the improvement of device performances. For example, for the demonstrated light-tunable bias-induced CDW phase transition in 1T-TaS_2 at room temperature (Figure 4.6b), the light response is very slow with the time constant larger than 20 s. However, in the report by Wu et al.,[7] the photo response could be very quick. The time resolved measurement from the ultrafast pulsed excitation (100 fs) showed a current rising time below 2 ns, after which the current could be held for about 30 ns, followed by a decay process for about 30 ns. The difference in the photo response time should be due to the laser intensity. In Figure 4.6b, the highest laser intensity is 160 mW/cm^2. While in the work by Wu et al.,[7] the intensity is 0.7 W/cm^2. Since this photo response is mainly due to the laser induced heating effect, a TaS_2 device on the substrate with a lower thermal conductivity may have a better photo response. On the other hand, the temporal response measurement after ultrafast photoexcitation shows that it takes about 60 ns for TaS_2 to restore its original state at room temperature, which is much faster than the current TaS_2 oscillators (about 1 MHz).[8,9] This means the frequency of TaS_2 oscillators can be improved further. To achieve this, multiple factors should be considered. For a shorter transition time from NCCDW to ICCDW and then back to NCCDW, the difference between the upper and lower threshold should be small, which however will lead to the small oscillation amplitude. A large resistance difference between the NCCDW and ICCDW is preferred, in order to get a wide

range of tunable frequency. A substrate with a high thermal conductivity should benefit the oscillation since a fast heat dissipation will speed up the transition from ICCDW to NCCDW. Besides, a small capacitance between the output and the ground is preferred.

For the light-induced controllable hole doping demonstrated in *Chapter 5*, as shown in Figure 5.13 and 5.14, a vertical-lateral hybrid P-N junction can be formed under small amount of ablation. This may be helpful to obtain a high photo responsivity. However, for logic circuit applications, pure p-type channels are desired. As a result, a thin channel is preferred for the logic circuit applications. However, when the sample is thinned to monolayer, its mobility will decrease with increased scattering.[10] The major advantage of the direct light writing of logic circuits is the great simplification of circuit fabrications, where the patterning and removing of passive layers are not needed. However, the demonstrated NOR gate device shows an ordinary performance. Its gain is smaller than the highest reported values of WSe_2 based inverters.[11,12] And the charge trapping is significant that the negative reset pulse is required to maintain the low output level. In the WSe_2 CMOS inverter reported by Yu et al., the highest gain value reached up to 38.[11] As shown in Figure 2.17a, the ambipolar WSe_2 was bottom-gated via a 20-nm thick Al_2O_3 layer. The n-type channel was achieved by n-type doping using AlO_x and with the low work function Ag as the contact metal. The p-type channel was achieved by p-type doping using F_4TCNQ and with the high work function Pt as the contact metal. Using metals with different work functions was aimed to decrease the Schottky barrier height, increasing the transconductance. A wide range of current saturation was achieved, leading to a low output conductance. These factors resulted in a high voltage gain. For the device demonstrated in Figure 5.15, one of the p-type channels was too short, which might lead to a poor current saturation. And all electrodes used Cr as the contact metal, leading to a high Schottky barrier and lowering the transconductance. And the p-type doping was insufficient that the p-channels were not completely turned off at high input voltages, making the low-level output unsatisfying. For the light-induced hole doping method, two issues need to be considered. One is the defect-induced scattering. The other is the relatively high power required for doping. For the latter, a substrate with a low thermal conductivity maybe helpful. For instance, do the doping on PDMS before the sample transfer.

For the light-tunable persistent switching of conductivity in BP/$SrTiO_3$ heterostructure, the main problem is its stability at room temperature. When the devices operated at low temperature, it showed a high performance with a large on/off ratio, a very long retention time and the multistage light tunability. However, when the device operated at room temperature, its performance was not good, especially the unstable off state (Figure 6.4a). As mentioned previously, UV light illumination will produce net positively charged defects near the interface, acting like a positive gate and turning off the BP channel. However, there is no barrier layer between the shallow region and the deep region in $SrTiO_3$. The low-level defect states in the shallow region will be easily refilled by electrons trapped in high-level defect states in the adjacent deeper region, leading to the relaxation of the off state. As mentioned in *Chapter 2*, a high potential barrier at the charge trapping layer is necessary to achieve a long retention time at the room temperature. For example, Lee et al. demonstrated a nonvolatile memory device based on graphene/Al_2O_3/AlO_x/Al_2O_3, where AlO_x was for charge trapping and Al_2O_3 was the barrier layer to reduce the back tunneling of trapped charges.[13] Xiang et al. reported a WSe_2/hBN/SiO_2 based nonvolatile memory device.[14] UV-light generated holes in the defect states of hBN were used for the nonvolatile storage. Instead of the spontaneously electron diffusion into nearby regions, a high gate voltage was applied at the same time to move the excited electrons into the WSe_2. The hBN has a bandgap of 5.9 eV and can form a type-I heterostructure with WSe_2.[15] Due to the large barrier height of mid-gap states, this NVM device showed a relatively stable storage. Both two kinds of devices required a gate voltage to write and erase the storage.

7.4 Outlook and Perspectives

As a localized excitation and heating tool, the light can be used to fabricate novel devices with arbitrary structures. For example, Chamlagain et al. reported the fabrication of ultrathin Ta_2O_5 from the TaS_2 using the thermal oxidation method.[16] The transformed Ta_2O_5 was uniform and atomically flat, with a high dielectric constant of 15.5 and few defects. With the transformed Ta_2O_5 as the dielectric layer, a high quality MoS_2 FET device

was demonstrated, with a mobility larger than 60 $cm^2V^{-1}s^{-1}$, a room-temperature near ideal subthreshold swing of 61 mV/dec and a wide current saturation. Light can transform arbitrary areas of TaS_2 to the Ta_2O_5, which can be used to fabricate patterned conductive channels in TaS_2 and study CDW behaviors under different patterned channels.

A good confinement of conducting channels of 2D materials is necessary for the studying of mesoscopic physics, such as the quantum transport in high-quality 2D electron gases[17] and valley filtering at the quantum point contact in bilayer graphene.[18,19] As mentioned in the previous section, in an hBN/WSe_2 heterostructure, with the photoexcitation and the back-gate voltage, electrons in the defects of BN can be excited and transferred into the WSe_2. Positive charges will leave in hBN and act as a positive gate, which will retain after the remove of light and control gate. This is called the photodoping.[14] With this photodoping effect with the help of shadow mask, Epping et al. reported the quantum confinement of the MoS_2 channel in the hBN/MoS_2 heterostructure.[20]

7.5 Outcomes Reflected in the Original Hypothesis

In the project, light control of electronic properties has been studied in three different systems, including the light-tunable CDW phase transition in the metallic 1T-TaS_2, the light-ablation-induced controlled hole doping in the semiconducting 2H-WSe_2, and the wavelength-dependent persistent switching of conductivity in the heterostructure of the narrow-gap BP and wide-gap $SrTiO_3$. Based on these control of electronic properties, different light-tunable electronic devices have been demonstrated, including the light-tunable CDW oscillator based on TaS_2, the WSe_2 NOR gate logic circuit directly fabricated by selected-area laser ablation, and the light-tunable multistage nonvolatile memory based on BP/$SrTiO_3$ heterostructure. These results prove that the light can be used in a wide range of 2D materials to control their electronic properties and the light-tunable 2D electronic devices with various functionalities can be achieved, which provide more opportunities for the wide range of applications of 2D materials in the future electronics and optoelectronics.

References

[1] S. Cho, S. Kim, J. H. Kim, J. Zhao, J. Seok, D. H. Keum, J. Baik, D. H. Choe, K. J. Chang, K. Suenaga, S. W. Kim, Y. H. Lee, and H. Yang. *Science* **2015**, 349, 625-628.

[2] G. Iannaccone, F. Bonaccorso, L. Colombo, and G. Fiori. *Nat. Nanotechnol.* **2018**, 13, 183-191.

[3] N. R. Pradhan, D. Rhodes, S. Memaran, J. M. Poumirol, D. Smirnov, S. Talapatra, S. Feng, N. Perea-Lopez, A. L. Elias, M. Terrones, P. M. Ajayan, and L. Balicas. *Sci. Rep.* **2015**, 5, 8979.

[4] H. C. Movva, A. Rai, S. Kang, K. Kim, B. Fallahazad, T. Taniguchi, K. Watanabe, E. Tutuc, and S. K. Banerjee. *ACS Nano* **2015**, 9, 10402-10410.

[5] H. J. Chuang, X. Tan, N. J. Ghimire, M. M. Perera, B. Chamlagain, M. M. Cheng, J. Yan, D. Mandrus, D. Tomanek, and Z. Zhou. *Nano Lett.* **2014**, 14, 3594-3601.

[6] S.-Y. Seo, J. Park, J. Park, K. Song, S. Cha, S. Sim, S.-Y. Choi, H. W. Yeom, H. Choi, and M.-H. Jo. *Nat. Electron.* **2018**, 1, 512-517.

[7] D. Wu, Y. Ma, Y. Niu, Q. Liu, T. Dong, S. Zhang, J. Niu, H. Zhou, J. Wei, Y. Wang, Z. Zhao, and N. Wang. *Sci. Adv.* **2018**, 4, eaao3057.

[8] G. Liu, B. Debnath, T. R. Pope, T. T. Salguero, R. K. Lake, and A. A. Balandin. *Nat. Nanotechnol.* **2016**, 11, 845-850.

[9] C. Zhu, Y. Chen, F. Liu, S. Zheng, X. Li, A. Chaturvedi, J. Zhou, Q. Fu, Y. He, Q. Zeng, H. J. Fan, H. Zhang, W. J. Liu, T. Yu, and Z. Liu. *ACS Nano* **2018**, 12, 11203-11210.

[10] M. W. Lin, Kravchenko, II, J. Fowlkes, X. Li, A. A. Puretzky, C. M. Rouleau, D. B. Geohegan, and K. Xiao. *Nanotechnology* **2016**, 27, 165203.

[11] L. Yu, A. Zubair, E. J. Santos, X. Zhang, Y. Lin, Y. Zhang, and T. Palacios. *Nano Lett.* **2015**, 15, 4928-4934.

[12] G. V. Resta, Y. Balaji, D. Lin, I. P. Radu, F. Catthoor, P. E. Gaillardon, and G. De Micheli. *ACS Nano* **2018**, 12, 7039-7047.

[13] S. Lee, E. B. Song, S. Min Kim, Y. Lee, D. H. Seo, S. Seo, and K. L. Wang. *Appl. Phys. Lett.* **2012**, 101, 243109.

[14] D. Xiang, T. Liu, J. Xu, J. Y. Tan, Z. Hu, B. Lei, Y. Zheng, J. Wu, A. H. C. Neto, L. Liu, and W. Chen. *Nat. Commun.* **2018**, 9, 2966.

[15] V. K. Sangwan, and M. C. Hersam. *Annu. Rev. Phys. Chem.* **2018**, 69, 299-325.

[16] B. Chamlagain, Q. Cui, S. Paudel, M. M.-C. Cheng, P.-Y. Chen, and Z. Zhou. *2D Mater.* **2017**, 4, 031002.

[17] R. Pisoni, Y. Lee, H. Overweg, M. Eich, P. Simonet, K. Watanabe, T. Taniguchi, R. Gorbachev, T. Ihn, and K. Ensslin. *Nano Lett.* **2017**, 17, 5008-5011.

[18] D. R. da Costa, A. Chaves, S. H. R. Sena, G. A. Farias, and F. M. Peeters. *Phys. Rev. B* **2015**, 92, 045417.

[19] A. Rycerz, J. Tworzydło, and C. W. J. Beenakker. *Nat. Phys.* **2007**, 3, 172-175.

[20] A. Epping, L. Banszerus, J. Guttinger, L. Kruckeberg, K. Watanabe, T. Taniguchi, F. Hassler, B. Beschoten, and C. Stampfer. *J. Phys. Condens. Matter* **2018**, 30, 205001.

Publications

Published as the first author:

1. **Chao Zhu**, Yu Chen, Fucai Liu, Shoujun Zheng, Xiaobao Li, Apoorva Chaturvedi, Jiadong Zhou, Qundong Fu, Yongmin He, Qingsheng Zeng, Hong Jin Fan, Hua Zhang, Wen-Jun Liu, Ting Yu, and Zheng Liu. Light-Tunable 1T-TaS_2 Charge-Density-Wave Oscillators. *ACS Nano*, **2018**, 12, 11203-11210.

Published as the co-first author:

2. Qundong Fu#, **Chao Zhu**#, Xiaoxu Zhao, Xingli Wang, Apoorva Chaturvedi, Chao Zhu, Xiaowei Wang, Qingsheng Zeng, Jiadong Zhou, Fucai Liu, Beng Kang Tay, Hua Zhang, Stephen J Pennycook, and Zheng Liu. Ultrasensitive 2D Bi_2O_2Se Phototransistors on Silicon Substrates. *Advanced Materials*, **2019**, 31, 1804945.

Published as a co-author:

3. Fucai Liu, **Chao Zhu**, Lu You, Shi-Jun Liang, Shoujun Zheng, Jiadong Zhou, Qundong Fu, Yongmin He, Qingsheng Zeng, Hong Jin Fan, Lay Kee Ang, Junling Wang, and Zheng Liu. 2D Black Phosphorus/$SrTiO_3$-Based Programmable Photoconductive Switch. *Advanced Materials*, **2016**, 28, 7768-7773.
4. Yongmin He, Qiyuan He, Luqing Wang, **Chao Zhu**, Prafful Golani, Albertus D. Handoko, Xuechao Yu, Caitian Gao, Mengning Ding, Xuewen Wang, Fucai Liu, Qingsheng Zeng, Peng Yu, Shasha Guo, Boris I. Yakobson, Liang Wang, Zhi Wei Seh, Zhuhua Zhang, Minghong Wu, Qi Jie Wang, Hua Zhang, and Zheng Liu. Self-Gating in Semiconductor Electrocatalysis. *Nature Materials*, **2019**, DOI: 10.1038/s41563-019-0426-0
5. Xiaowei Wang, Peng Yu, Zhendong Lei, Chao Zhu, Xun Cao, Fucai Liu, Lu You, Qingsheng Zeng, Ya Deng, **Chao Zhu**, Jiadong Zhou, Qundong Fu, Junling Wang, Yizhong Huang, and Zheng Liu. Van der Waals Negative Capacitance Transistors. *Nature Communications*, **2019**, 10, 3037.
6. Qundong Fu, Xiaowei Wang, Jiadong Zhou, Juan Xia, Qingsheng Zeng, Danhui Lv, **Chao Zhu**, Xiaolei Wang, Yue Shen, Xiaomin Li, Younan Hua, Fucai Liu, Zexiang

Shen, Chuanhong Jin, and Zheng Liu. One-Step Synthesis of Metal/Semiconductor Heterostructure NbS_2/MoS_2. *Chemistry of Materials*, **2018**, 30, 4001.

7. Rohit Abraham John, Fucai Liu, Nguyen Anh Chien, Mohit R. Kulkarni, **Chao Zhu**, Qundong Fu, Arindam Basu, Zheng Liu, and Nripan Mathews. Synergistic Gating of Electro-Iono-Photoactive 2D Chalcogenide Neuristors: Coexistence of Hebbian and Homeostatic Synaptic Metaplasticity. *Advanced Materials*, **2018**, 30, 1800220.
8. Hong Wang, Xiangwei Huang, Junhao Lin, Jian Cui, Yu Chen, **Chao Zhu**, Fucai Liu, Qingsheng Zeng, Jiadong Zhou, Peng Yu, Xuewen Wang, Haiyong He, Siu Hon Tsang, Weibo Gao, Kazu Suenaga, Fengcai Ma, Changli Yang, Li Lu, Ting Yu, Edwin Hang Tong Teo, Guangtong Liu, and Zheng Liu High-Quality Monolayer Superconductor $NbSe_2$ Grown by Chemical Vapour Deposition. *Nature Communications*, **2017**, 8, 394.
9. Shoujun Zheng, Fucai Liu, **Chao Zhu**, Zheng Liu, and Hong Jin Fan. Room-Temperature Electrically Driven Phase Transition of Two-Dimensional 1T-TaS_2 Layers. *Nanoscale*, **2017**, 9, 2436.
10. Fucai Liu, Jiadong Zhou, **Chao Zhu**, and Zheng Liu. Electric Field Effect in Two-Dimensional Transition Metal Dichalcogenides. *Advanced Functional Materials*, **2016**, 27, 1602404.
11. Jiadong Zhou, Fucai Liu, Junhao Lin, Xiangwei Huang, Juan Xia, Bowei Zhang, Qingsheng Zeng, Hong Wang, **Chao Zhu**, Lin Niu, Xuewen Wang, Wei Fu, Peng Yu, Tay-Rong Chang, Chuang-Han Hsu, Di Wu, Horng-Tay Jeng, Yizhong Huang, Hsin Lin,, Zexiang Shen, Changli Yang, Li Lu, Kazu Suenaga, Wu Zhou, Sokrates T. Pantelides, Guangtong Liu, and Zheng Liu. Large-Area and High-Quality 2D Transition Metal Telluride. *Advanced Materials*, **2016**, 29, 1603471.
12. Fucai Liu, Shoujun Zheng, Apoorva Chaturvedi, Viktor Zólyomi, Jiadong Zhou, Qundong Fu, **Chao Zhu**, Peng Yu, Qingsheng Zeng, Neil D. Drummond, Hong Jin Fan, Christian Kloc, Vladimir I. Fal'ko, Xuexia He, and Zheng Liu. Optoelectronic Properties of Atomically Thin ReSSe with Weak Interlayer Coupling. *Nanoscale*, **2016**, 8, 5826-5834.

To be submitted:

13. **Chao Zhu**, Xiaoxu Zhao, Xiaowei Wang, Jieqiong Chen, Peng Yu, Song Liu, Jiadong

Zhou, Qundong Fu, James H. Edgar, Junling Wang, Stephen J. Pennycook, Fucai Liu, Zheng Liu. Direct Laser Patterning of 2D WSe_2 Logic Circuit. *To be submitted.*